Three-Dimensional Routed Manifolds with Externally Inserted Cables

by

Keith J. Breinlinger

B.S. Massachusetts Institute of Technology (1996)

M.S. Massachusetts Institute of Technology (1997)

Submitted to the Department of Mechanical Engineering
in partial fulfillment of the requirements for the degree of
Doctor of Philosophy in Mechanical Engineering

at the

Massachusetts Institute of Technology

June 2003

Signature of Author: _____
Department of Mechanical Engineering
May 2, 2003

Certified by: _____
Alexander H. Slocum
Professor of Mechanical Engineering
Thesis Supervisor

Accepted by: _____
Ain A. Sonin
Professor of Mechanical Engineering
Chairman, Departmental Graduate Committee

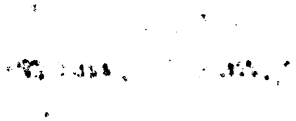

Three-Dimensional Routed Manifolds with Externally Inserted Cables

by

Keith J. Breinlinger

Submitted to the Department of Mechanical Engineering
on May 02, 2003 in partial fulfillment of the
requirements for the degree of Doctor of Philosophy
in Mechanical Engineering

ABSTRACT

The Automatic Test Equipment industry must maintain a tester accuracy of roughly one tenth the pulsewidth of the device under test (DUT). Funneling a vast number of electrical signals into a very tiny area to contact the DUT while still maintaining good signal fidelity is a problem not only in the ATE industry, but also for personal computers, network servers and supercomputers. As the speed of processors increase, ATE companies must find new ways to achieve the required accuracy.

A solution to this problem is investigated whereby a large number of semi-rigid coaxial wires are routed in 3D space from a low-density array (the tester side) to a high-density array (the DUT side). The three dimensional paths are subject to bend constraints and cannot intersect with any other paths. A software program has been written and tested that is able to find solutions to this 3D routing problem for many test cases. For relatively simple test cases with less than 15 wires, solutions can typically be found in under a minute. Once the geometries of the paths are determined, a block is made with 3D tunnels transversing through it. This part is created using a 3D additive process (e.g. stereolithography), and the coaxial wires are pushed into each tunnel. The maximum force used to insert a wire into a tunnel is limited by the force at which buckling occurs. Uncontrolled buckling of the coaxial wire will compromise electrical signal fidelity or cause opens and must therefore be prevented. To this end, models have been developed to predict the force required to push wires into a predetermined path. Relatively good experimental agreement, within 20% in many cases, was achieved for paths with radii of curvature to wire diameter ratios between 200:1 and 10:1. A perfectly elastic beam model is developed as well as an elastic-plastic beam model. Additional models are developed which account for the friction and the effect of clearance between the tunnel

and the beam. The model is used to guide the routing software such that no path is created that cannot have a wire inserted into it.

The solution proposed provides an excellent alternative to a printed circuit board for high speed electrical signals. The general method of using additive manufacturing to create tunnels to guide signal opens up many possibilities for not just coaxial cables, but fluid piping, optical fibers and solid wires. The solution has many further advantages and applications that are reviewed briefly but have not been investigated.

Thesis Supervisor: Alexander Henry Slocum
Title: Professor of Mechanical Engineering

Thesis Committee: Prof. Jeffery Lang
Prof. Sanjay Sarma
Prof. Alexander Slocum

Acknowledgements

I would like to thank all my friends, family, co-workers and professors who have provided support and encouragement throughout my time as a graduate student.

My co-workers at Teradyne have always been supportive of my endeavors especially Derek Castellano, Frank Parrish, and Simon Longson. I would like to thank those people who reviewed and edited my thesis in the final months without which this thesis would be riddled with even more errors than I'm sure it contains now. I would also like to thank Kevin Manning for enduring my brainstorming sessions on his whiteboard trying to resolve some mechanical issue or some better way to convey my thoughts onto paper. Many thanks to the software routing team, Arash Behziz, Christian Handsaker, Michael Gebis and Craig Robertson, who spent many a late evening talking about the difficulties of routing in 3D space. They not only provided support but taught me many real world essentials of programming and debugging as well as some incredibly valuable pieces of code that enabled the software router.

Many professors and colleagues have spent time discussing my thesis with me and I have gained insight and appreciation of the depth and richness of the problems I faced in each discussion. I would like to thank Prof. David Parks who spent multiple sessions with me discussing the intricacies of the insertion problem. I would like to especially thank Prof. Mike Brenner of Harvard University with whom I spent many hours talking about modeling of insertion physics and routing of multiple wires. He made me feel like an equal and was always patient and willing to listen. He provided me valuable insight to the solutions to of NP problems.

I'd like to thank Prof. Sanjay Sarma and Prof. Jeffrey Lang, two of my committee members, who have help guide my research and have always been patient with me despite my hectic schedule. I would especially like to thank Prof. Alex Slocum who has been a friend, an advisor and even a snowboard instructor to me over the years. He has supported and pushed me to excel in many different areas. From the lessons of Dr.Abbe and the principles of Saint-Venant to the best way to snowboard through moguls, Alex's eternal enthusiasm for life and design have provided me with the wisdom and energy to tackle almost anything.

My family has always supported me through all my educational endeavors. My mother is always lending a helping hand from making coffee to keep me awake or doing a final proofreading of this thesis, she is the best mom a guy could ever hope for. My dad, also a MIT alumni, has encouraged me and taught me (a lowly MechE) to understand some of the basics of course 6. My brother Josh has kept me sane and reminded me that nothing is worth worrying about too much. He always kept watch lest I study too hard and forget about having a good time.

Finally I would like to thank my wonderful fiancée, Shawndra who has always been supportive, loving and understanding despite her amazingly difficult work schedule. I am very fortunate to have her as such an integral part of my life. Words cannot express my gratitude.

Table of Contents

List of Figures

List of Tables

Overview of the thesis

The development of this thesis began with the need to improve the edge placement accuracy of the next generation of Automatic Test Equipment (ATE). The thesis covers the development of the project dubbed 3DST for Three Dimensional Space Transformer. The business of ATE is a complicated one, and is not well understood by the average person. Therefore, Chapter 1 is an introduction to the business of testing high speed processors. It describes some history of early test systems and how the need to test arose. It then briefly covers the evolution of ATE systems over the past 40 years. Finally, a brief discussion of the economics behind testing sheds some light on why the ATE industry can charge such a premium for a system with slightly better edge placement accuracy (EPA).

Chapter 2 discusses the basic requirements for a replacement to the PCB which will improve EPA. It briefly summarizes the work that has been done on the project so the reader can place the following chapters in the proper framework.

Chapter 3 reviews transmission line theory as it relates to EPA. It attempts to show why small coaxial cables are superior to printed circuit board (PCB) traces.

Chapter 4 highlights the technology of additive manufacturing (AM), with a particular emphasis on stereolithography (SLA) as this is the method currently used to fabricate parts for the project.

At this point, the thesis should have established the background of test, the importance of good EPA, the superiority (of its effects on EPA) of coaxial cable over PCB trace, and the methods of additive manufacturing. Now the reader should

understand why the 3DST project was undertaken and can appreciate some of the major difficulties in realizing such a goal. The initial two biggest challenges are determining the routing paths for the tunnels and understanding the forces involved when inserting cables into the tunnels created by the SLA method. The following two chapters discuss these two challenges which are the major academic contributions of the thesis.

Chapter 5 covers the forces involved when inserting wires into freeform paths. Multiple models are developed, starting with the simplest effects and adding complexity and accuracy to the model with each successive model.

Chapter 6 discusses the routing algorithms that were developed to solve the problem of non-intersecting, finite diameter, length-matched and length minimized paths with bend radius constraints in a constrained 3D volume.

Chapter 7 is a detailed account of the methods used to design and manufacture the 3DST.

Chapter 8 discusses future work and areas of research that might be pursued in both software routing and further development of insertion physics. It also covers other applications (beyond ATE) where this technology could be successfully used.

Chapter 9 summarizes the results of the thesis and makes some final conclusions and observations.

Chapter 1 – Introduction

1.1. The History of Computers and Automatic Test Equipment (ATE)

The first computer was the abacus and was invented in China around 3000 B.C and can be used to perform simple arithmetic operations [6] [72]. It consists of a series of beads mounted on rods and bound together in a wooden frame. It is used to "remember" the number by counting up the beads that are in contact with the center beam. The beads in the upper deck count as five and those in the lower deck count as one. Using the abacus, a human can add and subtract large numbers quickly and easily (multiplication and division can be performed as well).

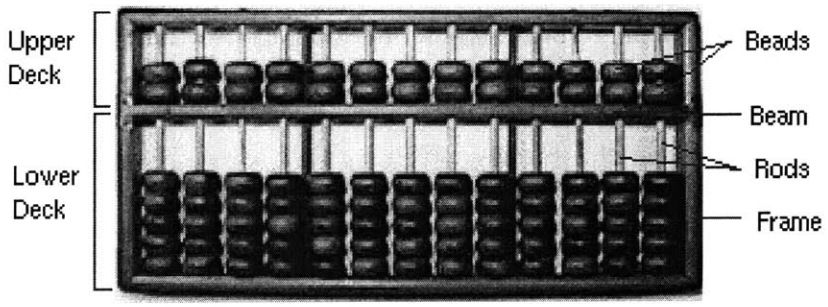

Figure 1 - A simple abacus

Although it is not documented, the testing of these devices by the manufacturer probably involved making sure all the beads slid relatively easily on the rods and perhaps counting that the number of beads on each rod and in each deck was correct. This testing could be done by visual inspection and moving the parts by hand. If some bead was

missing or broken it could be replaced. If a bead was sticking or did not slide well, perhaps the hole was made a little bigger or the rod it was sliding on was trimmed down. Assuming bead production was not perfect and roughly one percent of the beads had some problem, on average, 60% of the assembled abacuses would have a least one bad bead and would need to be reworked. If a manufacturer were trying to speed up production, the rework time would be a major factor (the abacus would need to be dismantled, the faulty bead replaced, and then put back together and re-tested.) Obviously, this is not an ideal situation. One solution to the problem is to test the beads individually, before they are used in the assembly. A simple go/no-go gauge (a wooden rod of a given size somewhat bigger than the rod which the bead would be slid onto.) might suffice. In this way, the assemblers of the abacus would only need to worry about interaction between the beads and rods, as the tested beads would be "known good beads". The builders of computers today face the same issues as the abacus builder; they need to test the components of the computer before they assemble the parts into a complete system. Today's computer chips, unfortunately, cannot be tested with a wooden rod.

The first mass produced semiconductor was a diode and was created by bonding two pieces of germanium or silicon together. One piece was doped as p-type and the other as n-type. These diodes were wired together to create simple circuits and more complicated computers from 1950 to the late 1960s. Millions of these diodes were created but due to processing problems and a poor understanding of the criticality of the surface and containments, yields were low. One technique diode manufacturers used to counter the yield problems was to ship 20% to 30% more than was ordered. The

manufacturers knew that some of the components were bad, and thus the extra parts shipped with every order helped ensure the desired amount of good parts was received. The overshipment technique has problems. First, the manufacturer is forced to ship more than ordered, cutting into profit margins. If the overshipment was not enough, customers would complain and the manufacturer might lose business and further cut into profit margins. Finally, the customer would assemble these components into larger systems with hundreds or thousands of diodes. Using the basic statistical formula of Equation (1.1), the results of which are shown in Table 1, it can be seen that computer manufacturers faced a daunting challenge for assemblies with a large number of diodes. Note that Equation (1.1) is the same governing equation that was used to determine the failure rate of the abacus assembly.

$$\text{Probability of a bad system } = 1-\left(1-P_{good\ diode}\right)^{(\#\text{ of diodes in system})} \tag{1.1}$$

If the probability of receiving a bad diode and installing it in the computer system was one in ten (a conservative estimate from overshipment percentage, i.e. 90% were good), a system with just 20 diodes would typically have a failure rate of 88% with an average of 2 bad diodes per system. Any system with over a hundred diodes would basically be guaranteed to fail without debugging and finding the faulty diodes. The table below further illustrates the magnitude of the problem.

Probability of a bad diode	# of diodes in system	% of systems that fail
.90	5	40.95%
.90	20	87.84%
.90	100	99.997%
.99	20	18.21%
.99	100	63.40%
.99	1,000	99.996%
.9 999	100	0.99%
.9 999	1,000	9.52%
.9 999	10,000	63.21%
.999 999	1,000	0.10%
.999 999	10,000	0.99%
.999 999	1,000,000	63.21%

Table 1 - The challenges of assembling working assemblies with many components

The need to test components before they were installed into a larger system quickly became an absolute necessity. Teradyne's first product was a diode tester designed for the express purpose of testing discrete components before they were installed into a larger subsystem [78]. The diode test limits were programmed with the rotary dials on the front panel and pushing a "start" button on the side executed a test. Once the front panel was set, a human operator would test a stack of parts one by one by continually picking a part from the untested bin, placing it in the test socket and hitting the start button. The result of the test was a green light to indicate a "pass" and a red light to indicate a "fail". The operator would then place good parts in one bin and bad parts in another bin (to be thrown away or analyzed for failure modes). The simplistic

diode test consisted of sending the limit voltages to the device and determining if they were within the desired limits set by the user.

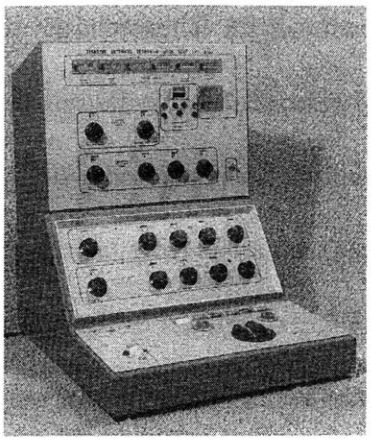

Figure 2 – Teradyne's first tester

Many test systems made by Hewlett-Packard and Teradyne would test diodes, Zener diodes, resistors and transistors. These components are now referred to as discrete components because in one package there is just one electronic device. These components were being used in the earliest supercomputers made by IBM and Sperry-Rand. They were huge machines that cost a small fortune and could only be used by atomic energy labs.

In 1959, nearly fifteen years after the first semiconductor device was produced, Jack Kilby made the first integrated circuit at Texas Instruments. Multiple diodes and transistors were connected together with gold wire. Diffusing dopants into the semiconductor allowed him to locally change the properties of the substrate from N to P and back to N.

Jean Hoerni and Robert Noyce at Fairchild Semiconductor invented a process to create aluminum wiring on the surface of the substrate. Jack Kilby and Robert Noyce

share the patent for the integrated circuit. The two inventions made it possible to create multiple transistors connected together on a single piece of silicon. This enabled companies to make far more complicated circuits in a very small area and at a fraction of the cost of a discrete component circuit. This technology took some time to be commercialized and the first integrated circuit did not show up until 1963.

With the advent of multiple transistors on a single piece of silicon, more complex functionality could be achieved. Inverters (implementing the NOT function), OR and AND gates became the basic building blocks of the more complicated computers. Within a short time, a single device had hundreds and then thousands of transistors on it. These devices would be combined with other devices to create a useful computer. The discrete component testers now had a more difficult task. Instead of measuring a one to one input to output device (such as a diode), the tester had to deal with the more complicated task of testing something like an AND gate. An AND gate should return a logical zero (roughly 0 volts) unless both its inputs are logical ones (roughly 5 volts) in which case it should return a logical one. The automated tester would need to verify all the different combinations of inputs that could occur and ensure that under all conditions, the device operated as intended.

Devices quickly grew in complexity and in 1968, Gordon Moore and Robert Noyce founded Intel and just three years later, they released the 4004, the world's first commercial microprocessor [33]. The 4004 had a clock speed of 108kHz and had 2250 transistors. By comparison, the 2002 Pentium 4 has 55 million transistors, and runs at 2200 MHz. As the computers and other electronic devices became more widespread, the volumes increased such that the human operator who fed the automated test equipment

could not test parts fast enough to keep up with demand. A means of automating the delivery of the device (replacing the human operator) became a necessity. The first handlers in the industry would take a tube of devices and using gravity, allow a device to slip into the test socket, test it and then eject the part and typically sort it into one of two bins (good or bad).

As the devices became more and more complex manufacturers began to realize that the packaging of the device was a significant portion of the overall cost of the device. If the abacus builder had a processing step to paint and decorate the beads and the painting step required a significant investment (time and money), it might behoove him to not paint bad beads. If he was able to test beads before the painting and decorating step, he could save money. The manufacturer of packaged electronic components has the same dilemma; testing before packaging will save the added cost of packaging bad parts. The impetus to test before packaging was thus born. The equipment used to move the bare silicon wafer to the test probes is called a prober. Once the prober and tester deem a die acceptable, it is referred to as a "known good die". The wafer is then sawed into pieces and the good parts are packaged. After packaging, a final test step is done with a handler and a tester. These three pieces of equipment (testers, handlers and probers) make up the Automated Test Equipment (ATE) industry.

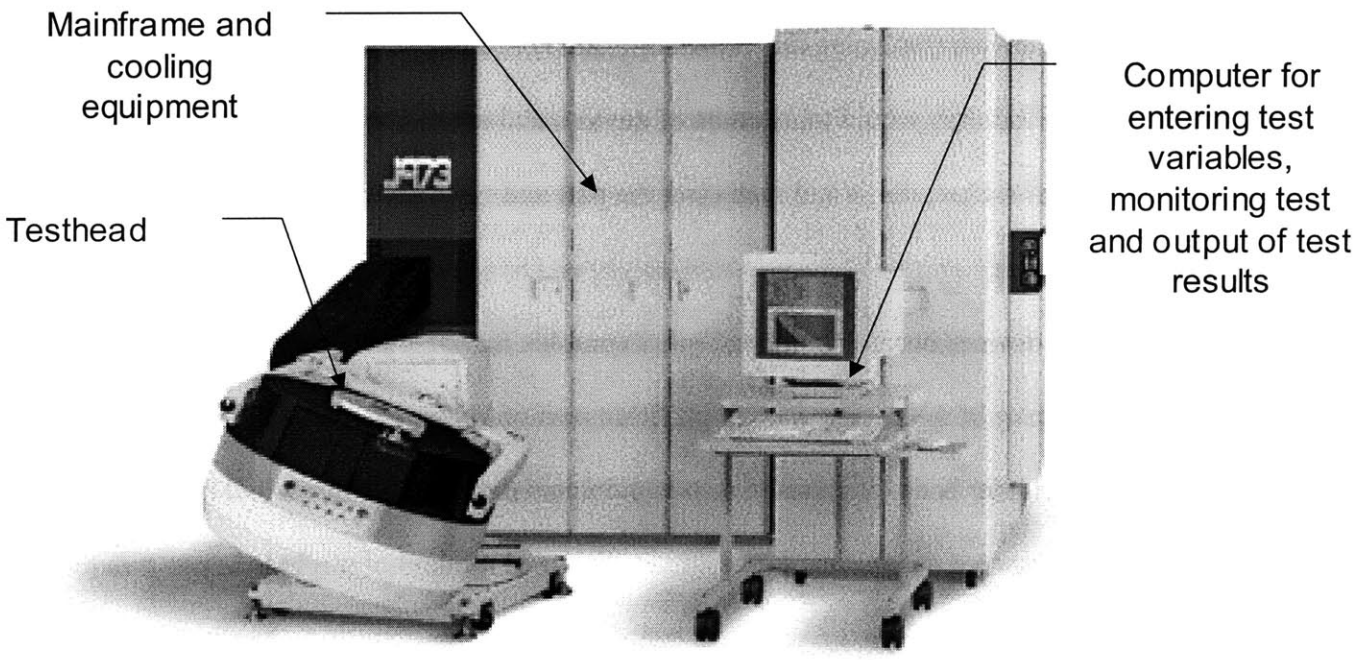

Figure 3 - A modern day ATE with a single testhead

As chip manufacturers have increased the speed and complexity of their devices the test companies have strived to keep the tester performance well ahead of the latest generation of devices. A general rule of testing is that the tester should be at least ten times more accurate than the object being tested. For example, if you wish to measure the length of a long bar to within an inch, the ruler should be graduated in at least tenths of an inch. This rule of thumb has been applied to electronics testing as well. For example, if the DUT (Device Under Test) should run at 1.5 GHz, the tester should be able to have "graduations" of 15 GHz, or said more accurately a tester used to test a 1.5 GHz device should have an EPA (Edge Placement Accuracy) of 67ps. The pulse width of a 1.5 GHz signal is 667ps, thus a 67ps accuracy is 10% of the pulse width. The rational for this rule of thumb is described in Section 1.8

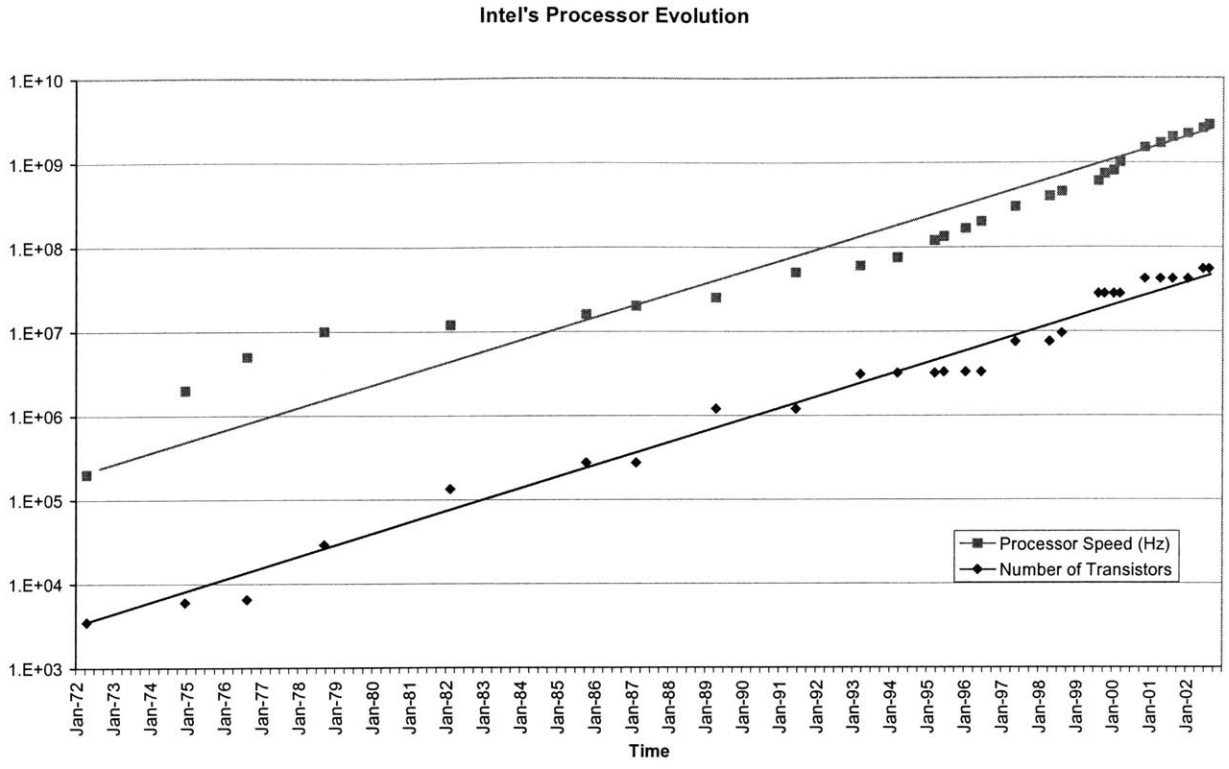

Figure 4- Speed and number of transistors of Intel processors vs. time

The pace of the microprocessor evolution has forced ATE companies to design exceedingly complex and fast test equipment to try to test all the functionality of these complex devices and still maintain accuracy an order of magnitude greater than the cutting edge of microprocessor development.

1.2. The funneling problem

ATE vendors have an extraordinary difficult problem trying to create a tester that can operate ten times faster than the latest processors produced by Intel, AMD and others. To test these devices at speed, multiple printed circuit boards are required to test a single device. A drastic difference in surface area (shown in Figure 5) exists if the test equipment's input area (area of all board edges) is compared to the output area (area of the DUT).

The signals sent to and received from the DUT (corresponding to drive and compare, respectively) must be funneled from the board edge to the DUT. This funnel typically consists of electrical cables, connectors and printed circuit boards. The electrical characteristics of the funnel directly impact the accuracy of the tester.

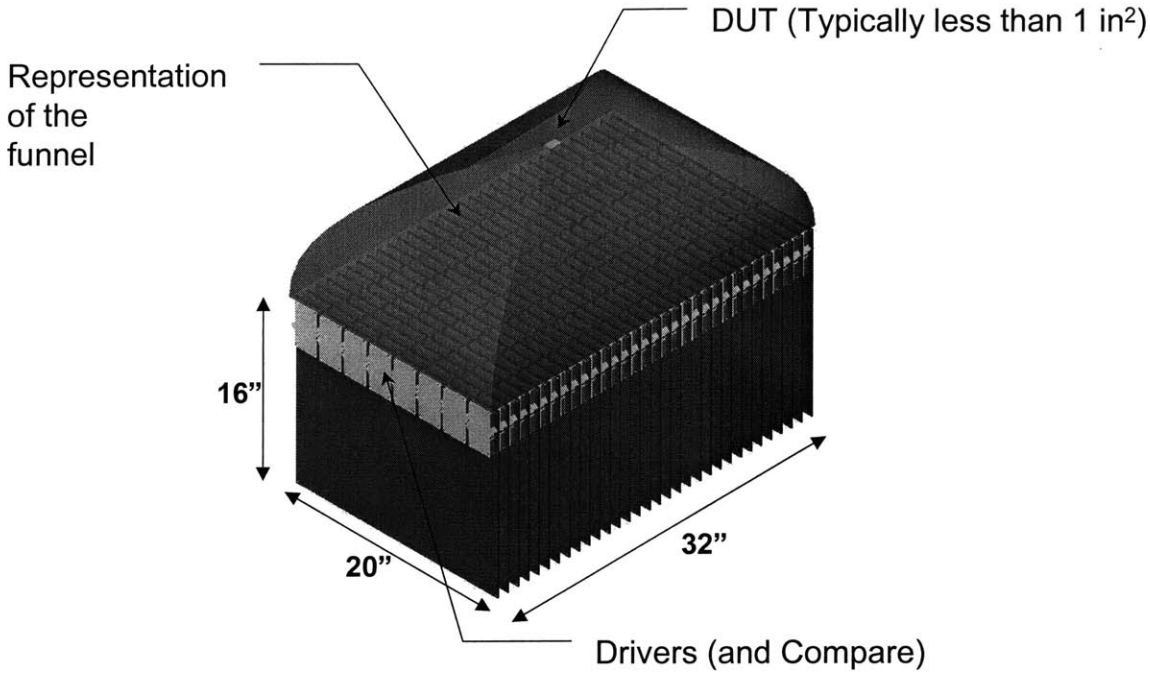

Figure 5 – A scale view of the inside of an ATE testhead compared to the DUT

1.3. What is the test?

Testing high speed devices requires a complex and proprietary test program developed for each specific device. Modern high performance microprocessors, such as the Intel Pentium 4, contain over 50 million transistors. To gain an understanding of the testing, one of the most basic logic devices, an AND gate, is considered. The functional testing of such a device would consist of sending each of the 4 input combinations and testing for the expected output values. In this example, not only would the tester need to

determine if the proper logic value was received, but if the value was within the given output voltage range specifications (e.g. 4V to 5V for a logical "1" and 0V to 1V for a logical "0"). If a 3.8V output level was detected (when given two logical ones within the input specs), then the tester would deem the device unacceptable. The tester should give the AND gate a variety of input range combinations and again verify the output. Testing the speed of the device requires the tester to send the AND gate the input combination at some specific time and then measure the incremental time required until the output reaches the appropriate level.

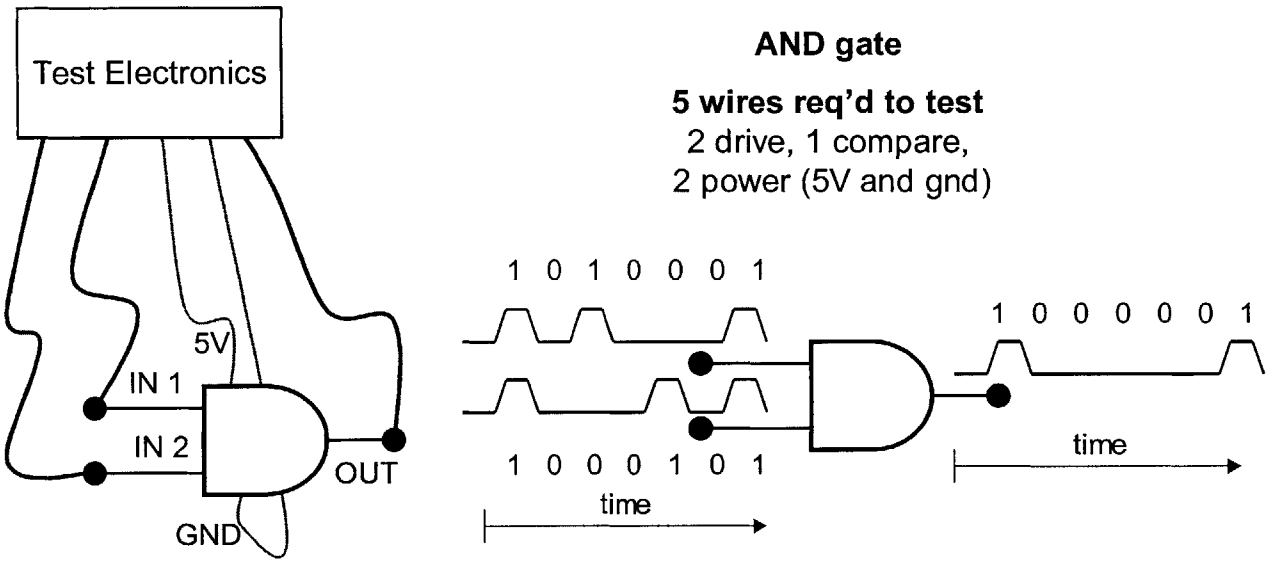

Figure 6 – A schematic of the test equipment to test a simple AND gate

Truth Table for AND gate		
Input 1	Input 2	Output
0	0	0
0	1	0
1	0	0
1	1	1

Table 2 - Truth table for AND gate

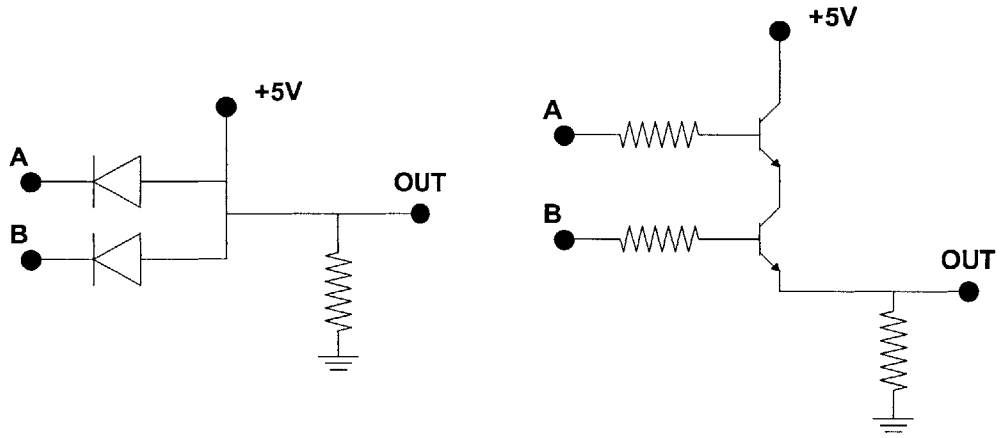

Figure 7 – An AND gate built from diodes (left) and transistors (right)

The AND gate is used extensively in larger circuits. It can be constructed using two diodes or two transistors (plus resistors) as shown above.

1.4. ATE Funnels

To accurately measure the timing of the device, an electrical signal must be sent down a wire and arrive at the device. The drive signal has a rise time associated with it as it leaves the drive circuitry. As the signal moves from the drive circuit to the DUT, the rise time and signal levels are degraded and the point at which the signal arrives at the DUT cannot be determined exactly. As the signal travels through the funnel, it is subject

to noise from other signals (crosstalk), distortions of the signal edge (due to discontinuities) and other influences that lower the tester's accuracy.

The signal from the drive chip circuitry transitions to the surface of the pin electronics board, and then travels (typically) through a via, along an internal printed circuit board (PCB) trace, through a second via, to a electrical connector, through a wire, to a connector on another printed circuit (an interface board) through another via, an internal trace on the interface board, and through a fourth via.

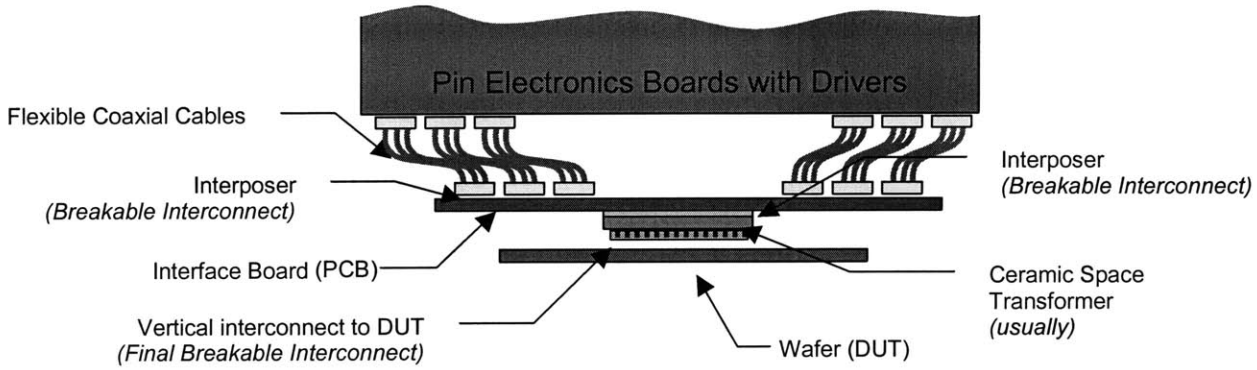

Figure 8 – A cross sectional view of a high performance ATE system

From there (interface board or probe card) the signal must transition through another interconnect before it reaches the DUT. The details of the interconnect and the final contact to the chip depends on the chip size, number of contacts, and whether the device is a bare die or has been packaged. Because of the multitude of different devices, there are a number of different technologies and configurations to contact the DUT. If the contribution of each of these components is analyzed, the greatest contributor to the detrimental effects of timing accuracy is typically the interface board.

The funnel can be broken into two functional groups: the interconnects and the transmission lines. The interconnects (typically) exist between every transmission line. Interfaces (and hence easily breakable interconnects) are required because testers are universal and DUTs are specific. Any time the DUT changes (e.g. a new device or a shrink of the same device), a new funnel must be implemented. Rather than changing the entire funnel, only a small piece needs to be changed if there are breakable levels in the funnel.

For interconnects, the key factor for high speed electrical performance is matching its impedance to the rest of the transmission lines in the funnel. The interconnect must be close to the nominal impedance throughout its entire range of travel to minimize reflections. Losses (that are not due to reflection) are not too important in the interconnect structure, as they are generally short in length when compared to the overall funnel length.

The transmission lines make up more than 90% of the length of the funnel. Consistency of impedance and minimization of loss is very important. These transmission lines are usually made up of cables (coaxial or other) and printed circuit boards. Eliminating the printed circuit board and replacing it with a cabled solution will drastically improve tester accuracy. Over the past five years ATE architectures have slowly eliminated nearly all printed circuit boards in the funnel, such that effectively only one printed circuit board remains. This circuit board is called the probe card or interface board and is the last level of funneling with the smallest traces. Changing this last level of funneling from a PCB to a group of cables would be feasible only for small ATE volumes (hand assembly of hundreds of small cables requires a human operator and a

significant amount of time.) Every change of a DUT type requires a new last level funnel (the interface board in Figure 8). A cable set is not easily changed and thus PCBs are preferred due to the ease of manufacture. This thesis specifically addresses a method to create an easily manufacturable, high density, coaxial cable assembly to replace the PCB in ATE applications.

1.5. Transmission Line Basics

A transmission line transmits a signal from one end to the other. At slow speeds, the details of the path through which the signal travels has little impact on the fidelity of the signal. A mechanical analog is a slowly changing pressure at one end of a series of

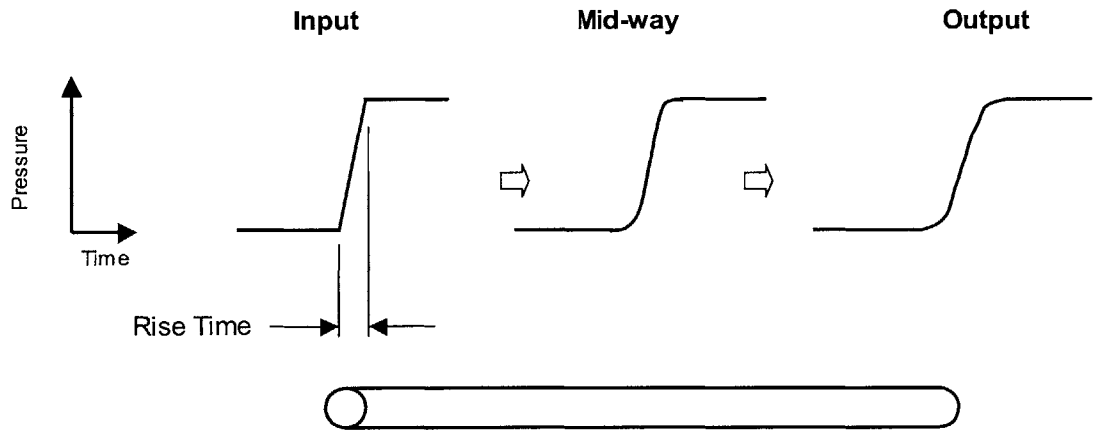

Figure 9 – A schematic representation of a rising edge as it moves along a transmission line

pipes with elbows, T-sections, partial clogs, and changing pipe diameters. If the pressure at one end is changed slowly, (with respect to the time constant of the piping) the pressure at the opposite end will track the pressure at the start nearly exactly. More precisely, if the rise time of the pressure is long when compared with the characteristic

time of the pipe (the length of the pipe divided by the speed of propagation), then the response can be modeled approximately as steady or DC.

If the pressure is changed rapidly (with respect to the pipe characteristic time), the situation can change dramatically. The frictional losses of the pipe will cause the rise time to be degraded as illustrated in Figure 9.

The quick changes of pressure are attenuated, such that when graphed we can see sharp corners become rounded. The slope of curve is decreased as the pressure wave travels down the pipe. The wavefront will be reflected whenever the effective diameter is changed. Reflections will also occur at bends (thus maximizing the bend radius is a good idea) and "T" junctions with one end closed off (Imagine the plumber ran out of 90 degree bends, but instead formed one using a "T" junction and capped one end.) The electrical transmission line has many close analogies. The "T" junctions are called stubs and are formed when vias connect to traces on an inner layer of a PCB. The frictional losses in the pipe are analogous to resistance. The head losses that occur in piping bends also occurs in a bent electrical wire, the greater the bend the greater the loss for both electrical and fluid transmission. The electrical transmission line details are explained in further detail in Chapter 3.

1.6. Funnels in the industry

The history and evolution of the ATE industry reveals many trends that can be extrapolated to future improvements. Looking back to the earliest testers, the basic

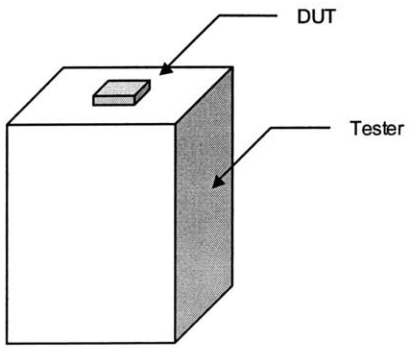

Figure 10 - A simple early tester

design consisted of a single box in which a device could be inserted into a socket and tested. This box (called the tester) contained all the test electronics boards and power supplies. This design typically used natural convection to cool the test boards since it was cheap, effective and the power levels of the test boards were low. This type of tester is shown in Figure 10.

As the device complexity increased, the requirements on the tester grew as well. The test boards had to contain all the functionality to test the device, so each board contained the drive and receive circuitry as well as analysis circuitry. The drive circuitry sends the input signals to the DUT that mimic the signals it should receive in its intended environment. The receive circuitry digitizes the output signal received from the DUT. Analysis of the digitized signal is compared with the specifications for the device (set by the user of the ATE.) The effect of growing complexity of the DUT was an increase in the size of the boards in the tester and hence an overall increase in the size of tester.

At the same time, the DUTs tended to increase in speed, thus making the characteristic time of the electrical path to the DUT to become a concern. The length of the electrical path to the DUT was growing in length (due to increasing size of the test

boards) while the rise time of the signal decreased. Both effects have a negative impact on the characteristic time of the electrical path. Designers of ATE were compelled to find a solution that decreased the electrical path length to the DUT. The designers did this by splitting the tester into two pieces.

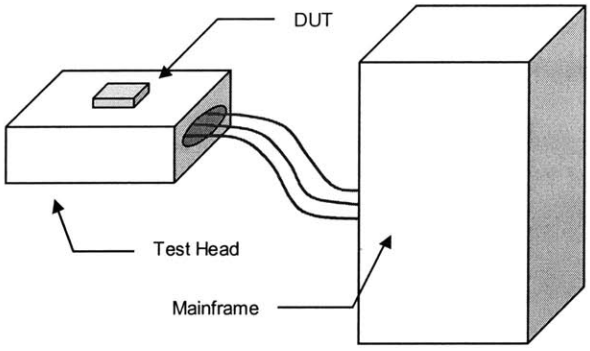

Figure 11 - A tester with a simple testhead and mainframe

One piece (the testhead) would be placed as close to the DUT as possible and the boards in that piece would be only the ones that sent and received the high speed signals. Other boards "told" the boards in the testhead what type of signal to send and when to send it. Analysis boards received the digital information from the testhead and determined if the DUT was operating within specifications. The architecture of the system placed the pin electronics (PE) boards in the testhead with the analog to digital converters (for comparing signals) and the digital to analog converters (for the drive signals) as close to the DUT as possible. All other functions, the analysis (of the received signal) and the pattern generator (tells the PE boards what to send to the DUT and when), existed in the mainframe.

The new testhead architecture allowed for very short electrical lengths from the pin electronics boards in the testhead to the DUT. As more and more electronics were packed into the testhead, the temperature of the PE boards rose. One solution would be to use larger heatsinks and space the boards in the testhead further apart (to increase the effectiveness of natural convection). However, by increasing the board pitch in the testhead, the length of the electrical path to the DUT is also increased, so this was not desirable. Instead, forced convection air cooling was used to pack more electronics into a smaller volume.

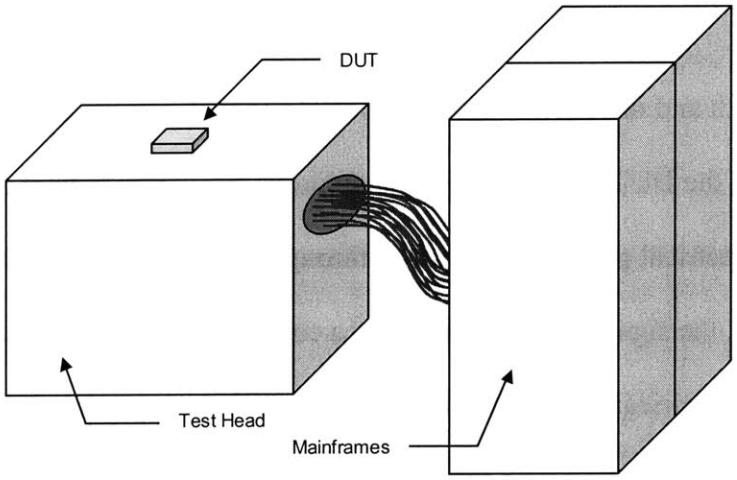

Figure 12 - Current ATE architecture: A large high density test head and mainframe

As one might expect, as time passed devices grew more complex and ran faster. The testhead and the support mainframes grew in size and complexity to match the devices being tested. The testheads, in the drive to keep electrical lengths short while increasing functionality, eventually required liquid cooling.

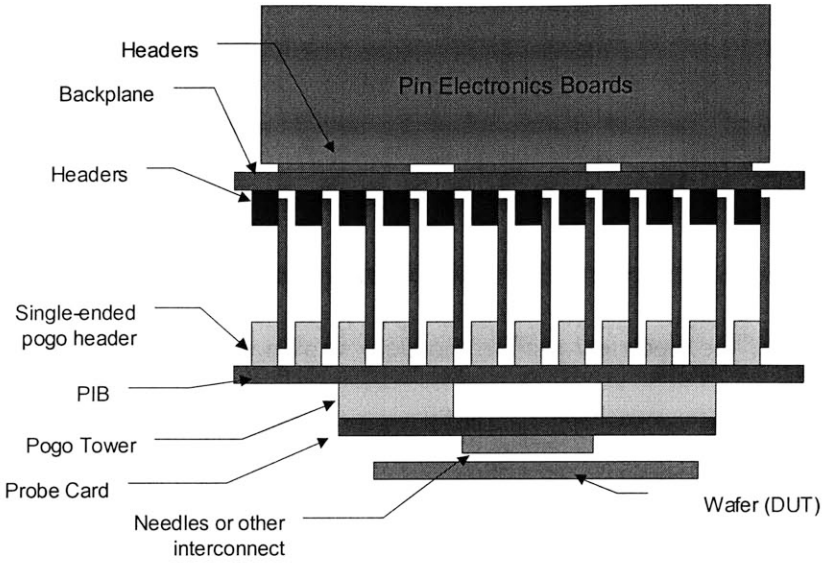

Figure 13 - Cross sectional view of testhead for testing of devices to 200 MHz

The length and integrity of the signals in the funnel is of utmost importance to the determination of the DUT characteristics. Examining the funnel system depicted in Figure 13, the electrical path must transition through many layers to reach the DUT. Tracing the path, the signal must pass through a connector on the PE board to a backplane. The electrical signal must then pass through the backplane to another bank of connectors to boards orthogonal to the backplane. From these boards, the electrical signal transitions through an interface board. This board is used to customize the tester for specific types of test; one type of board funnels signals to a round array for probing, while another board is designed for testing multiple devices in parallel (and thus forms a rectangular grid array of signals). From the array of pads, the electrical signals are passed through a spring pin array to a final PCB where the signals are funneled to an array of needles or similar compliant interconnect to touch the pads on the DUT. In summary, the electrical signal must pass through four printed circuit boards and five electrical connections. Each connection represents a discontinuity that degrades and

reflects the electrical signal. Each path on a printed circuit board typically has at least 2 vias and some length of internal trace. The vias have stubs which reflect and attenuate the signal. The sharp transition of the signal at the via and at bends on the internal trace reflect the signal. While a good high speed PCB design would minimize any sharp bends on a layer, there is no design freedom to smooth the transition from via to trace. It should also be noted that many PCBs are routed with the aid of CAD software and auto-router software, and these programs are not designed to make smooth sweeping curves. It is much easier for the human and the computer to route paths that are straight or have a few straight sections with sharp bends, and thus these paths are not optimized for high speed signals.

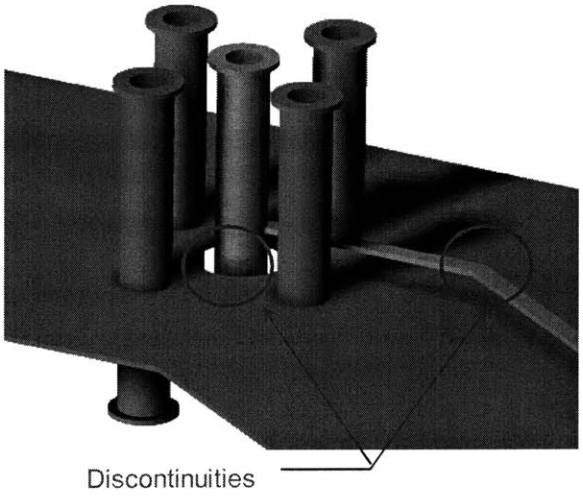

Figure 14 - A view inside a typical PCB. 4 ground vias surround a single signal via.

Due to these problems, we can see that one easy way to improve the performance of a high speed tester is to reduce the number of different interconnection levels and the number of printed circuit boards through which the electric signal must pass. Following the evolution of the ATE funnels, the trend of minimizing interconnections and elimination of printed circuit boards is seen. The tester funnel in Figure 13 was upgraded

after a few years to replace the orthogonal boards with cables to improve high speed performance and decrease some of the trace length on the interface board.

The next tester platform that was developed sought to get greater performance, and removed the backplane from the electrical path. The number of printed circuit boards in the funnel was reduced to two and the number of interconnects was reduced to four.

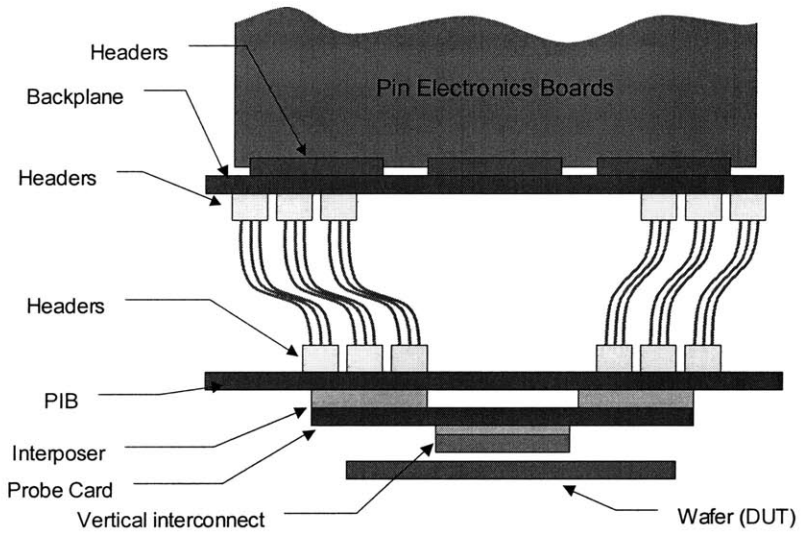

Figure 15 – Cross sectional view of testhead for testing of devices to 400 MHz

A few years later as the need for speed was increased, a new tester design was required. Shown in Figure 16, is the latest funnel architecture. All but one circuit board has been eliminated from the funnel and only three interconnects remain. Examining this funnel, the signals transition from the drive circuitry to coaxial cables. From the coaxial cables, the signal transitions to the probe card or interface board. The probe card still has two vias and an internal trace path, and this last remaining printed circuit board represents the worst piece of the electrical signal path. More precisely, if the

contributions of each section could be tallied individually, the printed circuit board would have the greatest electrical loss and would degrade the electrical signal the most.

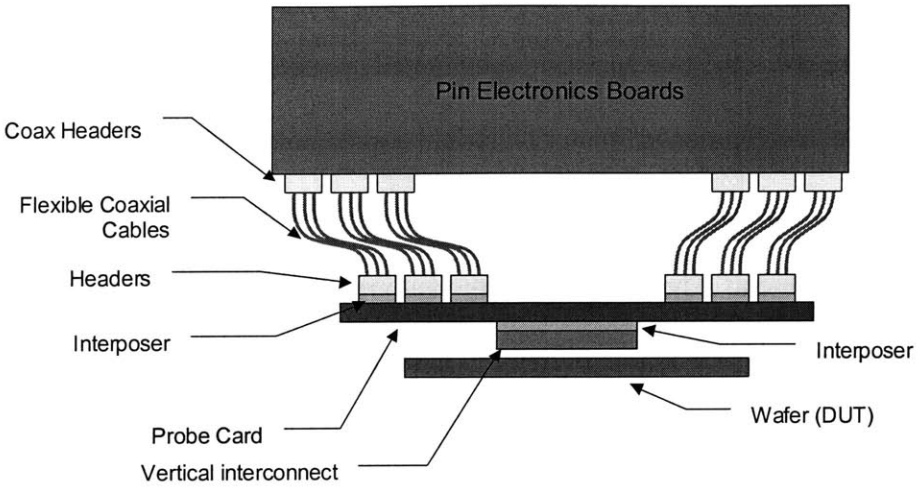

Figure 16 - Cross sectional view of testhead for testing of devices to 800 MHz

1.7. Trends of the industry

The ATE industry has developed a host of different technologies to address the ever increasing demands of testing high speed devices. As described above, the elimination of circuit boards and interconnects in the tester architecture has been evolving for many years. Many other solutions have been implemented in various stages of the ATE development. A brief listing of some of these techniques is given below.

Creative circuitry designers have found ways to squeeze more signal out of the existing pathways by first determining how the signal will be degraded and then sending a compensation signal on top of the signal to be sent. By partially compensating for discontinuities, the rising and falling edges of the signal when they reach the DUT will still be relatively clean. This is a type of feed-forward compensation.

Printed circuit board manufacturers have been hard at work developing lower loss dielectrics to allow for higher speed traces. Those that perform the best mix Teflon and other materials, but are still many times worse that pure solid Teflon.

Every interconnection between one medium and another requires some type of compliant interconnects as the two surfaces to be mated are not perfectly flat and planar to one another. The development of better electrical connections and coaxial connectors has improved the discontinuities (they are impedance matched closer to 50 ohms) that existed in earlier equipment. The designers of the automated test equipment have been pushing hard to make interface boards flatter and more planar such that the required stroke of the interconnect is smaller. This results in smaller overall height interconnects and thus many effects of the discontinuity are mitigated by the short overall length.

In an effort to reduce the overall length of the signal pathways that exist in the funnel, one could either increase the area of the DUT (spreading out the DUT signals to a lower density) or decrease the area of the tester. The area of the DUT also directly impacts its price (wafer cost and fixed processing cost per wafer (regardless of how many die per wafer)). In order to avoid huge, expensive personal computers, the choice is obvious. To accomplish this feat, ATE companies have switched from air cooled boards to liquid cooled boards. This allows greater packing density of circuits in the testhead and although it makes the testhead heavier and more expensive, it also makes it smaller. The smaller testhead uses shorter cables to reach the DUT and thus increases signal fidelity at the DUT.

1.8. Economic justification for high performance funnels

The manufacturer of high performance DUTs must guarantee that their devices do not fail. The test equipment determines the maximum speed of each DUT and the manufacturer sets the internal clock on the devices to operate at some speed lower than the maximum. To make a uniform product line, the manufacturer chooses a few speeds to set all devices to. If a DUT could operate at 1.579 GHz, the DUT will be put in the nearest lower bin (1.5 GHz). The importance of tester accuracy should now be readily apparent. If the tester determines that a particular DUT runs at 1.55 GHz successfully, but the tester is only accurate to ± .075 GHz, the device could operate as high as 1.55+ .075 = 1.625 GHz but it could also be only able to operate at 1.55 - .075 = 1.475 GHz.

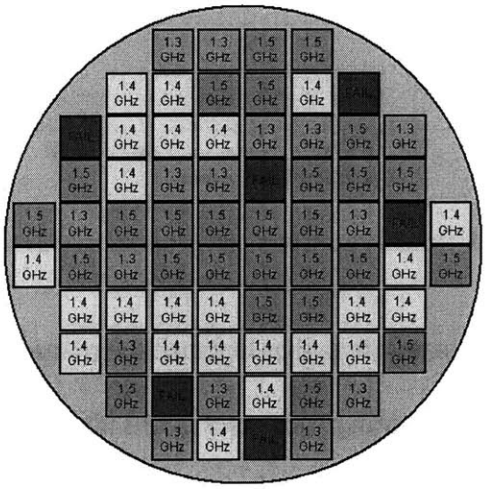

Figure 17 - An example of a tested wafer

The actual speed the device can operate at is not precisely known. The manufacturer must "bin" the DUT in the 1.4 GHz bin because it may not be able to be operated reliably to 1.5 GHz. Using the pricing information from June of 2001, the Intel Pentium 4 running at 1.5 GHz sold for $809 while a Pentium 4 running at 1.4 GHz sold for $538. Each time the manufacturer must bin a device that can run at 1.5GHz into a 1.4GHz bin,

the manufacture is losing substantial potential revenue. Thus, manufacturers of high performance devices will pay an extraordinary amount of money to get more accurate testers to determine the speed of their devices.

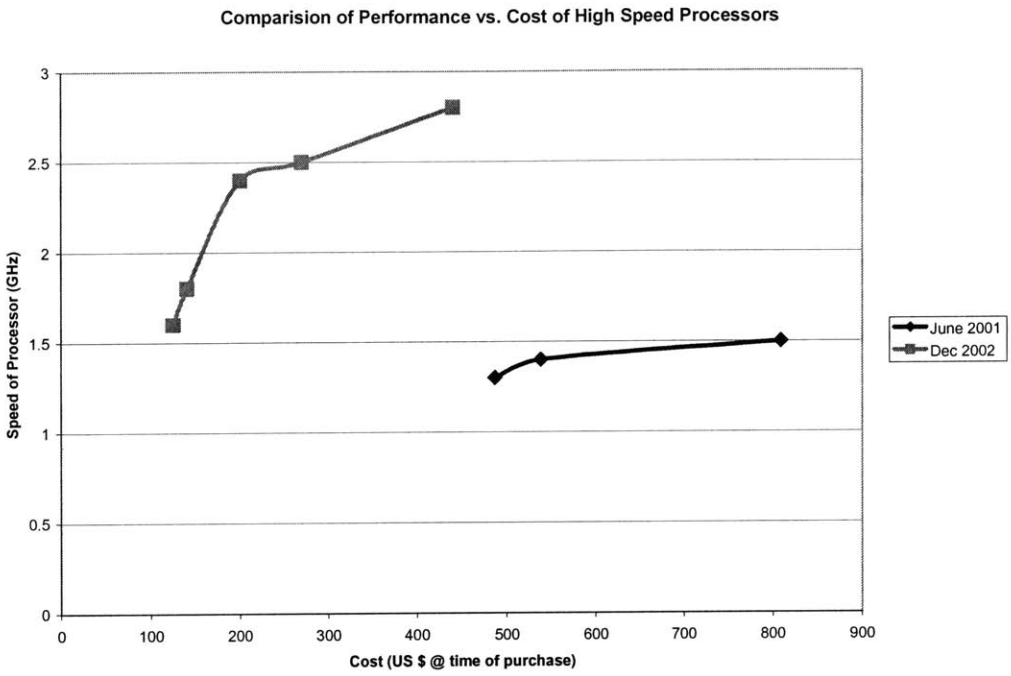

Figure 18 - Intel Processor's market price versus speed [56]

The caveat to the above example is that because the manufacturer is intent on maximizing profit, a pass/fail binning processes is not ideal. If the manufacturer determines the cost of shipping a bad product (i.e. – one that will not perform at the set clock speed) and compares that with the estimated amount of product that is not sold at higher speeds, the manufacturer can find an optimum between shipping more product at higher speed (thus more money) and getting returns on faulty product (thus losing money).

Many innovations have been described above but their cost may seem extravagant to those unfamiliar with ATE. If one examines the difference in price of the fastest

processor and the one in the next lowest bin, one can see that the manufacturer can sell the fastest processors at a large premium. Some data collected over the last few years is shown in Figure 18.

Current printed circuit board technology is, generally speaking, the only technology that allows mass production of fine wires in an arbitrary way (other than the much smaller processes used to create wires on a chip). Some existing alternatives to PCBs will be discussed later in chapter 2. PCB technology is limited by materials and planar geometry and consequently is unable to achieve the electrical performance afforded by semi-rigid coaxial cable. A PCB for testing a high performance DUT might cost upwards of $20,000. This is due to a number of factors including high material costs, tight process control and low yields (due to complete testing of the high speed paths to determine if they are all within some loss specification and impedance specification (typically ± 5 ohms)).

1.9. Summary

The ATE industry faces a daunting challenge trying to keep tester speeds an order of magnitude greater than the cutting edge processors from Intel, TI, AMD and others. Processor speeds are increasing at an exponential rate for every new processor evolution. The tester accuracy must be much better than the DUT's pulse width. As processor speeds reach into the multiple gigahertz range, the printed circuit board technology used to funnel signals to the DUT will be unable to keep the edge placement accuracy an order of magnitude better than the processor pulse width. Therefore, another technology is required to meet the challenge of increasing device speeds.

Chapter 2 - Overview of the 3DST

2.1. The Need (simplified list of Functional Requirements)

The need to test devices at increasing speed and precision drives the ATE industry to develop new innovative solutions. The printed circuit board (PCB), called the probe card or Device Interface Board (DIB) has been identified as the biggest contributor to the electrical performance degradation in a modern day ATE funnel. The PCB is not well suited for transmitting high speed, high accuracy (1+ GHz) signals due to impedance discontinuities, crosstalk and excessive loss. Thus, a new solution to replace the printed circuit board is desired.

The functional requirements for the replacement are as follows:

- Each electrical path should minimize losses, especially those at high frequencies.
- Each electrical path should minimize crosstalk from adjacent signals.
- The solution should be at least as reliable as a printed circuit board in the same environment.
- The solution should be able to be used at temperatures as low as –10 deg C and as high as 100 deg C at 0 to 100% relative humidity.
- The solution should be able to be produced in volumes of thousands per year.
- The solution should allow wires to be routed in any arbitrary pattern.

- The solution should accurately locate the electrical contacts of the board relative to some mechanical tooling holes for alignment to the connector.
- The solution should be relatively inexpensive compared to the high speed printed circuit board that it would replace.

2.2. The Concept

The basic concept is to use the ability of 3D additive manufacturing (e.g. – stereolithography, et.al.) to create tunnels in 3D space. These tunnels will serve to guide electrical cables to their proper locations. Three dimensional additive manufacturing allows the creation of any geometry and thus the tunnels can be of arbitrary complexity. The solution requires that cables be inserted into the tunnels, but the ability to force a cable into a path has limitations. For example, a sharp bend can be created using stereolithography but a cable cannot be forced through it. Even if the cable could be forced through a sharp bend, this creates an electrical discontinuity that should be avoided for high performance signals.

The smooth paths that can be created using stereolithography (SLA) allows for any path, but the geometry of each path must be determined before the SLA machine can build it. A three dimensional router was developed in software to create smooth, 3D, non-intersecting paths. For ATE solutions, some number of paths need to be length matched, and all paths should be minimized in length for electrical performance reasons.

Once the structure with internal tunnels is created, the cables must be inserted. The forces encountered during insertion can be calculated before any cable is actually inserted. If the maximum force encountered in a path can be estimated, then this

information can be passed to the auto-router and the router will avoid creating paths that require excessive insertion force. If the insertion of the cable can be automated, the solution can be manufactured with little human intervention.

2.3. The Implementation

The software implementation of the 3D router is programmed exclusively in Java. The solution of multiple non-intersecting paths in three dimensions is in a class of problems called NP (nondeterministic polynomial). This class of problems, which also includes the traveling salesman problem, the map coloring problem, and some classes of PCB routing problems, cannot be solved by any algorithm that does not test all possible cases. The computing power required to solve a given problem increases exponentially with the number of degrees of freedom in the solution, and the only algorithm that is guaranteed to find the optimum solution must test every possible combination. Fortunately, not all problems are NP and solutions to many well defined problems can be found in polynomial time. For example, Dijkstra's algorithm can find the shortest path in a interconnected network of points in $O(n^2)$ where n is the number of points in the graph. Although algorithms cannot guarantee finding the optimum solution (or any solution) to a NP problem, many algorithms exist that are able to find near-optimal solutions to NP problems in a short period of time. Some of these global minimization techniques were applied to the 3D routing problem with good success.

Very little literature exists on routing of non-intersecting, 3D freeform paths. The literature on auto-routing of printed circuit boards provides the closest analogy.

The 3D routing software developed for the project consists of three major categories: the preprocessor, the 3D path creation, and the path searching algorithms. The preprocessor tries to guess path variables (radii and section lengths) before any actual routing is done. The 3D path creation uses parameterized segments of various types to create splines in 3D space. The path searching methods use both PCB routing and global minimization techniques.

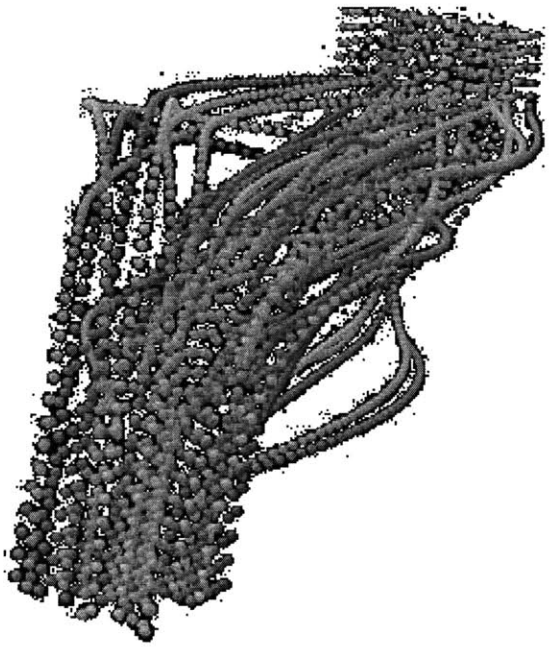

Figure 19 – Graphical Output of the 3D router

Once all the paths are determined, they can be plotted in 3D and transformed into a format that can be interpreted by the stereolithography machine to make an actual part. Stereolithography was chosen over other methods of additive manufacturing due to its ability to create the smallest structures at this time. The tunnels are roughly 0.040 inches in diameter and the spot size of the SLA machine is roughly an order of magnitude smaller to create a relatively smooth path for the cable to slide into.

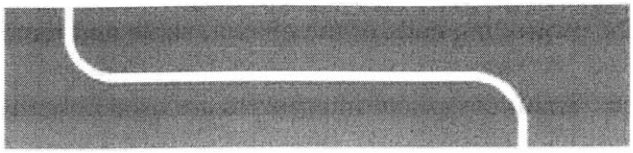

Figure 20 – A schematic representation of a single tunnel built using the SLA process.

Stereolithography is the most mature of the additive manufacturing processes, but as other methods improve, alternate manufacturing techniques could be used.

The machine to insert cables was designed specifically to measure the forces imparted on the cable as it is inserted and was not designed for volume manufacturing. The basic design could be copied in many respects to make a fast insertion machine for various wire diameters and types.

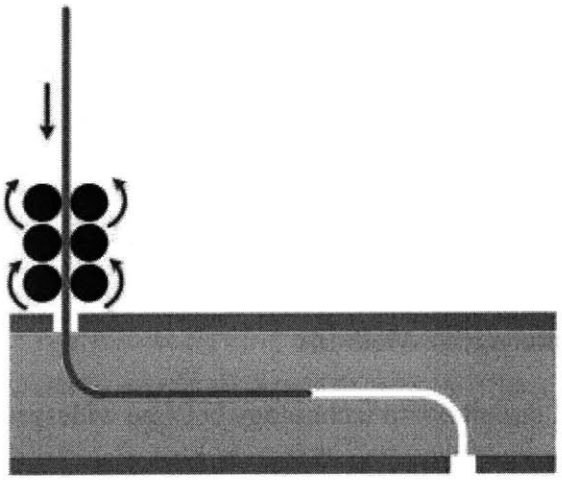

Figure 21 - Representation of machine pushing a coaxial cable into a SLA tunnel

After the software has found a solution, the SLA machine creates the tunnels and metal plates are affixed to the top and bottom of the SLA block. Wires are then inserted and are left sticking out of both ends. Both faces are then soldered to secure the cables in

place. This electrically connects the grounds of all the wires. Once this is done, a milling machine cuts off the protruding ends of the coaxial cable and removes excess solder to create a flat surface. Small compliant interposers are used at both ends to connect to the rest of the system.

Figure 22 - A SLA block created with 512 tunnels

2.4. Prior Art and Alternative Methods

Before the printed circuit board technology became widespread, many people connected discrete components using wire wrap technology (it is still used today in some applications). Multiple metallic posts are affixed to a board and solid wire is wrapped around a post, then routed over the surface of the board to another post. This technology is easy to implement for a few prototypes but is not well suited to high volume manufacturing as each wire is typically routed from post to post by hand. Note that

machines were created to automate this and some manufacturers still use this process; however, the printed circuit board is now the dominant method for creating interconnect structures. Wire wrap's major strengths are the ease of manufacture for low volumes, the ability to reconfigure the circuit easily, and the ability to use large or small wires depending on the application.

ATI and Kollmorgen have developed a process that is somewhat of a hybrid between wire wrap boards and printed circuit boards. The process (called "Multiwire" by Kollmorgen) uses equipment similar to that used for wire bonding on chips. An automated machine bonds a wire to a pad, then spools out the wire to a connecting pad. Multiple wires can cross over each other on a single layer because each wire has a small amount of insulation around it. The ground is formed using a ground plane with PCB techniques, and solid wires are routed over the ground plane. Kollmorgen [22] has developed a modified "Multiwire" process that uses 0.0095" outer diameter coaxial cable. The tiny coaxial wires must still use conventional via technology to connect from layer to layer.

Some methods to achieve large numbers of coaxial structures wired in a large point to point network, while utilizing simple manufacturing methods have been proposed. Salvage et. al. proposed a "near" coaxial structure built up of alternating layers of conductor and dielectric [59]. While this seemed promising, as the processes used would be very similar to PCB or VLSI circuits used today, the results of their work showed that they were unable to maintain good impedance control of the lines and suggested that more layers of dielectric (finer gradations) might solve the problem.

Another technique used a method similar to the Multiwire method. Rather than routing wires point to point with just a thin layer of insulation, the insulation is thick enough to form a proper dielectric core of a coaxial line [68]. Once all the wires are routed, a plating step over the insulation provides the ground return. One of the manufacturing issues with this method is that the insulation must be stripped and inserted into a hole rather than simply bonded to a pad. The method allows point to point wiring only from the same layer, thus it is not well suited to ATE applications but could be useful in backplane applications.

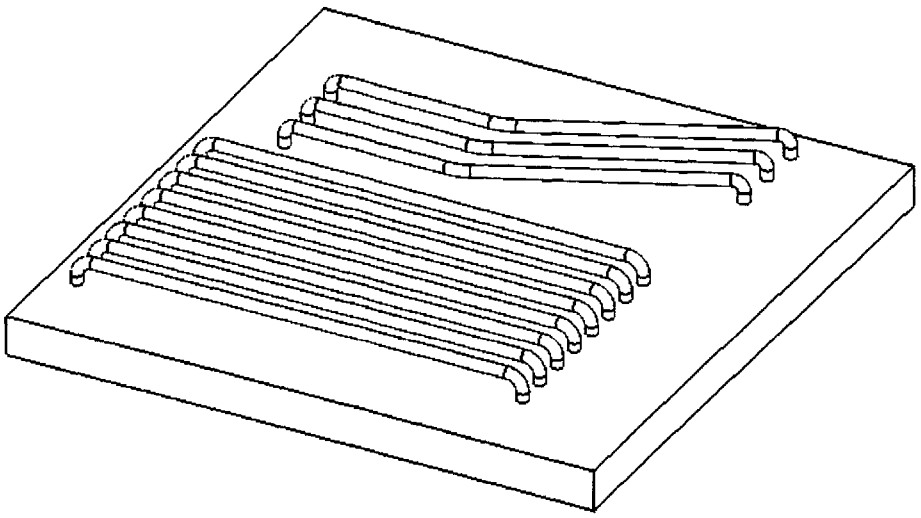

Figure 23 - A wiring board which connects only to 1 surface

Many systems, especially telecommunications, supercomputers and ATE must route a large number of wires to and from very specific locations. The general strategy for dealing with such large masses of wires is to use a variety of routing aids to assist in keeping the wires in their proper places. These guides can be as simplistic as cable ties

wrapped through holes on a surface to custom smooth transition manifolds. The wires are laid into these wire harnesses by hand and then locked down. Rarely are these wires constrained along their entire length and on an individual basis. The 3DST (Three Dimensional Space Transformer) provides an interwoven array of paths that constrain each wire individually. One of the unique features of the 3DST is that it allows connection to both sides of the board as shown below.

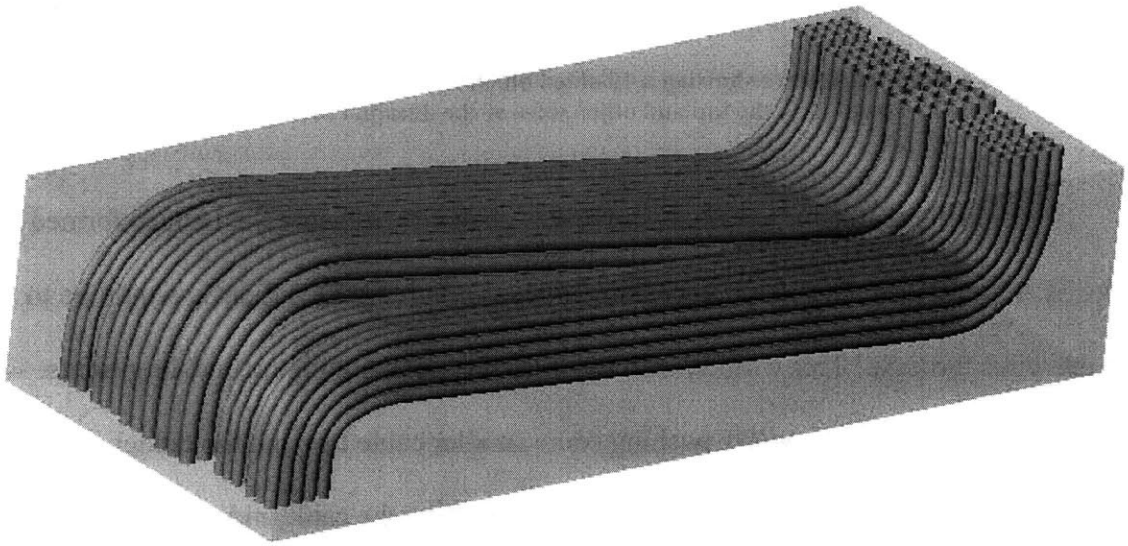

Figure 24 - A block showing the tunnels created in SLA from one surface to another

The 3DST can connect to all six sides of a cube, or using a multi-sided polygon, connect to all sides of the polygon. This might be useful for new high-speed, highly interconnected applications.

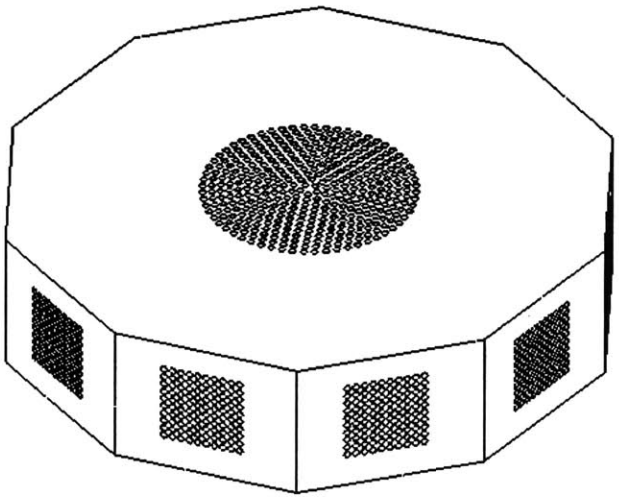

Figure 25- A conceptual picture showing a 10-sided block with connections made at all sides and routed to the top and other sides of the decagon prism

The ideal manufacturing process involves pushing wires into the tunnels formed in the SLA block. An alternative to pushing wires through the SLA matrix, would be to pull the wires through. This would avoid the difficulty of avoiding the buckling limits. This, however, would still require pushing some smaller cable through the tunnel and then affixing the cable to the coaxial wire and then pulling the cable and coaxial wire through the tunnel. The difficulty in using this method would come from the affixing of the cables to the coaxial wire in an automated method. The pushing of coaxial cables directly into the tunnels makes for a much simpler manufacturing method.

2.5. Summary

Semi-rigid coaxial wires have been proven to be the most effective transmission medium for high speed electrical signals, but they are not widely used due to the care with which they must be assembled, their relatively inflexible nature, and the difficulty in assembling large quantities of them in a confined volume. This thesis describes a method to manufacture a true coaxial cable board that can be used effectively for ATE

applications. The use of sterolithography tunnels to guide individual wires to a specified endpoint is a new manufacturing method that opens up nearly limitless possibilities. The research work has focused on predicting the insertion force of coaxial cables, although the insertion of fiber optics, solid wires, and hollow pipes (for cooling or media transfer) are easily extended from this work. As this is a completely new field, many possibilities for future work and applications are discussed in chapter 8.

Chapter 3 – Delivery of High Speed Signals

3.1. Background

Test equipment must send and receive a great number of signals to the DUT. The accuracy with which the tester can determine when the signal arrived is called the edge placement accuracy (EPA). As was described in Chapter 1, the edge placement accuracy of the tester directly impacts the yield of the tested device and hence the number of processors at higher speeds a supplier (Intel, AMD, TI and others) can sell. Thus, it is critical to understand each effect that impacts EPA and work to reduce or compensate for these effects to minimize EPA and maximize profits for suppliers of high speed processors.

3.1.1. Transmission line structures – Introduction

All electrical paths can be considered transmission lines. When the rise time of the signal sent down a transmission line is much longer than the length of the line, the signal behaves in a very different way than a signal with a fast rise time. Multiple characteristics of transmissions lines change with the frequency at which they are used. For example, the resistance of the conductor is directly related to the frequency of the signal being sent down it. Consider a coaxial wire that is one meter in length with a 0.008" diameter core, the resistance in the low frequency regime is given by:

$$R = \frac{\rho}{Area} = \frac{\rho_{copper}}{\pi(.008/2)^2} \quad \left[\Omega/\text{unit length}\right] \tag{3.1}$$

where ρ is the resistivity of the material. As the frequency increases, this equation cannot be used. The equation above assumes that the electrons flowing down the wire use all of the available area in the conductor. At high frequencies the electrons follow the path of least inductance and thus, flow as close to the ground return as possible. For a coaxial wire, the electrons are pushed to the outside edges of the wire and very few electrons move through the center of the conductor. This is referred to as the skin effect and the depth can be used to estimate the effective resistance at higher frequencies.

$$\delta_{skin\ depth} = \sqrt{\frac{\rho}{\pi f \mu}} \tag{3.2}$$

A first order estimate of the resistance is to use the area of the conductor defined by one skin depth. At 10 GHz, the skin depth is 0.000026 inches, thus the resistance a 10 GHz signal "sees" in a .008" diameter core is 75 times higher than the resistance a 1kHz signal would "see" in the same diameter core.

The coaxial structure works well for higher frequencies because the electrons build up equally around the outside of the core and the inside of the ground. Other geometries, shown in Figure 26, illustrate the electric and magnetic fields and from this the electron density can be inferred. The coaxial structure has a uniform field and thus electrons build up evenly, whereas the other structures are non-uniform and suffer increased resistance.

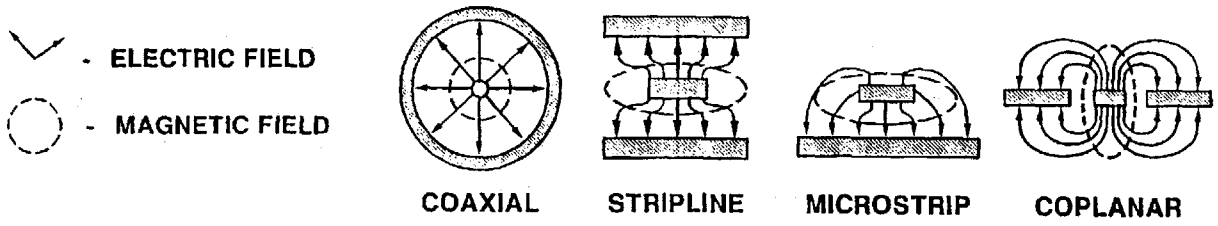

Figure 26 - Various transmission line geometries

Transmission lines are comprised of a signal path, a dielectric and a return path. With a few exceptions (waveguides and other higher order TEM structures), transmission lines use an electrically conducting material for the signal and return paths and an insulating medium for the dielectric. At DC and low frequencies, the resistance of the path is determined by Equation (3.1) and the shape of the output signal is (nearly) exactly the same as the input signal. The voltage at the input end and the output end (and along the entire length of the path) is always (nearly) the same. Note that all paths regardless of length and frequency, have some inductance, capacitance and a propagation velocity such that the input and output are not exactly the same. However, when the length of the path is small compared to the maximum frequency, the signal can effectively be treated as steady state. Table 3, on the following page, illustrates this.

Frequency of Signal	Wavelength (meters)	Wavelength
1 Hz	300,000,000	186,411 miles
1 kHz	300,000	186.4 miles
1 MHz	300	984.3 feet
100 MHz	3	9.84 feet
1 GHz	.3	11.81 inches
10 GHz	.03	1.181 inches

Table 3 - Frequency versus wavelength in free space

For the ATE industry and the makers of microprocessors, when frequencies approach 100 MHz (below this range, the details of electrical paths in the range of a few feet are relatively unimportant) the transmission path should be treated as a high frequency circuit. Typical path lengths on a motherboard (where the microprocessor is installed) are on the order of a few inches. For ATE funnels, the lengths of the paths might reach two to seven feet from drive electronics to DUT. The figure below illustrates the difference between the low frequency model and the high frequency model.

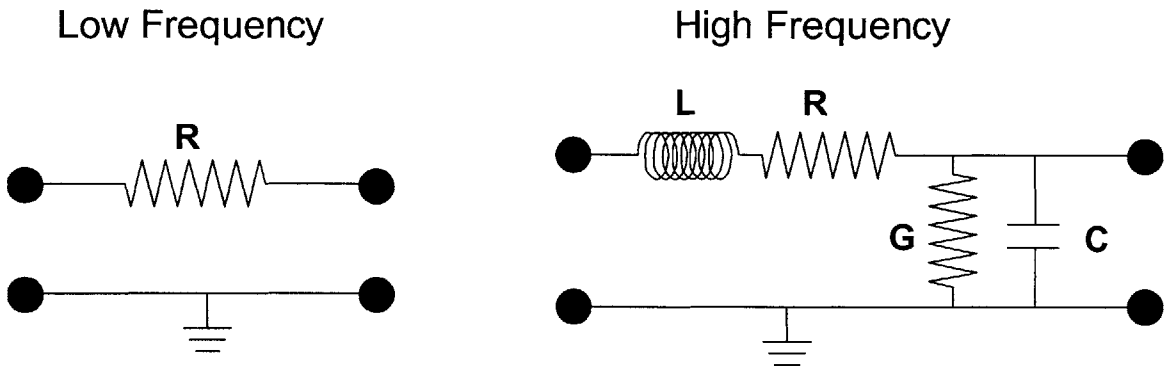

Figure 27 - Low and High frequency transmission lines

In the low frequency model, there is only a single component to worry about, the resistance which is described by Equation (3.1). The high frequency model, however, poses a number of challenges. The resistance from the conductors depends on the skin effect for the signal and the return path. Additional loss occurs due to the dielectric medium. Both of these losses depend on frequency. For a coaxial cable, capacitance and inductance of the path is determined by the ratio of the inner and outer conductors and the dielectric constant. The dielectric constant is not constant with frequency and, consequently, the impedance varies with frequency. Understanding each of these effects is important to mitigating the effects it causes on tester EPA.

Along the transmission line, energy is lost in the conductors due to resistance of the conductors and the skin effect. Losses also occur in the dielectric due to the energy that must be expended to align the dipoles to the traveling magnetic wave. Further losses are created in the form of radiation. Some of these losses can be predicted and compensated for in a variety of ways, but many of these factors depend on frequency, temperature and processing tolerances, making it difficult to compensate for all these losses. There are three major effects on the signal fidelity: noise, energy losses and discontinuities, and each of these should be minimized and/or compensated for in order to increase EPA. These effects can be a significant detriment to EPA depending on the details of the ATE architecture.

3.2. Resistance Effects

The most common conductors used in transmission lines are the highly conductive metals such as copper, and aluminum (gold and silver are sometimes used as a thin plating, but are generally not used as the bulk conductor due to the very high cost.)

The skin effect, described by Equation (3.2), depends on three variables: the resistivity of the conductor, the permeability of the conductor and the frequency of the signal. For most conductors, the relative permeability is very close to one, and thus the permeability of vacuum can be used without introducing much error.

Medium	Relative Permeability	Permeability
Vacuum	1 *(by definition)*	$4\pi \times 10^{-7}$ H/m
Copper[1]	.999991	12.56626×10^{-7}
Silver[1]	.99998	12.56612×10^{-7}
Gold[1]	1	12.56637×10^{-7}
Aluminum[1]	1.00002	12.56662×10^{-7}
Cast Iron[2]	60	753.98×10^{-7}
Steel[2]	300	3769.91×10^{-7}

1 – From Wadell 2 – From Hayt

Table 4 - Conductor properties – Permeability

As can be seen from the above table, as long as the material is not ferrous, the permeability can be assumed to be that of a vacuum. The resistivities of the conductors are quite different, however as shown in Table 5.

Medium	Relative Resistivity	Resistivity
Copper[1]	1 *(by definition)*	1.736×10^{-8}
Silver[1]	.9335	1.621×10^{-8}
Gold[1]	1.4049	2.439×10^{-8}
Aluminum[1]	1.5484	3.776×10^{-8}
Cast Iron[2]	55.93	9.71×10^{-7}
Steel[2]	9.62	1.67×10^{-7}

1 – From Wadell 2 – From Hayt

Table 5 - Conductor properties – Resistivity

Using the tables above, the skin depth for a 0.008 inch core of a coaxial cable can be calculated at multiple frequencies. The estimated resistance for a copper 0.008 inch diameter core is calculated by using the effective area of the conductor defined by one skin depth from the outer diameter. Note that when the skin depth is greater than the physical size of the conductor, only the full area of the conductor is used (if the skin depth is 2 inches but the conductor is less than 2 inches it effectively uses all of the conductor area but not more – thus the resistance has a lower limit equal to the DC resistance.)

Both coaxial cable and PCB trace use copper for electrical conductors so there is seemingly no difference. However, the process for creating the coaxial wire is as follows: Starting with a relative large diameter wire it is progressively drawn to smaller and smaller diameters until it reaches its final desired diameter (in this case 0.008 inches). This has the effect of stretching the copper grains along the direction of the wire, making the conductivity of the copper wire anisotropic. Consequently, in the direction of the wire, the resistance is roughly 20% less than normal to the direction of the wire [35]. This bodes well for conducting signals along the length of the wire. After the core is

formed, the Teflon dielectric is molded over the core. Finally, a larger copper tube is drawn over the dielectric in a similar process as described for the core, and thus, the same lower resistance effect exists on the shield. The ability to roll or draw each individual path is not possible on a printed circuit board which typically uses electrodeposited copper. Some advanced circuit board manufacturers do have the ability to roll copper onto printed circuit boards and the lowered resistance is seen in one direction, typical circuit board traces require routing in both directions, so the anisotropy can have negative impacts on signal fidelity.

Coaxial cables also show a significant benefit for high speed signals when the effects of skin depth are considered. In a coaxial cable, the skin depth effect happens uniformly around the entire circumference of the inside diameter of shield and the outside diameter of the core. A PCB trace, on the other hand, has a more complicated relationship, the current density is highest at the two edges of the trace and at the center. For the ground planes above and below, the electron density falls off rapidly and hence the effective area is greatly reduced for PCB traces when compared with coaxial cables of the same overall cross-sectional area.

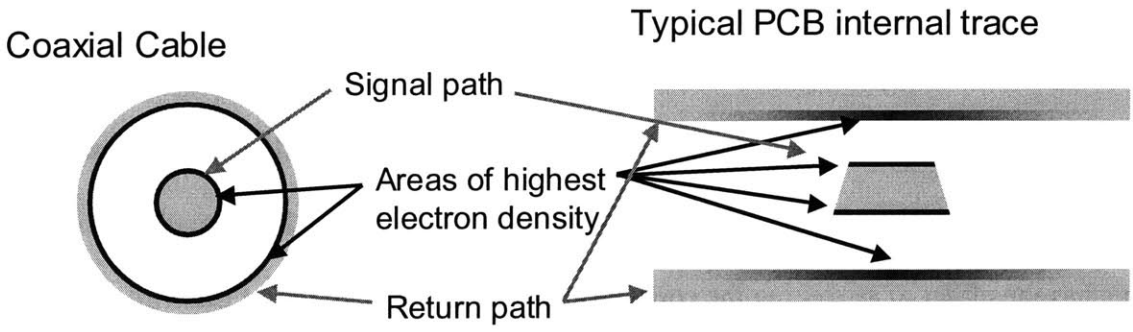

Figure 28 - Skin depth effects for coaxial cable and PCB trace

Another benefit of coaxial cables arises due to the difference in manufacturing methods. The coaxial wire surface roughness is very low due to the progressive drawing down of the wire and the smoothing action of the dies whereas the electrodeposited copper can have relatively rough surfaces [36]. The roughness of the surface impacts the resistance when the skin depth is of the same order as the roughness. For PCBs manufactured today and transmitting signals around 1 GHz, the roughness effect is attributed to a 10 to 50% increase in resistance over the skin effect itself. An approximation for this effect is given by {Johnson and Graham] as:

$$k_{rough} = 1 + \frac{2}{\pi} \arctan\left(1.4 \frac{f}{f_{rough}}\right) \tag{3.3}$$

where k_{rough} is multiplied by the estimated AC resistance calculated earlier. The onset frequency, f_{rough}, is the point at which k_{rough} is equal to 1.6 and is given by:

$$f_{rough} = \frac{2\rho}{\mu h_{RMS}^{\ 2}} \tag{3.4}$$

The effect of surface roughness is to attenuate the highest frequency components of the signal even faster than just the skin effect would predict because of the loss of area for the electrons to flow very near to the surface. The onset of this effect will usually occur for printed circuit boards before it does for the miniature drawn copper coaxial cables. Note that the coaxial cables used for the project have a thin silver plating over the inner conductor which serves to decrease the resistance (silver is a better conductor than copper) of the outermost area, and therefore staves of the skin effect even more.

Frequency	Skin Depth	Estimated AC resistance
1 Hz	2.61 inches	0.61 (DC)
1 kHz	0.0826 inches	0.61 (DC)
1 MHz	.00261 inches	0.61 (DC)
100 MHz	.000261 inches	5.4
1 GHz	.0000826 inches	17
10 GHz	.0000261 inches	54

Table 6 – Skin depth versus frequency for a 0.008" core in a coaxial wire

For all DC signals the resistance must take into account the return path.

$$R_{DC} = R_{DC\,signal} + R_{DC\,signal} = \frac{\rho_{signal}}{A_{signal}} + \frac{\rho_{shield}}{A_{shield}} \tag{3.5}$$

The AC resistance is calculated for a coaxial cable by [35]:

$$R_{AC} = \left(1 + \frac{d_{\text{signal outer diameter}}}{d_{\text{shield inner diameter}}}\right)\frac{\rho}{A_{AC}} \tag{3.6}$$

where A_{AC} (the effective AC area) which represents the area of the conductor one skin depth from the outer diameter of the signal is given by [35]:

$$A_{AC} = \pi\left[\left(\frac{d_{signal}}{2}\right)^2 - \left(\frac{d_{signal} - 2\delta}{2}\right)^2\right] \approx \delta\pi d_{signal} \tag{3.7}$$

The skin effect for the coaxial conductor is shown in Figure 29.

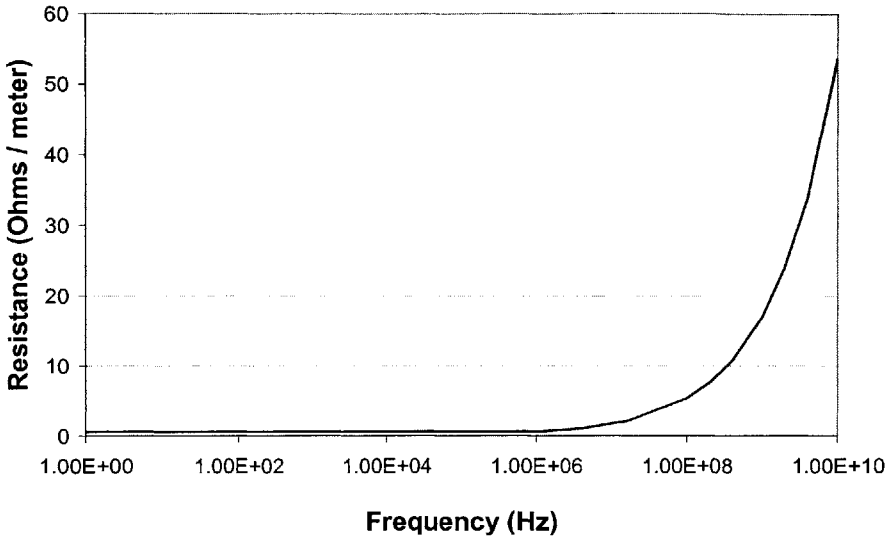

Figure 29 - Estimated resistance for a coaxial conductor showing the onset of the skin effect near 100 MHz

The skin effect onset is directly related to the size of the conductor, and PCB traces and the miniature coaxial cable are roughly the same size, but the onset occurs earlier in PCB trace due to the non-circular geometry of the trace. The skin effect onset is also influenced by surface roughness where the coaxial cable further shows its superiority.

Excluding the surface roughness, the total attenuation loss due to the conductor is given by [67]:

$$\alpha_{conductor} = \frac{11.39}{Z_0}\sqrt{f}\left|\frac{\rho_{core}}{d} + \frac{\rho_{shield}}{D}\right| \quad [\text{dB/m}] \tag{3.8}$$

More complicated expressions are used for the different PCB geometries, but for a given cross-sectional area and a 50 ohm environment, the coaxial cable is the best choice for minimizing resistance losses.

3.3. Dielectric effects

Material selection is important not only for the conductors but also the dielectric. The dielectric is the material between the ground and signal conductors. Just as the metal conductors had two key properties (resistivity and permeability), the dielectric has two important properties: dielectric constant (or relative permittivity) and loss tangent (or dissipation factor). The loss tangent is a measure of how much of the signal energy is lost due to the motion of dipoles aligning with the magnetic field which generates heat within the dielectric material.

Medium	Dielectric constant	Loss tangent
Vacuum	1 (by definition)	0
Air	1.0006	0
PTFE	2.1	.0002
FR-4	4.3	.020
G-10	4.3	.008
GE Getek	3.8	.0083
Rogers N5000	4.4	.009
Gore Speedboard	2.5	.0038
Cyanate Ester	3.5	.005
Alumina 99.5%	9.7	.060
Polyimide	3.42	.0116
Nylon 6,6	3.6	.04
Silicon (Si)	11.7	.005
SiO_2	3.9	.007
LCP Glass Filled	3.9	.006
Polysulfone	3.03	.0034

1 – All data at 1 MHz at ambient temperature Complied from multiple sources

Table 7 – Dielectric properties – Dielectric constant and loss tangent

From the table, it is clear that the best dielectric (excluding air and vacuum) is PTFE. Materials with weak dipoles have the lowest loss tangent because less energy is expended aligning and moving the dipoles to the traveling magnetic wave. As a further complication for digital signals, (which, due to the near square pulse, contain a wide spectrum of frequencies) the loss tangent and the dielectric constant vary with frequency. The figures below show these effects:

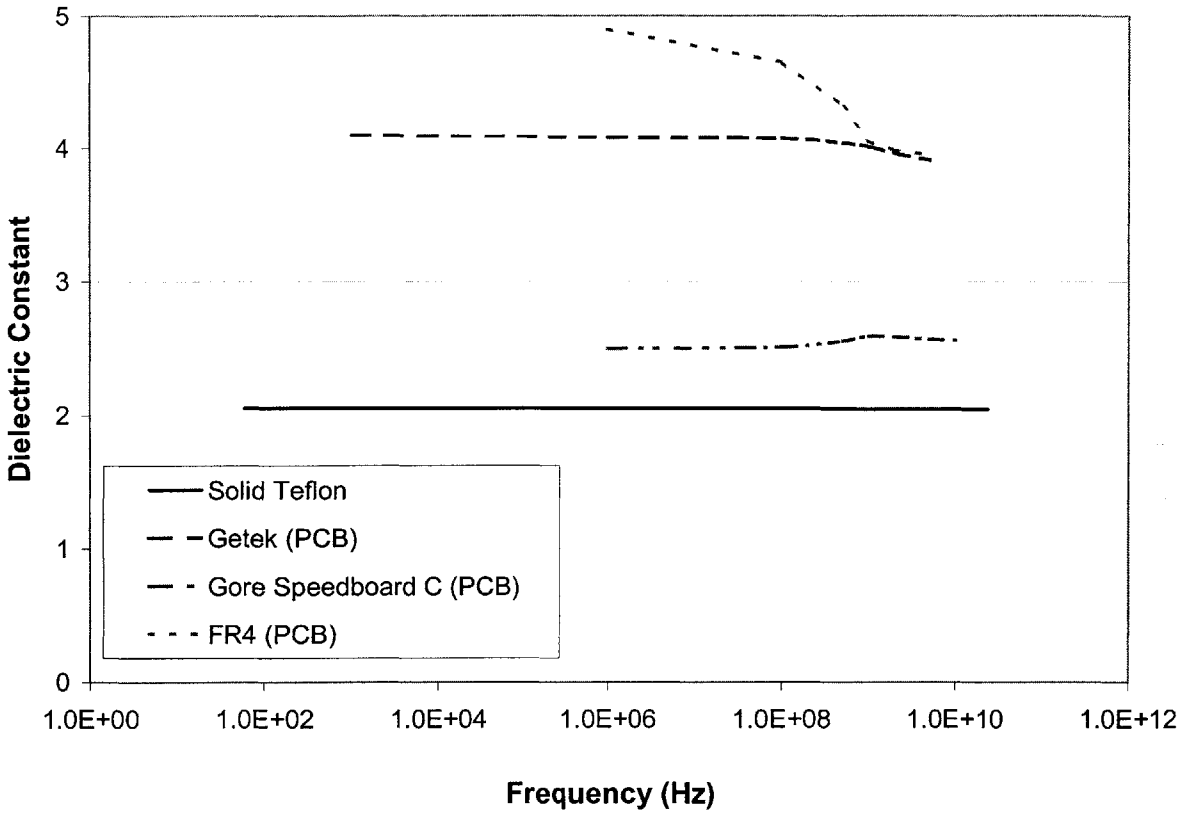

Figure 30 - Variation of Dielectric Constant vs. Frequency for Teflon and PCB materials
(Compiled from multiple sources)

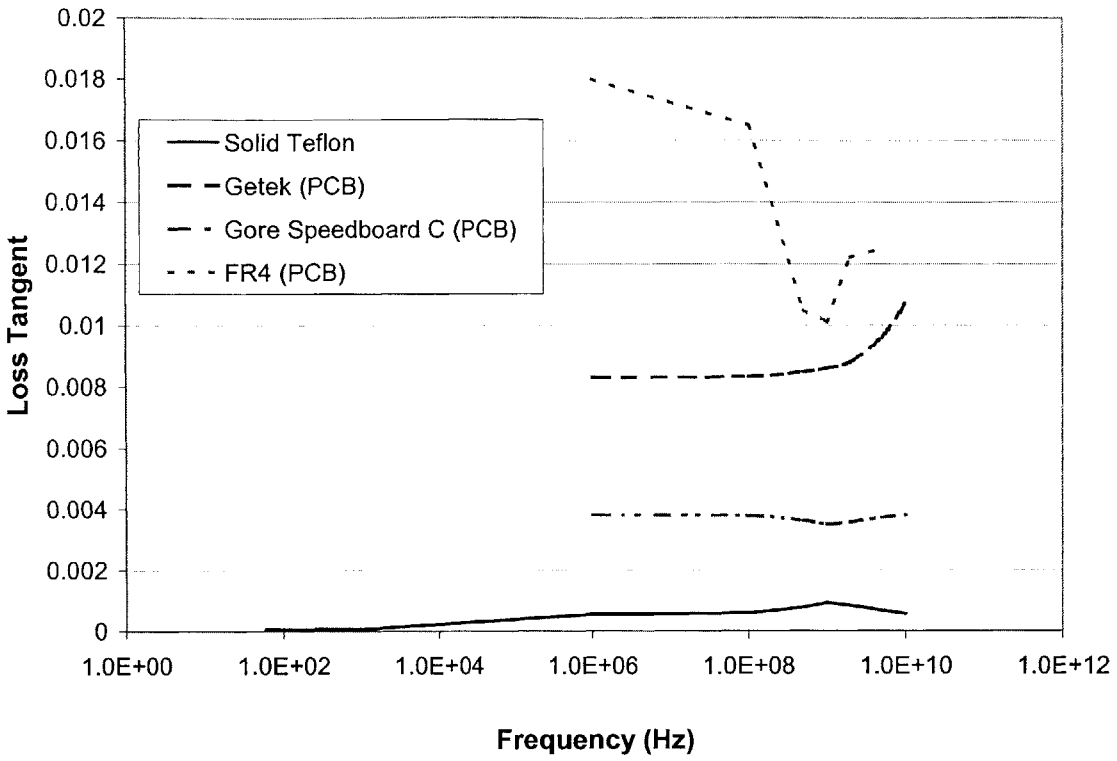

Figure 31 - Variation of Loss Tangent vs. Frequency for Teflon and PCB materials
(Compiled from multiple sources)

The total losses from the dielectric medium is given by: [67]

$$\alpha_{dielectric} = 90.96 f \sqrt{\varepsilon_r} \tan\delta \quad [\text{dB/m}] \tag{3.9}$$

And the total loss of the coaxial cable can be then calculated by summing equations (3.8) and (3.9). Note both equations use frequency in GHz and the dimensions d and D should be in millimeters.

Another reason why the coaxial wires are better for high speed signal propagation is the dielectric material choice. The coaxial cable manufacturing process is able to coat solid PTFE over the coaxial wires, and in many cases apply porous PTFE or splined PTFE dielectrics which serve to increase the percentage of air in the dielectric. As can be seen in Table 7, solid PTFE is one of the lowest loss materials that can be used.

Furthermore, as can be seen in Figure 30 and Figure 31, the variation of dielectric constant and loss tangent for PTFE varies much less with frequency than does most dielectrics used on PCBs. The changing dielectric constant and loss tangent distort the rising and falling edges of the signals and thus have a negative impact on a tester's edge placement accuracy.

3.4. Impedance tolerances

The characteristic impedance of a lossless transmission line is defined as:

$$Z_0 = \frac{\text{Electric Field Strength}}{\text{Magnetic Field Strength}} = \frac{\textit{Voltage Amplitude}}{\textit{Current Amplitude}} \tag{3.10}$$

For a lossless (all resistances equal zero) transmission lines, the impedance calculated from the ratio of inductance per unit length to capacitance per unit length:

$$Z_0 = \sqrt{\frac{L}{C}} \tag{3.11}$$

Including losses the impedance becomes:

$$Z_0 = \sqrt{\frac{R + j\omega L}{G + j\omega C}} \tag{3.12}$$

where R is the equivalent DC resistance per unit length, G is the conductance per unit length of the dielectric medium, and ω is 2π * frequency. To first order, the resistance and conductance terms can be ignored and the impedance of a coaxial line can be simply expressed as a ratio of the diameters:

$$Z_0 = \frac{60\Omega}{\sqrt{\varepsilon_r}} \ln\left(\frac{D}{d}\right) \tag{3.13}$$

where ε_r is the dielectric constant, D is the inside diameter of the shield and d is the outside diameter of the center core. For a coaxial line the parameters R, L, G, and C are given by [75]

$$R = \frac{\sqrt{\pi f \mu \rho}}{2\pi}\left(\frac{1}{r_{core}} + \frac{1}{r_{shield}}\right) \tag{3.14}$$

$$L = \frac{\mu}{2\pi}\ln\left(\frac{r_{shield}}{r_{core}}\right) \tag{3.15}$$

$$G = \frac{2\pi}{\rho \ln\left(r_{shield}/r_{core}\right)} \tag{3.16}$$

$$C = \frac{2\pi\varepsilon}{\ln\left(r_{shield}/r_{core}\right)} \tag{3.17}$$

Coaxial cable manufacturing can hold much tighter impedance tolerances than a PCB manufacturer can on traces. For the coaxial cable manufacturer, the critical aspects are maintaining the ratio of the inner and outer conductors, maintaining good concentricity between the two conductors and controlling the tolerance of the dielectric constant. PCB manufacturers, on the other hand, must concentrate on the tolerance between the spacing of the trace to the ground planes above and below the trace. The impedance is related to the width of the trace and the tolerance of the dielectric constant in the materials that separate the ground planes and the trace. Coaxial cable manufacturers are able to hold a 0.034" outer diameter 50 ohm semi-rigid cable to plus or minus 1.5 ohms or roughly 3%. Most PCB manufacturers must specify a plus or minus 5 ohms or 10% specification on impedance (some advanced shops can achieve 5% but this is typically a premium of at least 20%.) Typically such tight tolerances impact the yield of the PCBs. The difficulty

PCB vendors have in obtaining tight impedance specifications stems from the imprecise build-up and lamination process inherent in the PCB manufacture as well as the impedance control of the laminate itself.

The impedance control is of significant importance when multiple pieces are connected together to form a path to the DUT. The PCB or coaxial cables must connect to other cables in the ATE funnel and as will be described in section 3.6, impedance discontinuities are a major source of EPA errors.

3.5. External noise and Crosstalk

External noise is generated in the environment through which the cable passes due to other electrical sources in the area and background radiation (from sources such as: cell phones, the Sun and the remnants of the Big Bang). As these magnetic waves pass through the cable they affect the shape of the rising edge and impact EPA. The best shield is one that fully surrounds the signal, and the measure of shielding effectiveness is the best test to determine which geometries are most resistant to external noise sources. Internal noise (also referred to as crosstalk) is created by another signal radiating energy in the general vicinity of the conductor. While this effect can be controlled to some extent by simply spacing signals further apart from one another, the density requirements on the funnel force the signals close together. The shielding effectiveness works both ways for crosstalk. If two coaxial cables are run side by side, the full shielding of one signal does not allow much of the magnetic field to escape the shield and the full shield on the neighbor does not allow much in. Two striplines side by side have a great deal more crosstalk because they are not shielded as well. The unpredicatable nature of external noise and crosstalk make this a relatively large effect on EPA that is very

difficult to compensate for. Coaxial cable with its full shield is the clear winner as PCB traces often have to be spaced relatively far apart and sacrifice density to achieve acceptable levels of crosstalk.

3.6. Discontinuities

In addition to the losses due to material selection and geometry of the transmission line, it is necessary to connect either end of the transmission line to the test equipment and the DUT. In most ATE funnels, the entire path from driver to DUT includes multiple transitions from one transmission line to another. Shown below is a simplistic figure of a coaxial cable terminating to a printed circuit board.

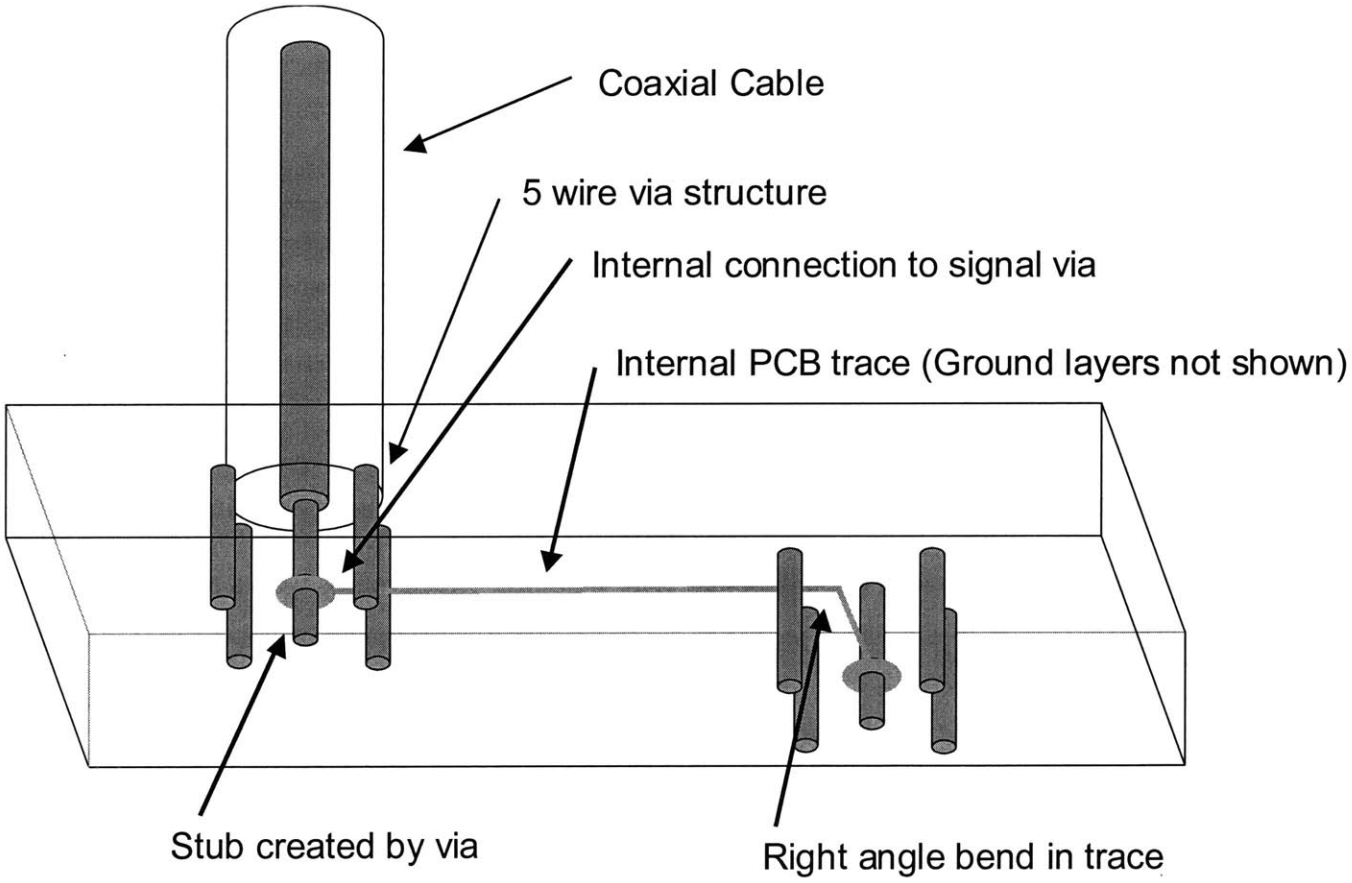

Figure 32 - A schematic representation of a coaxial wire terminating to a 5 via structure. (1 signal via, 4 return/ground vias) Also shown is an illustration of stubs that occur when connecting trace on internal layers and the sharp bends inherent in PCB manufacture.

Every transition is a potential impedance discontinuity that can seriously degrade EPA. If we take an example of a 5 GHz signal propagating down a 50 ohm transmission line and it encounters a 40 ohm discontinuity in the line, we can analyze what happens and try to understand its effect on EPA.

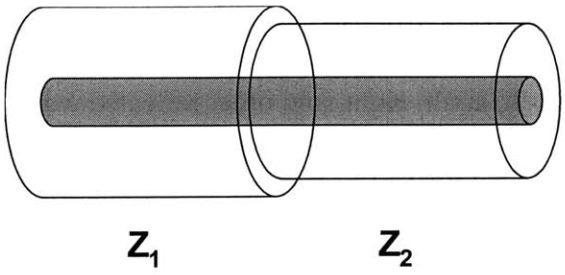

Figure 33 - An impedance discontinuity

In the figure, if a signal is propagating down the line from the right and Z_1 is 50 ohms and Z_2 is 40 ohms, the return loss is:

$$R_{loss} = 20\log\left|\frac{Z_2 + Z_1}{Z_2 - Z_1}\right| \quad [\text{dB}] \tag{3.18}$$

The ideal line would have an infinite return loss, and there would be no reflection of the signal. The reflected power and reflected voltage are calculated simply by:

$$\text{Attenuation} = \alpha = 10\log\frac{Power_{out}}{Power_{in}} \quad [\text{dB}] \tag{3.19}$$

$$\text{Attenuation} = \alpha = 20\log\frac{Voltage_{out}}{Voltage_{in}} \quad [\text{dB}] \tag{3.20}$$

One of the nastiest problems to deal with in digital design of ATE architecture, is reflections caused by discontinuities. It occurs when part of a transmitted wave is

reflected and it moves back along the line toward the driver. If a discontinuity exists at the termination to the driver, part of the reflected wave will be reflected again. This twice reflected wave is now propagating in the direction of the DUT and if another signal to the DUT is being sent, the twice reflected wave will modify the shape of the rising or falling edge. Almost any distortion of the edges impacts EPA, and twice reflected waves do just that in a very unpredictable way. Note that, in fact, the wave continues to bounce back and forth, and the fourth, sixth, eight, and other reflected waves will also effect the signal. However, due to attenuation of the signal every time it gets reflected and as it moves down the line, these other waves play a less important role.

Any bend or corner in the signal path also creates a place for waves to be reflected and the severity of the bend determines how much the wave is reflected. A sharp right angle bend occurs whenever a via connects to trace, and therefore at minimum there are two right angle bends in every circuit that connects from one side of the PCB to the other.

Figure 34 - A comparison of bends in transmission lines

In general, for transmission lines, the greater the bend radius the better the signal at the end of the line. The reason behind this is a local impedance discontinuity occurs at the right angle bend. Just before the bend, the inductance goes up as it is close to another part of the path, at the bend the width of the trace goes up and thus capacitance goes up

and impedance goes down. Finally, leaving the bend, the inductance goes back up again due to the proximity of the trace. These local impedance discontinuities cause reflections. In early PCB layouts, straight corners (shown to the far left in the figure above) were the norm. As the signal speeds grew, designers realized the negative effects of these sharp corners and started to use mitered corners (2^{nd} from right). As signal speeds continue to increase, designers must move to more sweeping organic curves to maintain the fidelity of high speed signals. One difficulty is that many boards today are routed with auto-routers that were programmed for straight lines. Adding mitered corners when the need arose was relatively easy to implement. However, the use of smooth curves and even mitered corners typically occupies more space than orthogonal routing and thus may be avoided in densely routed PCBs. Most auto-routers today are not yet at the point where they attempt to route smooth large bend radius curves rather than straight lines with rounded corners. Because of multiple bends, twice reflected waves create more EPA errors.

Discontinuities can have a number of negative effects on the signal's rising and falling edges. Reflections created by bends or impedance changes cause the signal to lose energy (note that energy is conserved, but the wave is broken in two: part of energy continues through the discontinuity and part of the energy is reflected back.). Reflections also create signals that distort the signals that follow it. The effect of reflections on an arbitrary pulse train for a line with discontinuities is exceedingly difficult to predict and cannot be easily compensated for. This makes it very important for the ATE funnels to minimize and eliminate any discontinuities in the signal path because they degrade the EPA.

Discontinuities in PCB manufacturing cause reflections and degradation of the signal. Stubs, in the form of vias connecting to internal layers create multiple reflections and act as a bandstop for a given frequency signal depending on its unterminated length. Sharp corners in PCBs, at via structures, and along the trace path, further degrade the signal and impact EPA. The impedance of a five wire via structure is typically not perfectly matched to the internal trace impedance causing further reflections and loss of signal quality.

3.7. Use in 3DST (The Design)

It should be readily apparent that the obvious choice for high speed signals is semi-rigid coaxial wire. The need for the 3DST sprung from the inability of PCB technology to meet the testing demands of the highest performance microprocessors. A 0.034" outer diameter semi-rigid copper coaxial wire was chosen for its performance characteristics. The size was an ideal choice based on the relatively standard pitch of microprocessor pads of 0.050" and the fact that most PCB traces are in the range of four to eight mils wide. The 0.034" coaxial wire has a core of diameter 0.008". The specifications are shown below:

Manufacturer / Part Number	Microcoax UT-34
Outer Conductor Diameter	0.034 ± 0.001
Dielectric Diameter	0.026 ± 0.001
Center Conductor Diameter	0.008 ± 0.0005
Maximum Length	15 feet
Outer Conductor Material	Copper
Dielectric Material	PTFE
Inner Conductor Material	Silver Plated Copper Wire
Characteristic Impedance	50 ± 1.5 Ohms

Table 8 - Microcoax UT-34 semi-rigid coaxial cable specifications

3.8. Summary

The attenuation of a standard PCB and a higher performance Rogers PCB with low dielectric was evaluated for backplane considerations at Teradyne Connection Systems. The effects of vias were removed, but the effect of a single stub acting as a bandstop is illustrated. The attenuation of the Microcoax UT-34 cable is also indicated on the graph. The point at which fifty percent (-3 dB) of the signal is lost is also indicated. Note that the typical PCB hits this limit at just over 2 GHz and the Rogers material makes it to 5 GHz whereas the coaxial cable does not reach this point until 22 GHz.

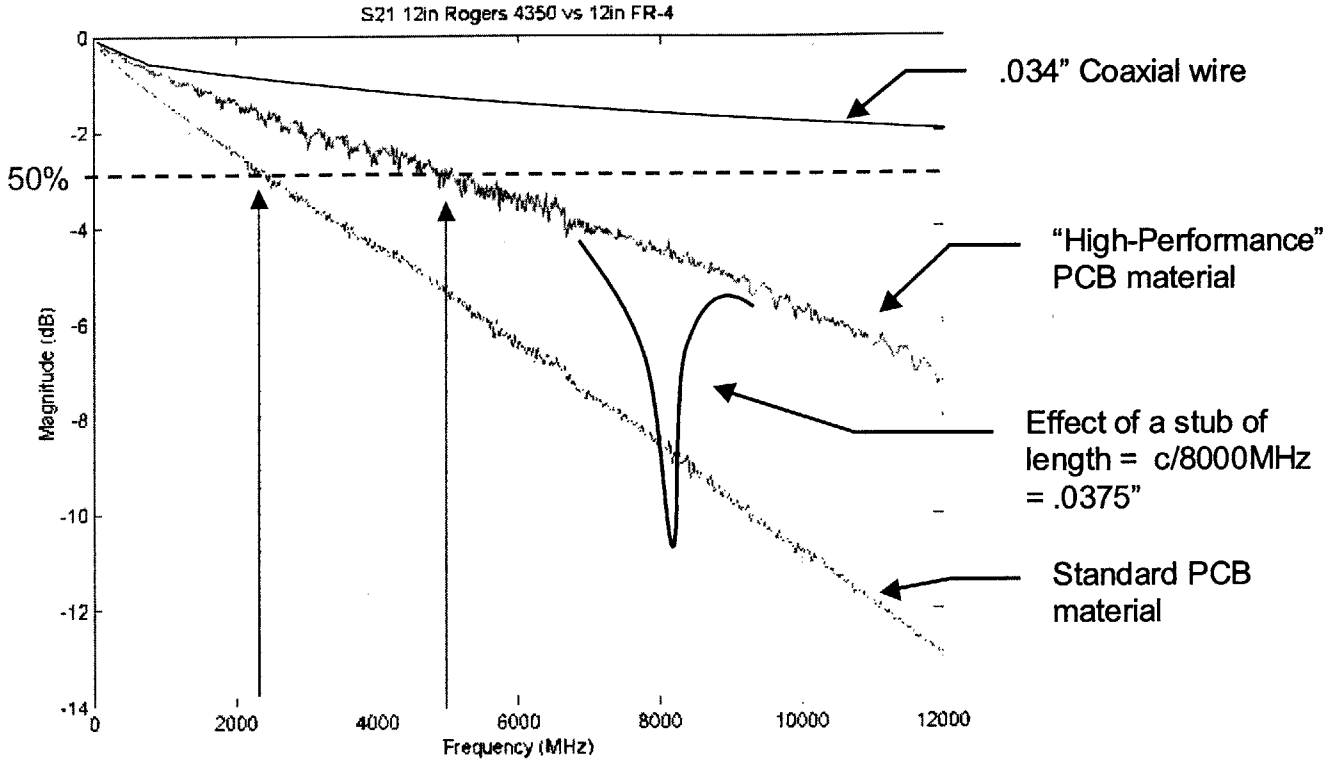

Figure 35 - Two 12" long PCB traces versus 12" UT-34 coaxial cable

Chapter 4 - 3D Additive Manufacturing Processes

4.1. Overview of RP Technology

The general field of rapid prototyping (RP) or, more precisely, additive manufacturing, builds parts by adding material volume in a layer by layer process. This type of process is unlike most manufacturing processes in which the material volume remains basically unchanged (forming, spinning, molding, etc) or is removed (milling, turning, stamping, etc.). Additive manufacturing (AM) allows for geometries that were impossible (or very difficult) to build with other processes. Most of the additive manufacturing techniques have been used for creating early prototypes for testing form and fit. New applications are using these RP process to create the molds for production parts. Some companies are even finding ways to use the RP part directly in their products, but many applications cannot tolerate their lack of strength and accuracy. The use of RP parts directly in OEM (Original Equipment Manufacturer) products is just starting and will likely grow rapidly as more companies take advantage of the benefits offered by additive manufacturing.

4.2. SLA Process

Invented by Chuck Hull, CTO of 3D Systems, the stereo-lithography process was the first of many rapid prototyping processes that are constantly being developed and refined. The SLA process uses a UV curable liquid polymer in conjunction with a scanning laser. An elevator in a bath of uncured polymer forms a thin layer (about 0.005 inches in thickness) and a laser is scanned across the layer. With the laser on, the polymer is cured in a tiny spot. Multiple spots link together to form a solid. Once the layer is completed, the elevator moves down a small amount, and uncured polymer flows over to form a new layer to be selectively cured by the laser. In some cases, a sweeper may be employed to fully cover the part.

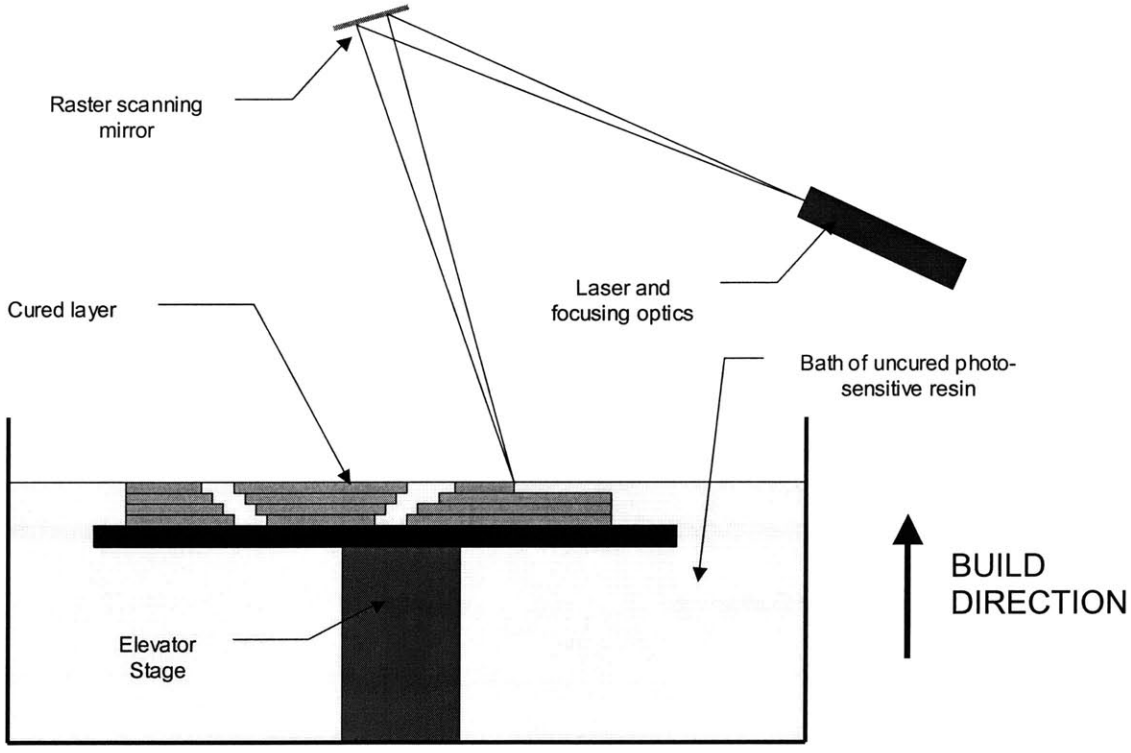

Figure 36 - A simplified model of the a SLA build machine

Usually, after the part is finished in the machine, any remaining liquid is allowed to drain out (or is forced out by air) and the part is placed in a UV oven to finish the curing processes. As stereolithography was the first additive manufacturing process invented (around 1986), it is also the most refined. It is the most accurate of the AM processes and is also one of the least expensive. Unfortunately, the material is also relatively weak and can warp and change shape over time if exposed to further UV light.

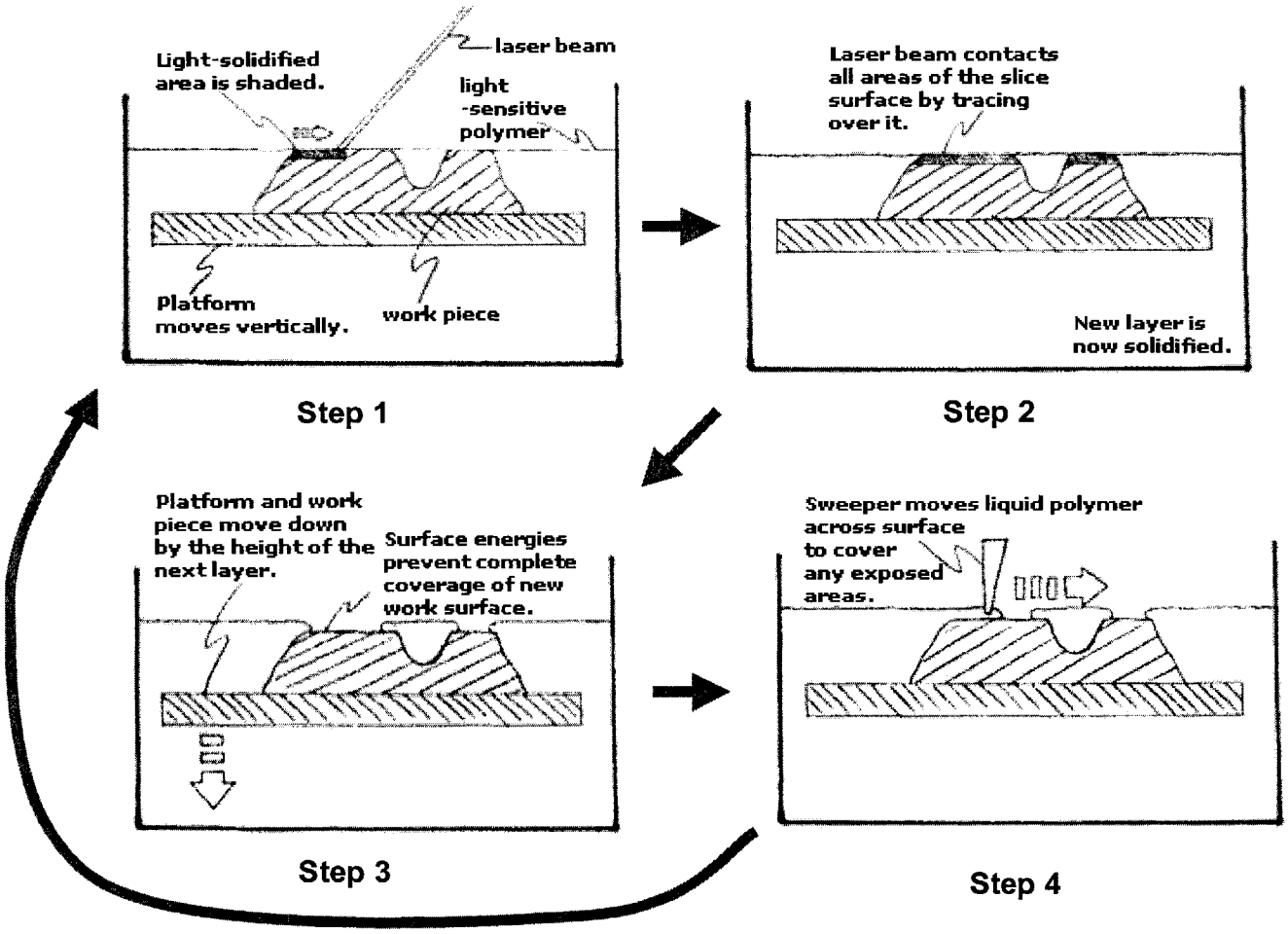

Figure 37 - The steps required to create an SLA part
Reprinted with permission, courtesy of eFunda Inc.

4.3. LOM Process

Laminated Object Modeling uses paper and glue to form successive layers and build a 3D shape. The result is a part with properties much like wood. As each layer is laid down, a laser burns away areas that are to be removed. These areas are cross-hatched into many smaller pieces but remain there to support the next laminated layer. The part must be broken apart by hand after the process is completed. This makes it difficult to build small internal cavities, as each cavity will be filled after the process is complete and will require mechanical removal of the pieces in that area. For this reason, and the current lower precision, LOM is not yet suitable for wiring small diameter coaxial wires, but may work well for systems that would require only a small number of large diameter wires.

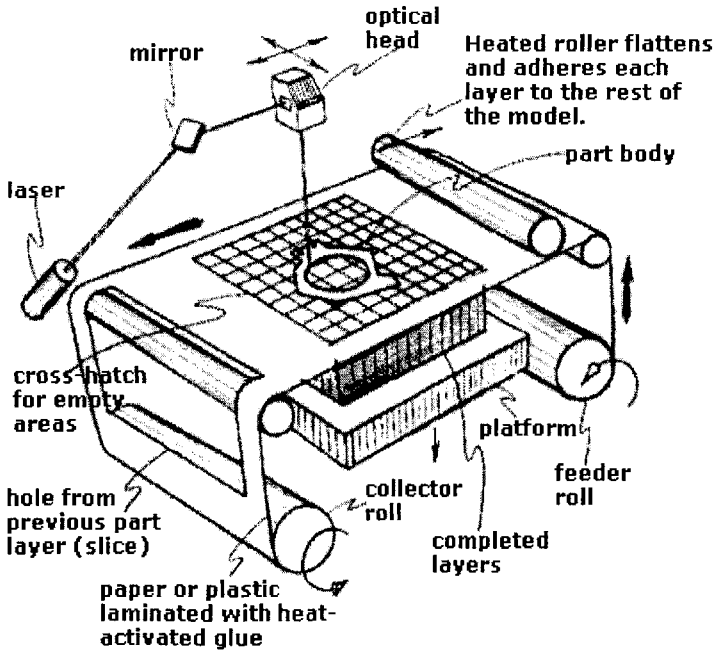

Figure 38 - A schematic LOM Machine
Reprinted with permission, courtesy of eFunda Inc.

4.4. FDM Process

The Fused Deposition Modeling uses a polymer filament that is heated and selectively deposited by a scanning head. The material must be heated and ejected out of the head in small droplets or in a continuous bead. The minimum size of the droplet determines the smallest features that can be created. Each droplet cools in place and bonds to any neighboring material. FDM is quickly approaching the resolution capabilities (currently minimum "spot" size is 0.0076" and minimum build layer is 0.005") of SLA and has the added benefit of using multiple different plastic materials (ABS and Polycarbonate).

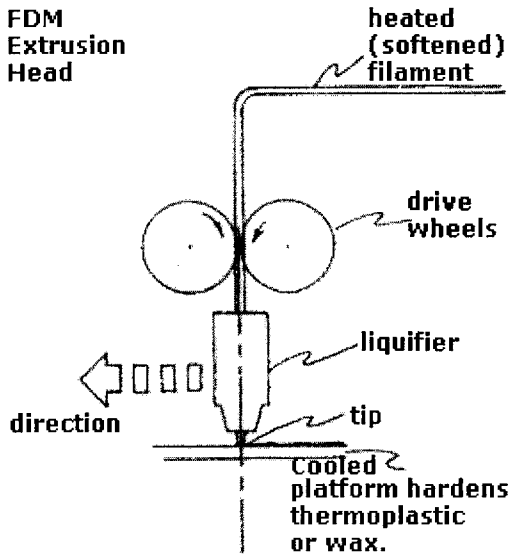

Figure 39 - A FDM Machine
Reprinted with permission, courtesy of eFunda Inc.

As the FDM process improves its resolution capabilities, it may be an effective substitute for the SLA process in the 3DST project.

4.5. SLS Process

Selective Laser Sintering is similar to SLA in concept, but it uses a powder rather than a UV curable polymer. Each bit of powder is melted slightly by a laser and becomes locally bonded to its neighbors. This process can be used on plastics and metals. When used with metal parts, the part is in a "green" state after exiting the SLS machine and must be heated in a kiln and infused with a binder metal. The binder metal will wick into the part and create a part that is nearly the strength of a part machined from a solid block of the same material.

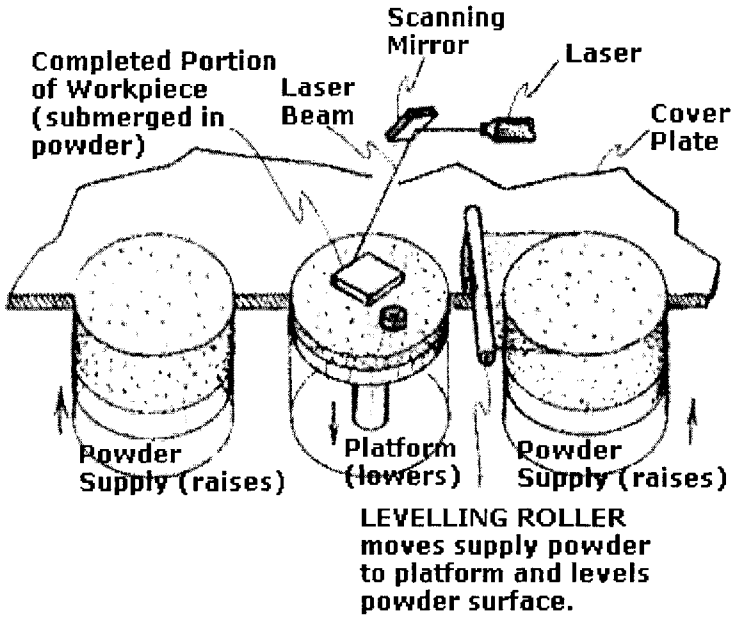

Figure 40 - A SLS machine
Reprinted with permission, courtesy of eFunda Inc.

Currently this process lacks the resolution capability required by the 3DST, but in time it may become an effective replacement.

4.6. SGC Process

Solid Ground Curing is a process developed by Cubital and is similar to the SLA process. Rather than using a single laser to scan across the part (as in the SLA process), the SGC process "prints" the entire layer onto a reusable glass-photomask using electrostatic toner. UV light is passed through the mask and cures the layer in the bath. The uncured resin is then vacuumed off and a liquid wax applied to fill the voids. The wax is cooled and the entire layer is then milled to the desired thickness, and then the process is repeated layer by layer until the entire part is built. One advantage the SGC process has over SLA is that large overhangs can be built (supported by the wax) rather than the limited bridging capability of SLA over uncured resin. The process is typically an order of magnitude faster than the single scanning laser system used in the SLA process. When the part is complete, the wax must be melted out of the part. This process is well-suited to the production needs for 3DST.

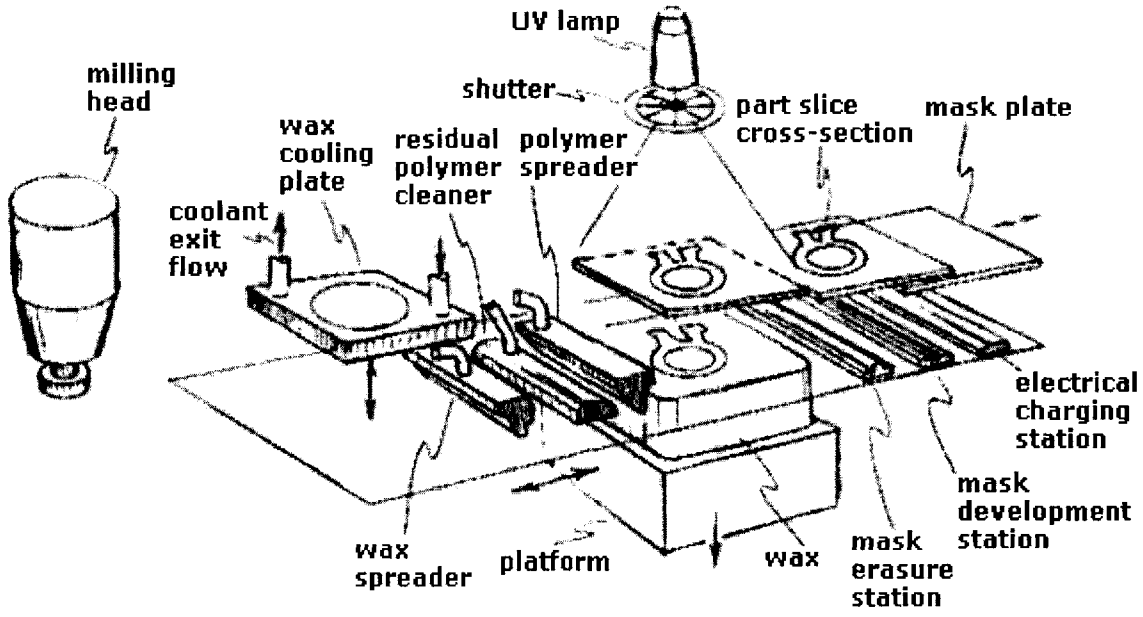

Figure 41 - A SGC machine
Reprinted with permission, courtesy of eFunda Inc.

4.7. Other 3D Additive Manufacturing Processes

Multiple other additive manufacturing processes exist and are being constantly refined and improved. As more advances take place in this nascent field, the 3DST project could take advantage of the new capabilities. As technologies develop to be able to control finer features, other processes besides SLA could be employed. A cheaper or reusable material would also be beneficial, and new developments in the creation of 3D printed ice sculptures may hold an interesting application. For example, if the internal tunnels were created in ice and the ice tunnels were used as guides for cable (as the SLA structure now does), after the cables had been routed to their proper destination, the plastic deformation undergone, the plates at the ends would hold the cables in place. The ice could be melted out, and the space could be filled with an epoxy. Other unique possibilities are discussed in chapter 8.

4.8. Use in 3DST (The Design)

To create the fine tunnels and the narrow walls that exist between them, SLA was chosen because it currently has the finest resolution of all macro additive processes (some additive processes can deposit atoms, but at their build rate, it would take years to build a single block). A 3D systems Viper Si2 System was used in its high resolution mode. In this mode it uses a spot size of .003" and builds layers in .002" increments. At this rate, a typical 5" x 5" x 1.5" block takes about 100 hours to build. The UV sensitive polymer is distributed by 3D Systems under the name 5510. Multiple other resins are available including ones that are more heat resistant, more flexible and optically transparent. The 5510 material is well suited to high accuracy builds; it has the following mechanical properties.

Metric	Test Method	Value	Units
Density		1.23	G/cc
Cost		~3	US $ / in^3
Tensile Strength	ASTM D 638	11,100	Psi
Tensile Modulus	ASTM D 638	478,000	Psi
Elogation at Break	ASTM D 638	5.4	%
Flexural Strength	ASTM D 790	14,400	Psi
Flexural Modulus	ASTM D 790	443,000	Psi
Impact Strength (notched Izod)	ASTM D 256	27	J/m
Heat deflection Temperature @ 66psi	ASTM D 648	87	C
Heat deflection Temperature @ 264psi	ASTM D 648	76	C
Glass Transition Temp	DMA, E" peak	68	C
CTE (< Tg)	TMA (T<Tg)	79	ppm / K
CTE (> Tg)	TMA (T>Tg)	184	ppm / K
Thermal Conductivity		.181	W/m K
Hardness	DIN 53505	86	Shore D

Table 9 – 5510 SLA material mechanical properties [1]

The build time is directly related to the layer size and the spot size. Other SLA build systems offered by 3D Systems use larger spot sizes and could build the part in a shorter time. The smallest step size and the smallest spot size was used in the first part to test the limits of the process. By altering the routing of the block to allow for greater wall thickness and tolerance between tunnels, faster build times could easily be achieved. For example, the 5" x 5" x 1.5" block using a spot size of 0.003 and in 0.002" steps took roughly 100 hours to build, but by doubling the step size (to 0.004") and increasing the spot size to 0.010", the part would take less than 5 hours build. The negative aspect of

this, is that the tunnels will be rougher and the maximum density of tunnel per unit volume will be decreased.

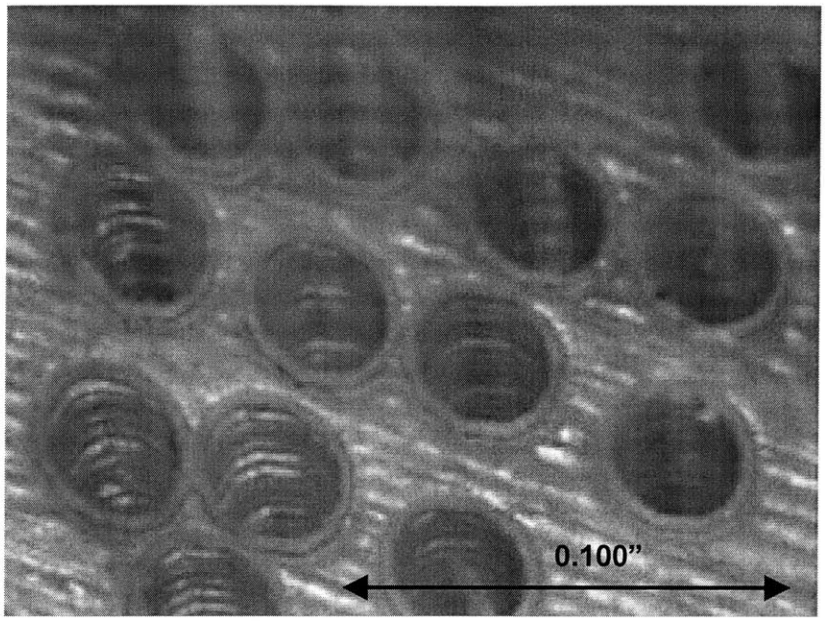

Figure 42 - A picture of multiple 0.037" holes normal to the build direction

As the figure above shows, the paths created on the Viper SLA machine can create fine features and relatively smooth circular walls at this dimensional scale. In the figure these tunnels are created normal to the build direction and the build steps can be seen.

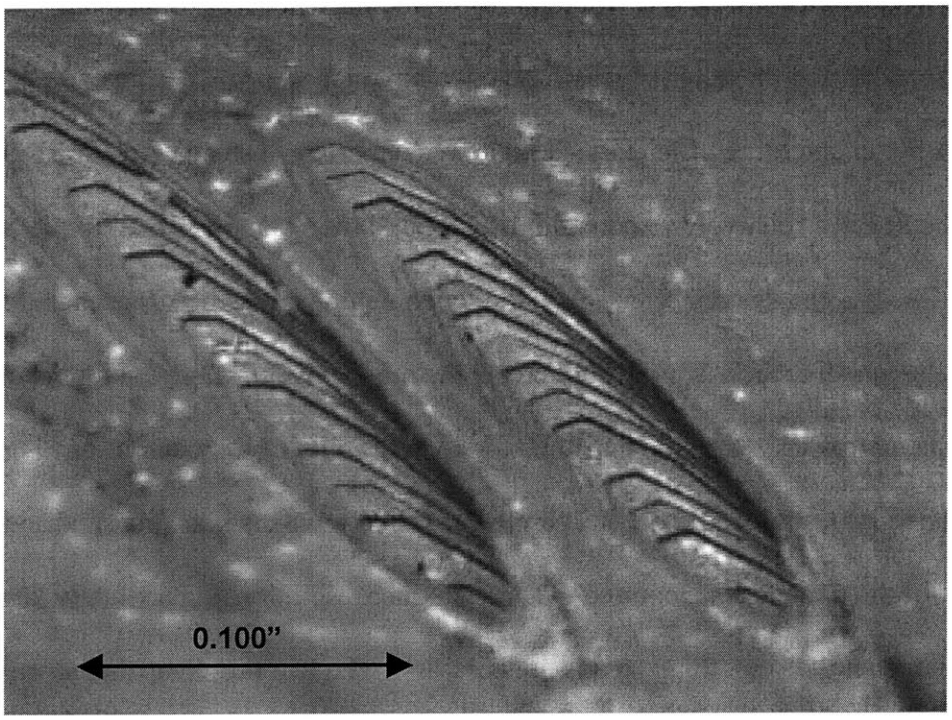

Figure 43- A picture of two paths nearly parallel to the build direction

In the figure above, the squared-off elliptical cross section of a round path can be clearly seen. The squaring off is due to the translation of the pure elliptical geometry in the CAD program to the meshed triangular sections inherent in the coding of a .stl file. This could be improved by creating a smaller mesh, however, the size of the file generated is already remarkably large for a 512 path block (>100 MB).

4.9. Post-processing on the SLA block

Early in the development of the 3DST, the roughness of the surface was deemed a problem area for insertion of wires. To solve this problem an abrasive machining operation was employed by hand. Two different techniques were used. The first involved pushing a thin diameter abrasive cord into each tunnel and once through the

other side, the cord was manually worked back and forth through the tunnel. The problem with this technique is it worked only on the inside curves of the path and left any straight sections and the outer edges of the curve untouched.

A better and more efficient technique was employed instead. An abrasive grit was immersed in a relatively viscous fluid. The fluid was then pumped through each tunnel. This had the desired effect; it would tend to erode away the surfaces that stuck out into the tunnel the most and would create the most erosion where the tunnel diameter became the narrowest. It would also tend to erode the outside diameter of any bends.

The first test blocks were built on lower resolution SLA machines and some post-finishing of the tunnels was required. Using a higher resolution and a slightly larger tunnel diameter, the smoothing step is unnecessary. The two problems that arose with large resolution were partial blockages of the tunnel and the formation of ridges at the start of curved sections, which are alleviated in the higher resolution build modes.

4.10. Summary

The ability of the SLA machines to build nearly arbitrary geometries gives tremendous flexibility to designers, yet very few OEM applications have yet to take advantage of the relatively new technology. Additive manufacturing is a rapidly growing and maturing technology, and as other processes become cheaper and increase their resolution and accuracy, they could be used as alternatives to SLA.

It looks like it will be a long time before additive manufacturing could ever be able to build the coaxial structure directly (eliminating the need to push wires in after the tunnel was created). To do this, multiple materials (a conductor and a dielectric) would need to be deposited with the accuracy and smoothness required for high speed signals.

In Chapter 3, one of the reasons PCB traces were so much worse than coaxial cable was the use of drawn copper cable that made the conductivity greater and made the surface roughness very small. A deposited material will be less conductive and rougher than nearly any semi-rigid coaxial cable and most PCB traces. The ability to deposit PTFE (the stuff that nothing sticks to) is sure to be a rather large challenge as evidenced by PCB vendors who have been unable to do this in a simpler layer by layer application. Thus, the dielectric that could be deposited would likely have a higher dielectric constant and higher loss tangent than Teflon and thus performance will suffer. For the near future, the use of semi-rigid coaxial cable inserted into a stereolithography part is likely the best high speed signal space transformer that can be manufactured with relative ease.

Chapter 5 - Insertion Physics

5.1. Overview of Prior Work

The act of inserting semi-rigid coaxial cable into a preformed three dimensional tunnel has not been studied before. Remarkably, many similar operations (the act of pushing a beam into a tortuous tube) exist in a variety of different fields, but these cases have also not received much analytical study. In general, most studies tend to be problem-specific and use finite element analysis or empirical data to draw conclusions.

5.1.1. Beading Operation in Sheetmetal forming

The act of beading a sheetmetal edge can be performed by a number of different methods, but one method in particular is similar to the act of inserting a tube into a preformed tunnel. In this operation, the edge of the sheet is forced up the side of a curved die, generally accomplished by clamping the sheet and moving the die toward the sheet [36]. The sheet is slowly bent and conforms to the shape of the die. Once the die is removed, some springback occurs and the radius is somewhat larger than the die radius. The amount of springback can be calculated easily and is accounted for in the forming of the beaded or curled edge. It depends on the yield stress of the material and the curvature of the die, and is given by:

$$\kappa_0 - \kappa_1 = \frac{3}{2}\left(\kappa_{yield}\right) \tag{5.1}$$

The above equation relates the initial curvature, κ_0, to using the die to the curvature of the beam after it is released, κ_1. (i.e - after elastic springback has occurred.)

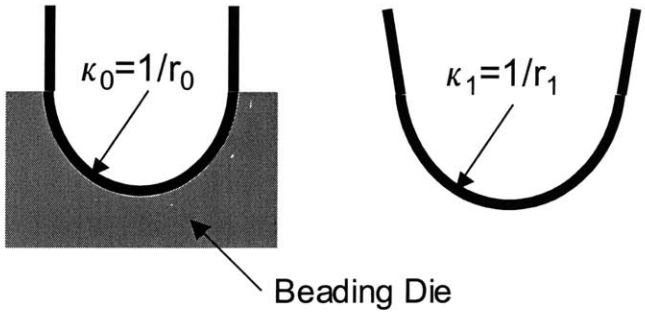

Figure 44 - A simple beading die and a piece of sheet metal showing springback

Equation (5.1) assumes a rectangular cross section of uniform modulus of elasticity. It further assumes that the beam was bent to the fully yielded condition. Unfortunately, very little literature exists to predict the forces involved in the beading operation process.

5.1.2. Oil Wellbore drilling

The oil drilling field has similar challenges of insertion of tubes into tubes. Basically, a very long drill (or a drillstring) is used to bore long, sometimes curved paths. The act of drilling this wellbore has received considerable attention in literature. The research investigates the forces required to force a drillstring from the surface down to the tip (where drilling occurs). Many of the newer drilling techniques have the ability to guide the tip of the drill, so that while drilling normal to the surface, the wellbore can be made to curve and even go horizontal to reach its desired destination. Some investigations attempt to deal with "high curvature" wellbores which are typically of radius less than 60 meters, and typical curved wellbores might have radii of 90 meters or

greater [61]. The investigations focus on inserting tubes of order a few inches in diameter, thus the bend radius to diameter ratio is of order 100:1 to 1000:1. At this ratio, the researchers found the effects of stiffness of the pipe were negligible. For reference, the 3DST would use ratios of order 1:10 to 1:40 where elastic and plastic deformations are significant forces. Most of the forces generated during insertion in the large curvature wellbore regime are dominated by the weight of the pipe, the buoyancy effects and the friction. No studies were found that dealt with the friction from first principles along a multiple curved surface during insertion. (A few studies exist but they consider only one bend [14] or resort to FEA methods [61] [62]). Furthermore, in many cases the key difficulty involved in oil drilling is transmitting a large axial force to the tip of the drill bit without buckling the drillstring [81](or after buckling still being able to transmit the required axial force to drill [39]). This problem is different from the problem of simply being able to force the pipe into the desired position.

The buckling of slender strings in tubes is the key limiter for insertion. The helical buckling of wires (or strings) under axial load in both curved and straight tubes is particularly applicable to oil drilling and has been studied both analytically and experimentally [39] [71] [81]. The formulas should be applicable at the smaller scale of the 3DST.

5.1.3. Endoscopes in GI tracts

The medical field (insertion of catheters, endoscopes, etc. into body tubes) has very little research that attempts to understand the basic physical processes of insertion. Instead, most of the research investigates the resulting effects of one catheter or endoscope design versus another. A typical study would investigate the post-traumatic stress undergone by patients as compared with a control group. The problem is perhaps complicated due to the flexible nature of most body tubes and the variable friction coefficient and stiffnesses of the tubes. Some research [80] tries to explore the physics behind endoscopes but does not explore friction or elastic deformation on insertion and instead focuses on buckling limits of different endoscopes. Another investigation of particular merit uses a load cell mounted between the operator and the endoscope to dynamically record the forces of insertion during a colonoscopy [51].

Despite these studies, there is little literature that analytically describes the forces of inserting a tube into another tube. Some finite element programs do have the ability to deal with such problems and ABAQUS [3] has a specific tube-in-tube element devoted to solving similar problems for the oil-drilling field and underwater cable laying. It is undesirable to require FEA calculations for each path generated due to the large number of paths that are generated. Instead, a relatively simple and quickly calculated formula was desired to describe the insertion forces and to understand the major contributors to the insertion force problem. To that end, an analytical model was developed in stages of increasing complexity and an experimental apparatus was built to test the theory.

5.2. Development of Experimental Test Apparatus

The basic requirement for the test apparatus was to be able to accurately measure the force required to push the cable into the tunnel as it proceeded along the path. To do this accurately, a force measurement method was required that did not depend on the driving mechanism. A beam load cell was selected for its high accuracy and it was mounted in such a way that all vertical forces felt by the cable would be transmitted to the load cell. The center of force was aligned with the center of the loading pattern of the load cell such that no extraneous moments were induced.

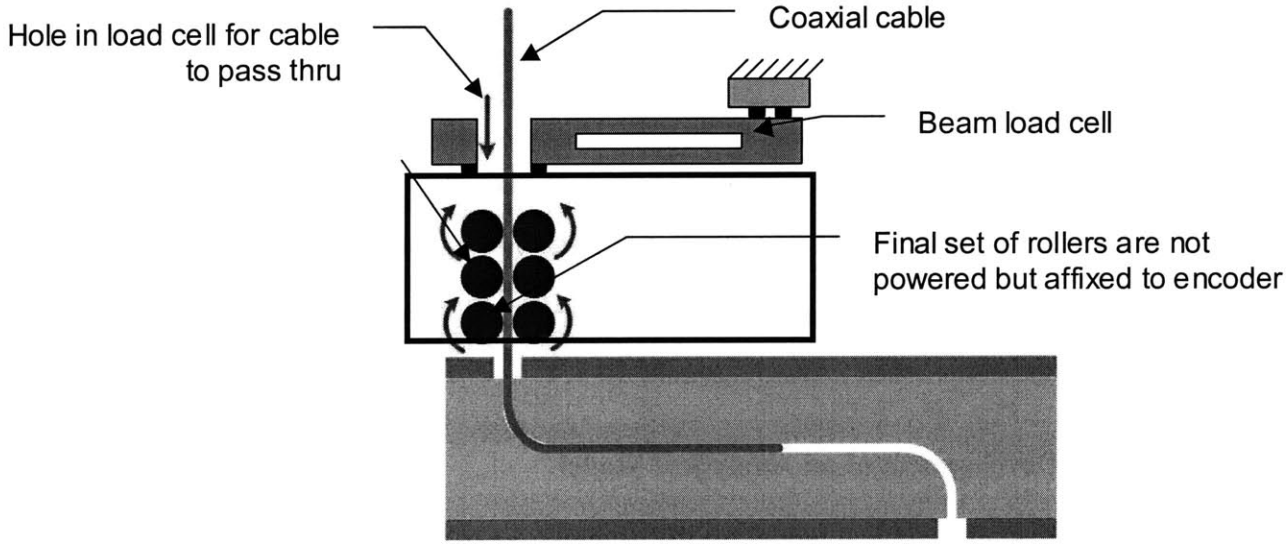

Figure 45 - A schematic of the insertion force measurement apparatus

The distance the cable has moved into the tunnel must also be determined. This was accomplished by use of a small unpowered roller just before the cable enters the tunnel. The roller is driven by the motion of the cable and an encoder measures the rotation angle of the roller. Because the roller diameter is known, the distance the cable has been

inserted can easily be determined. Any slippage of the drive rollers does not influence the measurement of the distance since the third roller is unpowered.

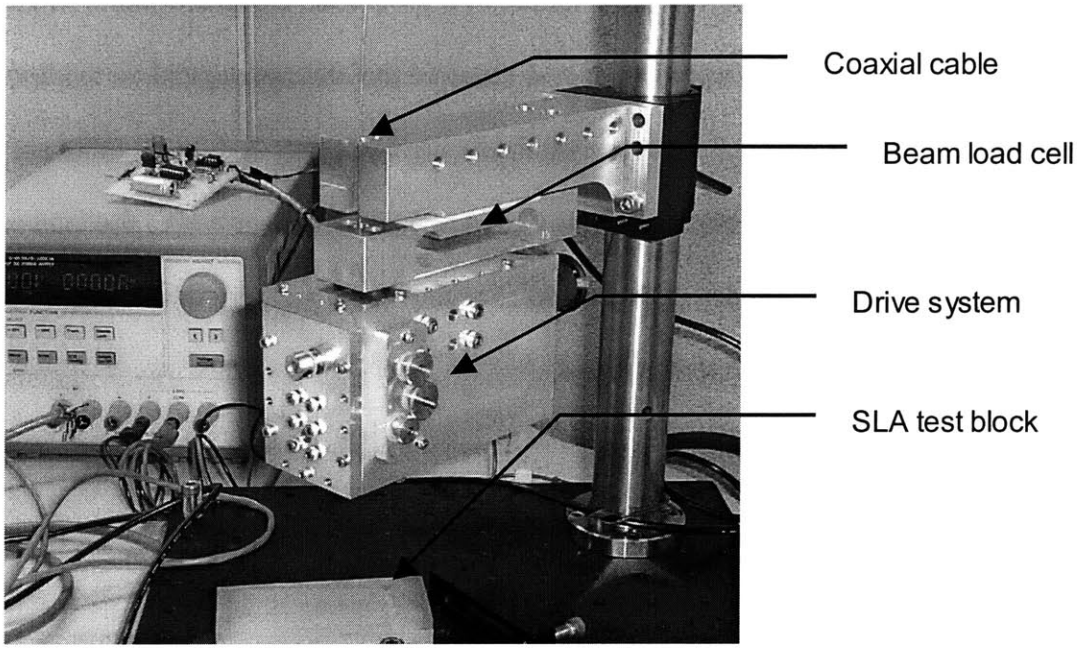

Figure 46 - The insertion force test apparatus

The output of the apparatus is a plot of force versus distance of cable insertion for a given tunnel. The development of the analytical model seeks to predict this graph of force vs. distance.

5.3. Development of an Analytical Model

Developing an analytical model for the general case of inserting a beam in a tube with any number of bends, any degree of curvature and any clearance is a very difficult problem. To address these difficulties, multiple models are developed below; starting with a simple first-order model and incrementally increasing the complexity and scope of the model. In the first and simplest model, only the geometry of the tunnel and internal elastic bending forces (of the beam) are considered. All other factors are ignored

including friction, elastic compression, and plastic yielding of the beam. In the second model, plastic effects are considered. In the third model, friction effects are considered. The fourth model specifically takes into account the clearances that typically exist between beam and tunnel. The fifth model expands the fourth to deal with composite beams. The sixth model explains how some of the models can be extended to deal with truly 3D freeform paths. A final section specifically mentions other effects that were neglected in the earlier models.

The first step toward developing a model was to determine what things should be modeled and how the beam progresses through the tunnel. For this analysis, three example tunnel paths are used throughout the next few sections to illustrate the effects of the different models. The first and simplest example is simply a short straight section (0.050" long) followed by a ninety degree bend, one inch in radius.

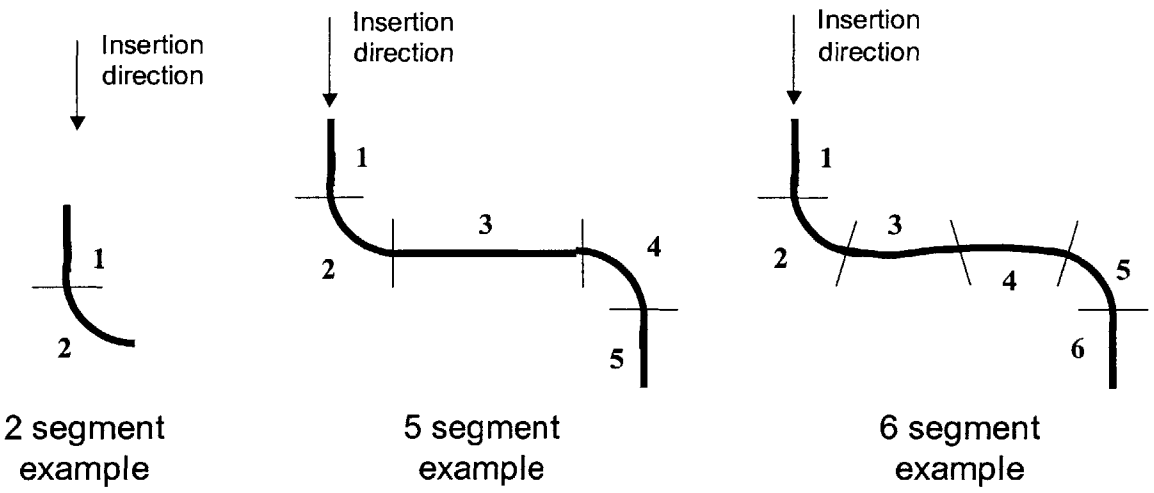

Figure 47 - 3 Example Paths for Analytical Modeling

The second example is a typical five segment path used by the 3D router algorithm. It starts with a straight section 0.100" long, followed by a ninety degree bend with a 0.5" radius. The tunnel then runs horizontal for a 2" straight segment. Then, the tunnel has another 0.5" radius bend for ninety degrees (in the opposite direction as the first bend) and finally the fifth segment is a straight segment 0.100" long. Finally, the third example is a six segment path used to illustrate transitions from a large radius to a smaller one and vice-versa. It starts the same as the second example with a 0.100" straight segment followed by a 90 degree, 0.5" radius bend. The third segment is a bend of less curvature with a bend radius of 2.0" for 29 degrees. It illustrates how the models deal with transitions from a high curvature segment to a lower curvature segment. The fourth segment has the same dimensions as the third (2" radius and 29 degrees), but is bent in the opposite direction. The fifth segment in this example is another 90 degree bend with a 0.5" radius in the opposite direction as the second segment, but the same direction as the fourth one. This transition illustrates the model's ability to deal with a change from a low curvature segment to a higher curvature one. The final sixth segment is a straight section 0.100" long.

For these examples, each segment has a constant curvature and each segment is tangent to its adjacent segments. The entrance and exit of the paths are always normal to the face of the surface to make electrical connections easier.

5.3.1. The first model – Elastic only

In the first model the following assumptions are made:

1. All paths are made up of segments of constant curvature.
2. Each segment has tangent continuity to adjacent segments.

3. Only paths in a single plane are allowed (2D only).

4. The beam and tunnel are both of circular cross-section.

5. The beam is of constant modulus throughout and the modulus under tension is the same as the modulus under compression.

6. There is no gap between the tunnel diameter and the beam diameter.

7. All surfaces are smooth.

8. No friction between the walls of the tunnel and the beam.

9. All forces on the beam are due to elastic bending (pure bending) only. Compression and shear forces are ignored.

10. No buckling or other catastrophic failures occur when inserting the beam.

11. Beam starts with zero curvature and no residual stresses.

12. The tunnel walls are perfectly rigid.

The inputs required to solve this model are:

1. A n-segment path with known curvatures for each segment

2. The beam stiffness = EI

For the first example, the beam feels no forces in the first segment because the starting curvature is zero and so is the first segment. No work is required to push the beam until the start of the second segment. The beam is shown below inserted to the start of the second segment. The force that must be applied to the beam to follow the curvature of the tunnel must be determined. The external work (from pushing the beam) must equal the internal strain energy in the beam and thus the force of insertion can be calculated from Equation (5.2).

$$\Delta W_{in} = \Delta U_{beam} + \Delta W_{out} \tag{5.2}$$

Setting the work in equal to the push force required to insert the beam, F_{insert}, times a small distance, Δx, and solving for the internal strain energy in the beam.

$$\frac{1}{2} F_{insert} \Delta x = \frac{1}{2} M_{bend} \Delta\theta + 0 \tag{5.3}$$

Converting $\Delta\theta$ to $\Delta x/R$, where R is the radius of curvature of the beam at the neutral axis, and dividing by Δx on both sides,

$$F_{insert} = M_{bend} \left(1/R\right) \tag{5.4}$$

For pure bending, the strain at any point in the beam can be obtained from the curvature of the neutral axis and the distance y from the neutral axis by calculating the arc length at that point.

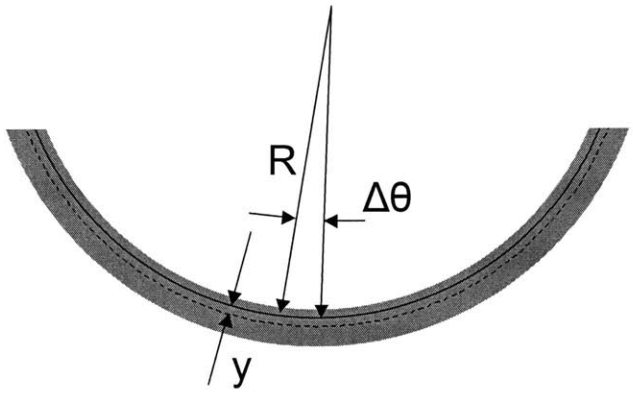

Figure 48 - A curved beam model

$$\varepsilon = \frac{\ell_{deformed} - \ell_{original}}{\ell_{original}} = \frac{\left(R + y\right)\Delta\theta - R\Delta\theta}{R\Delta\theta} \tag{5.5}$$

$$\varepsilon = \frac{y}{R} = y\kappa \tag{5.6}$$

where κ is the curvature and is defined as the reciprocal of the radius and specifically denotes the curvature of the neutral axis of the beam. The definition of elastic modulus (or Young's modulus) is:

$$E = \frac{\sigma}{\varepsilon} \tag{5.7}$$

The stress for pure bending at a given distance y from the neutral axis is found by using Equation (5.6) and (5.7):

$$\sigma = \frac{Ey}{R} = Ey\kappa \tag{5.8}$$

For pure bending of elastic beams with uniform elastic modulus,

$$M_{bend} = \int_A y\sigma dA \tag{5.9}$$

using (5.8), the bending moment becomes:

$$M_{bend} = \int_A yE\left(\frac{y}{R}\right)dA = \frac{E}{R}\int_A y^2 dA \tag{5.10}$$

The moment of inertia, I, about the neutral axis is also known as the second moment of the beam and is given by:

$$I = \int_A y^2 dA \tag{5.11}$$

For a circular solid beam,

$$I_{circularbeam} = \frac{\pi d^4}{64} \tag{5.12}$$

Equation (5.10) can then be combined with (5.11) to yield the following relation:

$$M_{bend} = EI(1/R) = EI\kappa \tag{5.13}$$

Substituting Eqn. (5.13) into (5.4),

$$F_{insert} = EI\left(1/R\right)^2 = EI\kappa^2 \tag{5.14}$$

Thus, the work required to push the beam through the curved segment is constant throughout the entire segment. The force depends only on the radius of curvature of the tunnel and the beam stiffness, EI. For a solid copper beam of diameter 0.034", E is 17×10^6 psi and I is 6.56×10^{-8} in^4. The predicted force of insertion is graphed below for each of the three examples.

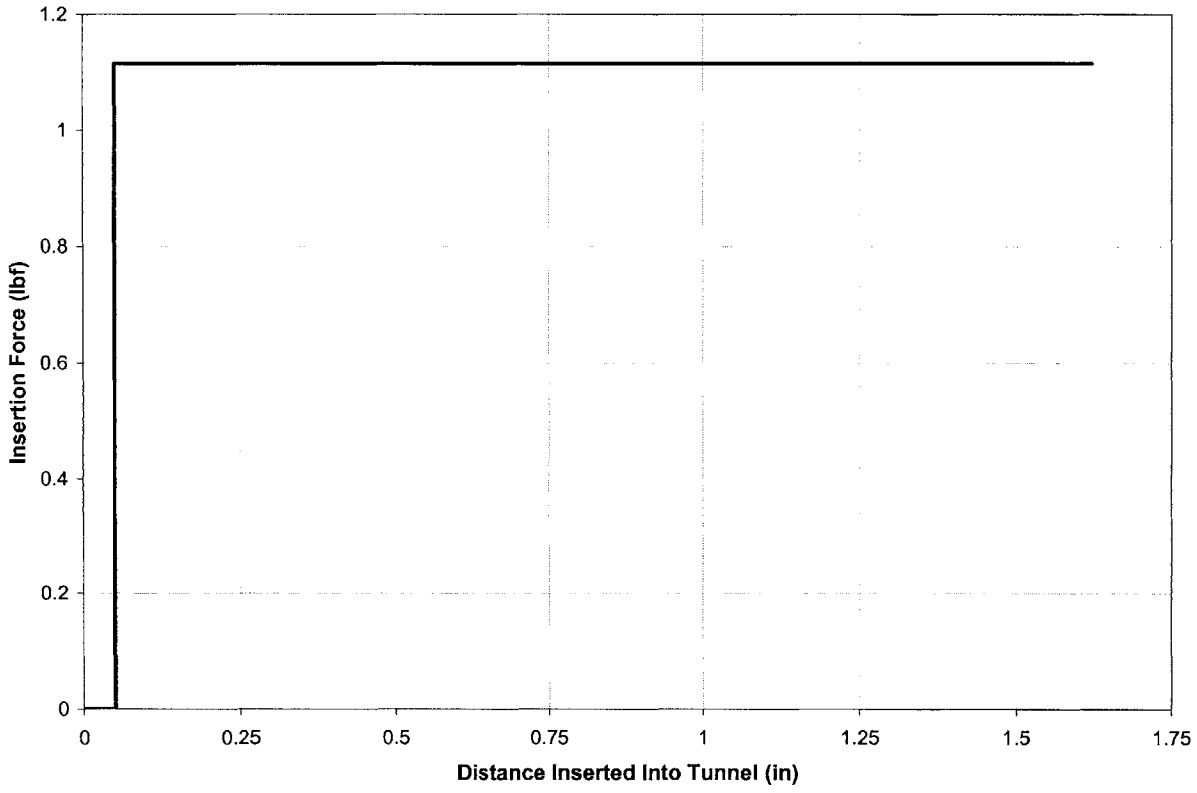

Figure 49 - Force versus Insertion Distance for the 1st example using the all elastic model

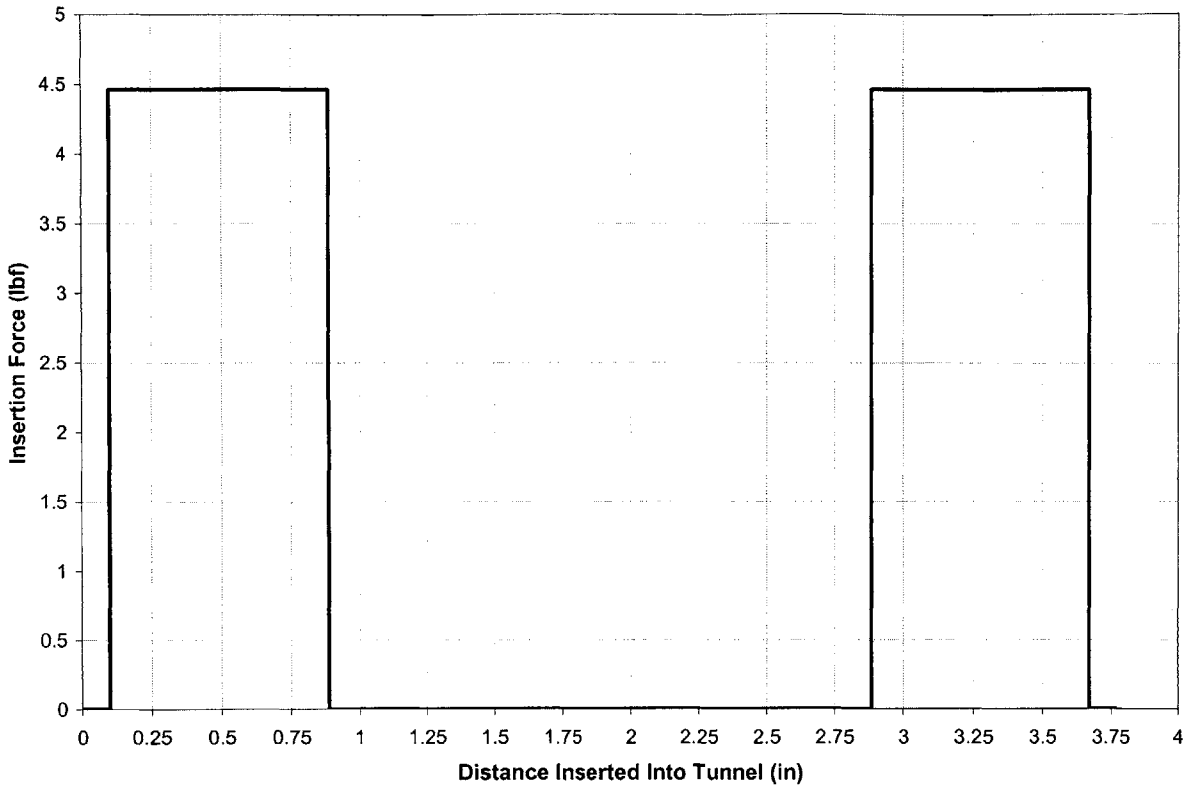

Figure 50 - Force versus Insertion Distance for the 2nd example using the all elastic model

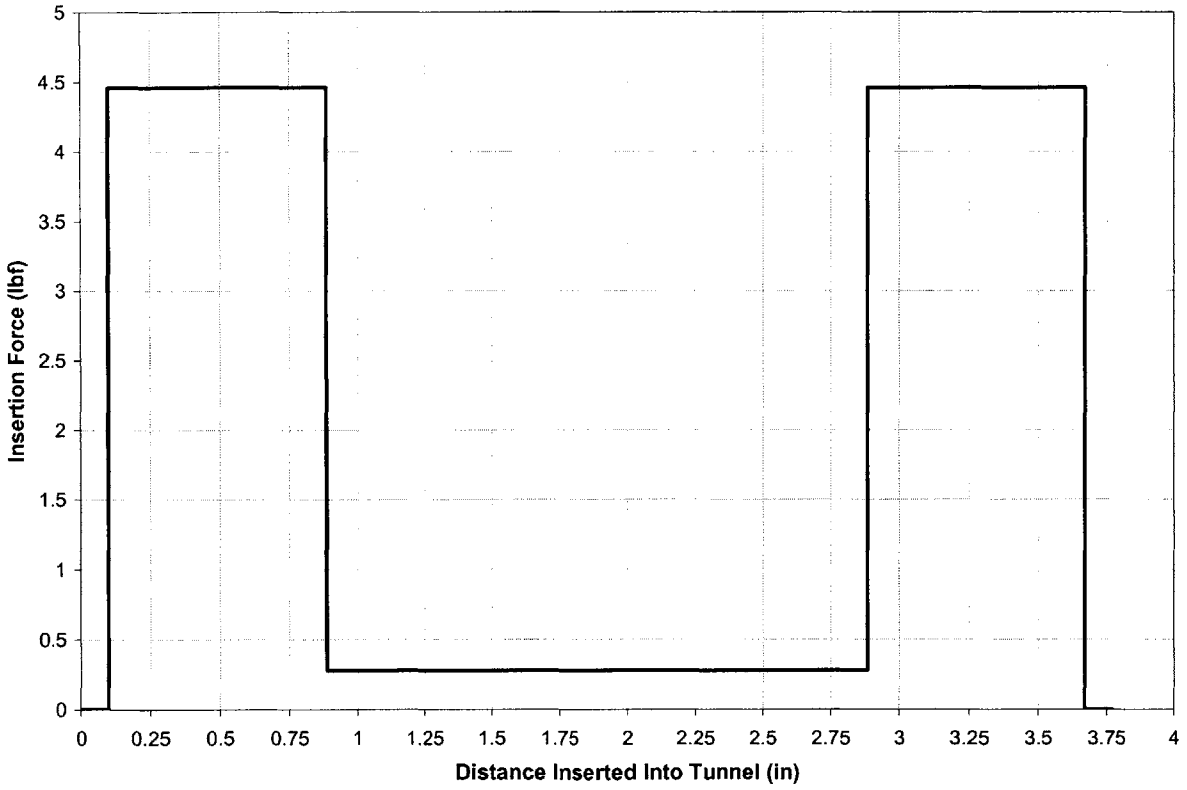

Figure 51 - Force versus Insertion Distance for the 3rd example using the all elastic model

These three examples illustrate the effect of curvature on the insertion force. It is interesting to note that for example two, once the beam exits the first curved segment (segment #2), it is free to straighten out and because the beam is perfectly elastic (in this model), all the energy is recovered. The beam unbends to a curvature of zero without any additional work. If we analyze this from a virtual work perspective, we see that no work is actually being done. For each tiny element that must be bent to a given radius, a piece the same size is unbent and the work is recovered. Drawing a control volume around the bend area, it is apparent that the length of beam in the curved segment remains constant as the beam is forced further along the tunnel. Furthermore, the sum of the two lengths of straight sections (before and after the bend) remains constant. Thus, no work is being done (neglecting friction and plastic effects), and thus the predicted insertion force in this stage is zero.

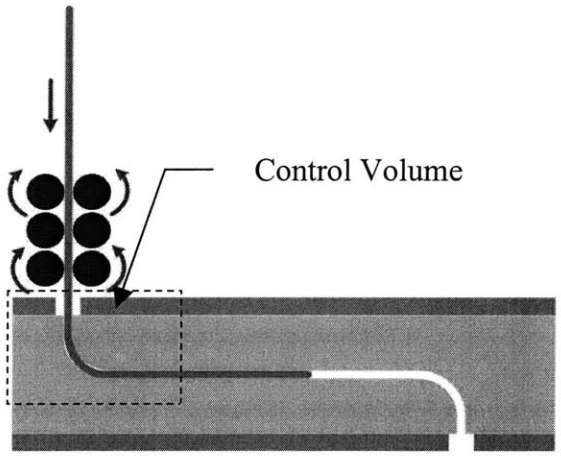

Figure 52 - Control Volume showing no work done after first bend (all elastic model)

In summary, the all elastic, pure bending, no friction model has a great deal of elegance. The model depends only on the curvature of the path at the tip of the beam. This model

will be applicable whenever the beam does not yield plastically and the friction is kept low between the wall and the beam. The model also requires very little clearance between the beam and the tunnel walls. The model, because it depends only on the curvature of the path at the tip of the beam can be used for 3D paths of arbitrarily changing curvature. The history of the path and the beam stresses can be completely ignored as the beam always returns elastically. This makes the elastic model extremely easy to use and understand.

5.3.2. The second model – Elastic and Plastic only

In the second model the following assumptions are made:

1. All paths are made up of segments of constant curvature.
2. Each segment has tangent continuity to adjacent segments.
3. Only paths in a single plane are allowed (2D only).
4. The beam and tunnel are both of circular cross-section.
5. The beam is of constant modulus throughout and the modulus under tension is the same as the modulus under compression.
6. There is no gap between the tunnel diameter and the beam diameter.
7. All surfaces are smooth.
8. No friction between the walls of the tunnel and the beam.
9. All forces on the beam are due to elastic and plastic bending (pure bending) only. Compression and shear forces are ignored. No strain hardening (or softening) occurs. The material is elastic-perfect plastic.
10. No buckling or other catastrophic failures occur when inserting the beam.

11. Beam starts with zero curvature and no residual stresses.

12. The tunnel walls are perfectly rigid.

The inputs required to solve this model are:

1. A n-segment path with known curvatures for each segment

2. The beam stiffness = EI

3. The yield stress of the beam = σ_y

4. The beam diameter = d_{beam}

Plastic deformation occurs when a material is loaded but does not fully return to its original undeformed state when unloaded. The first model always assumed that all the loading was elastic only and no plastic deformation ever occurred. This is a good assumption when the bend radii in the tunnel are large and the yield stress of the beam is high.

Fortunately, plastic deformation limits the maximum force that a beam can exert (unlike the all elastic model), and consequently lower the insertion force in first curved segment. Unfortunately, because not all the energy is recovered when a beam is bent plastically, the model predicts there will a finite force in any straight segments following a curved segment. In fact, every bend or unbend operation of the cable that exceeds the yield stress of the beam adds to the insertion force in any subsequent segments.
The stress in a beam can never exceed the yield stress (for a non-strain hardening perfect plastic material) and thus rearranging equation (5.8) the minimum radius a given beam can be bent to before it starts to yield is:

$$R_{onset} = \frac{Ed_{beam}}{2\sigma_{yield}} \tag{5.15}$$

where d_{beam} is the outer diameter of the beam.

The 0.034" diameter copper beam has a yield stress of about 40,000 psi and thus R_{onset} occurs at a radius of 7.2 inches or a curvature of 0.1389.

For the application being developed, the bend radii of the tunnels are typically in the range of 0.25" to 1.25", thus the plastic yielding effects are significant.

When a beam is bent to a radius smaller than R_{onset}, the total moment must be calculated as the sum of the elastic and plastic contributions. The outermost fibers of the beam are in the plastic regime and the inner fibers (closest to the neutral axis) are in the elastic regime. The contribution of each to the total moment is calculated as follows:

$$M_{total} = M_{elastic} + M_{plastic} \tag{5.16}$$

For a circular beam with symmetry about the neutral axis and the plane normal to it, the moments can be calculated for one quarter of the beam area, hence the two "4" terms.

$$M_{total} = \frac{E}{R}\int_A y^2 dA + \sigma_{yield}\int_A y dA \tag{5.17}$$

$$M_{total} = \frac{4E}{R}\int_0^{y_c} y^2\left(r^2 - y^2\right)^{1/2} dy + 4\sigma_{yield}\int_{y_c}^{r} y\left(r^2 - y^2\right)^{1/2} dy \tag{5.18}$$

where y_c is the distance from the neutral axis where the beam stress is equal to the critical yield stress and r is radius of the cross section of the beam.

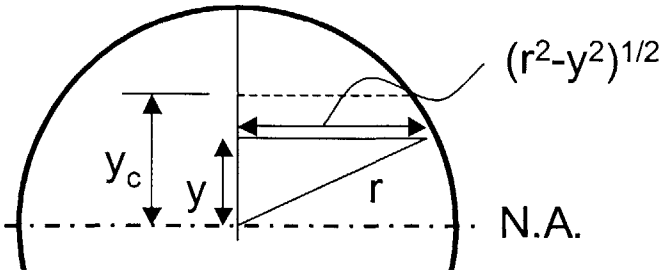

Figure 53 - Cross section of elastic plastic beam

From equation (5.8):

$$y_c = \frac{R\sigma_{yield}}{E} = \frac{\sigma_{yield}}{E\kappa} \tag{5.19}$$

Integrating the combined moment,

$$M_{total} = \frac{1}{2}E\kappa\left(r^2 y_c X - 2y_c X^3 + r^4 \tan^{-1}\left(\frac{y_c}{X}\right)\right) + \frac{4\sigma_y}{3}X^3 \tag{5.20}$$

where

$$X = \sqrt{r^2 - y_c^2} \tag{5.21}$$

The combined moment can be used in equation (5.4) and thus the required insertion force becomes:

$$F_{insert} = M_{total}(1/R) = M_{total}\kappa \tag{5.22}$$

The total moment calculated above assumes that the beam was initially unbent and was bent to a radius which caused plastic deformation. These equations work well in our examples up to the first curved segment. In the first example, the beam will exit the second segment and will be wholly unconstrained. At this point the beam will spring

back elastically some amount. Because some plastic deformation occurred, the beam will not return to its initial unbent condition but will instead have some curvature less than the curvature of the tunnel segment. This new curvature the beam takes will henceforth be referred to as the exit curvature. It is calculated from the knowledge that the beam will return along the same slope of its elastic loading.

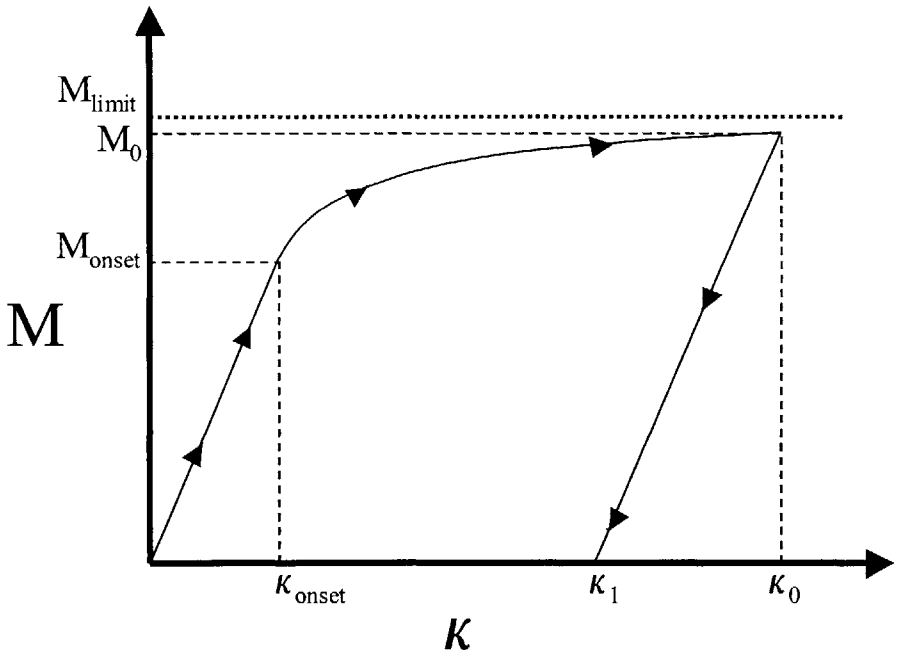

Figure 54 - Moment-curvature diagram for an elastic – perfect plastic beam in pure bending. A plot of equation (5.20)

$$\frac{M_{onset}}{\kappa_{onset}} = \frac{M_0}{\kappa_0 - \kappa_1} \tag{5.23}$$

where all values are known except for κ_1.

$$\kappa_{onset} = \frac{2\sigma_{yield}}{Ed_b} \tag{5.24}$$

$$M_{onset} = EI\kappa_{onset} \tag{5.25}$$

For a circular beam, the fully plastic moment is (from Equation (5.18)) where $y_c = 0$:

$$M_{limit} = \frac{1}{6}\sigma_{yield} d_{beam}^3 \tag{5.26}$$

The force of insertion can be determined easily for any curvature according to Equation (5.22), however, the situation becomes much more complicated when the beam has a residual stress state and does not have an initial curvature of zero. This situation occurs after exiting the first curve. Up until this point, all segments have had their starting curvatures equal to zero and the residual stress in the beam is zero.

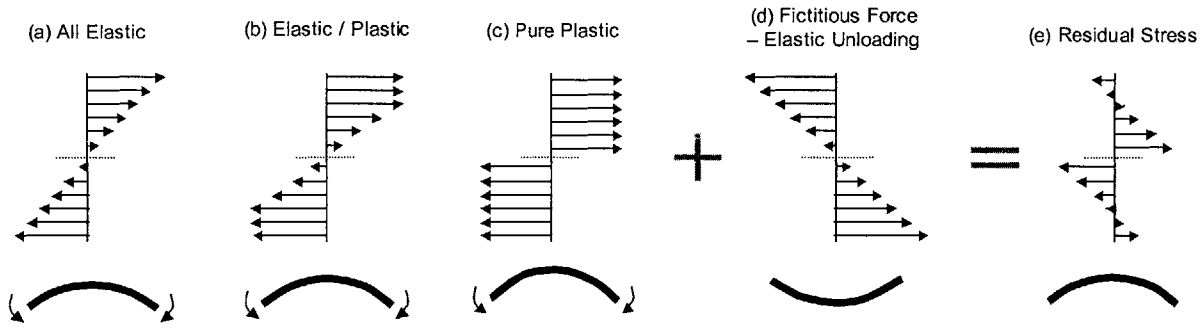

Figure 55 - Beam subjected to pure bending and their associated stress diagrams

The figure above shows a beam being bent in (a) pure bending without exceeding the yield stress. In (b), the beam is bent beyond the elastic limit and is partially yielded. In (c), the beam has been bent to its full plastic limit (the entire cross section has been plastically deformed.) To determine the stress state after a bend operation, the fictitious force shown in (d) which represents the elastic springback moment is added to the stress state in (c). The resulting stress distribution is shown in (e) and it represents the stress state of the beam after elastic springback.

The difficulty of keeping track of the moment that must be applied to the beam is illustrated in the following two figures. Once the beam has residual stress, each new curved segment must take that stress state into account for the next bend. The magnitude and direction of the stress state must be known as bending the beam further in the same direction results in behavior markedly different from bending it in the opposite direction. Figure 56 below shows the moment-curvature diagram for a beam bent in one direction to curvature κ_0, then allowed to relax to the springback curvature κ_1.

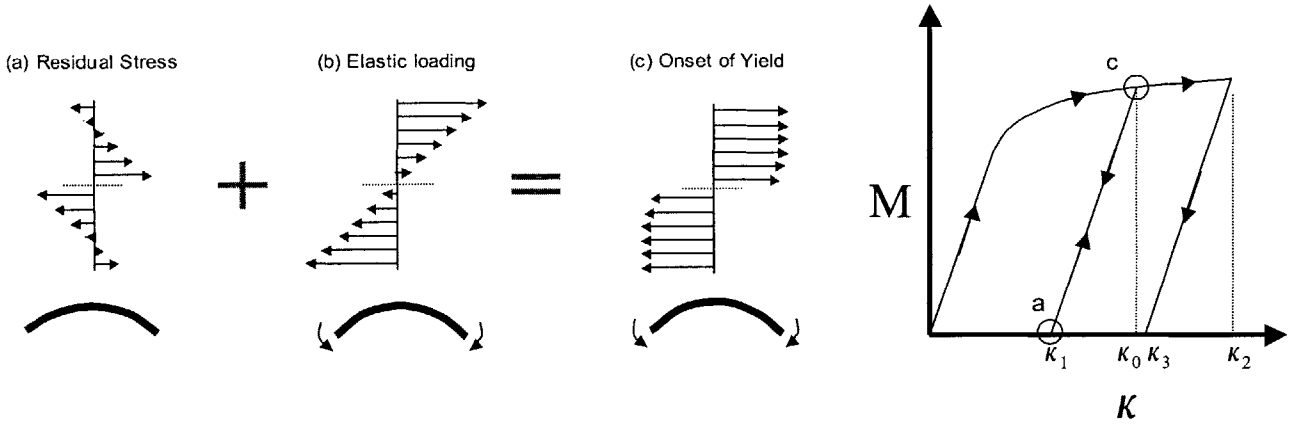

Figure 56 - A beam subject to plastic bending, then unloaded. The beam is then subject to further loading in the same direction.

The beam is then bent in the same direction back to κ_0, following the unloading path, then beginning to yield again as it is bent to κ_2. Note that because of the residual stresses of the beam (a), the beam can be bent to an effective elastic curvature (b) higher than the one it initially yielded at. The beam is then allowed to spring back to κ_3. Thus, predicting the moment required for any curvature after an initial bend and relaxation to κ_1, follows one of two equations depending on the degree of curvature. For curvatures less than κ_0, only a minor modification is necessary to the all elastic equation (5.14):

$$F_{insert} = EI\left(\kappa_f - \kappa_i\right)^2 \tag{5.27}$$

where κ_i represents the initial curvature or springback curvature and κ_f represents the final curvature. For curvatures greater than κ_0, the residual stress state after springback must be known to accurately predict the moment.

Another complexity occurs when the beam is bent backward toward zero curvature or beyond. As shown in the figure below, the stress distribution when bending the beam backward is not nearly as simple as when the residual stresses are zero.

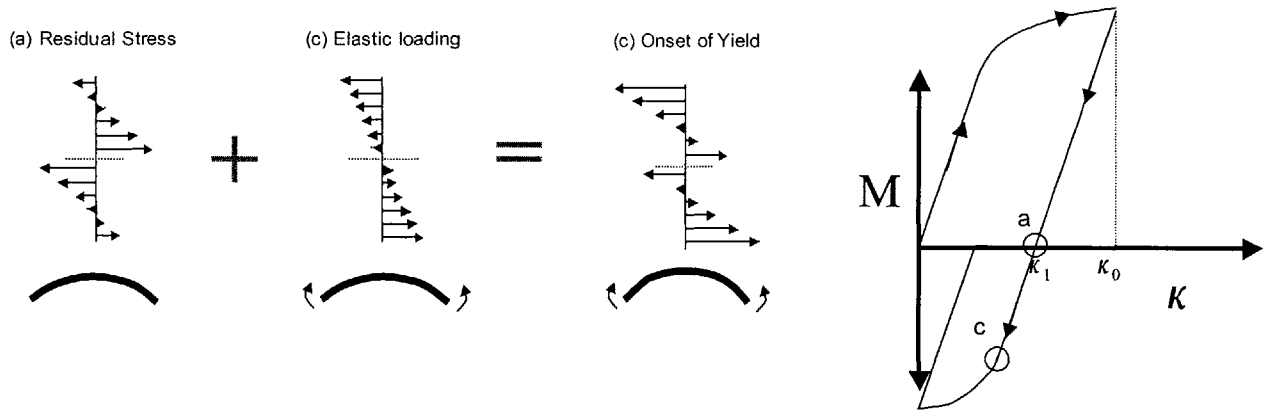

Figure 57 - A beam subject to plastic bending, then unloaded.
The beam is then subject to further loading in the reverse direction.

It should be clear that it is difficult to keep track of the residual stresses and associated moments for an arbitrary sequence of bends without resorting to numerical methods. For the 3DST project, a simple model that predicts the force in any condition is required, but some inaccuracies in the model can be tolerated if there is a significant gain in the speed of computation. The 3DST has as many as 1024 routed paths (for current applications) and the search for each path may require thousands or millions of trial paths. Therefore,

a simplified model that can easily be applied to a number of different paths types is desired.

To accurately model the forces in a beam that is bent in one direction and then bent back in the opposite direction, a simple finite element model was created using Excel. The bending moment was calculated to a high degree of accuracy into the plastic regime. The Excel model allowed modeling the residual stress state and calculation of the moment required to bend the beam back to straight after it was plastically deformed. The stress states for various curvatures of a .034 copper beam are shown below. In Figure 58, arrows are shown for the first stress state when the initial unbent beam is bent to a curvature of 0.1 or a radius of 10 inches. All subsequent states are shown without arrows for clarity.

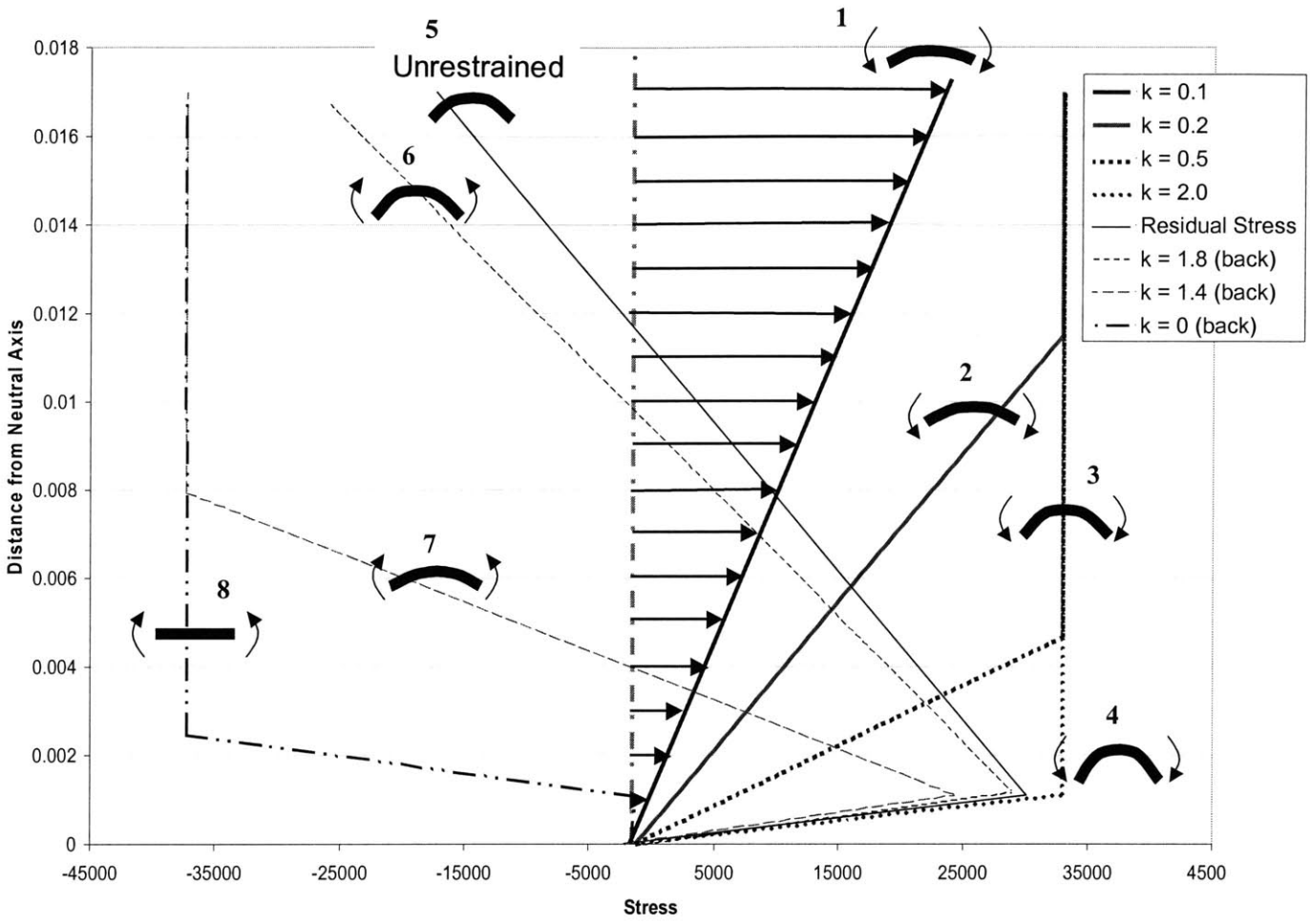

Figure 58 - Stress states of a 0.034" diameter beam subject to a sequence of increasing pure bending (to a curvature of 2), then allowed to relax and forcibly bent back to straight.

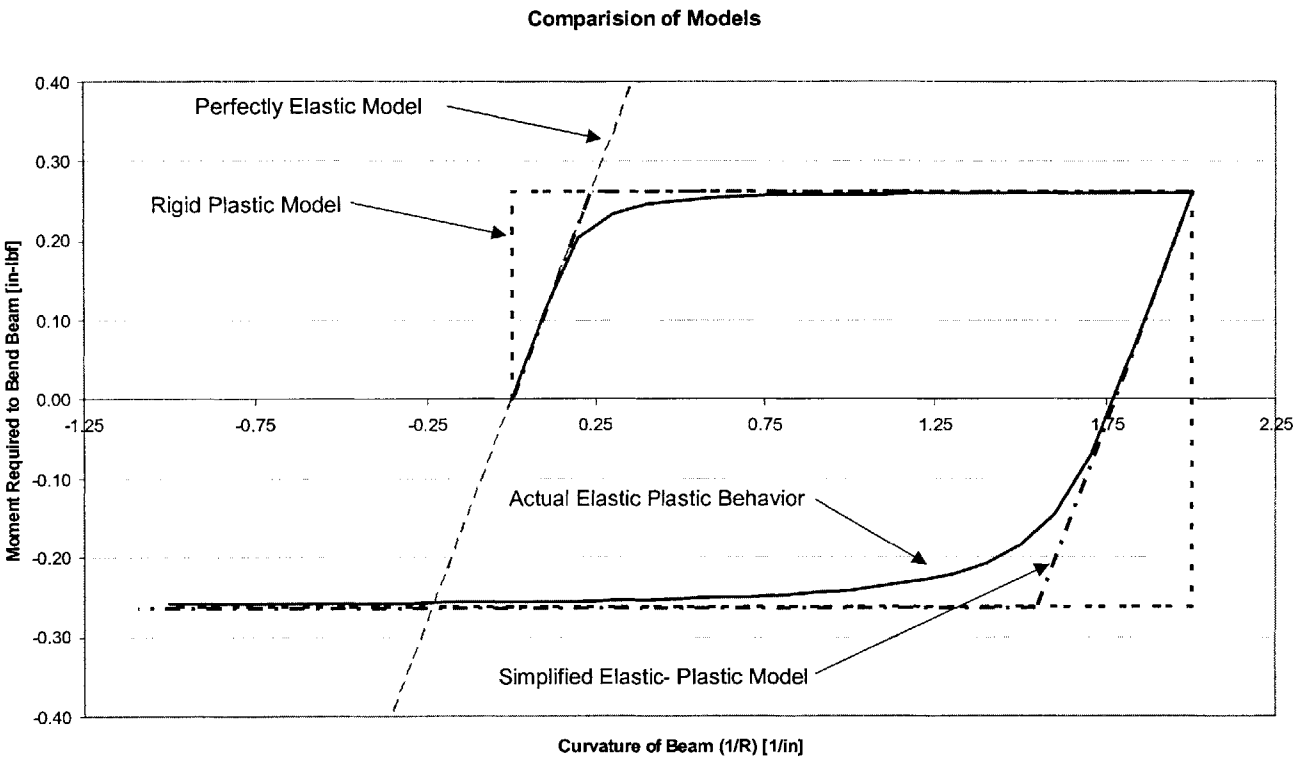

Figure 59 - Bending Moment vs. Curvature diagram for Perfectly Elastic Model, Rigid Plastic Model, and Elastic - Plastic Simplified Models compared to Actual Elastic - Perfect Plastic

The 34-element (FE) elastic plastic model created in Excel agrees with the mathematical elastic-perfect plastic equations within one half of a percent (higher accuracy could easily be obtained by increasing the number of elements) for the first bend and the springback. The FE model was then used to calculate the effect of the reverse bend and is plotted above. Once the true moment versus curvature diagram was calculated, three simple mathematical models were proposed to estimate the moment for the 3DST program. The first model, all elastic, assumes that regardless of the curvature, the beam never yields (described in section 5.3.1). It predicts the moment accurately up to an initial curvature

of roughly 0.2 (or equivalently a radius of 5 inches) after which it predicts much higher moments as it is not stress limited.

The second mathematical model is based on a rigid plastic material. It assumes that regardless of curvature, the beam is always bent to the maximum moment possible (or the fully yielded condition). There is therefore no elastic springback in this model since the elastic modulus is infinite. As can be seen in the figure above, this model accurately predicts the moment from roughly 0.3 to 2 (on initial bending) and from 1.2 to –1.0 (on back bending). This model is especially easy to use but suffers accuracy for low curvatures and does not take into account the recovered energy due to elastic springback.

The third mathematical model, (and the one that will be henceforth used), is a simplified elastic plastic model. It assumes that the beam is entirely elastic until the moment equals the fully plastic moment. On a reversal, the elastic springback curvature is calculated and the elastic portion of the model follows (5.27). This model accurately predicts the moment required to bend the beam in all cases except near the transition between elastic and plastic. In this case, the model overestimates the required moment and thus is conservative. For modeling purposes, a new term called κ_{limit} is introduced which is defined as the curvature at which the elastic model predicts a moment equal to the fully plastic moment.

$$\kappa_{limit} \equiv \frac{M_{limit}}{EI} \tag{5.28}$$

Although plastic behavior starts to occur at κ_{onset}, the use of κ_{limit} provides a good estimation of the moments without consideration for the residual stress of the beam. This

greatly simplifies the analysis for all bends after the first bend, since κ_{onset} changes after every bend and unbend cycle and depends on the residual stress state of the beam and the orientation of the next bend relative to the stress state while κ_{limit} is constant.

For the first segment:

$$F_{insert} = EI\kappa^2 \quad \text{when } \kappa \le \kappa_{limit} \tag{5.29}$$

$$F_{insert} = M_{limit}\kappa \quad \text{when } \kappa > \kappa_{limit} \tag{5.30}$$

$$F_{unr} = 0 \quad \text{when } \kappa \le \kappa_{limit} \tag{5.31}$$

$$F_{unr} = M_{limit}\kappa \quad \text{when } \kappa > \kappa_{limit} \tag{5.32}$$

$$\kappa_{exit} = 0 \quad \text{when } \kappa \le \kappa_{limit} \tag{5.33}$$

$$\kappa_{exit} = \kappa - \left(\frac{M\kappa_{onset}}{M_{onset}} \right) \quad \text{when } \kappa > \kappa_{limit} \tag{5.34}$$

where κ is the curvature of the tunnel and thus represents the curvature of the beam because there is no clearance between beam and tunnel.

For the n^{th} segment, κ_{exit} from the previous segment equals κ_{enter}. F_{unr} stands for the unrecoverable force from a segment. The total force in a given segment is then the sum of the force of insertion for bending or unbending the beam in the current segment and all the previous segments' unrecoverable force.

$$F_{insert} = F_n + \sum_{n-1} F_{unr} \tag{5.35}$$

$$F_n = EI\left(\kappa - \kappa_{enter}\right)^2 \quad \text{when } \left|\kappa_{enter} - \kappa\right| \le \kappa_{limit} \tag{5.36}$$

$$F_n = M_{limit}\left|\kappa_{enter} - \kappa\right| \quad \text{when } \left|\kappa_{enter} - \kappa\right| > \kappa_{limit} \tag{5.37}$$

$$F_{unr} = 0 \quad \text{when } \left|\kappa_{enter} - \kappa\right| \le \kappa_{limit} \tag{5.38}$$

$$F_{unr} = M_{limit}\kappa_{exit} \quad \text{when } |\kappa_{enter} - \kappa| > \kappa_{limit} \tag{5.39}$$

$$\kappa_{exit} = \kappa_{enter} \quad \text{when } |\kappa_{enter} - \kappa| \leq \kappa_{limit} \tag{5.40}$$

$$\kappa_{exit} = \kappa - \left(\frac{M\kappa_{onset}}{M_{onset}} \right) \quad \text{when } \kappa > \kappa_{limit} \tag{5.41}$$

Note that equations (5.35) thru (5.41) could be used for the first segment as well by simply setting κ_{enter} to zero and F_{unr} to zero. Also note that because the springback occurs depending on the previous state of the beam, the curvature of the tunnel segments must also have associated with them a direction. For the 2D case, simply a positive or negative curvature is needed. From this data, the springback moment and curvature can be calculated properly for each segment.

The next three figures re-plot the predicted force of insertion from the perfectly elastic model (Section 5.3.1) and the forces of insertion for the rigid plastic and elastic-plastic models for the same three examples described in Figure 47. The rigid plastic model is shown specifically to illustrate the difference between it and the elastic plastic model which recovers some work from the elastic springback.

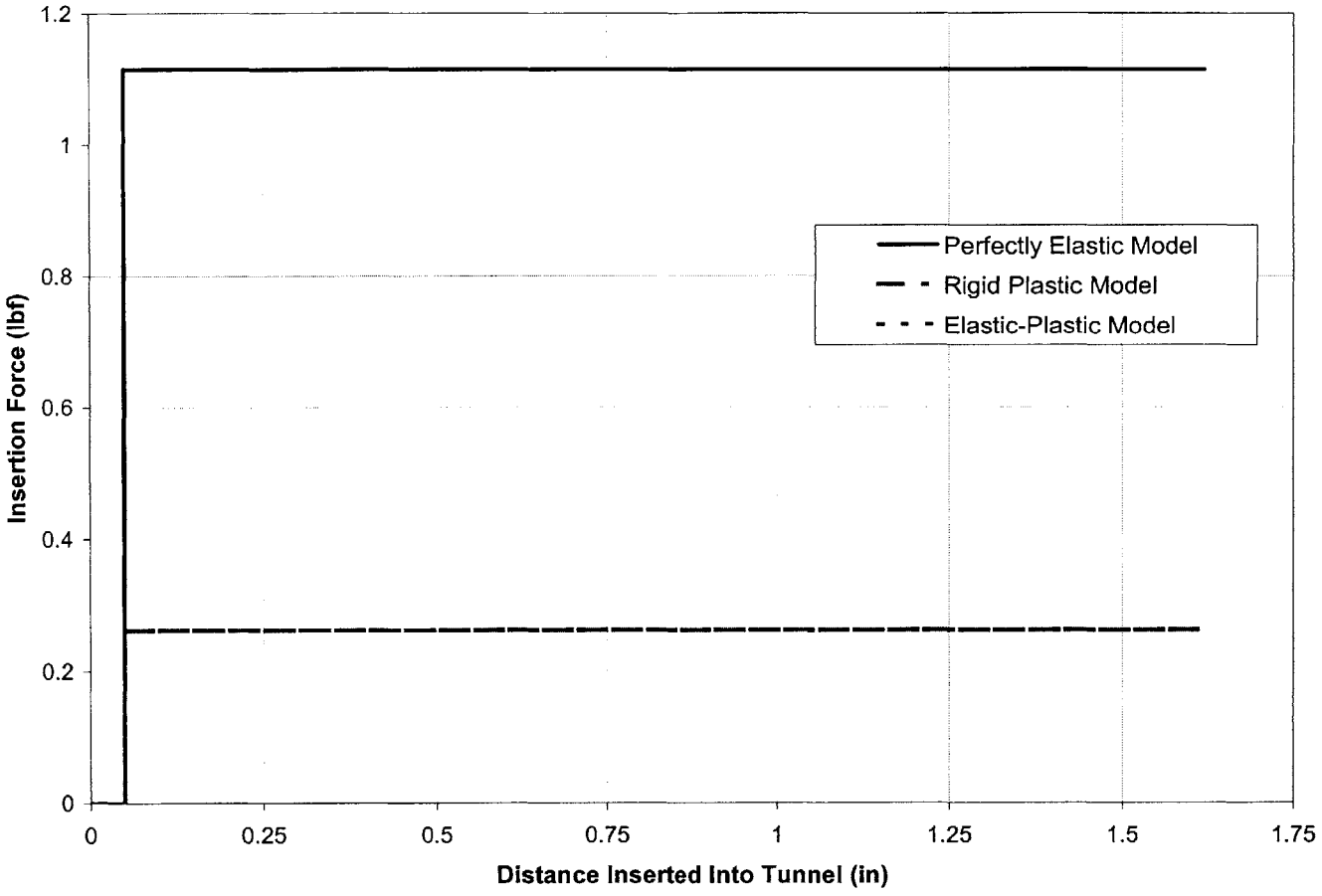

Figure 60 - First example (2 segment path) showing the elastic only force and the dramatic reduction on insertion force when the plastic limit is taken into account.
Note that the rigid plastic and elastic plastic models predict the exact same force profile since there is only one bending operation and the curvature in that segment is greater than the limit curvature.

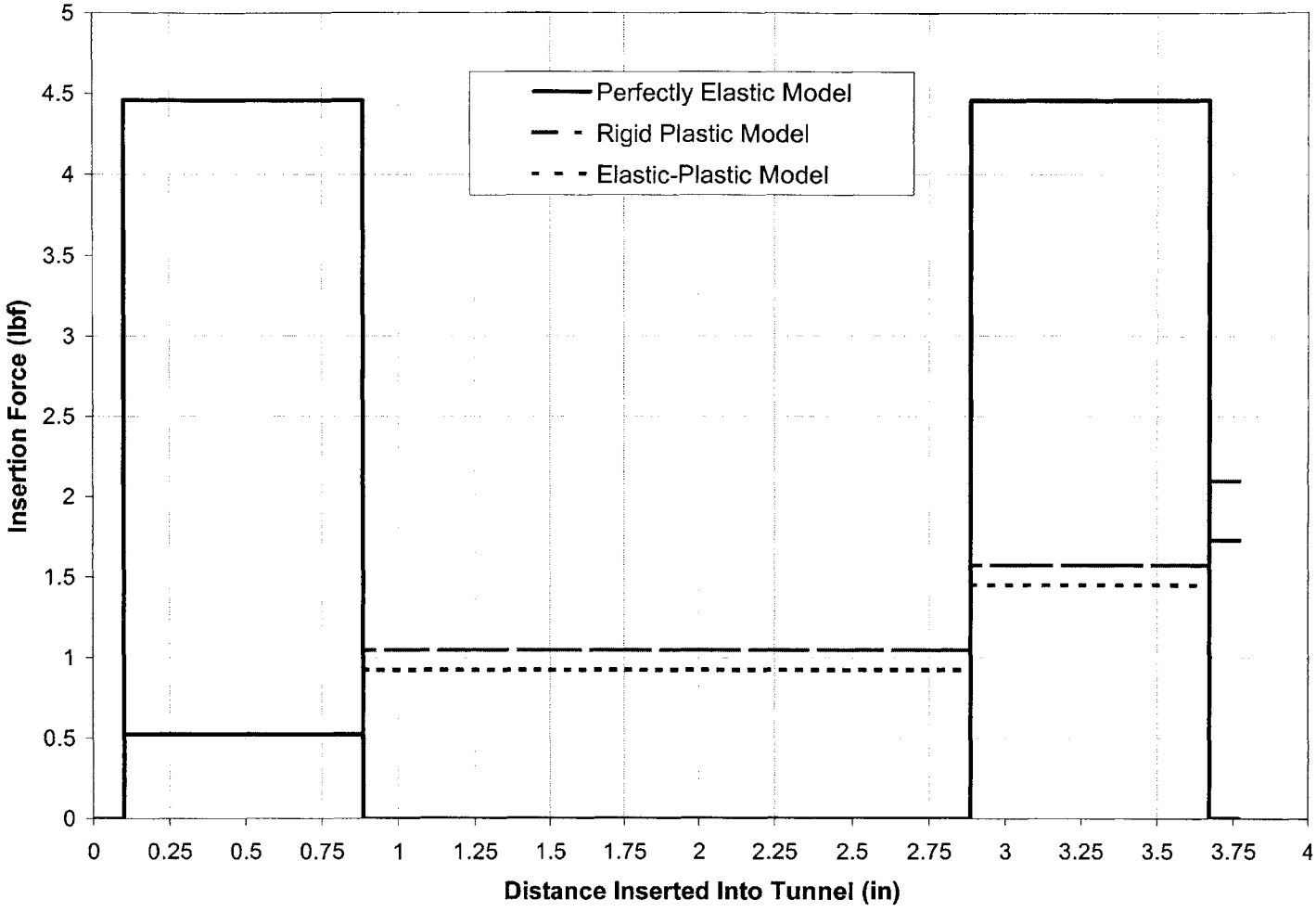

Figure 61 - Example 2 (5 segment path) with three different models of insertion force. Note the difference between the rigid plastic model and the elastic plastic model increases with each segment. This is due to the energy recovered by the beam due to elastic springback after the beam has been plastically loaded.

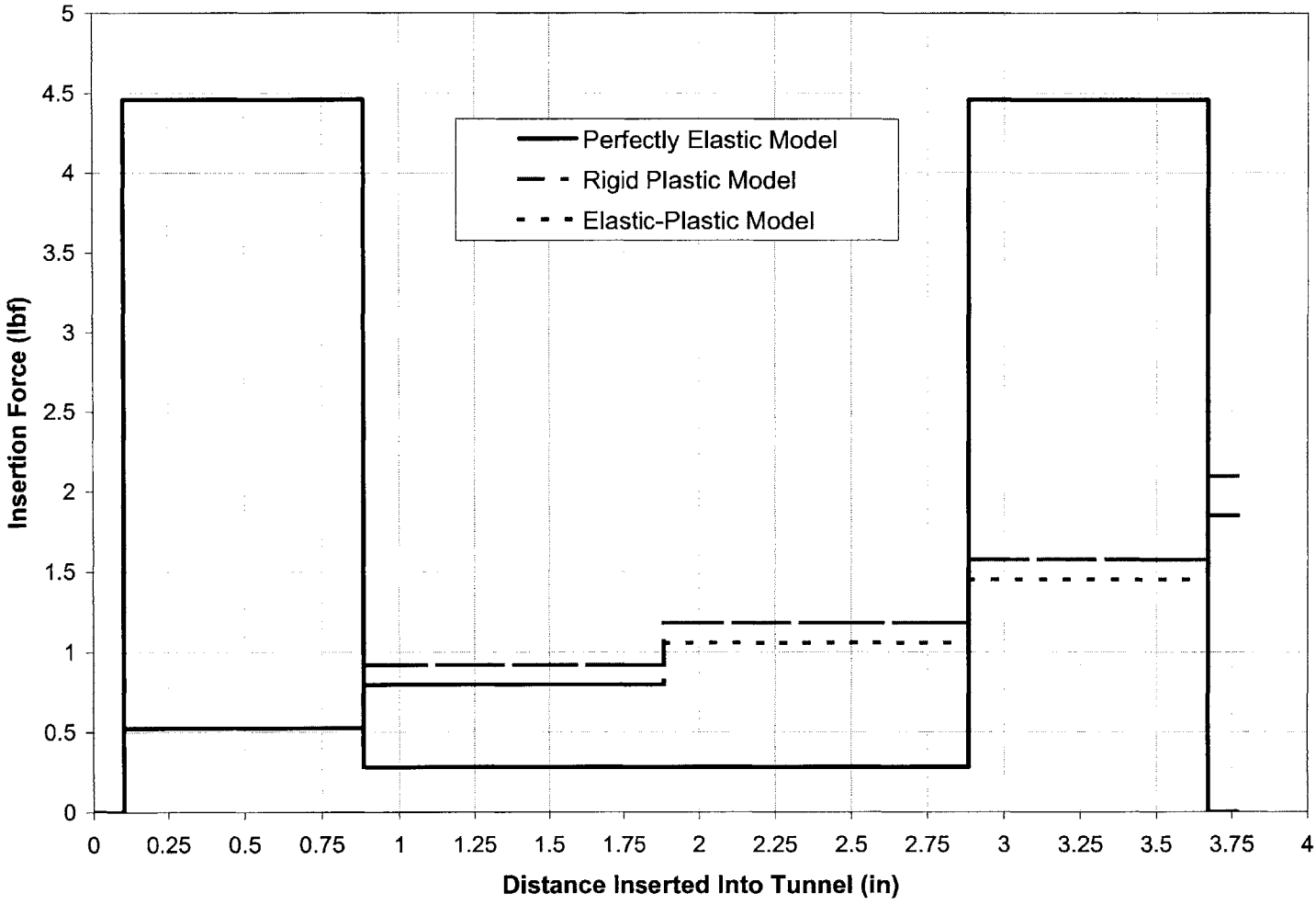

Figure 62 - Example 3 (6 segment path) illustrating the decrease in insertion forces due to elastic springback.
Note that in this model (and the previous one) it is essential that the direction of curvature (positive or negative) must be considered to get the proper results.

5.3.3. The third model – Elastic-Plastic and Friction

In the third model the following assumptions are made:

1. All paths are made up of segments of constant curvature.
2. Each segment has tangent continuity to adjacent segments.
3. Only paths in a single plane are allowed (2D only).
4. The beam and tunnel are both of circular cross-section.
5. The beam is of constant modulus throughout and the modulus under tension is the same as the modulus under compression.
6. There is no gap between the tunnel diameter and the beam diameter.
7. All surfaces are smooth.
8. Friction occurs between the walls of the tunnel and the beam. The friction force is independent of area and velocity. The dynamic friction coefficient was determined experimentally with a simple pull test.
9. All forces on the beam are due to elastic and plastic bending (pure bending) only. Compression and shear forces are ignored. No strain hardening (or softening) occurs. The material is elastic-perfect plastic.
10. No buckling or other catastrophic failures occur when inserting the beam.
11. Beam starts with zero curvature and no residual stresses.
12. The tunnel walls are perfectly rigid.

The inputs required to solve this model are:

1. A n-segment path with known curvatures for each segment

2. The beam stiffness = EI

3. The yield stress of the beam = σ_y

4. The beam diameter = d_{beam}

5. The dynamic friction coefficient = μ

When the beam is inserted into the first segment in the first example, the equations developed to this point predict that no insertion force is required. Because there is only incidental contact to the walls of the tunnel, nearly no normal forces are exerted on the walls and thus the friction in this segment is predicted to be zero.

However, as the beam enters a curve, forces develop at the tip of the beam due to the moment that must be applied to bend the beam. As the beam starts to enter the tunnel, the beam makes three points of contact, one at the tip of the beam, one at the start of the segment and one midway between the two.

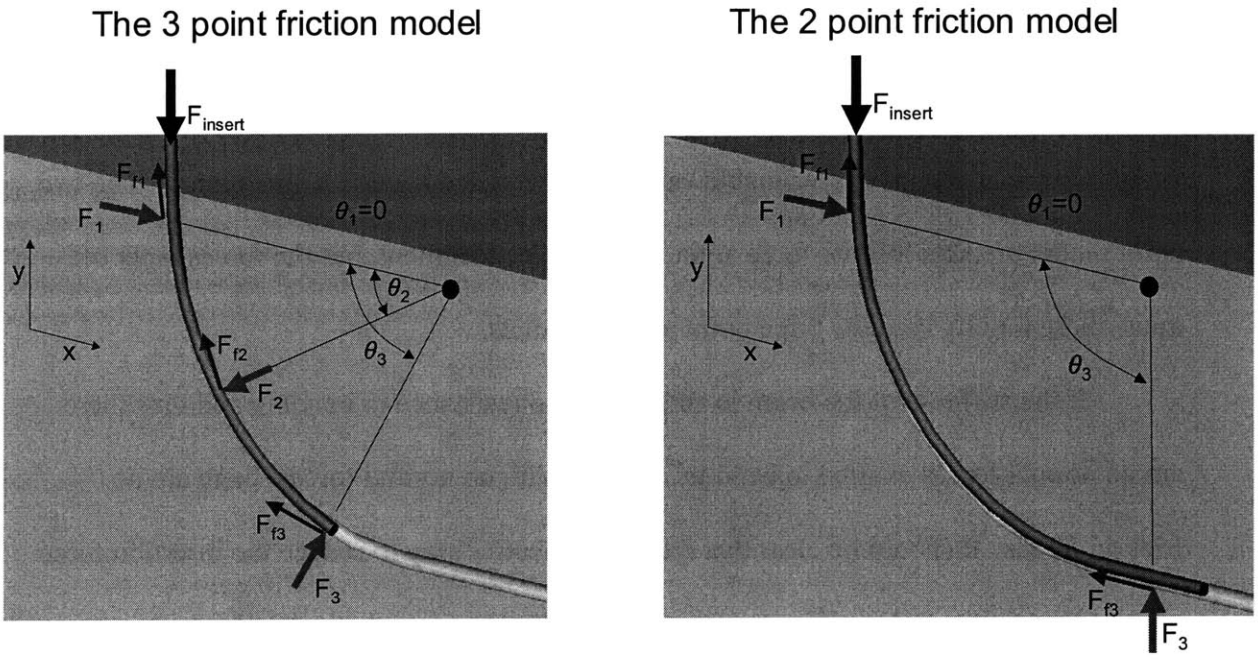

Figure 63 - 3 point and 2 point friction models

As the beam continues to move along the curved segment, the insertion force and the friction force at F_3 tends to push the beam off of the inside wall and thus only 2 points of contact exist. The two point model also describes the behavior of initially curved segments entering straight segments as shown below.

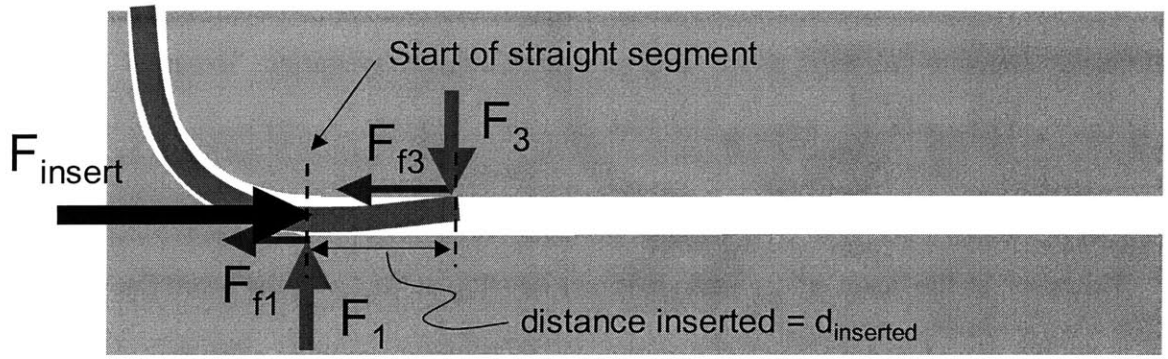

Figure 64 - The two point model for a curved beam entering a straight segment

The 3 point model was solved (see Appendix) but predicts exceedingly high insertion forces. Instead, a two point bending model was developed in which, the force F_3 is determined by the internal moment of the beam. The two point model is much simpler to solve and gives reasonable values for the added friction of the tunnel. The two point model predicts infinite force at the start of every segment, but the forces taper off much more rapidly than the three point model predicts.

If the stiffness of the beam is zero, it has no resistance to bending and thus there are no normal forces exerted to bend the beam. With no normal forces, there are no friction forces. It should be clear that the most effective way to reduce the insertion force of a cable is to lower the stiffness. The stiffness directly impacts the bend energy required and the friction forces developed.

In a straight segment F_3 and F_1 are equal and described by:

$$F_1 = F_3 = M/d_{inserted} \tag{5.42}$$

In a curved segment F_3 is (using Castigliano's method) [65]:

$$F_3 = \frac{M\kappa_{beam}}{\sin(\theta_3)} \tag{5.43}$$

And F_1 (from balancing of the forces in the x-direction) for a curved segment is:

$$F_1 = F_3(\mu \sin\theta_3 - \cos\theta_3) \tag{5.44}$$

To finish the third model, the equations from Section 5.3.1 must be modified to include friction. The friction force "felt" at the end of a segment adds to the unrecoverable force for all subsequent segments.

$$F_{unr} = F_{unr\ (from\ plastic\ deformation\ )} + F_{friction} \tag{5.45}$$

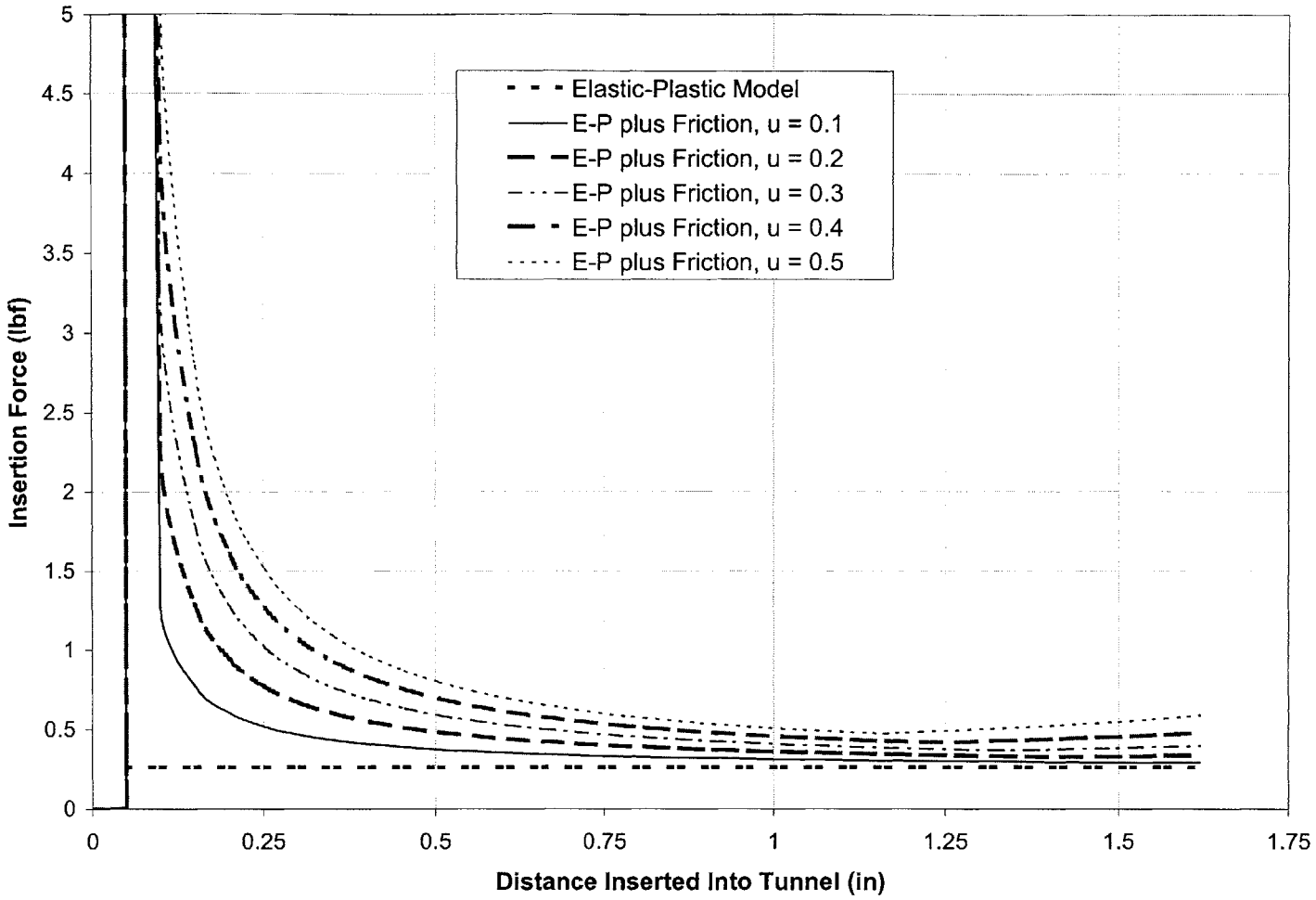

Figure 65 - First example showing the forces of insertion for multiple friction coefficients. Note that because there is no gap between the tunnel diameter and the path diameter, at the start of the radiused section, the beam must be immediately bent to a radius of one inch over an infinitely tiny segment. So, although the moment is finite, the moment arm is infinitely small and thus the normal forces are infinite and thus the friction force becomes infinite.

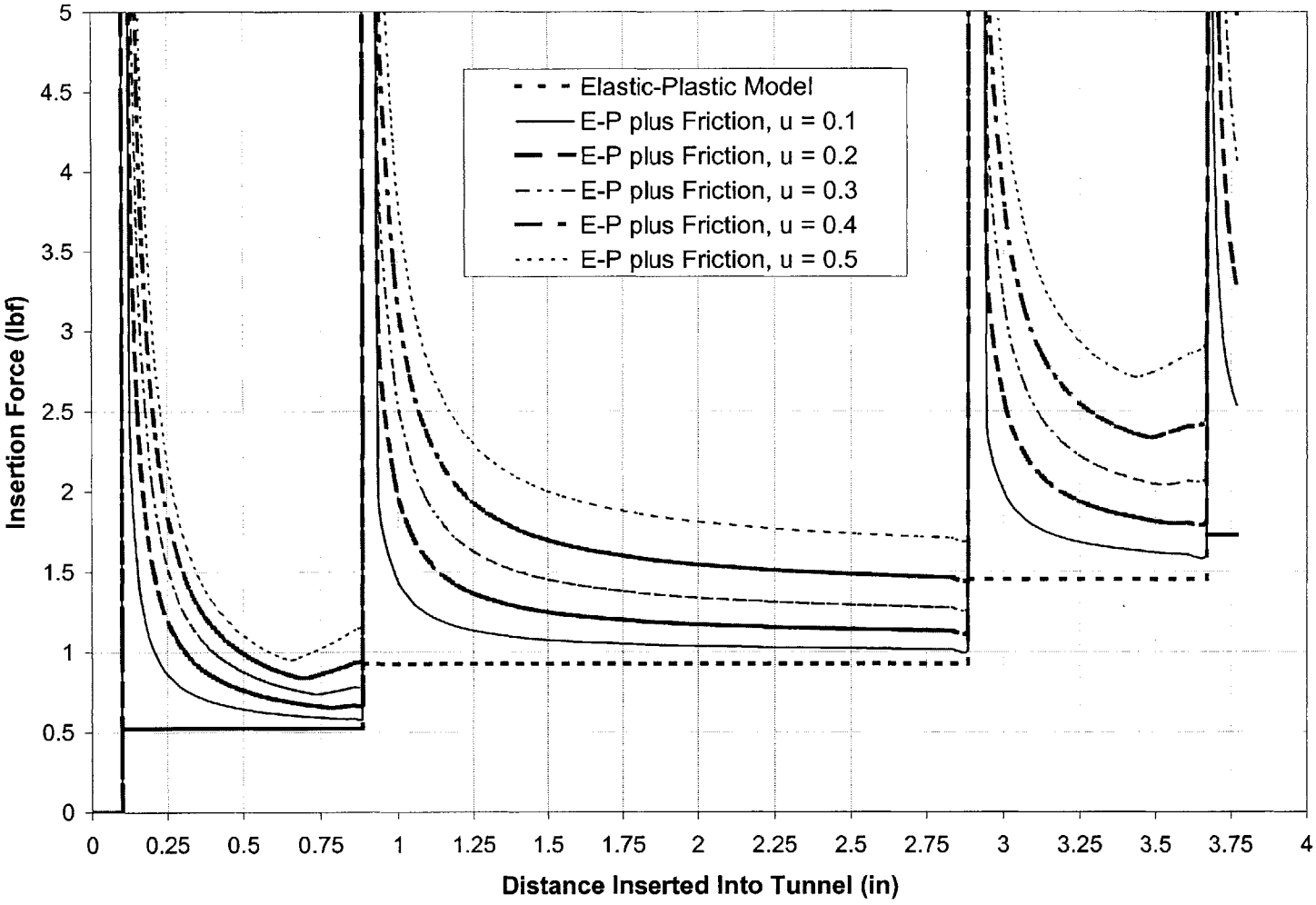

Figure 66 - 2nd example (5 segments) showing the effects of friction on the model.
Note at that every transition between segments, the predicted insertion force goes to infinity.

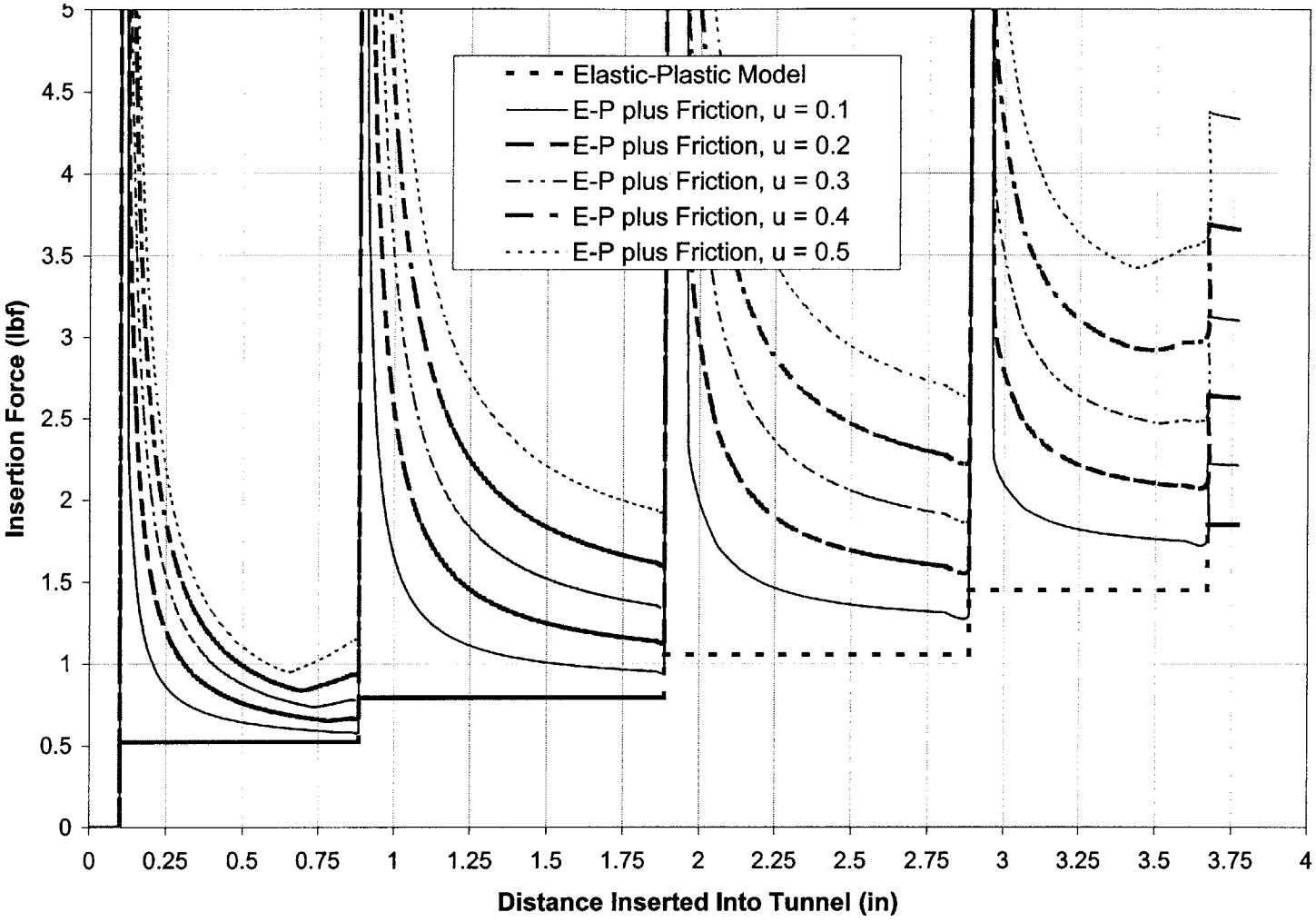

Figure 67 - 3rd example (6 segments) illustrating the effects of various friction coefficients.

5.3.4. The fourth model – Elastic-Plastic Friction and Clearance

In the fourth model the following assumptions are made:

1. All paths are made up of segments of constant curvature.
2. Each segment has tangent continuity to adjacent segments.
3. Only paths in a single plane are allowed (2D only).
4. The beam and tunnel are both of circular cross-section.
5. The beam is of constant modulus throughout and the modulus under tension is the same as the modulus under compression.
6. There is a small gap between the tunnel diameter and the beam diameter.
7. All surfaces are smooth.
8. Friction occurs between the walls of the tunnel and the beam. The friction force is independent of area and velocity. The dynamic friction coefficient is determined experimentally with a simple pull test.
9. All forces on the beam are due to elastic and plastic bending (pure bending) only. Compression and shear forces are ignored. No strain hardening (or softening) occurs. The material is elastic-perfect plastic.
10. No buckling or other catastrophic failures occur when inserting the beam.
11. Beam starts with zero curvature and no residual stresses.
12. The tunnel walls are perfectly rigid.

The inputs required to solve this model are:

1. A n-segment path with known curvatures and tunnel diameters for each segment
2. The beam stiffness = EI
3. The yield stress of the beam = σ_y
4. The beam diameter = d_{beam}
5. The dynamic friction coefficient = μ
6. The tunnel diameter = d_{tunnel}

An exact description of the curvature of the beam along its length is required for an accurate description of the insertion force. In previous models, the curvature at each point was described by the tunnel path curvature. Now the curvature is determined by the boundary conditions of the tunnel, the forces on the beam (insertion force, normal force and friction forces, the stiffness of the beam, the geometry of the tunnel, and the distance inserted into the tunnel. The exact curvature of the beam is therefore difficult to determine exactly. When the beam to tunnel clearance is zero or nearly zero, a beam of constant curvature almost exactly approximates the beam in any given segment. When the clearance between tunnel and beam grows larger, the beam shape can be described by a cubic polynomial. For the tunnels and beams considered, the gap is relatively small (typically less than 25% greater) and thus the assumption will be made that the beam has a constant curvature in any given segment. The beam can be bent to multiple different curvatures along its length, but in any given segment, the curvature will be assumed to be constant. Since the curvature will be used to calculate the strain energy and thus the insertion force, the curvature can also be thought of as the curvature that determines the average strain energy in the beam.

The tunnel diameter is sized so there is always a running clearance between the beam and the tunnel and so only incidental contact occurs in the first straight segment. The contact normal force is very small and thus no bending occurs. The beam enters the first curved section, but it does not immediately start to bend. Due to the clearance between the tunnel diameter and the beam diameter, the beam can enter into the curve a distance d_c before it hits the wall of the tunnel. This distance can be calculated using simple geometry as shown in Equation (5.46). R is the centerline radius of the curve, d_{tunnel} is the tunnel diameter and d_{beam} is the beam diameter

$$d_c = \left(2Rd_{tunnel} - 2Rd_{beam} + d_{tunnel}d_{beam} - d_{beam}^2\right)^{1/2} \tag{5.46}$$

Once the beam has been inserted up to distance d_c, the beam contacts the wall and starts to bend. The derivation of this equation can be found in the Appendix.

As the beam enters a curve with some clearance, it slowly increases its curvature from zero to slightly bent. The beam is elastic and thus will take the least energy configuration possible (i.e. –the greatest bend radius that can be accommodated by the radius of the tunnel and the clearances that exist between beam and tunnel). R_o is the outer radius of the tunnel (=R+½*d_t), R_i is the inner radius of the tunnel (=R–½*d_t).

$$r_o = \frac{R_o^2 + d_{beam}^2 + 2d_{beam}R_i + R_i^2 - 2R_o\left(d_{beam} + R_i\right)\cos\left(\theta_3/2\right)}{2\left(d_{beam} + R_i - R_o\cos\left(\theta_3/2\right)\right)} \tag{5.47}$$

where r_o is the outside radius of the beam (not one-half it's section diameter). Thus, as the beam is inserted into a curved section of the tunnel, the forces for insertion quickly climb from zero just before d_c to a value that is close to the force required to bend the beam to the conform to the outer radius of the tunnel wall. How close the bend radius gets to

conforming depends on the angle of the bend. Examining the two examples shown below helps illustrate the effect tunnel diameter can have on the curvature of the beam.

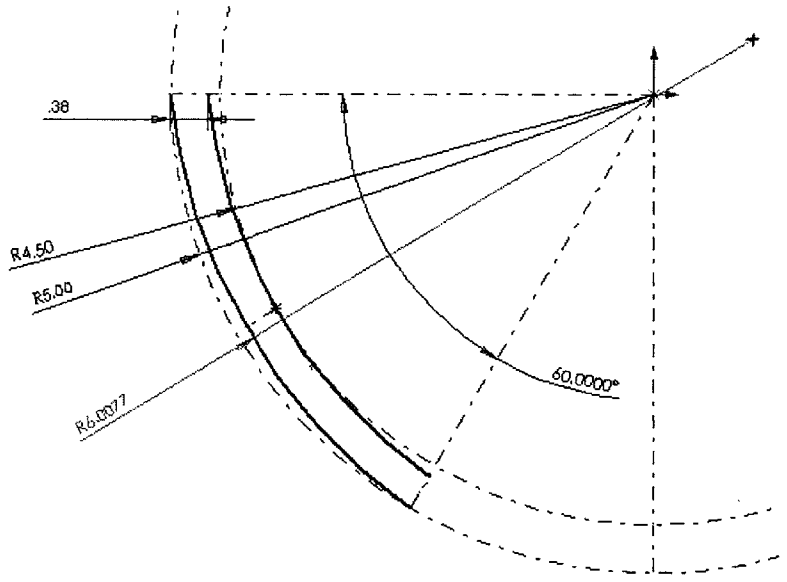

Figure 68 - An example of a beam taking the lowest energy path for a tunnel with Ro = 5" and a beam inserted into the curve 60 degrees

Figure 68 above shows a beam of diameter .38" in a tube with an outer radius equal to 5.00" and an inner radius equal to 4.50". Thus the tunnel diameter, d_t , would be 5.00 – 4.50 = .500". There is 0.12" of clearance between the tunnel diameter and the beam diameter. In the figure the beam has been inserted into the curve of the tunnel 60 degrees (this angle is referred to later as the insertion angle and θ_3) and the maximum outer radius (lowest energy) of the beam is 6.0077". If a beam was inserted into the same geometry tunnel but with a smaller beam diameter (.25" vs. .38"), the beam would be able to accommodate a greater radius as shown in the Figure 69 where for the same angle of

insertion, the maximum radius is 7.6527". This is similar to the path a race car driver might take around a curve for maximum speed.

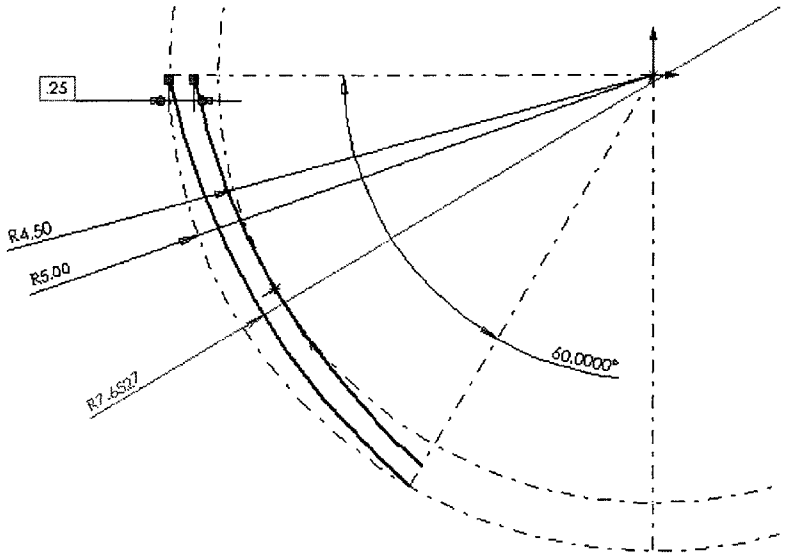

Figure 69 - Another example of a beam in a tunnel with clearance, with a smaller beam diameter than the previous figure.

Note that these equations and assumptions assume that the entire beam is bent to a constant radius and therefore, the beam is not tangent to the outer radius at the starting edge. Furthermore, the minimum curvature model assumes that each segment has just three distinct contact points: one at the start of the segment, one at the tip of the beam, and a third midway between the other two. The curvature taken by the beam is dependent only on the geometry of the segment it is currently in and the springback curvature (or entering curvature) from the previous segment.

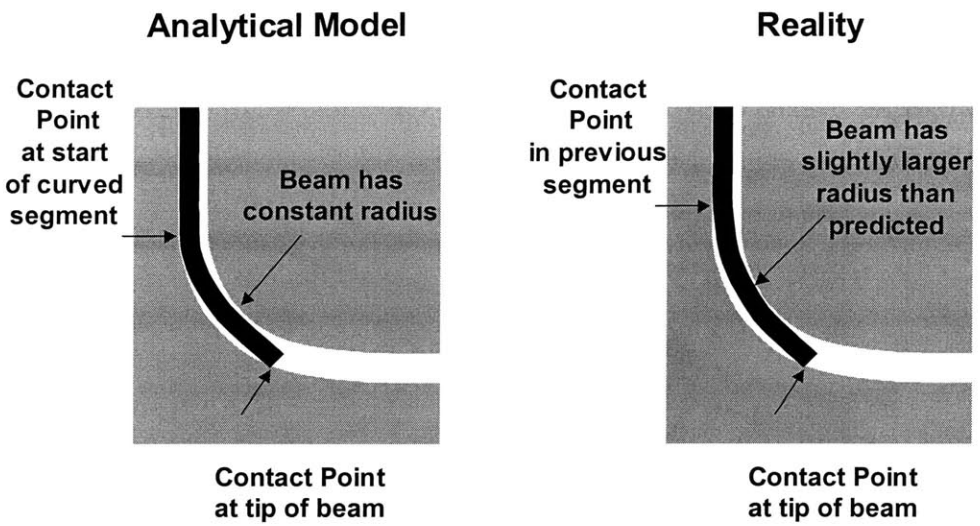

Figure 70 - The differences between the analytical model and reality for predicting minimum curvature in a tunnel with clearance

As the figure above shows, the model predicts the beam will be bent to a slightly greater curvature than reality, which would lead to a slight over estimation of the required force. This magnitude of this effect depends on the size of the gap between the tunnel and the beam, the distance the beam is inserted into the tunnel and the curvature of the segments. As long as the diameter of the tunnel is relatively close to the diameter of the beam, this effect is relatively negligible, especially as the distance inserted into the segment grows. The segmentized equations will fail to predict a gradual relaxation of the insertion force as the beam exits a segment because the equations fix a contact point at the end (and start) of each segment. Therefore, although the equations predict a sharp drop in the insertion force at the end of most segments, it is understood that, in fact, there will be a gradual decline of the insertion force.

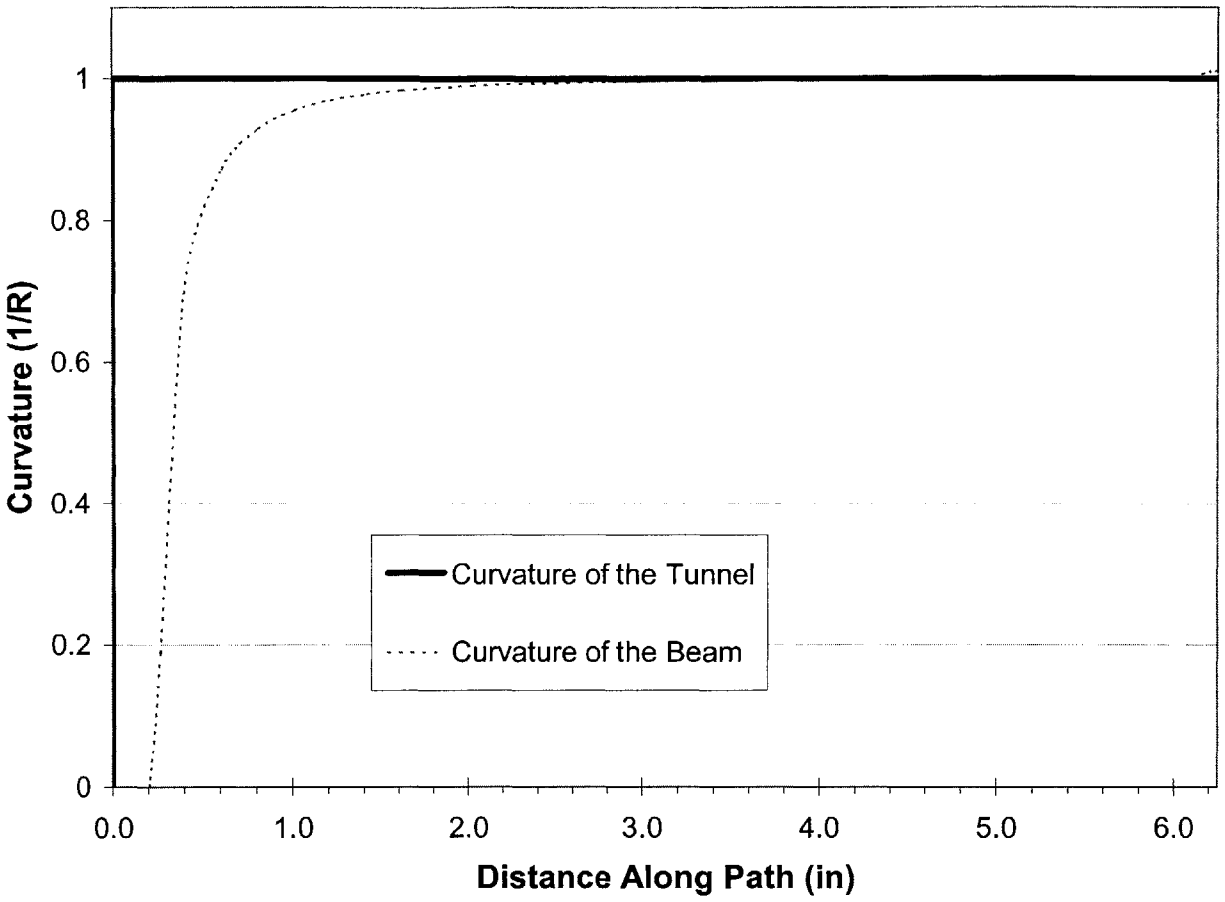

Figure 71 - A beam inserted into a 360 degree loop illustrating the effect of taking the path of least resistance

The figure above shows the effect of inserting an initially straight beam 0.034" in diameter into a tunnel with 0.006" of diametrical clearance (tunnel diameter is 0.040"). The position of the tip of the beam is tracked through a full 360 degree loop with a curvature of 1. As can be seen, the beam does not start to bend until it has been inserted to almost 0.2 inches (corresponding to roughly 11 degrees). At this point, the beam contacts the outer edge of the wall and is forced to start bending. The curvature the beam

takes quickly ramps up to nearly that of the curvature of the tunnel. The addition of clearance into the model prevents the infinite friction force problem that was encountered in section 5.3.3. At 90 degrees the beam radius is typically within 95% of the radius of the tunnel, but this depends on the clearance between the beam and tunnel (with a large enough clearance, a beam can be inserted unbent into a 90 degree curve.)

The first example is now illustrated below using multiple different tunnel diameters.

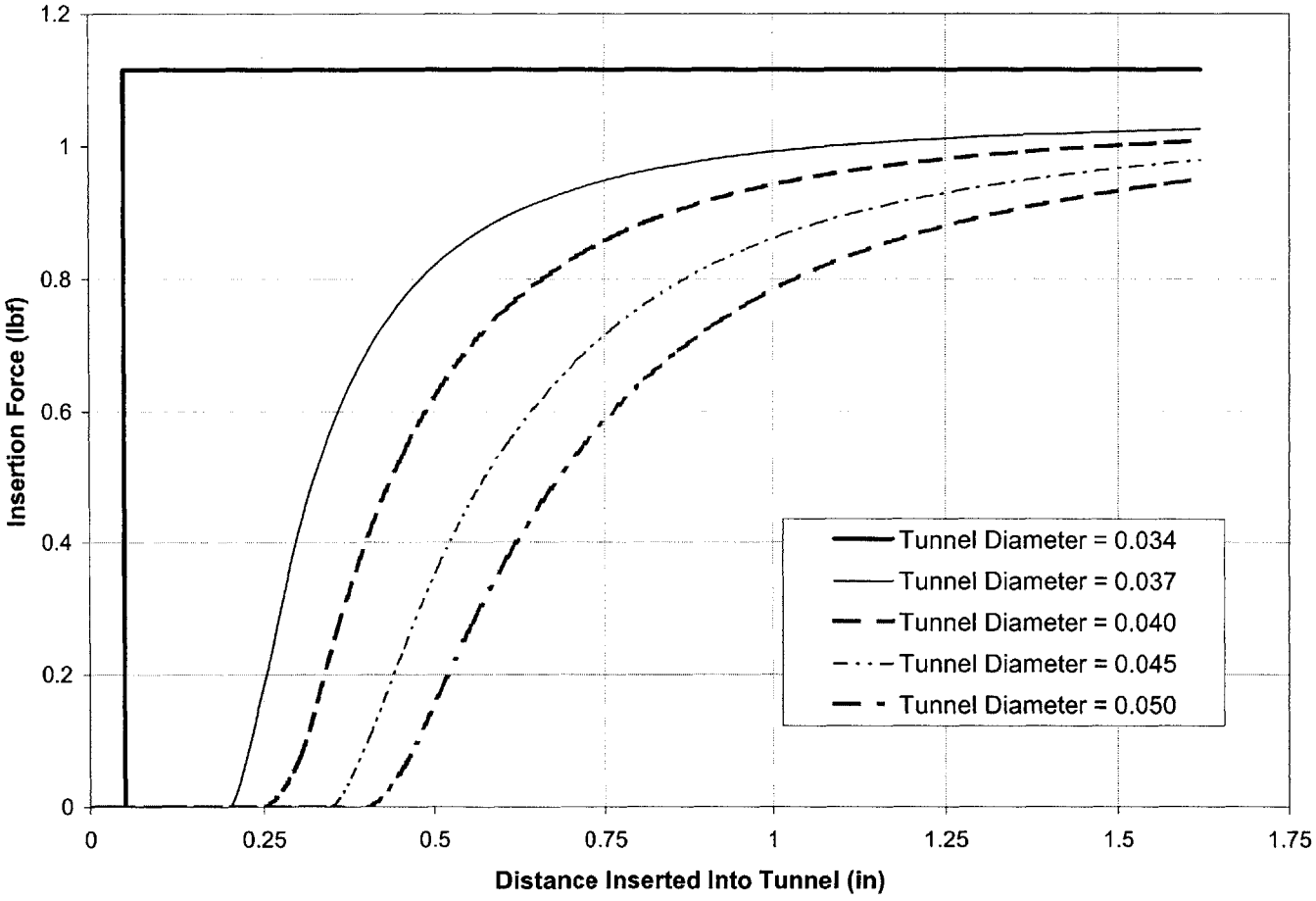

Figure 72 - Example 1 illustrating the effects of tunnel diameter on the perfectly elastic insertion force prediction.

Before the clearance model (which calculates the curvature of the beam) is applied to the elastic plastic and friction model, it is instructive to back all the way up to the elastic only model and work back to the elastic-plastic friction model. It is relatively straight forward to use the minimum curvature equations for the all elastic model, because the all elastic model always "wants" to take the path of least resistance and it always "wants" to have a curvature of zero. The three simplest cases for segment transitions are shown below.

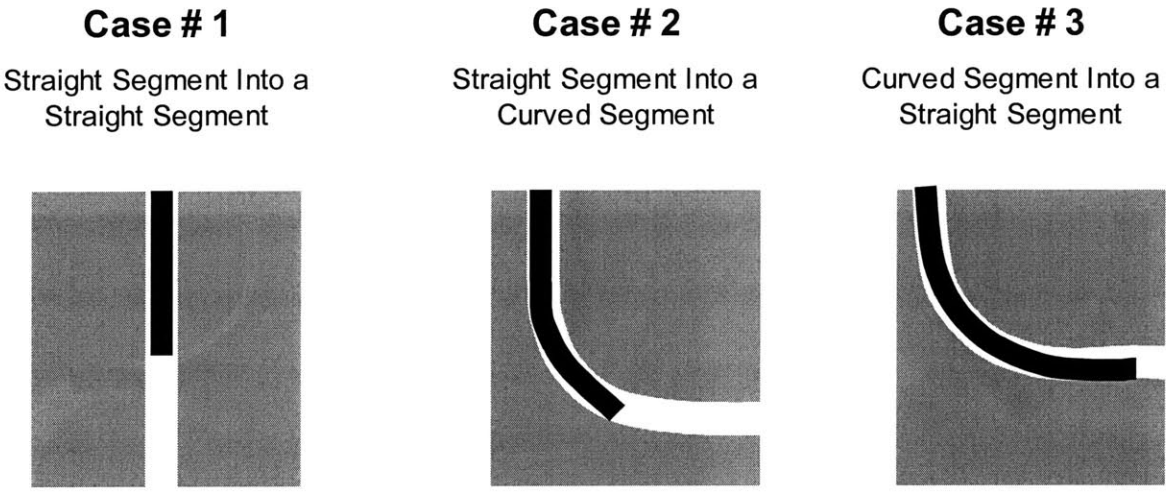

Figure 73 - The first three cases for segment transitions

Case #1 is the trivial case of inserting a beam from a straight segment into another straight segment. This is what the first segment typically "sees" as the insertion machine pushes the cable from a straight position into a straight segment and is used only for the first segment. The curvature of the beam for this case is zero and thus the forces are always zero. The second case is described by Equation (5.47). When the calculated value of r_o is less than zero, the beam has yet to hit the wall and thus Equation (5.46) does

not even need to be used if a check on the value of r_o is performed. To get the curvature of the beam (at the centroid of the beam), the equation (5.48) is used.

$$\kappa_{beam} = \frac{1}{r_o - d_{beam}/2} \tag{5.48}$$

For case #3 and the perfectly elastic model, the beam simply returns to zero curvature. Note that in these models, it is assumed the beam's curvature is zero to start. Other cases arise that exist in example #3. These cases are:

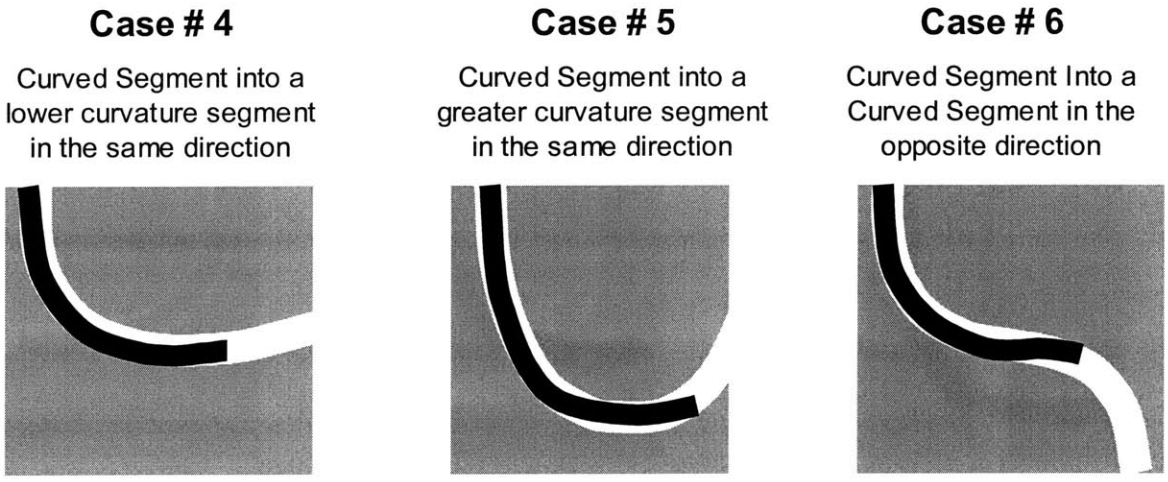

Figure 74 - The other 3 cases for segment transitions

Case #4 is a superset of case #3. Case #4 accounts for any path transition from a large curvature to a smaller one in the same direction. This would include a path with a curvature of zero and hence case #3 is a subset of case #4. The behavior for a perfectly elastic beam is the same, the beam rides on the outside wall of the curve and thus the curvature of the beam is given by:

$$\kappa_{beam} = \frac{1}{\left(R_o - d_{beam}/2\right)} \tag{5.49}$$

Case #5 is a superset of case #2, where a beam is inserted from a low curvature into a high curvature segment in the same direction. In this case, Equation (5.47) can still be used, but when it evaluates to less than zero, the beam has not yet hit the greater curvature limit and thus the curvature is the entering curvature of the beam (defined by the previous lesser curvature segment).

Finally, case #6, for the perfectly elastic beam, is described by the same equation that describes inserting a beam from a straight section to a curved section. As soon as the perfectly elastic beam exits one curvature, it is free to springback to zero curvature.

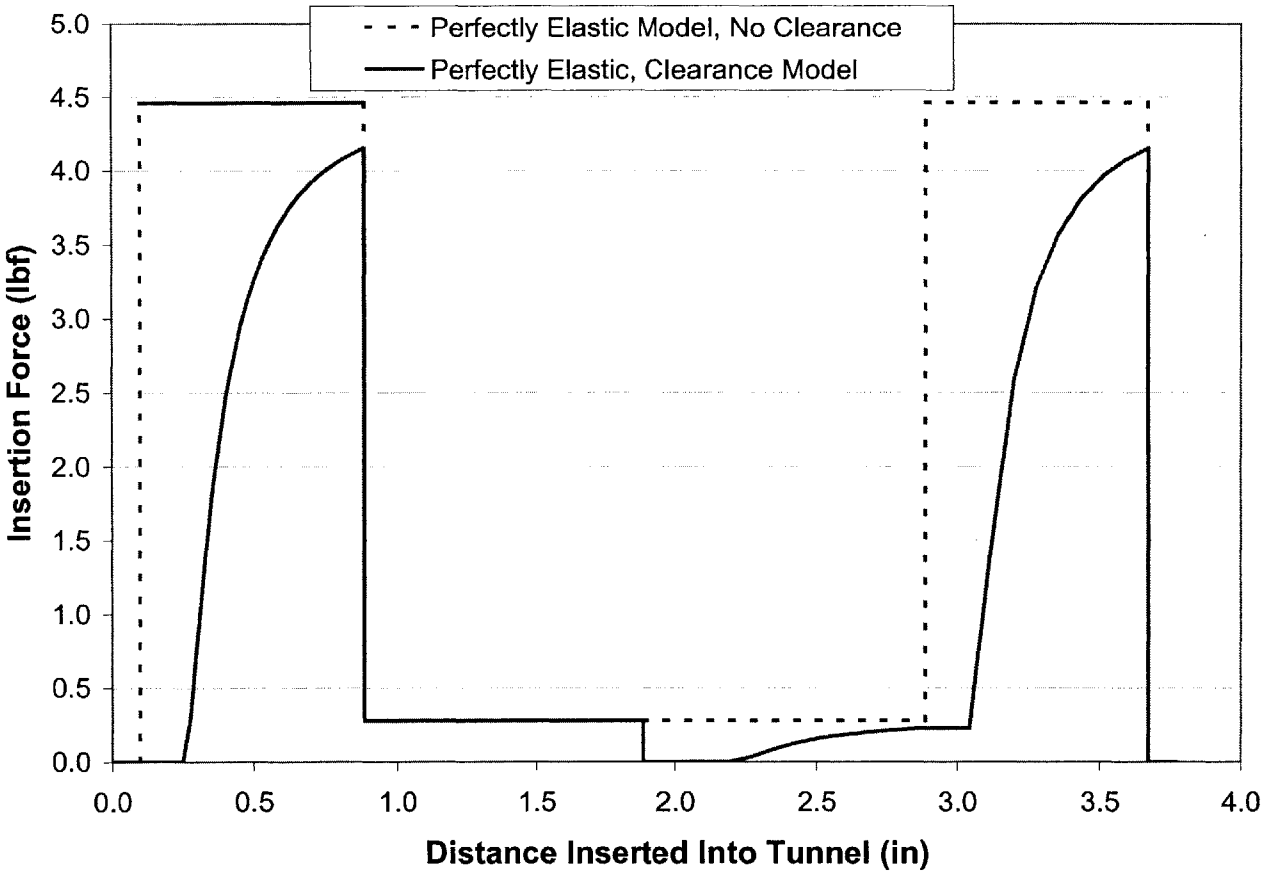

Figure 75 - Example #3 comparing the Perfectly-Elastic Model #1 with and without clearance. (Clearance is 0.006" on a 0.034" diameter beam)

As Figure 75 shows, the beam quickly approaches the curvature of the tunnel and hence the insertion force in the second segment (the first curve) also quickly ramps to the

insertion force predicted for a zero clearance tunnel. In the third segment, the insertion force drops to that predicted by the zero clearance model. Because the beam springs back to a curvature in the same direction, it instantly follows the curvature of the path (as opposed to ramping up to the curvature). It instantly follows this curve because it is coming from a segment with higher curvature in the same direction. As soon as the beam leaves this lower curvature segment, the beam is free to spring back to zero curvature and thus the force drops to zero. It proceeds for a short distance (until roughly 2.1" on the graph) and then it is forced to slowly increase its curvature. As it enters the fifth high curvature segment, it does not immediately conform to the greater curvature, but continues to take the path of least resistance. This behavior is analogous to that predicted by equation (5.46) except in this case the beam is initially curved. A short distance into the higher curvature segment the beam remains at the lower curvature until it is forced to quickly increase its curvature (around 3.05" on the graph).

Having tackled the perfectly elastic model with clearance, the effect of clearance must now be accounted for in the elastic plastic models. This becomes more difficult than the perfectly elastic model because now the beam does not always reset to zero curvature. Furthermore, accounting for springback in the direction of the last curve must be considered.

Reexamining the six cases in the elastic plastic regime adds some nasty complications. Case #1 is still the trivial case used to start the first straight segment. Case #2 still uses Equation (5.47), but when it evaluates to less than the springback curvature from the previous segment or the entering curvature, the value that must be used is the entering curvature.

Case #3 adds a new wrinkle as the entering curvature is not straight. The curvature of the beam is defined by the springback curvature. It will proceed some distance before contacting the wall after which the beam will slowly and forcibly be unbent.

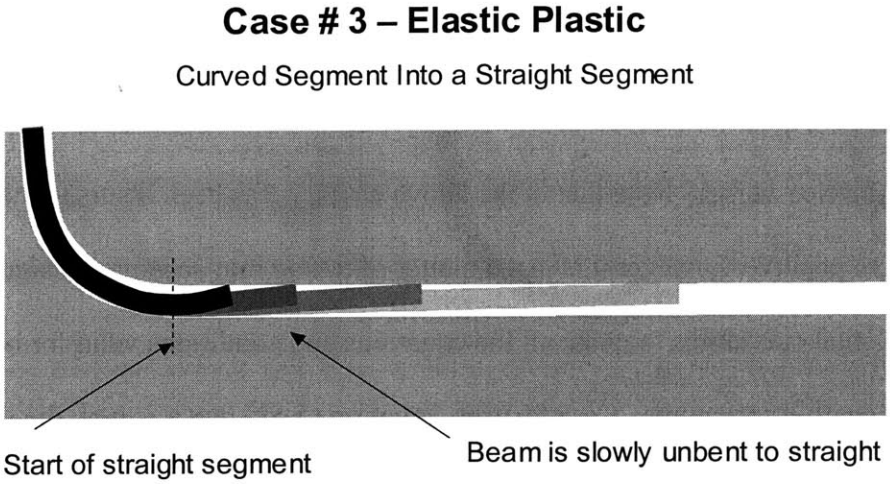

Figure 76 - Case #3 for an Elastic Plastic Beam

For case #3 a new equation must be used. It is derived in the Appendix and given below:

$$r_o = \frac{d_{beam}^2 - d_{tunnel}^2 - d_{inserted}^2}{2\left(d_{beam} - d_{tunnel}\right)} \tag{5.50}$$

Once Equation (5.50) is evaluated, and the curvature determined, if the value is greater than the entering curvature, the entering curvature is used.

Case #4 is the more general case, and a slightly more complicated equation must be used: (derived in the Appendix)

$$r_o = \frac{d_{beam}^2 - d_{tunnel}^2 - y^2 - 2yd_{tunnel}\sin\left(\theta_3/2\right)}{2\left(d_{beam} - d_{tunnel} - y\sin\left(\theta_3/2\right)\right)} \tag{5.51}$$

where y is the chord on the inner radius of the tunnel that runs from the start of the segment to the tip of the beam (where it contacts the inside wall of the tunnel.)

$$y = 2R_i \sin(\theta_3/2) \tag{5.52}$$

Case #5, does not need any new equations. Equation (5.47) is used and its result is compared with the entering curvature (from the springback of the previous segment) and the greater of the two curvatures is used.

Finally, Case #6 introduces the complication of a positive curvature into a negative one (or vice-versa). Note that in the above cases, it has been assumed that all curvatures were positive, however it is just a matter of taking into account the sign of the entering and actual curvatures to make all the equations and conditions valid for both positive and negative curvatures. Case #6 uses Equation (5.51), but y is now the outside chord:

$$y = 2R_o \sin(\theta_3/2) \tag{5.53}$$

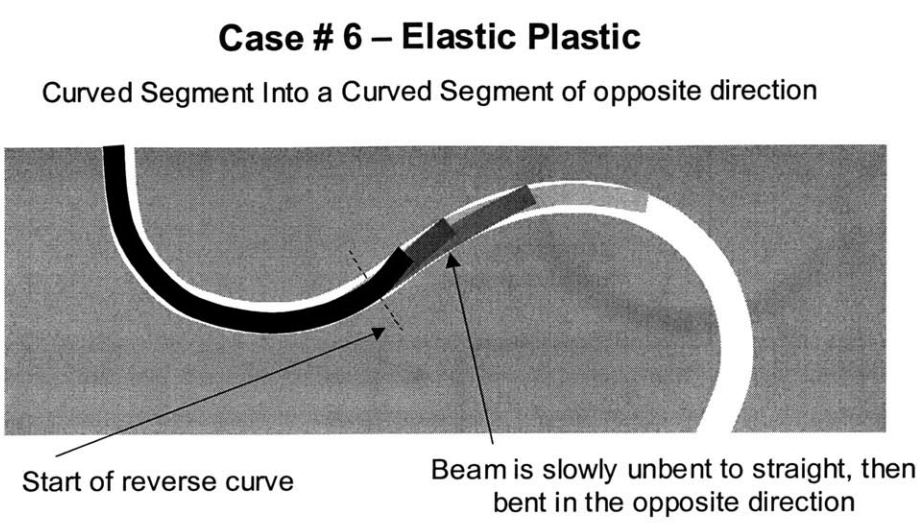

Figure 77 - Case #6 for an Elastic Plastic Beam

In this case, the beam makes three transitions. First, the curvature is determined by the entering curvature until Equation (5.51) and (5.53) determine the curvature is less than the entering curvature. The beam is slowly unbent until Equation (5.47) evaluates to a positive value. At this point the curvature may be negative but the absolute value of the curvature becomes positive. Now, the beam has transitioned to taking the curvature direction of the segment it is in and follows equation (5.47).

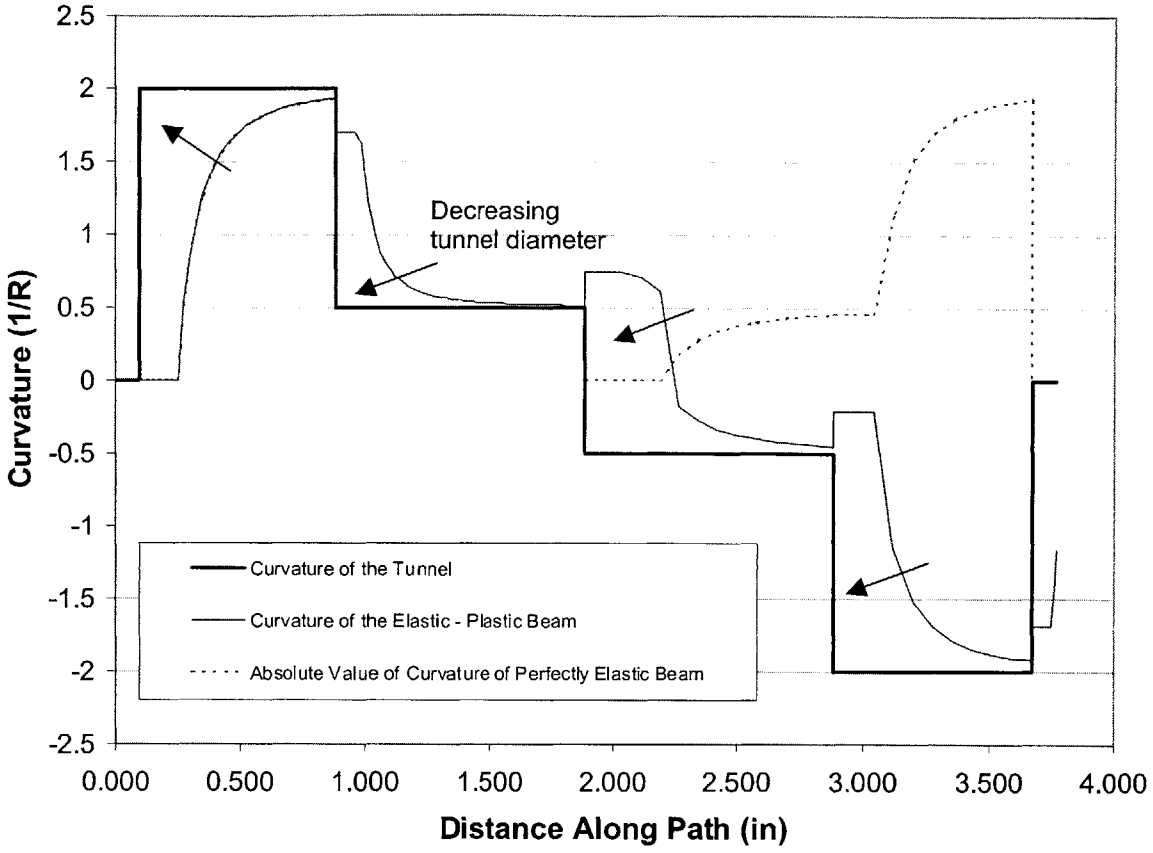

Figure 78 - The curvature predictions for Example 3 using a zero clearance model, a perfectly elastic model and an elastic plastic model with springback

Figure 78 represents the instantaneous curvature of the path in the current segment as it is pushed through example #3. The graph is the representation of the curvature of the beam for the segment which contains the tip of the beam. Therefore, the graph should be read as follows. The thin line traces the curvature of the beam and it can bee seen it does not instantly start to bend (the tunnel starts to curve after 0.10 inches yet the beam does not start to bend until nearly 0.30"). Once the beam hits the outer wall of the tunnel, it increases its curvature slowly as it proceeds along the curved segment. Once the beam exits the curved section, the beam is allowed to springback some amount,

which it does as indicated by the sharp transition between segments. Once in the straight segment, the beam is slowly unbent and slowly approaches a curvature of zero. Once the curvature of the beam has been calculated it is straightforward to reapply the simplified elastic plastic equations and the friction model.

The only difference that needs to be considered is that the previous equations assumed the beam was always bent to a given radius for a segment; the radius of curvature of the beam did not change as it was inserted. Now the curvature equations predict the curvature slowly increases (or decreases) as it is inserted along a segment. Therefore, the instant forces must be modified to include the added strain energy that must be applied to change the curvature from the previously calculated value to the current curvature. Thus, equations (5.29) (5.30) (5.36) and (5.37) must be modified with an additional term to account for the added strain energy stored in the beam.

$$F_{insert} = EI\kappa^2 + EI\left(\kappa - \kappa_{prev}\right)^2\left(\frac{dx}{d_{prev}}\right) \quad \text{when } \kappa \le \kappa_{limit} \tag{5.54}$$

$$F_{insert} = M_{limit}\kappa + M_{limit}\left(\kappa - \kappa_{prev}\right)\left(\frac{dx}{d_{prev}}\right) \quad \text{when } \kappa > \kappa_{limit} \tag{5.55}$$

$$F_n = EI\left(\kappa - \kappa_{enter}\right)^2 + EI\left(\kappa - \kappa_{prev}\right)^2\left(\frac{dx}{d_{prev}}\right) \quad \text{when } \kappa \le \kappa_{limit} \tag{5.56}$$

$$F_n = M_{limit}\left|\kappa - \kappa_{enter}\right| + M_{limit}\left|\kappa - \kappa_{prev}\right|\left(\frac{dx}{d_{prev}}\right) \quad \text{when } \kappa > \kappa_{limit} \tag{5.57}$$

Where d_{prev} is the distance of the beam in the current segment that was bent to the previously calculated value = κ_{prev}.

The insertion force with a friction coefficient of 0.1 is shown below for all 3 examples. Example #1 also shows friction coefficients of 0.2 thru 0.5.

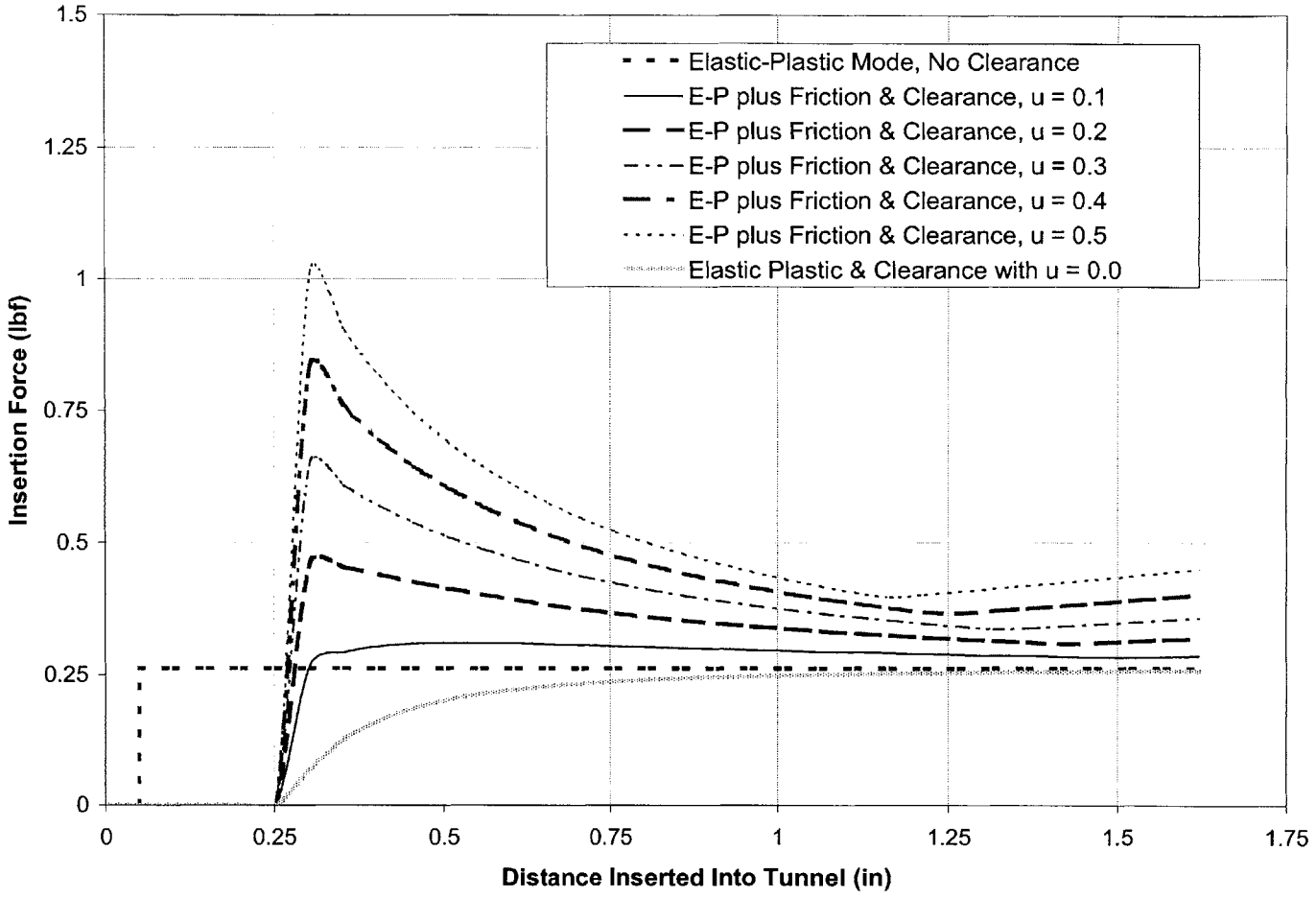

Figure 79 - The first example with the elastic-plastic equations, friction and clearance.

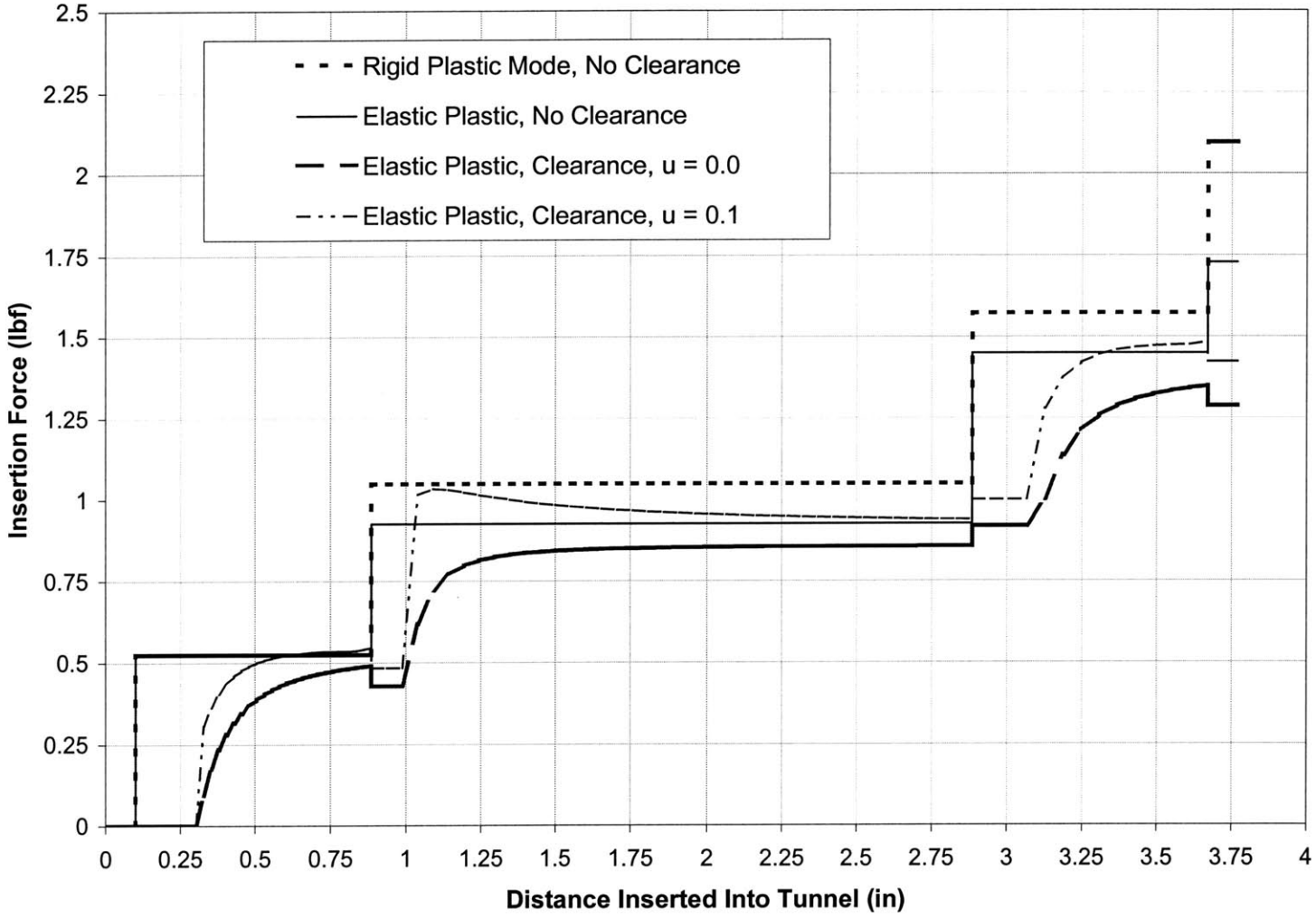

Figure 80 - Example #2 with the elastic-plastic equations, friction and clearance

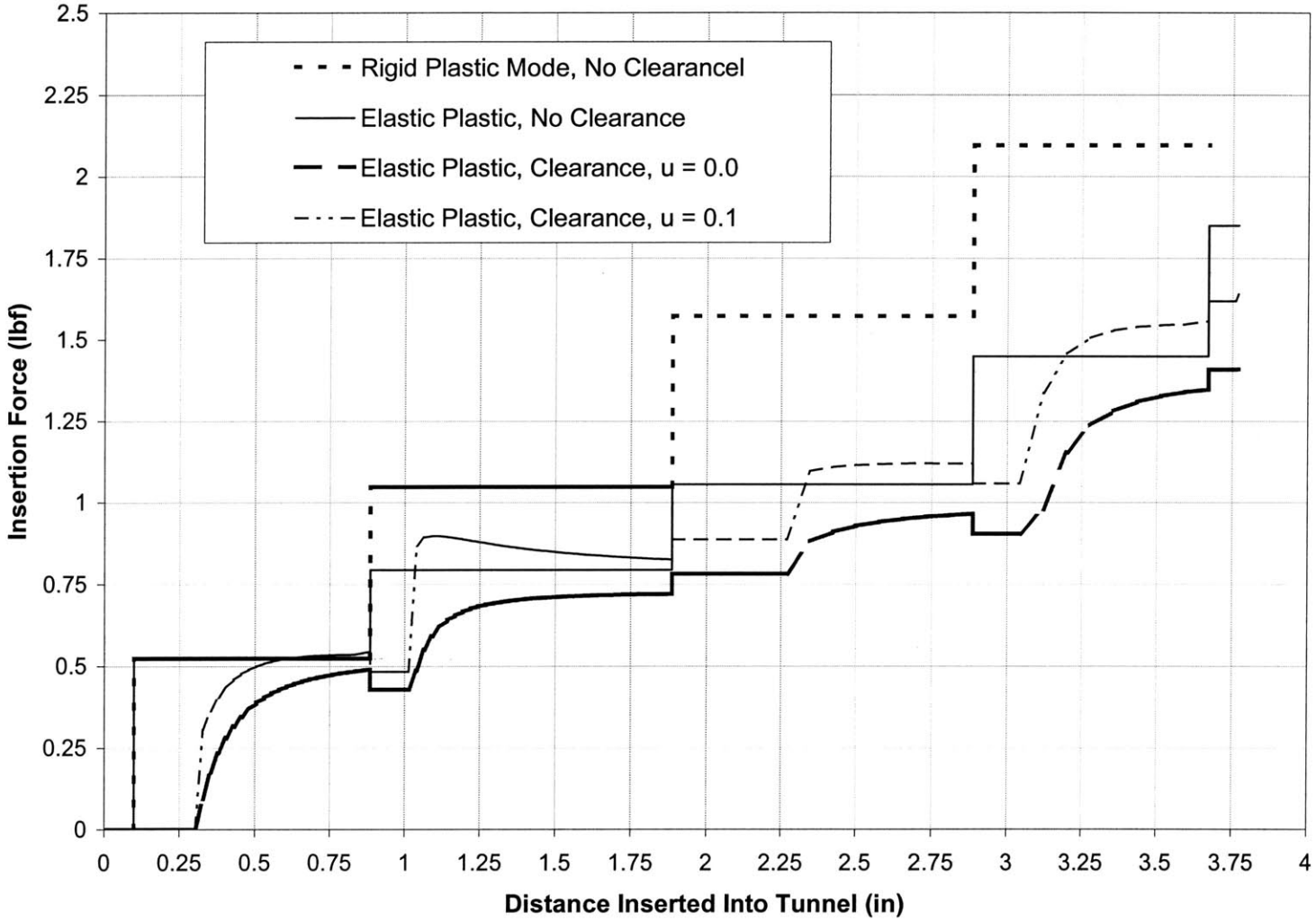

Figure 81 - Example #3 with the elastic-plastic equations, friction and clearance

5.3.5. The fifth model – Fourth model + Composite Beam

For the coaxial wire that is inserted there are three materials and the construction of the coaxial cable is shown below.

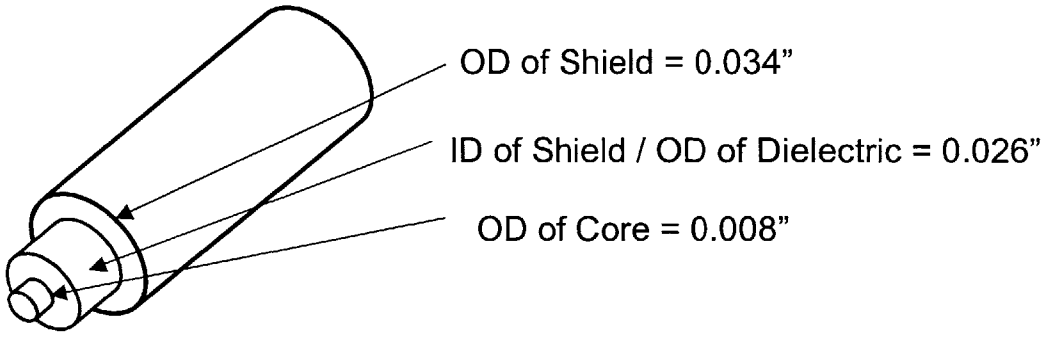

Figure 82 - Semi-rigid coaxial cable

Shield – Drawn Copper Tube		
Outer Diameter	0.034	inches
Inner Diameter	0.026	inches
Young's Modulus	17,000,000	psi
Yield Strength	40,000	psi
Dielectric – Teflon (PTFE)		
Outer Diameter	0.026	inches
Inner Diameter	0.008	inches
Young's Modulus	70,000	psi
Yield Strength	8,000	psi
Core – Steel with Silver Coating		
Outer Diameter	0.008	inches
Young's Modulus	30,000,000	psi
Yield Strength	60,000	psi

Table 10 - Properties of Microcoax UT-34 coaxial cable

The table shows the minimum radius each component of the composite coaxial beam can be bent to before some plastic yielding occurs:

	Outer diameter	E (ksi)	σ_{yield} (psi)	R_{onset} (inches)
Shield	0.034	17,000	40000	7.2
Dielectric	0.026	70	8000	0.11
Core	0.008	30,000	60000	2.0

Table 11 - The plastic onset radius of curvature for each component of the coaxial cable

For the application being developed, the bend radius of the tunnel is typically in the range of 0.25" to 1.25", and plastic yielding effects are significant. Only the Teflon dielectric never yields, while the core and shield are typically very near full plastic yield. Comparing the moment exerted by each component in the coaxial cable shown in Figure 83, it is apparent that the shield is the major contributor to the forces required to insert the cable.

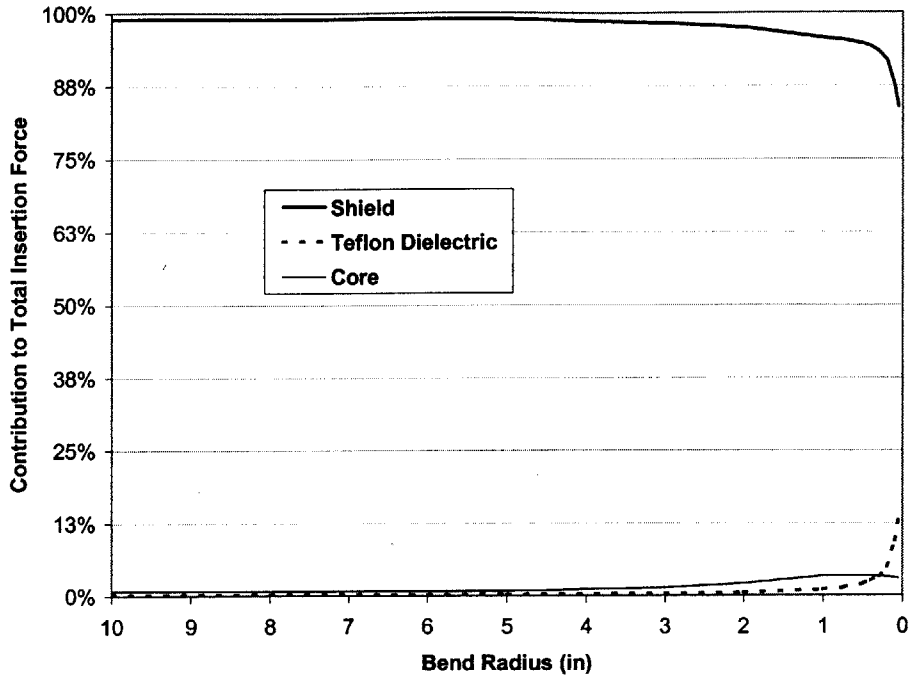

Figure 83 - Graph of the contribution of each component to the insertion forces

It is a very simple exercise to apply the composite beam to the models thus developed. Since each component of the beam has the same neutral axis, each of the three beams are analyzed and summed together to find the force at any given point. When calculating the curvature of the inner components (the core and the dielectric), the outside diameter of the shield is used to calculate the tunnel to beam gap for the minimum curvature equations. As Figure 83 shows, only at very tight bend radii does the moment of the dielectric and the core matter for the calculation of the forces. At very small radii, the elastic forces of the Teflon dielectric begins to become significant, but the shield is still the overwhelming driving force. At the smallest radius allowed by the auto-router, the shield still contributes 93% of the total force of insertion.

As a side note, if a geometry is used that is not a circular beam, the ratio K can be used to simplify many of the equations used in the elastic-plastic model. K is defined as the fully plastic moment divided by fully elastic moment just before yield occurs.

$$K = \frac{\text{Fully plastic moment}}{\text{Fully elastic bending moment}} = \frac{\sigma_{yield}\int_A ydA}{E\kappa\int_A y^2 dA} = \frac{M_{limit}}{M_{onset}} \tag{5.58}$$

The following chart gives some typical cross-sections and the associated K values. K is illustrated to show the differences between circular sections, hollow section and square beams. Most of the equations developed can be applied to non-circular cross sections so long as care is taken to use the proper terms for each specific geometry.

Cross Section	K
Rectangle	1.5
Solid Circle	1.7
Typical thin walled hollow cylinder	~1.3
Typical I beam	~1.2

Table 12 - K values for various beam cross sectional geometries

5.3.6. The sixth model – Applicability of models to 3D paths

The models developed up to this point are used in a 3D context, but each path is limited to a single plane (different paths can be on different planes). To address a truly 3D freeform path with deviation from the plane (torsion), only some minor modifications need to be made to the equations for the simpler models. The sixth "model" describes how to upgrade each of the earlier models to a truly 3D path.

For the all elastic model with no clearance, no corrections are needed. The curvature of the path completely determines the insertion force, regardless of whether or not the beam is restricted to a plane.

For the rigid plastic model with no clearance, no corrections are needed. Again, the curvature of the path completely determines the insertion force.

For the elastic – plastic model with springback, things get a little complicated. Now rather than tracking whether the springback is positive or negative and what the curvature of the path is, the polar orientation of the curve must be known. The simplest way to modify the equations developed thus far would be to calculate the curvatures in XY plane and the YZ plane. Then, the forces could be calculated again and care would need to be taken to ensure that the sum of the moments do not exceed the limiting moment defined by the fully yielded plastic condition. This would cause some error in calculations as two different contact points at the tip of the beam would result.

A more elegant and more correct method that would take the polarity into account transforms the coordinates in the previous segment to the next segment. Consequently, the springback curvature from the previous segment would be transformed into the rotated coordinates of the following segment and would be defined as the entering curvature.

The friction model as defined would need no changes as long as the rotation model is used. Using the two plane method would typically result in multiple contact points that may not match reality. Furthermore, the normal forces would need to be vector summed to get the proper normal force. Generally speaking the rotation transformation method is preferred.

5.3.7. Neglected effects

One assumption that was made in the first model was that shear and compression effects were negligible. This is true for long slender beams and consequently the highest errors will occur when the beam is inserted only a small distance into a segment. Fortunately, this is also the period where the beam is usually not touching the walls or is defined by the springback of the previous segment. A more complete model would take these forces into account, but would lead to complicated differential equations as the stress state at each point on the beam depends not only on the beam curvature, but also on the insertion force applied, the normal forces and the friction coefficient.

Taking into account the shear and compression forces will also lead to a complex state of stress and thus the yield point would use the von Mises equivalent stress [19]:

$$\sigma_{von\ Mises} = \frac{1}{\sqrt{2}}\sqrt{(\sigma_1 - \sigma_2)^2 + (\sigma_2 - \sigma_3)^2 + (\sigma_3 - \sigma_1)^2} \tag{5.59}$$

where σ_1, σ_2, and σ_3 are the three principal stresses. In the models developed, only σ_1 was considered (σ_2 and σ_3 were assumed to be zero.) Note that using the von Mises criterion on a uniaxial stress state gives the stress state unaltered. That is when σ_2 and σ_3 are both equal to zero:

$$\sigma_{von\ Mises} = \sigma_1 \tag{5.60}$$

The effect of not considering the other two states of stress is that the onset of yield predicted in the models would typically be higher than the actual value, but this depends on the loading and curvature of the beam, and the onset of yield may be lower than the predicted value in some special cases.

Another complication that has been ignored up to this point is the contact angle at which the beam hits the wall. At extreme contact angles, which might occur if the tunnel diameter became very large compared to the beam, a wedging action can occur and the beam will stop its forward progress. The beam could also get caught up on a small ledge formed in the SLA process. The assumption of smooth walls has been made in all models, but the nature of the build process is such that tiny ledges occur regularly throughout the tunnel path. For those cases when the contact angle is greater than the friction angle (= tan μ) and the surface is relatively smooth, the beam starts to slide along the wall and slowly increases in curvature. This has been the assumption in all models.

However, if the contact angle is equal to or less than the friction angle or the beam catches on the ripple in the tunnel wall, locking can occur. In either case, there is only one solution to escape: buckling. The free-body-diagram of this situation is shown below. If the beam can be unlocked by buckling to the right, it is not a catastrophic buckling, as the walls of the tunnel limit the beams movement.

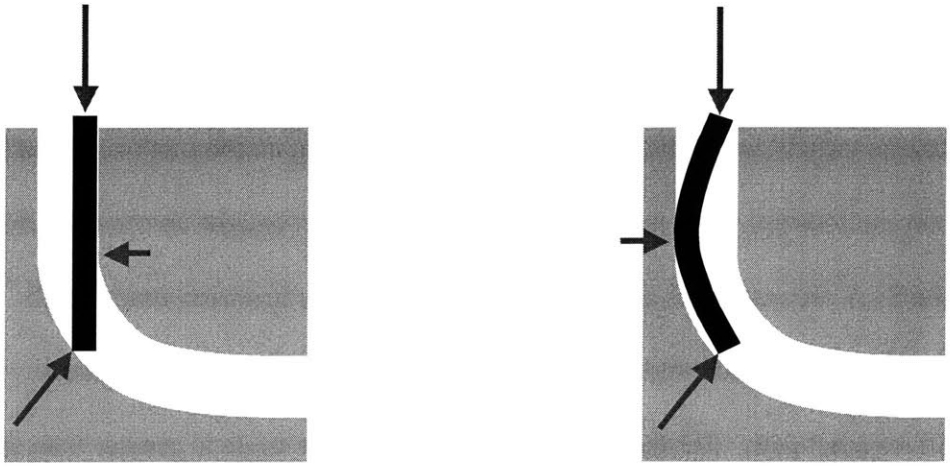

Figure 84 - Locked beam and unlocked after buckling

The sequence of events is therefore the following: The beam hits the edge of the wall and under some conditions it locks. Increasing the force at the insertion end also increases the normal force on the contact point and no slip occurs. This continues until the beam is loaded enough to buckle according to Equation (5.65). At this point, the beam contacts the opposite wall and the normal force at the contact point is reduced. The other possibility is that the beam buckles to the near wall (due to eccentricities or other factors) and the beam is completely locked. The eccentric loading of the beam and the non-straightness of the beam also affects the buckling load.

The simplified beam bending model that was used does not predict the forces well in a narrow region of beam curvatures near the transition from the all elastic regime to the all plastic regime. The calculation in this area can be done (as shown in Figure 59), but becomes complicated by the multiple cycles and the change of this calculation due to

residual stresses developed. To accurately model this a FEA solution is probably the most effective means.

Another neglected effect is that the curvature of the beam causes the neutral axis of the beam to shift slightly toward the center of curvature of the beam.

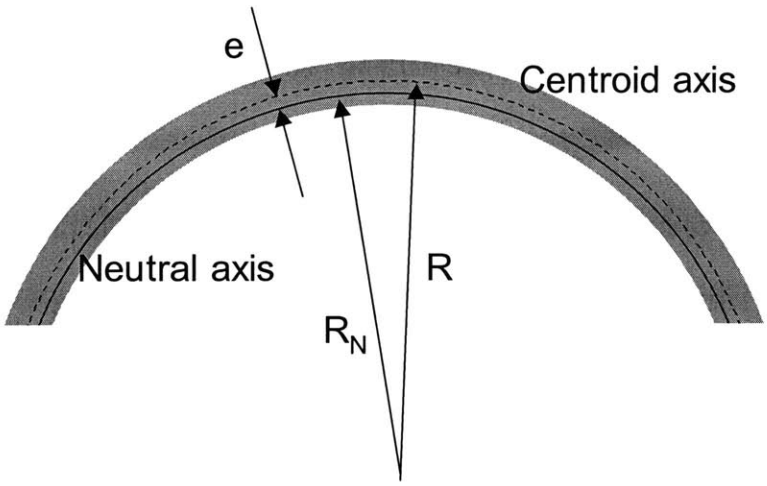

Figure 85 - A curved beam with a shift of the neutral axis

The radius of the neutral axis in a curved member is given by [65]:

$$R_N = \frac{A}{\int \frac{dA}{r}} \tag{5.61}$$

for a solid circular beam this integrates to:

$$R_N = \frac{d_{beam}^2}{4\left(2R - \sqrt{4R^2 - d_{beam}^2}\right)} \tag{5.62}$$

The magnitude of this shift is very small for all but the largest curvatures. With the minimum bend radius of 0.25" and a beam diameter of 0.034", this works out to a shift of the neutral axis, e, of 0.0003", and thus this effect can safely be ignored.

As the beam is bent back and forth through multiple curves, strain hardening or softening can occur (depending on the material and its heat treatment). The assumption has been that the material is elastic-perfect plastic, but most materials exhibit some strain hardening behavior. This effect was ignored for the application however the effect in annealed copper is quite strong and would tend to make the models under-predict the forces as the beam progressed through higher strains. The basic formula is [36]:

$$\sigma_{true} = K\varepsilon_{true}^{n} \tag{5.63}$$

where K is the strength coefficient (not the K from before which was the ratio of the elastic limit to the plastic limit) and for annealed copper is roughly 45,000 psi (315 Mpa) and n, the strain-hardening exponent, is 0.54. This effect would be easy to account for with a single bend from a straight condition, however, taking this effect into account over multiple bend cycles becomes relatively troublesome and was not considered in the model. Note that the copper shield which is the primary driver of the stiffness of the beam has already undergone relatively significant strain hardening when it is compressed over the dielectric in the manufacturing process. The effects of strain hardening were not discernable in the tests performed.

As a beam is inserted into a curved path, it starts out with 3 points of contact and transitions to two points as the friction at F_3 increases and the deflection of the beam goes up. The transition from a 3 point bending model to a two point bending model has been disregarded. Since the two point bending is easier to calculate and appears to be more valid for larger values of insertion angle,θ_3, the two point model is simply used throughout the entire range. Furthermore, the two point model is valid for all low curvature segments preceded by a higher curvature one. To use both models, the

transition point between three and two would need to be determined for each curve. This transition depends on a number of factors including friction, the curvature of the tunnel, the insertion force and the stiffness of the beam. Once the clearance of the tunnel is considered, the range in which the 3 point model could be effectively used is rather limited. Despite this, further work on the 3 point model in the first curved segment may lead to more accurate predictions of insertion force.

Another effect that has been simplified is the curvature calculations. Because a robust and universal method for calculation was desired, the simplification that the beam always has a point of contact at the start of a segment was made. In fact, as illustrated in Figure 70, the curvature the beam takes is a more complicated function involving the curvatures of the current segment and the previous segment. In the case of reversing bends, another case arises whereby the beam, which was in a minimum bend mode, transitions to a S-bend as illustrated below for a straight segment.

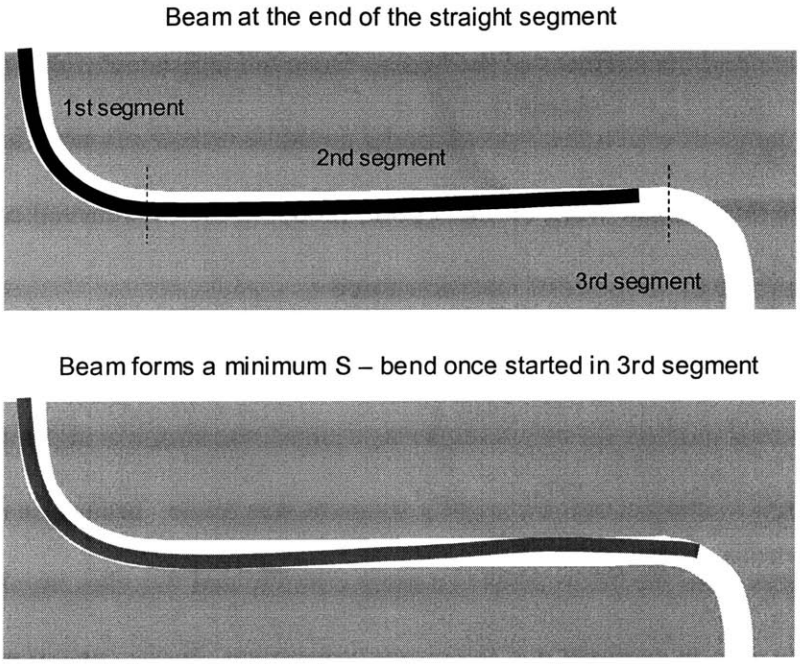

Figure 86 - The S - bend formed after entering a reverse bend

This effect influences the curvature of the beam on previous segments and adds a further complication to the calculations. The simplification of using the unrecoverable force does not take this into account. In this case, after each incremental step along the path, the entire beam and the curvature at each point would need to be re-evaluated. The radius of curvature of this S-shape has been derived in the case of a straight section separated by two curves of opposite direction (as shown in the figure above):

$$R = \frac{\ell^2_{\,straight\ segment}}{4\left(d_{tunnel} - d_{beam}\right)} + \frac{d_{tunnel} - d_{beam}}{4} \tag{5.64}$$

Thus, for the case above, the force required to move the bend to this position , for this component of the beam, would be calculated from the radius described by (5.64) and the moment required to move the beam from the single curve to the S-shaped profile. To be

complete, the case of two opposite curves with no straight segment would also need to be considered.

The insertion forces in the beam can cause local deformations of the beam which are not considered. This local deformation occurs when the 2 point model (shown below) has a span that causes the beam to bend so much that it touches the opposite wall (it no longer follows the minimum bend radius of an elastic beam). Note that the occurrence of this effect (the beam pulls away from the minimum bend radius) is the reason the two point friction model is valid. Under dynamic loading of the beam, the insertion force drives the beam off of the inside wall. At some point however, if the forces become high enough the beam will make contact with the outside wall and an additional contact point will occur. Note that the difficulty in dealing with scenarios such as this, is that the forces that make this case occur depend on the insertion force and the insertion force depends on the model. Thus, the case in which the beam will reside cannot be known *a priori*, and thus the way to solve this type of problem is to make a guess at the case, then follow through with all the equations for that case, and then check to see if the initial guess was correct.

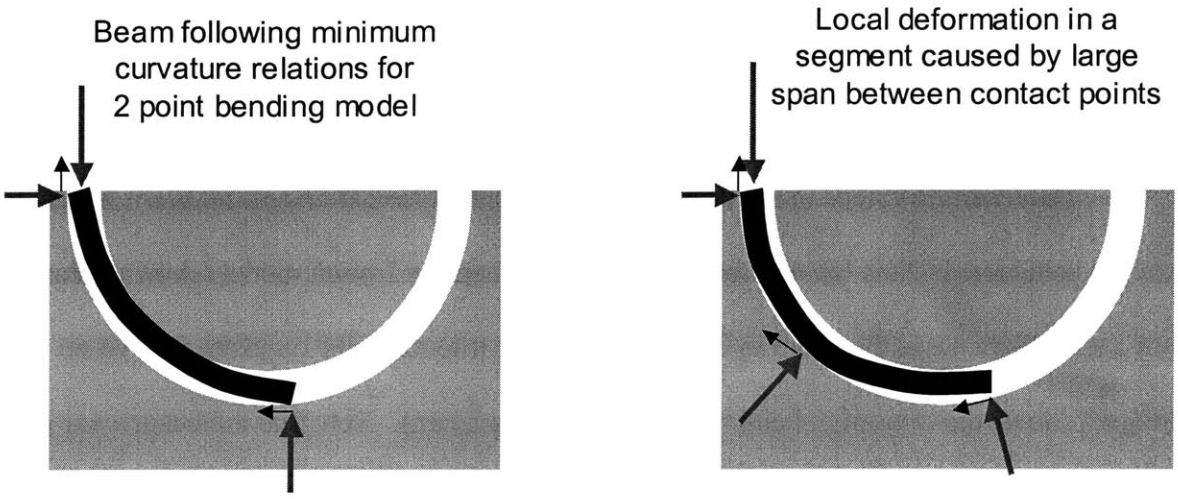

Figure 87 - Transition from 2 points of contact to 3 points of contact due to open span of the beam

There are a wide range of other effects that have not been specifically mentioned above including, but not limited to, stiffness of the tunnel (some work is done on tunnel walls), tip geometry of the beam, the frictional force dependence on area, roughness and speed of insertion. Furthermore, tunnel geometries with constantly varying radii or with very short segments (when compared to the beam diameter) are not handled accurately due to the path segment independence of effect assumption.

Despite all these simplifications and assumptions, many complexities of the problem have been dealt with to produce a model which can easily be applied to a wide range of problems with any number of segments which have nearly any curvature or tunnel diameter.

5.3.8. Failure of the insertion process

As was mentioned earlier, the failure of the insertion process occurs when the forces become so high as to cause buckling of the beam. For the case of a coaxial wire, failure occurs when the wire is bent into a sharp bend and the outer fibers of the coaxial jacket tear. This causes a significant electrical discontinuity even if the shield is still somewhat intact. Furthermore, this tear will prevent further insertion of the coax and

thus the situation must be avoided. We calculate the critical buckling load by first determining the longest unsupported length that exists in the path and insertion machine. This is complicated by the fact that the compression force on the beam is not constant along its length, but this effect will be ignored.

The simplest approach to determining the maximum load is to use the linear buckling model for slender members. It is given by: [5]

$$F_{critical} = \frac{n^2 \pi^2 EI}{L^2} \tag{5.65}$$

where L is the unsupported length and n =1 for the first bending mode (buckling the beam into 2 or 3 waves requires 4 and 9 times more force, respectively). This equation assumes that the beam is perfectly straight to start and is simply supported on each end.

When this buckling is constrained by cylindrical walls, after linear buckling occurs (and no failure has occurred), helical buckling occurs at higher forces. This is given by [71]:

$$F_{critical} = \frac{2\pi^2 EI}{t^2} \tag{5.66}$$

where t is the pitch of the helix (or the length along the cylinder that is occupied by one half wave of the helix (180 degrees of rotation)).

$$t = \sqrt{\left(\frac{l_{helix}}{n}\right)^2 - \pi^2 R^2} \approx \frac{l_{helix}}{n} \tag{5.67}$$

For most applications, t in Equation (5.66) can be substituted for the unconstrained length of the tube, since the first mode is one and the length of the tube is usually much greater than half the circumference of the tube. [39] and [81] describe helical and sinusoidal buckling of beams in curved segments.

As has been briefly mentioned, there are two potential ways in which to insert cable: by hand with a pin vise or using friction drive rollers. Using the friction drive roller setup, the maximum unconstrained length outside of the tunnel path is shown below.

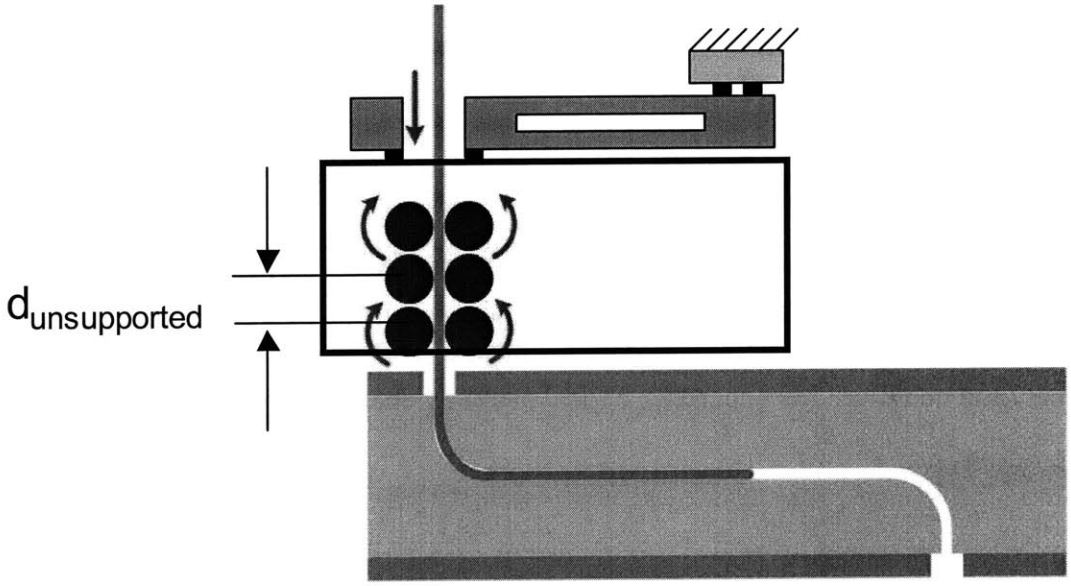

Figure 88 - Maximum unsupported distance outside the tunnel path

The maximum unsupported distance is 0.310" (the distance between the last drive roller and the measuring roller). Using this value the force at which a buckling would occur between the rollers is 75 lbf. The typical maximum force of the paths used in the 3DST project is less than 3 lbf, so there is relatively little danger of an external buckling occurring between rollers.

Using the hand insertion method is far more dangerous. Here, the human hand can apply side loads and cause failure even when the unsupported length is kept very short.

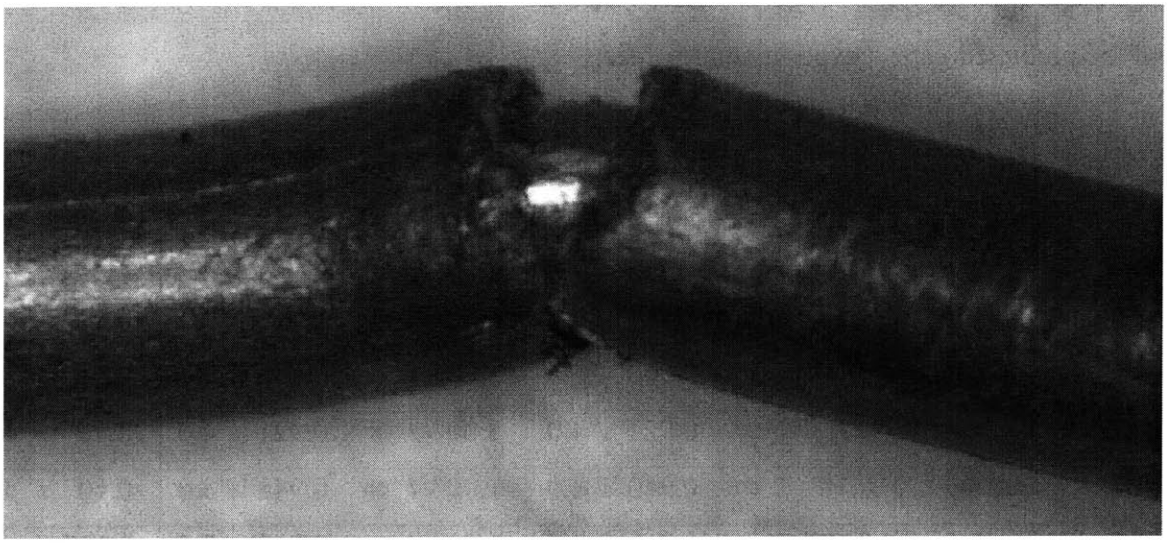

Figure 89 - A picture of 0.034" coaxial cable after buckling occurred during hand insertion.

The other place where buckling can occur is inside the tube. In this case, the buckling could be catastrophic if the beam is buckled to a tight enough radius. Linear buckling will occur first, followed by helical buckling. Depending on the clearances in the tunnel, it may or may not be catastrophic. The ability to continue pushing the beam further along the path after buckling has been studied for drillstrings in curved wellbores [81] and [39], but has not been investigated in this thesis.

5.4. Comparison with tested values

Multiple different geometry tunnels were created to test the validity of the models developed. The path geometries that were tested are tabulated below followed by graphs of the predicted versus experimental values.

Test path #	Tunnel Dia	1st segment	2nd segment	3rd segment	4th segment	5th segment
1	~ 0.46	0.10" / ∞	0.903" / 10	1.00" / ∞	0.903" / 10	0.10" / ∞
2	.~0.45	0.10" / ∞	0.906" / 7.5	1.00" / ∞	0.906" / 7.5	0.10" / ∞
3	~.046	0.10" / ∞	0.921" / 4.0	1.00" / ∞	0.921" / 4.0	0.10" / ∞
4	~.046	0.10" / ∞	0.940" / 3.0	1.00" / ∞	0.940" / 3.0	0.10" / ∞
5	~.046	0.10" / ∞	0.960" / 2.5	1.00" / ∞	0.960" / 2.5	0.10" / ∞
6	~.054	0.15" / ∞	0.75" / 0.44	2.17" / ∞	-	-
7	~.054	0.15" / ∞	0.64" / 0.38	2.17" / ∞	-	-

Table 13 - Table of tunnel paths that were tested and correlated to analytical models

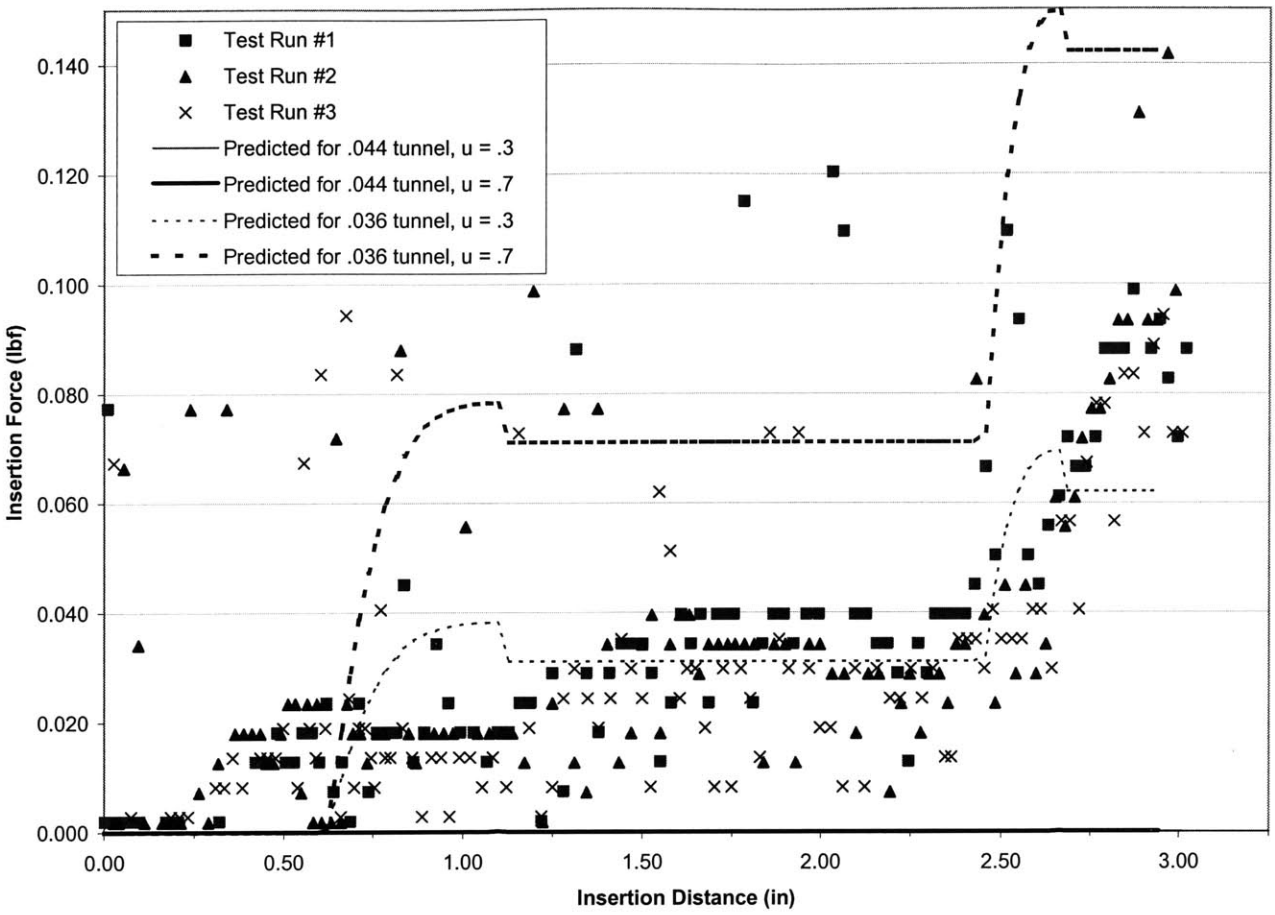

Figure 90 – Experimental vs. Prediction - Test path #1

3 insertions were made using the insertion machine. The predicted force for the tunnel diameter and path is nearly zero due to the way the segment minimum curvatures are calculated. The path is so close to straight, the math which determines minimum curvature for a given tunnel diameter is not valid for such a sequence of low curvatures.

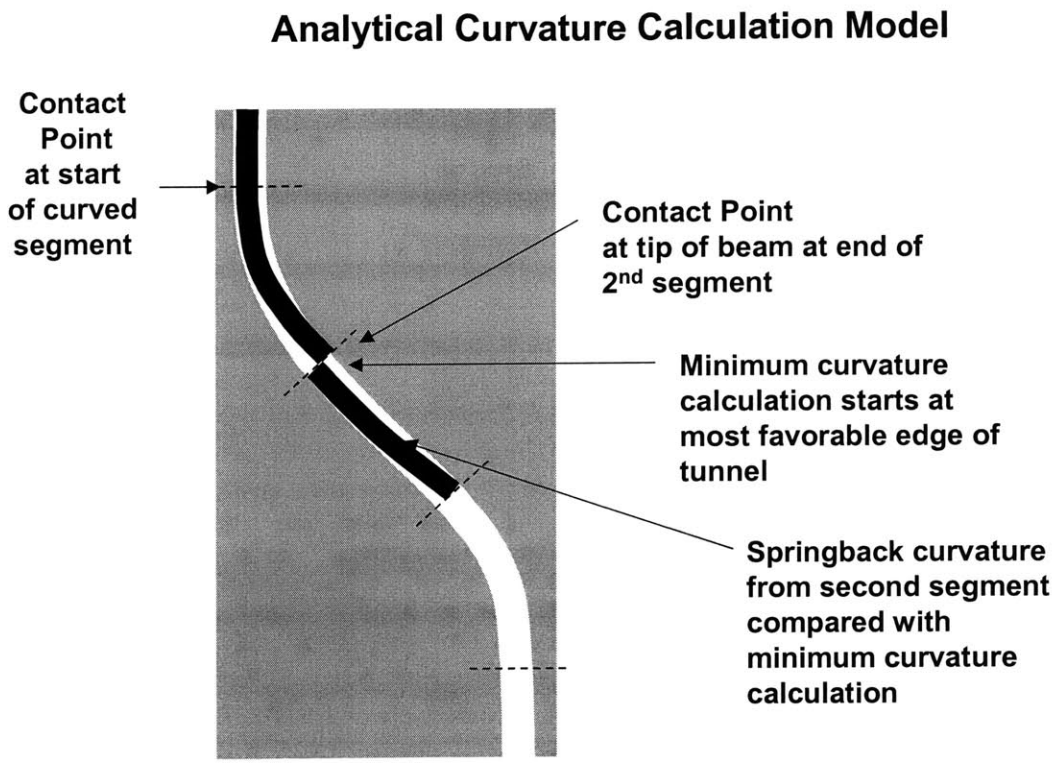

Figure 91 - Why the analytical model fails for low curvature, large clearance models

The curvature calculation method relies on the fact that the curvatures of the path are significant and the tunnel diameter is close to the beam diameter. When both conditions are broken, a significant error develops because the model effectively allows a discontinuity between segments. As shown above, if the springback curvature is nearly zero, but it is up against the far wall, the next segment calculation does not take this into account and predicts that a near zero curvature beam can exist in the large clearance tunnel without bending. If the entering curvature was greater or the tunnel diameter smaller, the predicted insertion force error would be insignificant.

For the curvature model to properly deal with this effect, it would need to calculate the minimum curvature between two segments (of differing curvature) to get the right answer. This would require a much more complicated model and is a recommended action for future work, and was described in section 5.3.7.

Two other plots were made using tighter fitting tunnels of .036" diameter. These plots more accurately represent the forces when the curvatures are very low. In all subsequent plots, the tighter fitting tunnel diameter will also be plotted. These plots are meant to represent an upper bound of the predicted insertion force, especially for the high friction, tight fitting (.036" diameter) plot.

As a final note, the actual diameter of the tunnel created by SLA is not especially well controlled and thus it is probable that the tunnel diameter is not perfectly consistent throughout its length. Due to manufacturing intricacies, the curved sections of the tunnel are likely to be somewhat smaller than the straight sections and this is borne out by the insertion force data, however the diameter at each point along the path has not be measured (it would require destroying the part).

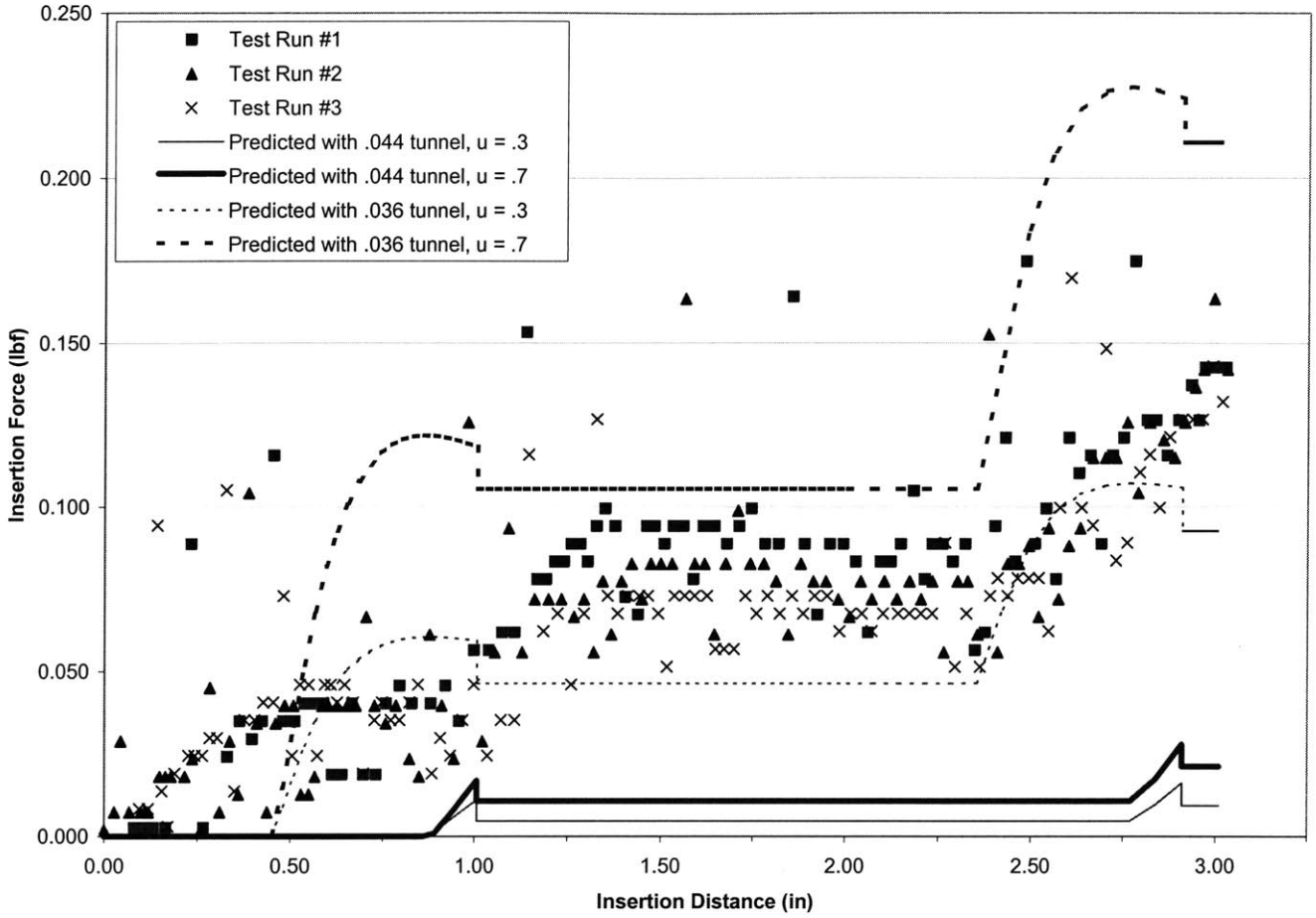

Figure 92 – Experimental vs. Prediction - Test path #2

This path (Figure 92) also has low curvatures, and thus the adjustment of the path diameter is made to make the curvature math with tunnel clearance more valid. In this case, however, the curvature in the path with respect to the beam diameter is approaching 200:1, and the forces predicted by the 0.044" tunnel are coming closer to the experimental values. The friction coefficient was measured on the outside surface as roughly 0.3, however it had some dependence on orientation relative to build direction. It

is believed that the internal cavities exhibit higher friction characteristics, but this has not been proven conclusively in this thesis.

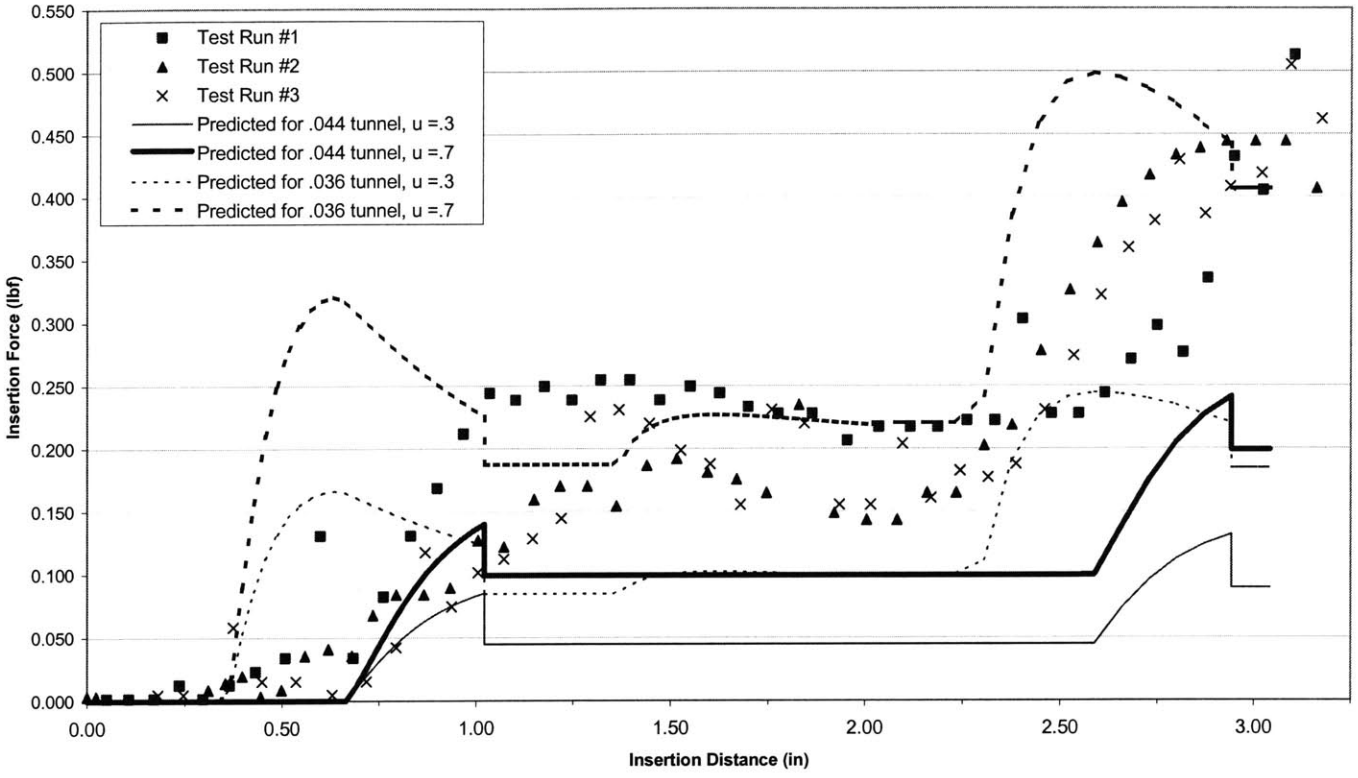

Figure 93 – Experimental vs. Prediction - Test path #3

This model (Figure 93) has higher curvature than the previous two models (ratio is roughly 120:1) and the tunnel diameter of .044, $\mu = .7$ make a relatively good prediction for the start of force and the slope and magnitude in the first curved section. The force recovery of the beam does not appear in the experimental data, however, some springback has occurred but it is likely masked by the friction force. The model that best predicts the insertion force, is one with a tunnel diameter somewhat smaller than expected with a higher than measured friction coefficient.

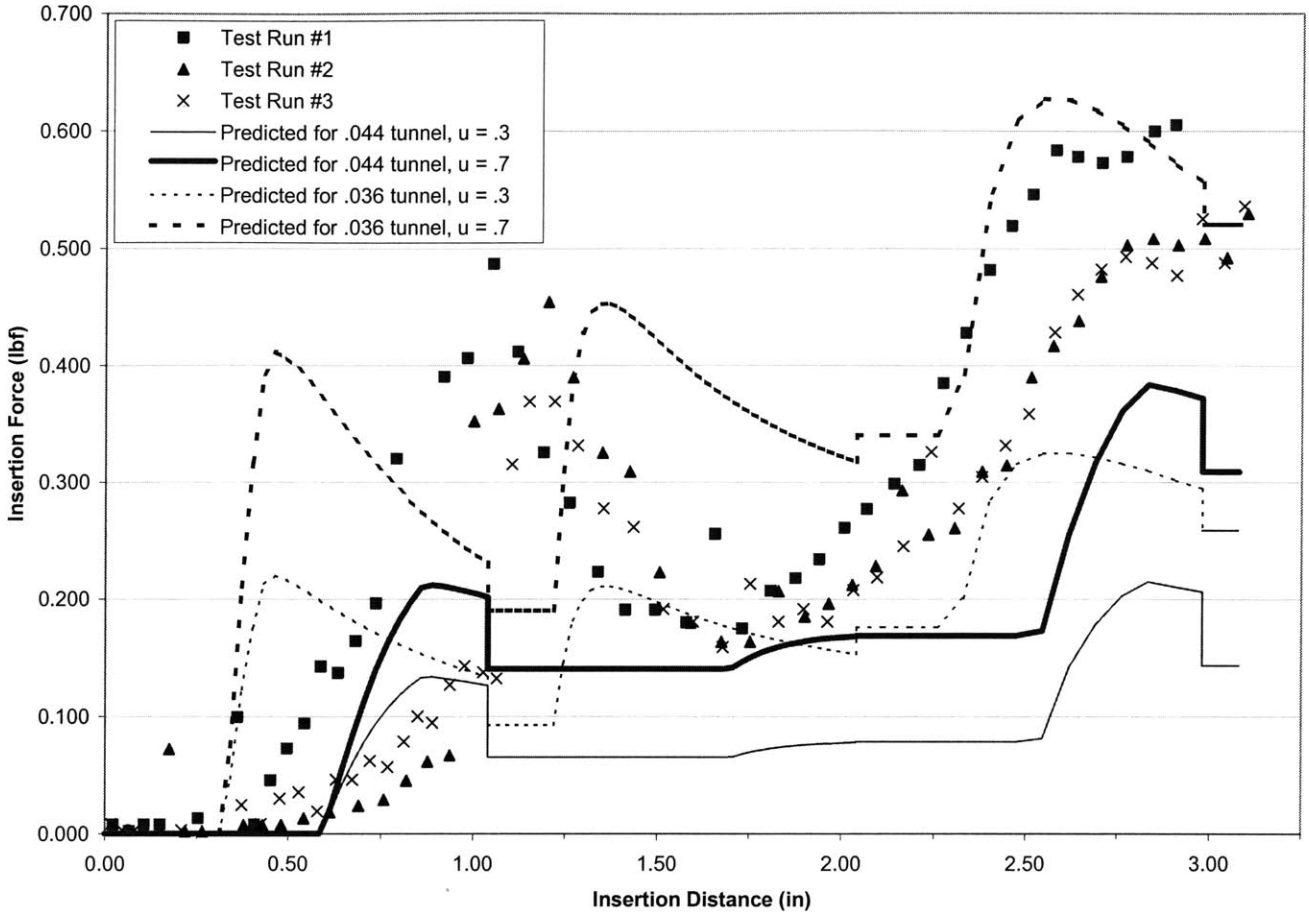

Figure 94 - Experimental vs. Prediction - Test path #4

The curvature ratio is now roughly 90:1 and forces predicted by the high friction model are closer to experimental data. The model predicts a sharp decline at the end of the first segment, but experimental data shows a gradual decline. The data shows that work is being recovered, but not instantly as the segmentized curvature model predicts. It fails to predict the slow decline of the force from the first segment and does not predict that the forces are as high as they actually are in the first segment. There is just one

reason for both phenomena. If the beam was to conform to the outside of the wall of the beam (rather than taking the elastic minimum curvature) the moment and thus the friction forces would go up. This would also mean the beam would springback to a slightly higher curvature and would exert force earlier in the straight section. This is seen in the last two high curvature examples very clearly.

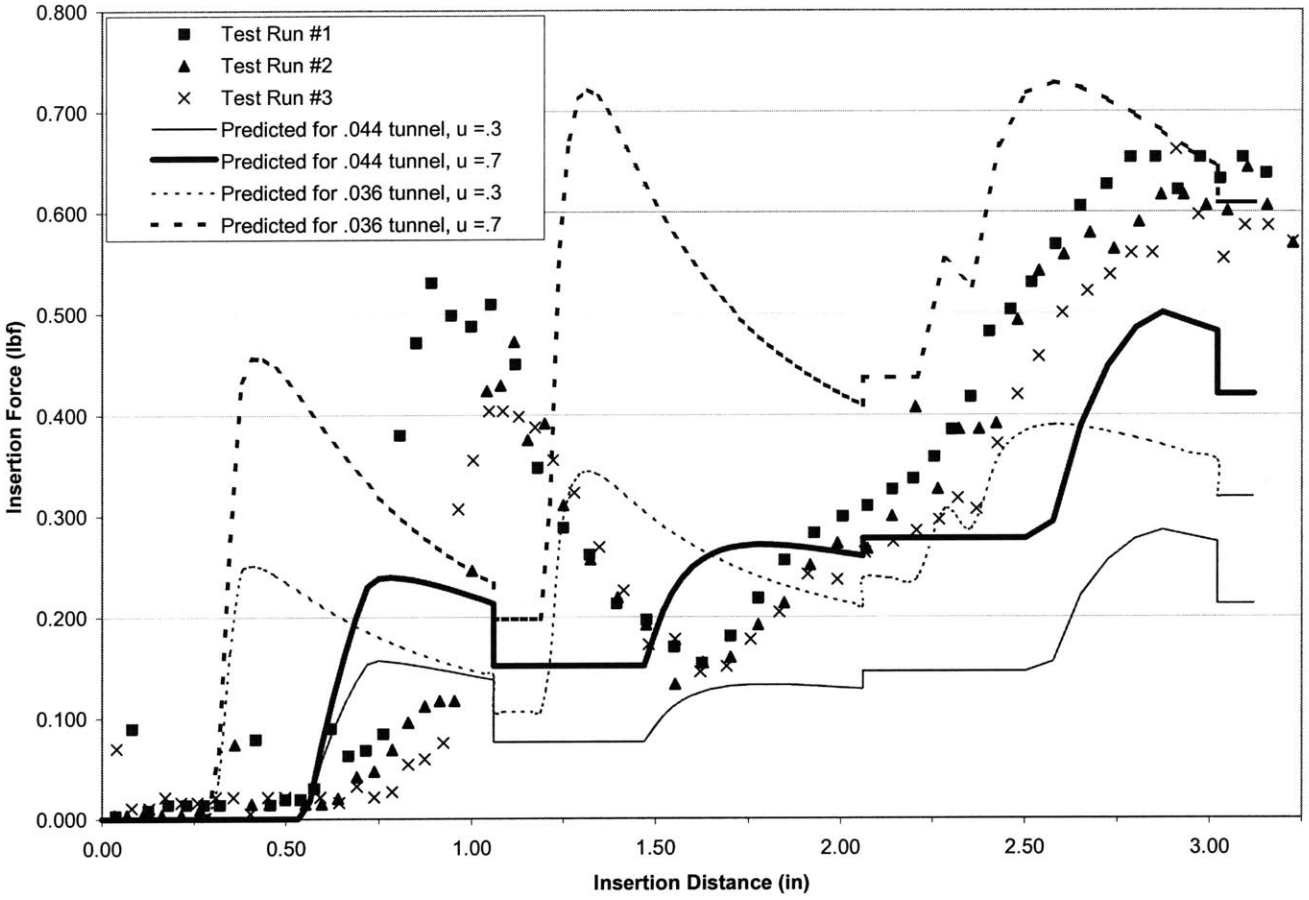

Figure 95 - Experimental vs. Prediction - Test path #5

The curvature ratio is now 75:1 and the same effect can be seen in the first segment as was described in test path #4. The unsmoothness of the predicted curve is a

direct result of the simplifications taken to predict the curvature so that at each incremental step along the path, the entire path spline would not need to be calculated.

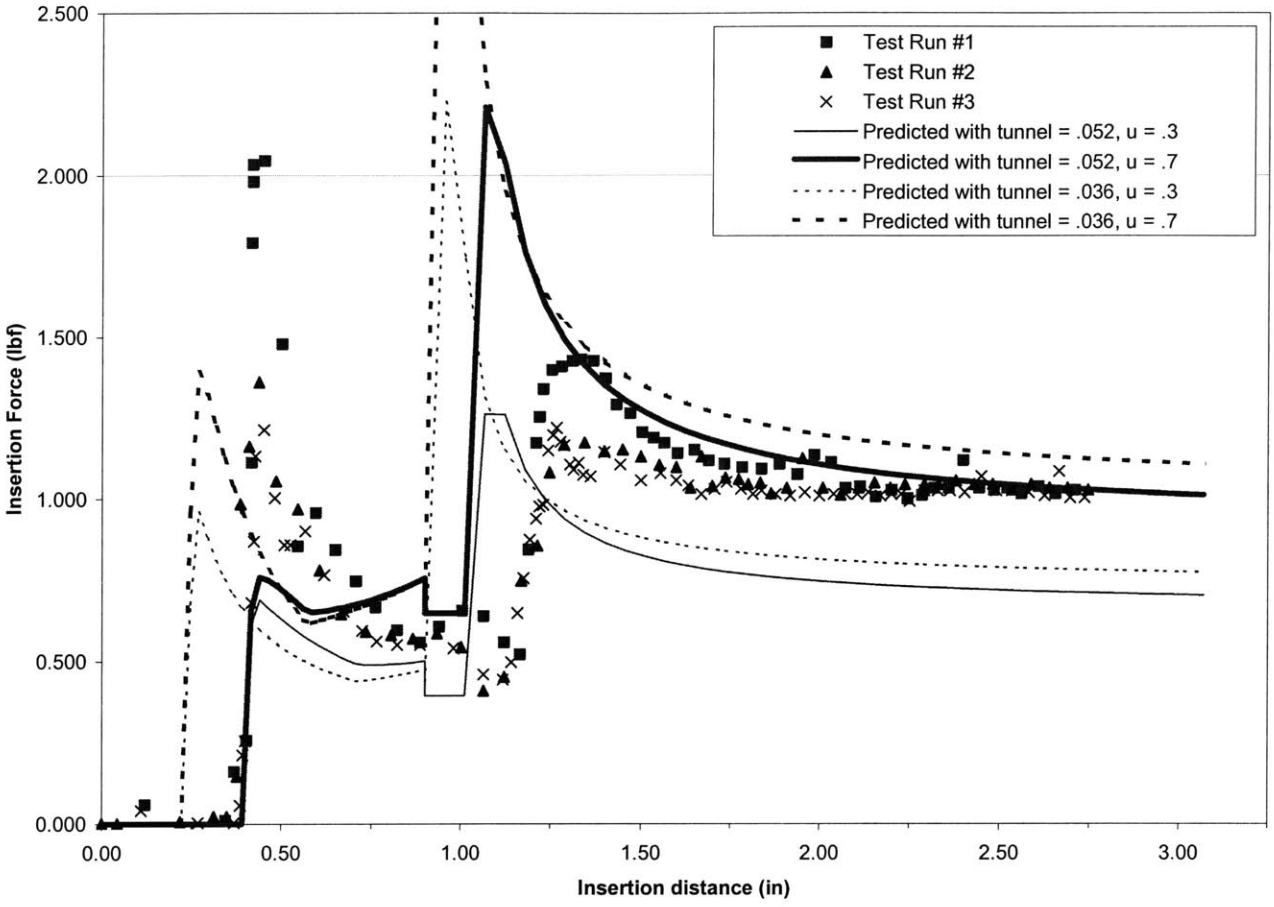

Figure 96 - Experimental vs. Prediction - Test path #6

The curvature ratio in the above figure is 13:1 and the prediction in the third straight segment is much improved over previous examples. The initial spike in force occurs when the beam first contacts the wall and the model underestimates this initial force. This may be due to the beam hitting a rough edge or may be an area where a 3 point bending model would be a better predictor of the insertion force. As can be seen, the tighter tunnel diameter in the first segment is a better predictor of the force.

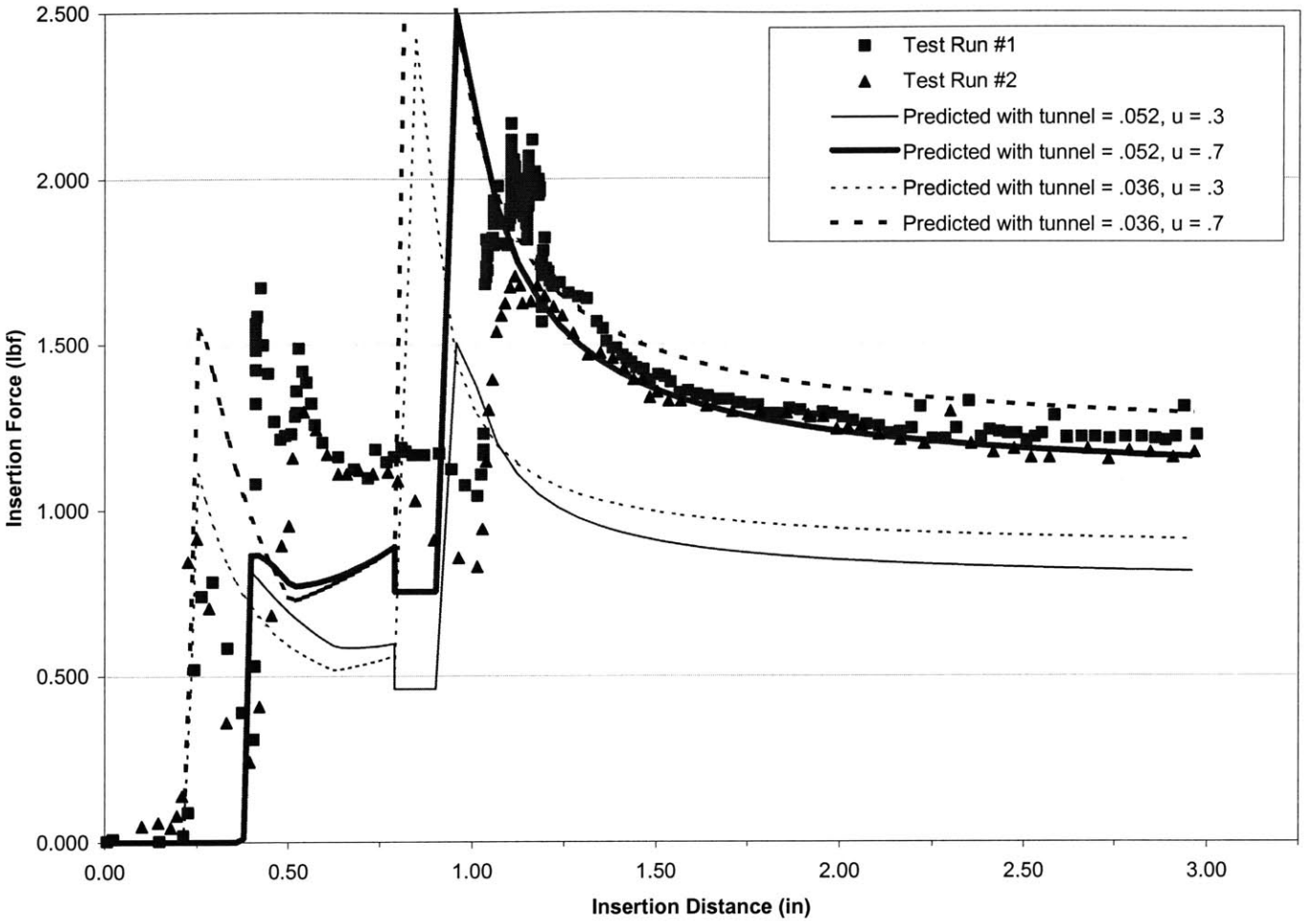

Figure 97 - Experimental vs. Prediction - Test path #7

In this model, the curvature is now almost 10:1 and the correlation between the model and the experimental results in the third segment are extraordinary. In this regime, the bending forces clearly dominate over any small perturbations or changes in the path geometry. In the first test run, some slipping of the beam is seen near the peak of the force at just over 2 lbf. On the second run in the same path, the normal force applied to the friction drive rollers was increased and the voltage on the motor increased from 10 to 13 volts so no slippage occurred.

5.5. Summary

The models developed in this chapter progress from the straightforward perfectly elastic model, to a relatively complex elastic plastic model with friction and tunnel diameters accounted for. The analysis developed is well suited to a path of any number of segments provided they are a few times greater than the beam diameter. The development of these models is particularly well suited to a segmented path that is generated by the auto-router (discussed in the next chapter). As was demonstrated in the above graphs, the model correlates reasonably well to multi-segmented paths from the ranges of 200:1 down to 10:1. However, uncertainties in friction and perhaps surface irregularities in the SLA tunnels yield to under-predicting the insertion force. The results show that the models predict the insertion force of the curved segment better with tighter tunnel diameters whereas the larger path diameter is a better predictor in the straight segments. The models could easily be changed to accommodate this effect, but more investigation is required to determine if this is due to the actual tunnel path diamter changing or is the effect of some other effect that has not been considered. It is expected that good correlation would continue up to very tight curvatures of 3:1. At ranges tighter than 3:1, other effects will start to become more prominent that have been ignored (shifting of the neutral axis, strain-hardening, etc.). The inaccuracies in the SLA build process may also influence the results of the experimental data by making some sections of the tunnel narrower than the expected diameter. As can be seen in the above figures, two tunnel diameters were graphed along with two friction values. It appears that many of the curved sections correspond better to a tighter tunnel diameter whereas in straight

sections, the predictions of the expected tunnel diameter predict better. This hypothesis could only be preformed by a destructive test that sliced the tunnel path into sections and accurately measured. It is likely that the nature of the build process makes curved sections more difficult to control and therefore would account for this trend. The insertion machine that was developed is able to insert at speeds of roughly an inch per second. With further development and more sophisticated electronic controls, the automation of insertion of cables should be achievable. Now that a relatively accurate model of the insertion forces has been developed (especially in the range of the 3DST project which has curvature ratios in the range of 40:1 to 10:1), the model can be used to verify that no path has too high of an insertion force before it is even created.

The software routing algorithm uses the high values (mu = 0.7 and tunnel diameter somewhat smaller than the expected diameter). In this way, the routing algorithm will usually be conservative in predicting the forces of insertion. Currently, the only check the software performs is to verify the insertion force does not exceed a given value, however, more sophisticated controls could perform perturbations to the solution to minimize insertion force. Furthermore, long straight internal sections could be another area where buckling could occur, especially when the tunnel diameter is much larger than the beam diameter. Some suggestions for future work are covered in chapter 8.

Chapter 6 - Routing techniques

6.1. Overview of Prior Work

Routing multiple non-intersecting freeform paths in 3D space has received only limited attention in scientific literature. The lack of literature likely stems from the limited number of applications that require such accuracy in 3D routing. Similar problems include routing of air traffic or multiple spacecraft in flight. This motion path planning problem has bend constraints from the maximum acceleration limits. However, the paths of the aircraft are allowed to intersect as long as both aircraft do not occupy the same space at the same time. The intersection avoidance is much simpler than trying to maintain non-intersecting paths along the entire path length.

Figure 98 - A schematic of the robot / airplane routing problem

The figure above illustrates how two aircraft (designated by the circles with arrows indicating their present direction) following the paths and traveling at the same speed will collide. An adjustment of the paths still has a crossing but it is timed such that the lower aircraft crosses the other's flight path earlier than the other and thus avoids a

collision. An alternate solution would be to speed one aircraft up and slow the other one down and use the flight paths shown on the left. Algorithms to do this type of flight planning have been created and typically involve a relatively small number of aircraft that are well separated [66] [47].

The routing of piping in a building or a large transport (e.g. – submarine or aircraft) has also been addressed in the literature [70]. These algorithms typically use a Lee-Moore [40] [49] algorithm or a Dijkstra [18] algorithm to find the shortest path around fixed obstacles. These algorithms are limited by their ability to deal only with straight segments and thus all bends are sharp (and typically at 90 degrees). These algorithms are well suited to the purpose of routing piping as straight segments connected by 90 degree elbows.

6.1.1. Lee-Moore Routing Algorithm

The Lee-Moore algorithm is a very elegant way to find the shortest path in 2D or 3D space. If the start and end points are known and the obstacles are defined, the algorithm fills the cells adjacent to the start cells with a value of one. The next step is to fill the cells adjacent to those with ones, with twos. This process is repeated over and over until the next cell to be filled is the finish cell. At this point, the algorithm follows the gradient back to the start, and the path is thus determined.

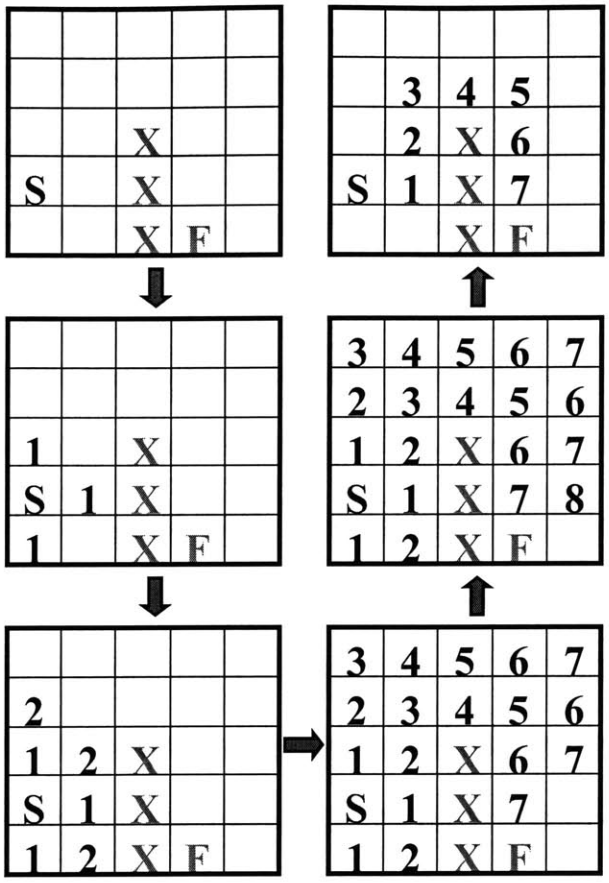

Figure 99 - Six steps showing the execution of a Lee-Moore algorithm. The "X" represents an obstacle. (Some filling steps are skipped between the 3rd and 4th step)

This is a greedy algorithm which takes the best path first. That is, the first path the router chooses to route will take the best path. The next path that is chosen to route takes the best path and avoids the first path that was routed. This strategy is referred to as greedy because the first path does not take into consideration any other paths and may block some paths entirely. The algorithm is limited to 90 bends but in a 2D array, 45 angles can be used. When using 45 angles, more care is needed, however, if two paths cannot cross over in an "X" pattern. This would require the use of a "fat" path or "fat" graphs [20].

6.1.2. Dijkstra's method

Dijkstra algorithm (named after its discoverer E.W. Dijkstra) finds the shortest path from A to B in a connected weighted graph. It is also a greedy algorithm when applied to multiple paths. It operates by selecting nodes one by one and filling the node with the minimum value required to reach it from the start node. The algorithm starts by assigning all nodes to a value of infinity. The nodes (or vertices) adjacent to the start node are assigned the value of the connecting edge. The next step is to choose the node with the lowest value that is not already selected. From this node, the algorithm updates all nodes connected to it. If the value to be put in the node is greater than the current value, the current value remains. If, however, the value to be put in the node is lower, the node is updated with the lower number. The process repeats by selecting the node with the lowest value (that has not been previously selected) and the process repeats until the each node has been selected. Then it is simply a matter of following the predecessor list (each node records from what node it got its value) back to the start node.

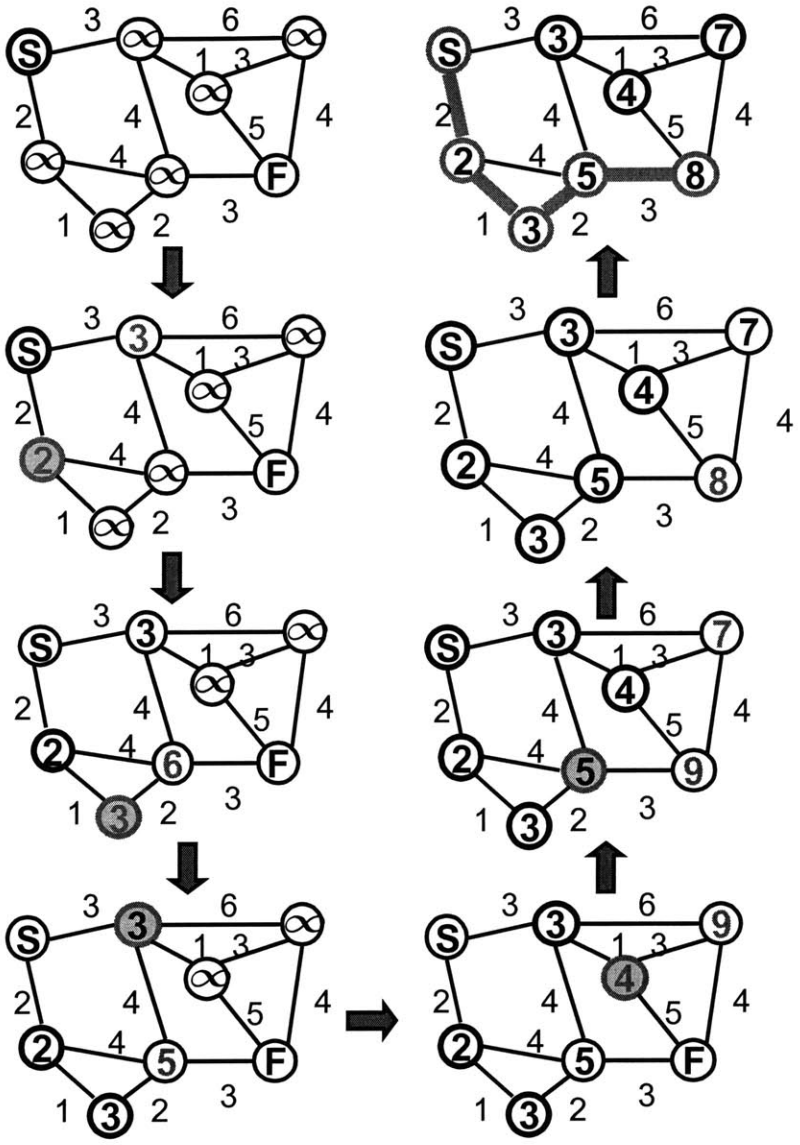

Figure 100 - 8 steps illustrating the Dijkstra algorithm.
Numbers on the links represent the weights of the path. The highlighted node is the one being updated by the algorithm.

6.1.3. PCB and VLSI Layout Algorithms

An enormous amount of literature has been published concerning the routing of PCBs and VLSI chips. These routing methods are generally limited to planar (2D)

problems or 2.5D (multiple-level planar) problems that are connected by vias (or vertical shafts). These algorithms typically minimize objectives such as minimum bends, minimum layers, minimum vias, minimum area, minimum cross talk, or maximum RF performance. Most of these algorithms are based on Manhattan routing (90° bends only) using Lee-Moore or Dijkstra based algorithms, but in recent years some algorithms have been developed to use non-orthogonal routing. Even these non-Manhattan routers typically route with limited path angles (either ± 45° or ±60°).

6.1.4. Divide and Conquer – Global channel routing

The divide and conquer approach is a general approach used to break down difficult problems into many smaller and hopefully less difficult problems [11] [8]. It has been applied to the PCB and VLSI routing problem by grouping multiple paths headed to the same local area from the same local area into one big path. This is called global channel routing. The larger paths are chosen in a way to minimize breakouts of its internal paths. The problem is then attempted with a much smaller number of large paths. Once this problem is solved, each of the larger paths is broken into its smaller paths and the router tries to solve the routing for the paths inside the larger path or channel. This second step is often referred to as the detail routing. The divide and conquer approach is one of the most powerful approaches for VLSI and PCB routing.

6.1.5. Cleanup (post-routed) algorithms

All router algorithms are trying to successfully route every path, however, most algorithms typically fall short of 100% success. At this stage, a cleanup algorithm can be used to attempt to route the last few paths. There are two general categories of cleanup algorithms: rip-up and re-route and shove aside [15] [64]. The rip-up method selects

some paths to be completely removed. Once removed, the paths are attempted to be re-routed since a potential interferences may have been removed. The figure below shows a two path problem solved by a rip-up and reroute method. The problem is to connect from A to A and from B to B while keeping both paths entirely inside the box.

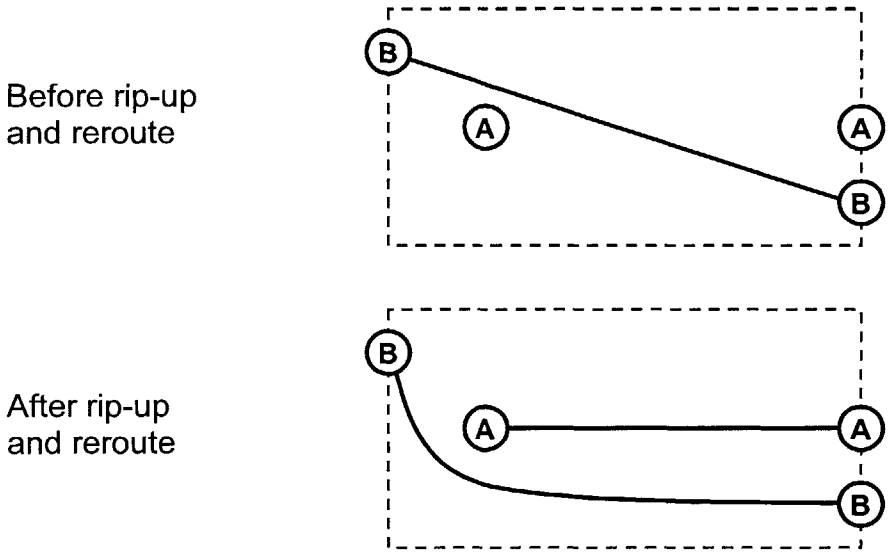

Figure 101 - Rip up and re-route schematic

The rip-up and reroute method only works when an alternative path is found for the path that was removed and a new successful path was found for a path that was heretofore unable to be routed.

The other main class of cleanup routers can be described as shove aside. These algorithms do not remove any paths, but instead try to shift the paths of existing, successfully connected paths to make room for paths that have not been successfully routed. A simple example is shown below, that allows path A to be routed.

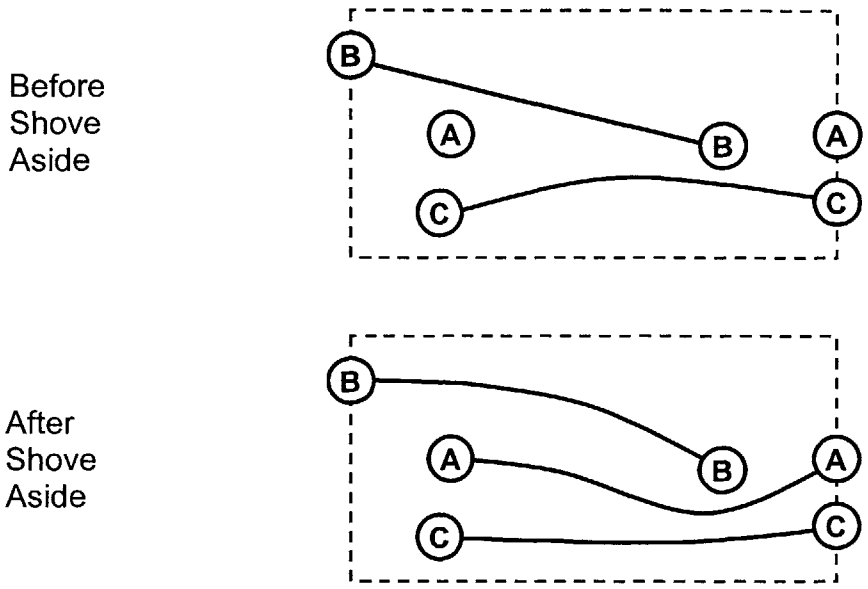

Figure 102 - Schematic of shove-aside algorithm

6.1.6. Layer/Via Heuristic Rules

Many of today's commercial PCB routers rely heavily on heuristics. A heuristic in this class of routers is a general rule of thumb or a guideline that tends to work well. An example of such a heuristic used in PCB routing is to define a layer as mostly x directed and the next layer as mostly y directed. In this way, path avoidance is generally accomplished as traces on a single layer run in the same direction. By holding to this heuristic, a typical router may be able to route a complicated maze of interconnections in only two or four layers. The use of this guideline simplifies the task for the auto-router computer algorithm and generally has good success. However, these heuristics tend to be problem specific and in the example above, they do not work well for a probe card which

is trying to funnel signals from a large diameter circular pattern to a denser pattern in the center.

6.1.7. Same length routing

The problem of routing same length wires on a printed circuit board adds an interesting complexity to wire routing algorithms. Because a multitude of signals from the tester must arrive at the DUT at the same time, the line lengths need to be the same length or circuitry in the tester needs to compensate for differing lengths. Although circuitry could be designed to compensate each driver, for cost savings, the circuitry is typically spread across two or four drivers and thus cables in groups of two or four must be length matched. The same length requirement exists for differential signals and for those signals that do not have individual time compensation circuits.

Some algorithms deal with this constraint in the 2D case by first routing all signals and then if the paths do not match up, adding a meander path to one or some wires. This is not the optimal method to match line lengths for high speed signals as every turn creates crosstalk couplings and discontinuities. Some of the newest PCB auto-routers appear to handle these situations in a somewhat cleaner fashion by making a simple loopback.

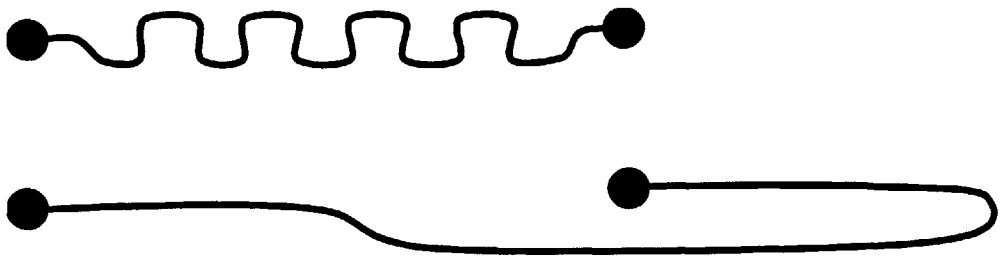

Figure 103 - A meander path (with many turns) and a simple loopback path

6.1.8. General Global Optimization Techniques

There are many problems in mathematics that have no easy solution and cannot be solved by following a simple algorithmic procedure. A seemingly simple problem is can a map (e.g. - the 48 states in the continental US) be colored with just 3 colors such that no border has the same color on both sides. This problem has 3^n possible color combinations where n is the number of vertices (or states). For the US map this means there are 7.179×10^{23} (or 718 billion trillion) possible combinations. The simplest way to solve this problem is to try a combination and then check to see if any violations of the border rule occur. If no violations occur, a solution has been found. Unfortunately, no one has found a way to find a solution, if it exists, without searching through all possible solutions. That is not to say this problem cannot be solved; it simply says that an algorithm is not guaranteed to find a solution. In some cases, it may be possible to determine a 3 coloring does not exist. Using a divide and conquer algorithm, if a local area of the map cannot be three colored, the entire graph does not have a solution. In many cases, when a solution does exist, many algorithms can find a solution without searching though each solution blindly. One relatively simple algorithm is to arbitrarily assign a vertex (or state) a color and then assign neighbors such that no border conflicts occur. This process is repeated until either a conflict occurs (in which case the algorithm will backtrack some number of steps and try again) or all vertices are filled with no conflicts. This algorithm will work for many k-color problems but it is not guaranteed to work [30]. This is the crux of all algorithms that solve NP (nondeterministic polynomial) problems. That is, many algorithms succeed in solving a NP problem but they may fail even when a solution does exist.

NP problems are typically described (for explanation purposes) by a landscape where the lowest points have minimum energy or minimum conflicts and peaks represent high energy or a great many conflicts. A general characteristic of NP problems is that it is relatively simple to determine the energy at a given state, but hard to find the lowest energy in the landscape. The landscape for typical global optimization problems typically has many degrees of freedom, but we will confine our examples to one with just two directions (x and y) with the z direction representing the value of the function at that point. It is easy to imagine a computer will be able to search a space with more dimensions, even if it is difficult to picture what the landscape would look like. If the landscape represented the potential energy of a cluster of atoms, the peaks would be high energy configurations and the valleys would be lower energy configurations. If a hiker is used to represent the current state of the algorithm, then the algorithm (the brain of the hiker) seeks to find the lowest point on the landscape. Unfortunately, the hiker can't tell how high or low any point is until he actually steps on it. (Pretend there is a lot of dense fog).

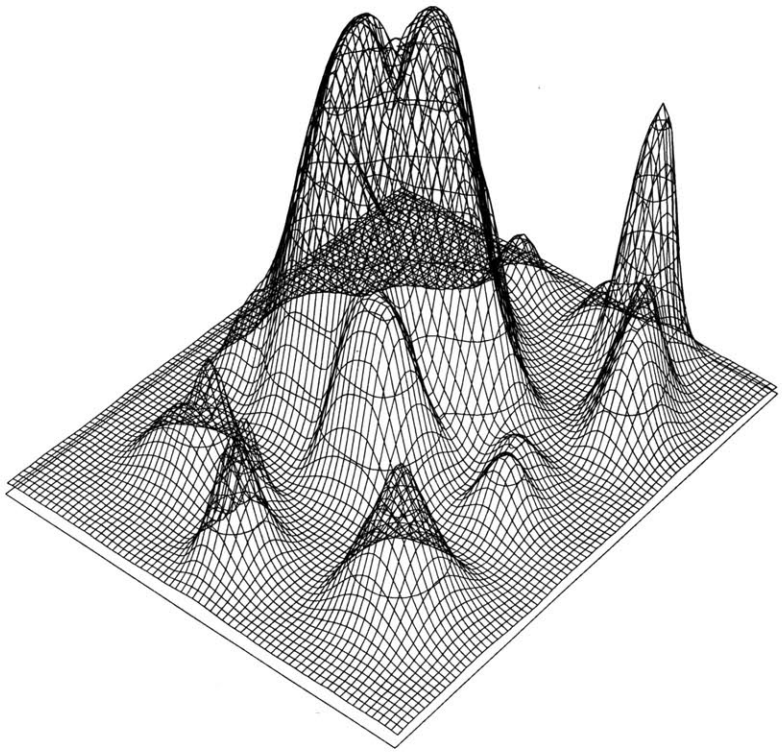

Figure 104 - A 2D representation of a relatively simple solution space. There are almost no local minima, and a high percentage of the area is near the optimum global minimum.

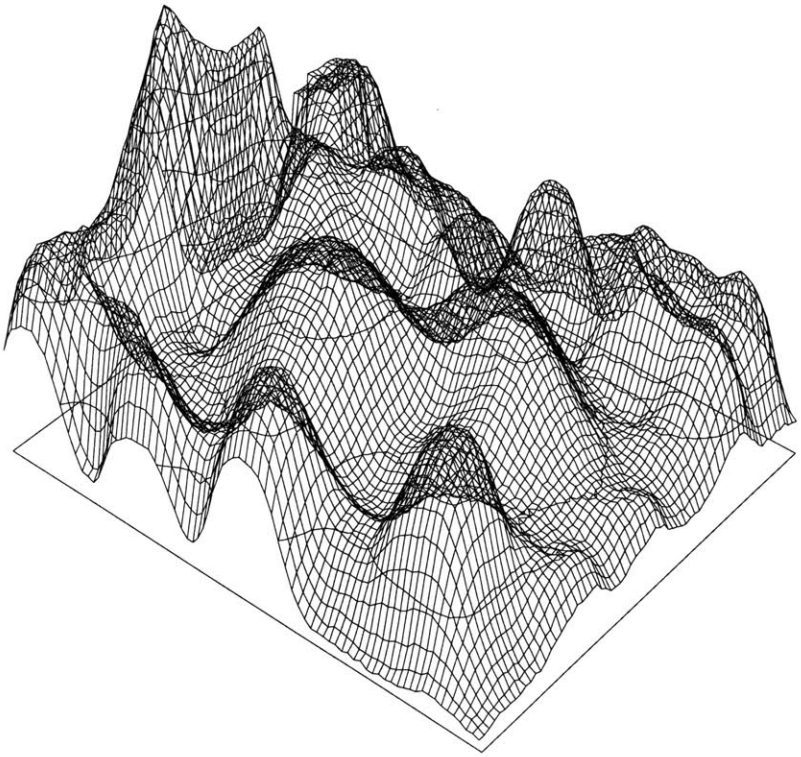

Figure 105 - A 2D representation of a more difficult solution space.
There are many local minima to get stuck in and only a small area is near the global minimum.

6.1.9. Steepest descent

The steepest descent method is the most common iterative improvement method in global searching. It should be noted that for a function which can be differentiated, the steepest descent algorithm simply heads in the direction of the gradient. For a global minimization problem in which the function cannot be differentiated (or it is difficult to do so), the steepest descent algorithm heads in a random direction and if the direction is down, it continues. If the direction is up, the steepest descent algorithm returns and tries a different direction. One can imagine the hiker standing on an arbitrary point in the landscape. If he takes a step in a random direction and the step carries him down, he stays there. If a step takes him upward, he returns to his previous position. The process is repeated many times and the solution continuously gets better (the hiker gets lower). This approach will find a minimum of a multi-dimensional problem, however it is not guaranteed to be the lowest minima. The problem with the steepest descent algorithm is that it can get stuck in a local minimum. If the hiker is at the bottom of a small pit and a lower point is nearby, but up and over a hill, the hiker (the steepest descent algorithm) will remain stuck in the bottom of the pit.

6.1.10. Metropolis Algorithm and Simulated Annealing

The mathematician Nicholas Metropolis invented the Metropolis algorithm in the 1940s while working for the Los Alamos National Laboratory [73]. If we place the hiker in an arbitrary position on the landscape, he can record how high he is and then take a step in a random direction. If the step carries the hiker to a lower position, he repeats the process. If the hiker takes a step higher, he compares his new height with his old height and based on the height difference and a roll of the dice, he decides to stay where he is or

return to his previous position and tries to take a step in another direction. For example, if his step was four feet higher but he rolled a high number (say a six), he would stay put. However, some percentage of the time the hiker would take a step up of four feet, but a lower number would be rolled and the hiker would return to his previous position. In this way, the Metropolis algorithm takes into account the height of the step, and thus small steps up are accepted more often than large steps up. The advantage of this algorithm is that it is able to escape local minima.

Simulated annealing is an approach introduced by S. Kirkpatrick, C. Gelatt and M. Vecchi [37] which attempts to improve on the Metropolis algorithm. The basic premise stems from statistical mechanics where a block of matter (which has roughly 10^{23} atoms per cubic centimeter and thus a huge number of degrees of freedom for all but the tiniest of blocks) is able to "find" the lowest energy state at low temperatures. If matter is in a liquid form, its atoms have a lot of energy (the temperature is high) and the atoms bounce around a lot. As the block cools, the atoms lose some of the energy and the system of atoms "seeks" the lowest energy state. If however, it is rapidly cooled, the atoms do not always have time to adjust to the lowest energy state and the crystal that is formed may have many imperfections and dislocations (and thus higher energy than a state without dislocations). The way to avoid this is to cool the system slowly and especially to hold the system at a temperature just above freezing point for a long period of time. This annealing of the material allows the system time to find a low energy state. The annealing of crystals can be extended to global searching algorithms trying to minimize some function such as energy. Thus, simulated annealing takes the approach of using perturbations (or steps) to the solution in which the temperature determines the

strength of perturbation. Imagine the hiker is placed at some arbitrary location that is relatively high on the landscape. The hiker records his elevation and takes a large step (because his energy is high). An acceptance criterion (similar to that of the Metropolis algorithm) allows some possible moves to higher ground but tends to prefer downward moves. As the temperature lowers, the size of the steps are decreased and the acceptance criteria changes, allowing fewer and smaller steps up. This method will typically home in on a more global minimum than the steepest descent algorithm. The strength of the simulated annealing comes from its ability to escape local minima and find a more global optimum. Simulated annealing has been shown to find good solutions to the traveling salesman problem, box packing problems and wire routing problems.

Of course, the simulated annealing algorithm and the Metropolis algorithm do not try all possibilities and depending on the surface topology they can miss better solutions. For example, a very steep pit or trench with high surroundings may never be found if the hiker never steps over the high surroundings and into the lower area.

6.1.11. Pachinko Method

This method used by Bob Leary of the University of California, San Diego takes its cue from the Japanese chance game called pachinko [73]. The pachinko machine drops many balls and each ball finds its way down the game board by the action of gravity (steepest decent) and hopefully lands in a winning slot. This is one type of a class of algorithms called multi-start algorithms. In contrast to simulated annealing or the Metropolis algorithm, the algorithm chooses many arbitrary (or potentially not so arbitrary) start locations and follows the steepest descent approach on each. This would be like air-dropping hundreds of hikers randomly over the landscape and giving them

strict instructions to just run downhill. This algorithm is well suited to parallel processing, as many computers (or processors) could each be assigned a hiker at an arbitrary location and the final resting places of each hiker would be sent back to a master computer. This method may also succeed in cases where high peaks surround very deep pits or valleys, where a simulated annealing approach would be unlikely to stray up to. The disadvantage of this approach is that many hikers may end up in the same basin (local minima).

6.2. Development in the 3DST

The simplest spline used by the 3D router consists of just 3 segments, a start arc of constant radius, an end arc of constant radius and the tangent line segment that connects the two arcs. In this case the spline has just two degrees of freedom (DOF): the start and end radii. The plane in which the spline lives is determined by the line that connects the two end points and the start and end tangent vectors. Using a typical 3DST example, there might be 128 wires to route to a central array. The typical bend radius limits enforced are from 0.25" to 1.25" (larger bends will not be able to fit in the limits of the block) and if the approximation is made that the bend radii to be selected are discretized (not an infinite number between .25" and 1.25") into 100 sizes (radii can be 0.25", 0.26", 0.27", etc., but not 0.255"), then each 3 segment path has 10,000 possible combinations. With 128 wires each with 10,000 possible configurations, the number of possible combinations in the 256 degree landscape (2 DOF per path multiplied by 128 wires) is $10{,}000^{128}$ which is 10^{512}, a number so huge it is beyond the comprehension of most people. In fact, the number is drastically conservative; some 3DST problems have six or more degrees of freedom, have 512 wires and are not discretized. The search space

for paths with six degrees of freedom and 512 wires is a landscape with over three thousand dimensions. This is clearly a vast expanse for the sole hiker to search.

6.2.1. 3D Lee-Moore Routing work

Initially the use of a 3D version of the Lee Maze algorithm was thought to hold promise for the 3DST problem. The idea was to create a 3D maze routing algorithm and then once all paths were complete and routed in a non-intersecting manner, smooth the paths to create bend radii. The algorithm was not very successful and many extra bends per path were created. Once the path was routed successfully, the addition of bend radii would likely cause new interferences. This method was abandoned in search of a better approach.

6.2.2. Preprocessing

If one examines the paths that a dense array of signals must take to get from one site to another, it should be apparent that the innermost paths in the inside of the array will be the most difficult to "get out" as these path must pass through areas where other paths must also go. In the same vein, those paths on the border of the array will have the easiest time "getting out". If all paths start normal to the start plane, one can see that the outermost paths can begin to turn or peel away from the array immediately, while those paths in the inner regions of the array must "wait" before they can start turning (or turn with a larger bend radius). This was called the "chip pyramid", as typically the densest area represented the chip that would be tested and the pyramid came from the fact that the height at which a path could start turning increased as one moved to the center of the chip. This is shown below. It became the basis of the first and only heuristic used by the 3D router software.

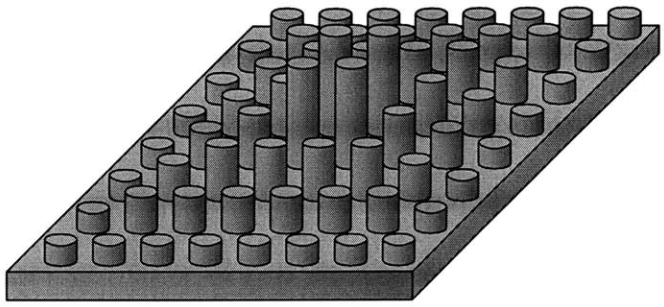

Figure 106 - The preprocessor guesses for the start segments form a pyramid.

The paths were projected onto the start plane and those that had to cross the greatest distance across the chip (using a line directed toward the end point) received the greatest start segment bias. The process was repeated for the end "chips" and the values were sent to the 3D router algorithm as an initial seed for the start and end radii (and for the 5 segment paths start and end straight segments as well).

The first attempts to route paths in 3D space used the simplest 3 segment splines and had no preprocessor. An algorithm would chose a start and end radius, create the 3D path, and attempt to put the path in the universe. If no intersections occurred, the path was added to the universe. The next path in the queue was selected, the algorithm again chose start and end radii and the path was checked in the universe against all other obstacles (including existing paths added to the universe). If the path intersected with another path, the algorithm would try another start and end radii combination. As one might imagine this strategy makes the first few paths very easy to add (there are few

obstacles) and the last few paths very difficult to add as they must avoid all other paths in the universe.

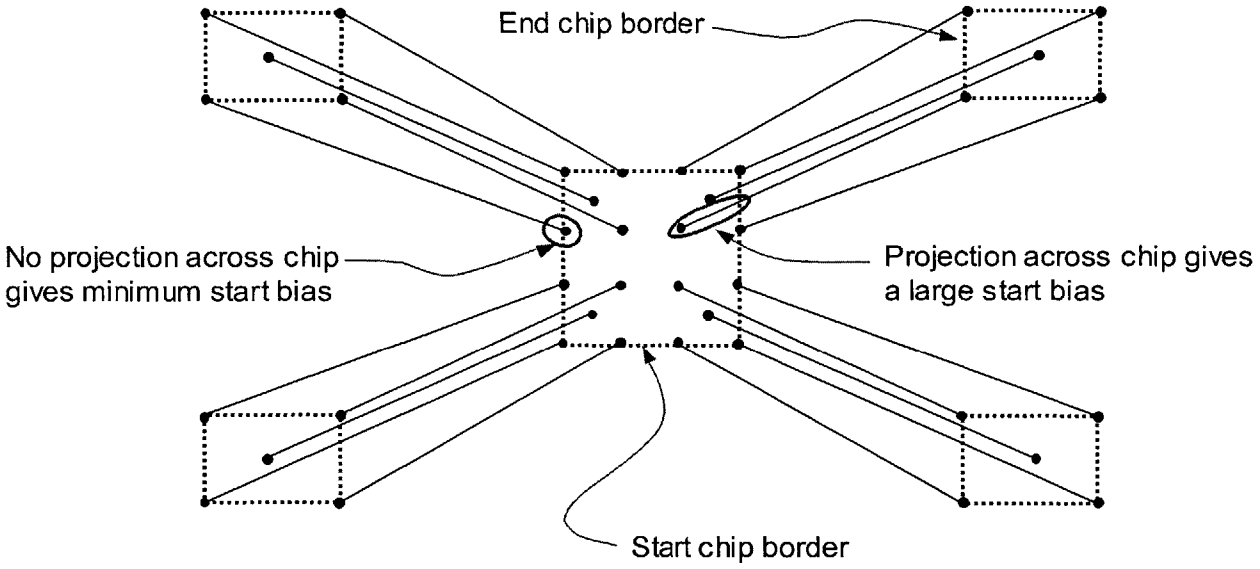

Figure 107 - Schematic of the algorithm the preprocessor uses.

6.2.3. Single path searching

6.2.3.1. Directed Searching (Deterministic)

The first algorithm developed to pick start and end radii had limited choices. The radii had a lower bound based on insertion force guidelines (e.g. 0.25") and an upper bound based on the minimum linear dimension of the routing volume (e.g. 1.0"). Given this data, the directed algorithm would attempt to route the path with the average of the two values at both ends. If that attempt failed it would search through each path combination. For example, if the min and max radii for both ends of a 3 segment path were 0.25" and 1.00" and the search increment was defined at .125", there are 6 possible radii for each end and thus 36 possible combinations. The directed algorithm would

simply search all 36 combinations until it found one that worked. If none were found, the algorithm would skip that path and move on to the next one. This type of routing algorithm is called deterministic.

6.2.3.2. Random Searching (Non-deterministic, oblivious)

The directed algorithm described above did not perform with great success when the path density became high and thus rather than continuously decreasing the increment and thus exponentially growing the number of combinations to search, a random searcher was developed. This algorithm would again get the limits of the start and end curves (for a 3 segment path) and would randomly select a value for the start and end radii. It would continue to try paths until a path was found with no intersections or it reached some user defined limit. This algorithm was much more successful in finding solutions to dense routing problems, but it would consume a lot of time, in some cases, to find a given path.

This algorithm is classified as oblivious, non-deterministic, since it has no knowledge of what would be a good guess or choice; it is completely random.

6.2.3.3. "Smart" Random searching (Non-deterministic, adaptive)

If the random selection of radii fails, as in the above algorithm, no information is transmitted back to the randomizer. For example, if a start radius of 0.30" is chosen and interference occurs on that radius, the randomizer could just as easily select a start radius of 0.30" (or some radius very close to it) again. Therefore, a "smart" randomizer (non-deterministic, adaptive algorithm) was coded which uses previous fail data to seed the randomizer preferentially for those radii that have not failed. In this way, failed paths pass information to the randomizer so that if start radii near 0.30" fail often, the randomizer will be less likely to select it again. This negative feedback is balanced by a

positive feedback to the randomizer, which increases the likelihood of choosing a given radius if it passes. Note that even if the start arc has no interferences, the end arc may fail and thus the entire path would fail. This change required some additional processor overhead and memory and would tend to slow the router down on very simple problems, but would speed up the successful location of paths in more difficult problems. This became especially apparent when the number of DOF of each segment was increased from 2 to 4 DOF.

The preprocessor (based on the distance across the chip) initially seeds the randomizer, such that paths at the edges of the chip are more likely to get the smallest radii and those at the center of the chip would get the largest radii. This is implemented by using a randomizer with a Gaussian distribution centered on the suggested radii from the preprocessor. The preprocessor can seed both the random and the "Smart" random algorithms.

6.2.4. The initial global solution search algorithms

6.2.4.1. Greedy one-at-a-time path search algorithm

The one-at-a-time algorithm works by selecting a path to route, (sometimes suggested in a particular order by the preprocessor) and then tries to add a path that does not intersect with any other paths. If the path is routed without any intersections, it is added to the universe and the next path in the queue is selected to be attempted. If a successful path is not found, the algorithm gives up and the next path in the queue is attempted. If 64 paths were trying to be routed in a dense array, this algorithm would (on the first try) typically route 30 to 45 paths successfully. For similar problems, the one-at-a-time router performed very differently as shown in the table below:

# of paths to be routed	Typical # Successful
8	**5-8**
64	**30-45**
128	**50-70**
256	**60-80**

Table 14 - Success rate of the initial search algorithm

The inherent problem with this algorithm is that once a path is placed in the universe, it is unmovable and if it is placed in a non-ideal location, it may block a large number of paths. Thus, the selection of the first few paths can greatly influence the routability of the remaining paths.

6.2.4.2. Group at a time search algorithm

The group at a time algorithm is a similar to a divide and conquer strategy but is not precisely such a strategy because it does not try to remerge the results. The results are merged as the solution progresses. For the 64 path example stated above, the problem was broken into 8 pieces of 8 paths each and the text output of the routing program is shown below for this example:

```
Group-at-a-time algorithm started
1st 8 paths selected.
1st attempt...6 of 8 routed successfully
2nd attempt...5 of 8 routed successfully
3rd attempt...6 of 8 routed successfully
4th attempt...8 of 8 routed successfully
8 of 8 paths in 1st group – 8 of 64 successful.
2nd 8 paths selected.
1st attempt...5 of 8 routed successfully
2nd attempt...7 of 8 routed successfully
3rd attempt...6 of 8 routed successfully
4th attempt...7 of 8 routed successfully
5th attempt... 4 of 8 routed successfully
7 of 8 paths in 2nd group – 15 of 64 successful.
```

This algorithm works well because the first path in the group has the most influence on the succeeding paths and thus multiple attempts are made to see which of these work the best for a smaller subset. This algorithm for the 64 path case mentioned above would typically end with 40 to 55 paths routed successfully. A table shows its general performance across multiple solution sizes. For the 64, 128 and 256 cases, groups of 4, 8 and 16 were tried and groups of 8 tended to work the best, most likely due to the 8 x 8 array of paths to be routed. For the case of just 8 paths, the group sizes attempted were 4 and 2, but it typically would perform slower and no better than the one-at-a-time algorithm. Clearly, these two routers work more effectively at different scales.

# of paths to be routed	Typical # Successful
8	**5-8**
64	**40-55**
128	**60-80**
256	**80-100**

Table 15 - Success rate of initial search - group at a time algorithm

6.2.4.3. Pachinko method – multiple start search algorithm

This method as described above simply involves running multiple trials and taking the best one or ones. Ideally this would happen in parallel across multiple machines in a network. The design of the code in Java has been architected to allow the use of a single master computer to send the problem to many different computers on a network. While the master scheduling code has not been written, the basic building blocks to do this have been coded. The program has been run in parallel on a few computers and the best solution copied manually. After running for a few hours, each computer's best attempt was compared and then the solution was distributed back to the other computers to continue optimizing.

The pachinko technique was evaluated only to a limited extent, but at the present time but the best solution was typically only 5% to 10% better than the worst solution for 10 to 20 global attempts. With thousands of attempts performed over a large network, it is expected that a few would be significantly better than average. The distribution of the percentage of successfully routed paths is expected to be steeply Gaussian. For the 64-path problem, the mean is close to 40 successful paths with a standard deviation of roughly 4 paths. Extrapolating from this data, the chances of an initial guess with 64 of 64 paths routed successfully is 1 in a billion. However, finding a solution with roughly 90% successful paths (56 paths) is just 1 in 32,000 and the chances of finding a 50 path solution is 1 in 160. Therefore, the multi-start algorithm is a good way to start with good solutions but it would require an immense number of hikers to find a perfect solution without the use of some other optimization algorithm.

6.2.5. Optimization algorithms

6.2.5.1. Rip up and reroute algorithms

This technique, borrowed from PCB auto-routing has been implemented with very good success and works well in all but the densest cases. The basic methodology is to select a path that has heretofore been unable to be routed (i.e. – one of the paths that was passed over without success in the first search using the one-at-a-time or the group-at-a-time algorithm.) Once the path has been selected it is once again attempted, however this time, if an intersection occurs it is recorded on the "hitlist". The hitlist is an array that contains an integer for each path. Each time an intersection of the path occurs with an existing path, the number is incremented. Thus, after a hundred or so unsuccessful attempts, the hitlist might look like (for 8 paths):

[0]	0
[1]	16340
[2]	0
[3]	1509
[4]	10
[5]	0
[6]	0
[7]	0

Thus, it can be seen that path #1 has the most number of "hits" and is thus the path that interferes most often with the path that is trying to be routed (in this case path #2). The algorithm would therefore decided to "rip-up" path #1 and attempt to re-route the pair of paths (#1 and #2). In this mode, the algorithm will perform a number of attempts much like the group-at-a-time algorithm. If complete success is not found after some number of local attempts (i.e.- solutions are found that route path #1 or path #2 but not both at the same time), the algorithm will also rip up the next worst offender (in this

case path #3). Again the process of group-at-a-time routing occurs and hopefully a successful solution is found. In most modes of the algorithm, it will keep any solution that is equal to or better than the existing solution. Thus, in the above example, if paths #1 and #3 were successfully routed before, then ripped up, and a solution was found which routed path #2 and #3 successfully, the algorithm would accept that solution.

A few versions of the rip-up and reroute algorithm have been created. Other variants of the rip up and reroute method start with not one, but 2 or 3 unrouted paths and again determine hitlists and paths to be routed up. This variant tends to work well when the two or three paths are in relative proximity or both interfere with the same paths.

Another variant creates a new hitlist for the group-at-a-time routing. That is, in the above example, path #1 was ripped up and paths #1 and #2 were attempted. In this case, for example, the set of paths being attempted may interfere with paths differently than the initial hitlist did and may interfere with path #0 which did not interfere with path #2. However, attempting to route path #1 may sometimes interfere with path #0. Thus, a new hitlist is created, and if the routing of #1 and #2 is unsuccessful, the new hitlist is used to choose the next path to rip up and thus paths #0, #1 and #2 will be attempted next.

A final variant tries to be more specific about which paths are removed. All previous algorithms relied on testing a few hundred paths to find the worst offender, however, one might suppose that on a particular attempt the routing of path #2 was unique and did not interfere with path #1 or #3, but instead only barely interfered with path #4. However, because this was a rare occurrence, it gets lost in the averaging of all the path attempts. Thus, this algorithm finds the least intersecting path geometry in the

first hundred attempts. After a hundred widely varying attempts (a random search with square distributions is used), a fine tuning search occurs. Here, a Gaussian search is performed close to the values of the least intersected path. After two hundred initial attempts (100 coarse and 100 fine), the hitlist is produced for the least intersected path and group-at-a-time routing proceeds. This coarse-fine approach requires the most processing power and takes the longest of any of the rip-up methods but tends to work better on the denser areas.

6.2.5.2. Shove aside algorithm

Most commercial PCB auto-routers are not able to route the densest boards without human intervention at some point. Typically, the best auto-routers might route 90% to 95% of the paths and leave the last few to be routed by a human. For the 3DST project, the tools to route paths in 3D are very difficult for a human to interact with. Perhaps with a 3D viewing tool and virtual reality interface, this might be possible and this is suggested in chapter 8 (Future Work). In the interim, the goal was established to have the 3DST auto router be able to route 100% of the paths.

Using another PCB technique referred to as shove aside, an algorithm was employed to try to get those last few paths to route successfully that were unable to be routed initially or using the rip-up and reroute methods. The technique built on the coarse-fine initial search used in the final variant of the rip-up and reroute method. After finding the least intersecting path, the effective path diameter was changed from .040" to some much larger number (e.g. - .120"). The engorged path now intersected a great number of other paths (assuming a dense routing area). A hitlist is created for the enlarged path and the path numbers are put into a bin. Paths are then selected at random

from the bin and perturbed a small amount. If the pertubation of the path still does not intersect with any other paths (remember, this path in the bin is successfully routed amongst its neighbors), and it reduces its degree of intersection with the enlarged path, the change is implemented. If the pertubation causes the path to intersect other paths or it does not lower the density of paths in the desired volume, the previous state is restored. This process is continued for some time, and at some point, the enlarged path is shrunk down some amount (but not all the way, e.g. – diameter of .080") and the process of lowering the local density is repeated. Further shrinks continue to occur until, the path is ready to be attempted again. At this point the path should have more room in which to route, and multiple attempts are made very close to the initial least intersected path. This process of lowering density is especially slow and tends to make other areas more dense, and thus is only used as the solution approaches 100% success.

6.2.6. Length matching algorithm

The length matching algorithm was set up as steepest descent algorithm that worked independently of the other algorithms. Its typical mode of operation was to be used once all paths had successfully been routed without any intersections. The basic algorithm is:

```
do
  randomly select a path in the universe
    orig ← length of the current selected path
    avg ← average length of all paths in the length match group
    perturb the path without creating any new intersections
    new ← length of the perturbed path
    if (abs(new-avg)<abs(orig-avg))
          accept the path
    continue
```

The algorithm is repeated over and over until some user defined maximum is reached or all paths are length matched to one another to within some user defined specification. The algorithm has shown good success in a number of test cases. It works well because if one of the paths is unable to move (due to an obstruction or some surrounding paths), the other paths in the group will slowly be perturbed toward the stuck path length. It will sometimes fail when two paths in the same group are fixed, however, the algorithm is able to perturb the path outside of the bounds of other paths (i.e. – change its crossovers) such that this is a relatively unlikely event.

Although the length matching algorithm described here is a steepest descent one, a simulated annealing method (described below) may also be used. Part of the energy function would be derived from the degree of length mismatch among groups.

6.2.7. Simulated Annealing and Metropolis algorithm

Simulated annealing has been shown to be an effective means to solve NP problems. The first step is to define an energy function. For this project, the degree of intersection became the chief component of the energy function. The basic algorithm is:

```
do
 randomly select a path in the universe
        e ← energy of the system is total of all paths degree of intersection
        i ← degree of intersections in the path
        if i > 0
                perturb the path based on value of e
                n ← degree of intersection in the new path
                if n < i
                        accept the path
                        continue
                p ← energy of the new perturbed system
                s ← energy scheduler, a random Gaussian number from(-x, y)
                if p < e*(1 + s)
                        accept the path
                        continue
        continue
```

The algorithm uses the energy to determine the strength of the perturbation of the path from its original path. Furthermore, the simulated annealing algorithm always accepts paths that lower the energy, but also sometimes takes paths that do not improve the energy. The times when the energy is allowed to go up is determined by the values of x and y. If x is much larger than y, the mean will be less than zero and hence the number of times that jumps in energy is allowed will be lower. Also note that the size of the jump up allowed is proportional to the current energy in the system, hence when the energy is high, relatively large jumps up are allowed, yet when the energy is low only small jumps up are allowed.

6.3. Test cases

Most of the test routing cases were taken from specific applications, however some test cases were made to demonstrate the power of the multiple routing techniques developed. The first test case created involved nine wires in a simple three by three regular 0.100" grid array.

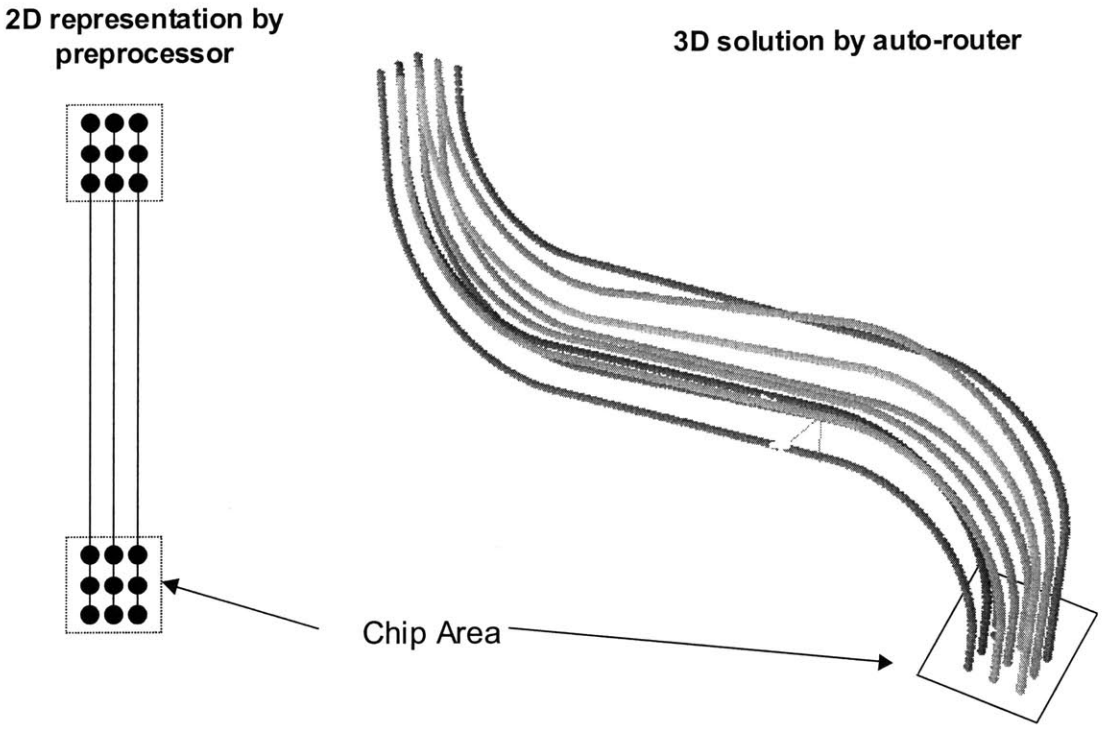

Figure 108 - The first test case. 9 cables with bend constraints and no overlap. Distance between connections is 0.100", effective cable diameter is 0.040"

The first test case took less than 3 seconds to find a solution (much of this is overhead in loading the program) and 2 minutes of perturbation to length match all 9 segments to under 0.001". The next test case tried to make the routing paths more difficult to route by creating the most number of crossovers. The upper-right path in the start "chip" was routed to the lower left corner in the end "chip".

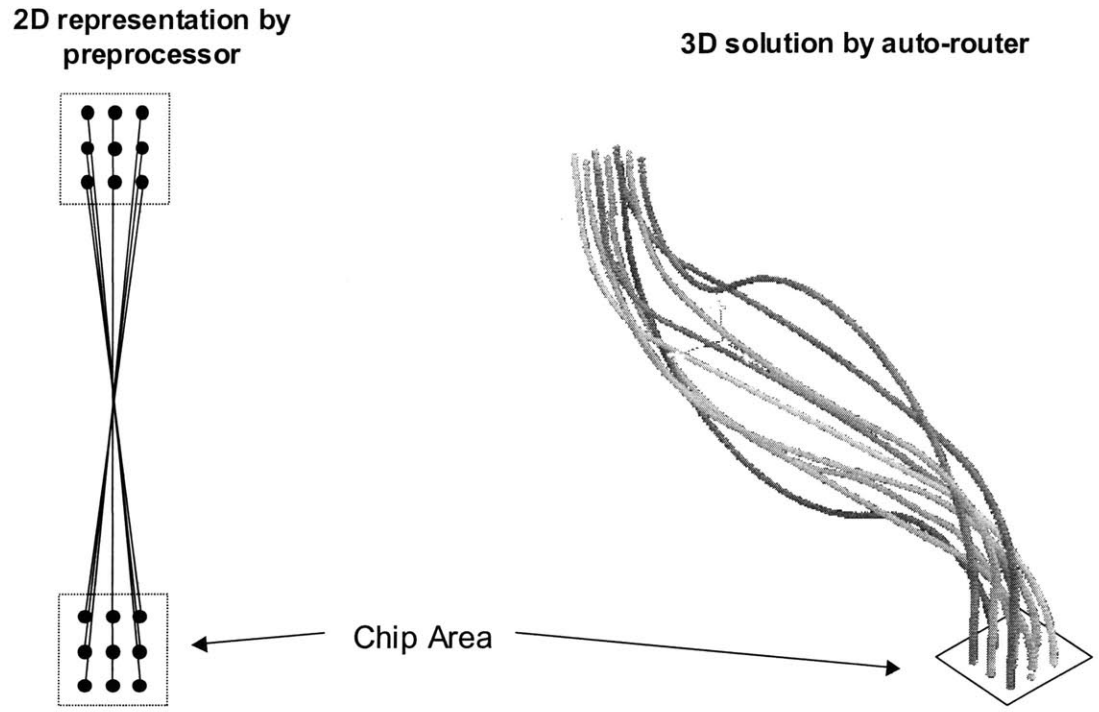

Figure 109 - Test case #2 - 9 wires with maximum cross-over

The test case shown in Figure 109 represents the most difficult routing challenge for these 9 wires. All paths want to cross over in the same volume. The auto-router found a solution in less than 3 seconds (same as before) as the density of this problem is relatively low despite the crossovers.

In the next test case, the number of wires to route was increased from nine to fifteen while the area in which to route remained constant. The distance between wires was decreased from 0.100" to 0.050", and the worst case cross over geometry was maintained. This represents a significant challenge.

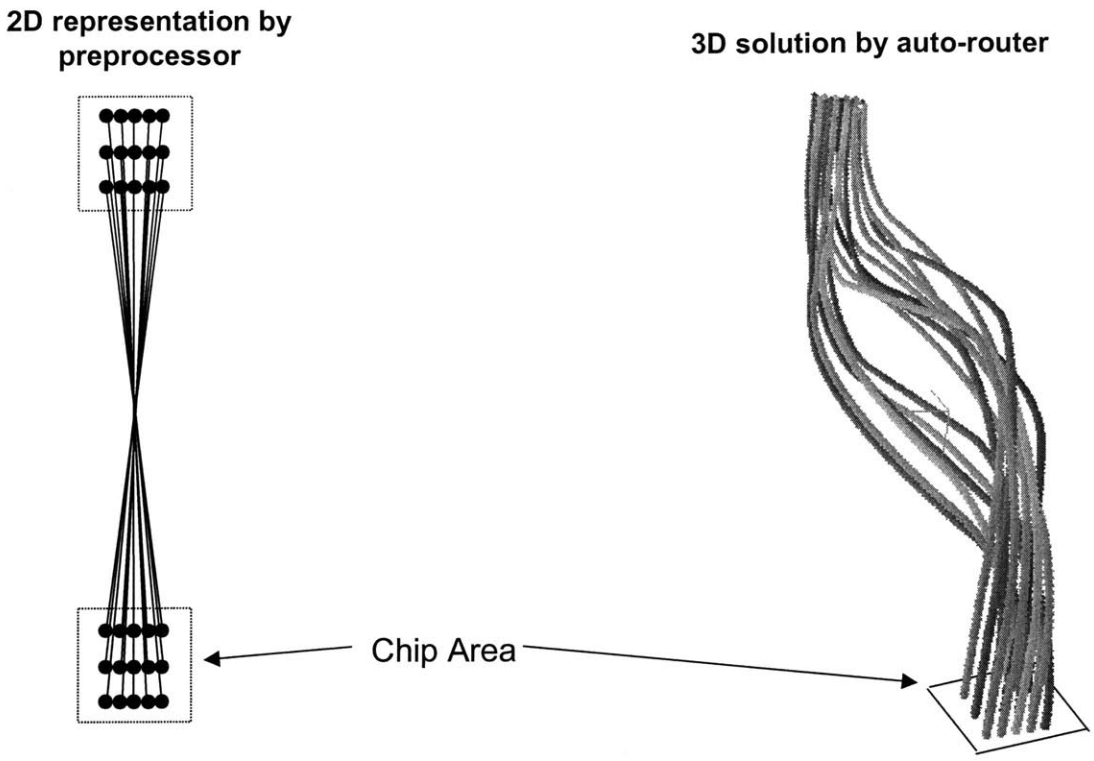

Figure 110 - 15 wires routed in 3D space with maximum crossover.

The auto-router was able to find a solution to this problem in just a few minutes.

6.4. Test cases for ATE applications

The first application that was attempted was 64 paths in a quadrant. This represents the highest density application in which the signals start on a staggered array with a pitch of .120" (maximum packing density configuration for multiple wires in parallel). These were routed in a confined box that would allow mirroring the solution about both the XZ and YZ planes. The wires were routed to a 0.050" square grid array as shown below.

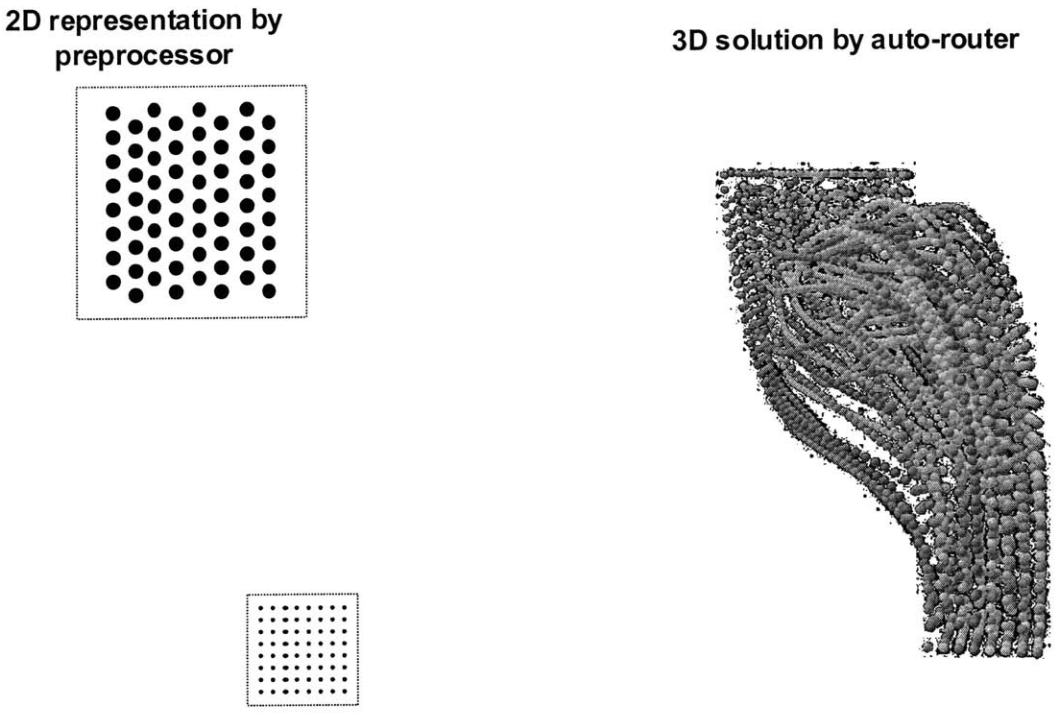

Figure 111 - 64 paths routed in one quadrant.
Picture shown before length matching algorithm started.

The next test was to route 128 signals in a quadrant (or 512 total signals). It took the router about a week to find the solution and length match all paths to within 0.001". The solution before the length-matching algorithm was applied was exported to SolidWorks and then manufactured using stereolithography.

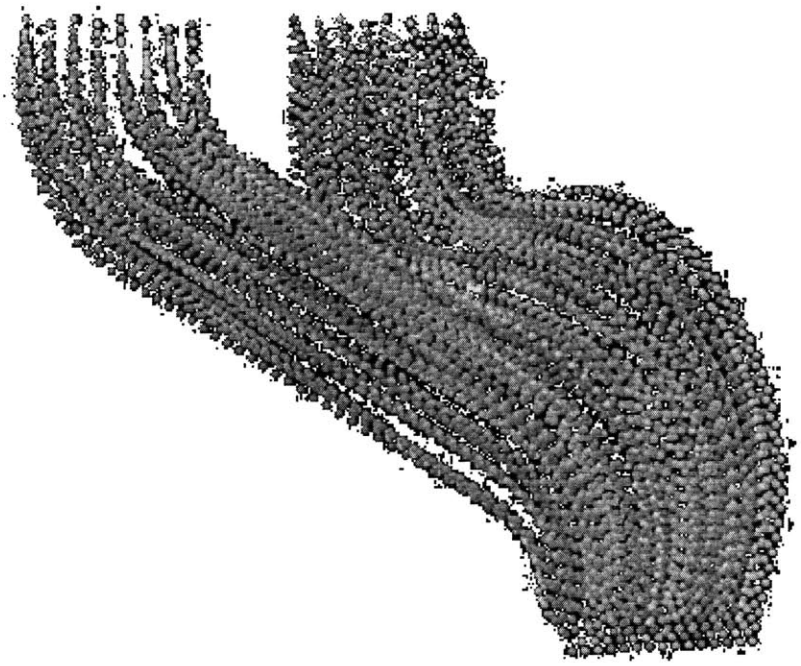

Figure 112 - 128 paths length matched and routed in one quadrant.

The maximum configuration (at this time) was for 1024 signals or 256 paths in a single quadrant. The auto-router took about a week to get the solution to roughly 220 of 256 paths. At this point the rip-up and re-route method was losing steam fast. The simulated annealing and shove aside algorithms were both attempted to continue improving the solution. The simulated anneal method was able to drastically reduce the degree of intersection for this case, but after two weeks had still not found a solution. The cooling schedule used was probably too abrupt and further work is being pursued to

refine the cooling schedule and complete this routing problem. The simulated anneal algorithm was implemented after the rip-up and reroute method had been running for nearly a week. These two algorithms view the solution "goodness" in different ways and thus when the simulated anneal algorithm took over, the solution was in a particularly bad state. The problem is also being attempted with a fresh start, using the simulated anneal algorithm from the start and forgoing the use of the rip-up and reroute method.

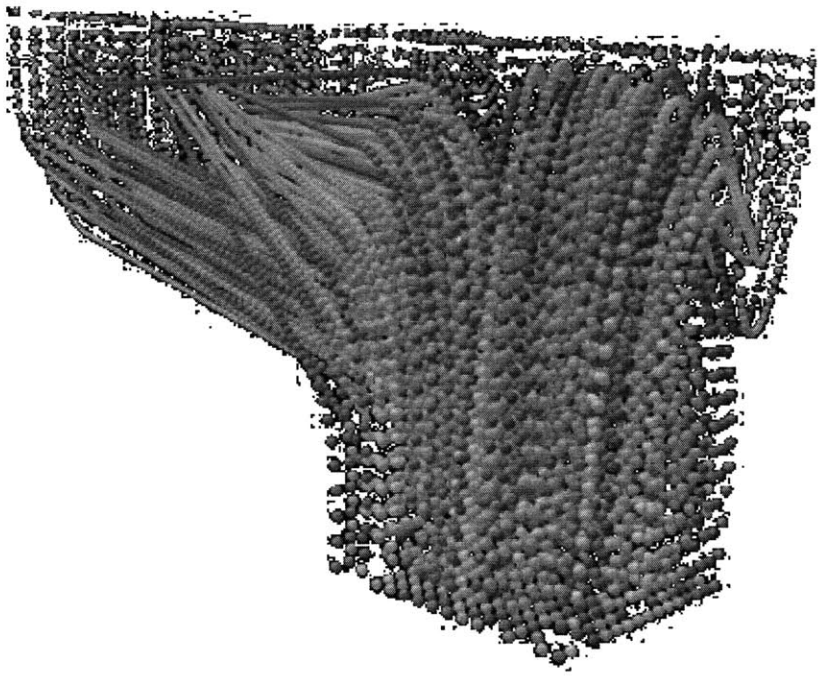

Figure 113 - 256 paths routed in one quadrant

6.5. Other Details of the 3D Router

6.5.1. Path elements – Segment 3D interface

The 3D router was written entirely in Java and made significant use of OOP (Object Oriented Programming). The most basic elements are 3D points and 3D vectors. 3D vectors could be added, scaled, and crossed or dotted with another vector. A vector at

a specific point in space could be represented by a "6D vector" which had a 3D point at its origin and a 3D vector indicating direction. The first and simplest 3D segment created was the line segment. It is parameterized from 0 to 1 inclusive. In 3D, the equation of a line given by:

$$\mathbf{P}(x,y,z) = \mathbf{A}u + \mathbf{B} \tag{6.1}$$

where P is the coordinate of a point on the line segment for all u values from 0 to 1. **A** and **B** are 3D vectors. Setting u=0 gives the 3D point at the start of the segment and u=0.5 gives the 3D point at the midpoint of the segment and u=1 gives the point at the end of the segment. The slope at any given point on the line is found by taking the derivative of Equation (6.1) which is simply:

$$\mathbf{S}(x,y,z) = \mathbf{A} \tag{6.2}$$

The program allows line segments to be created from two end points, from an end point and a vector, and from another existing line segment. The next object was a plane curve which has the following form:

$$\mathbf{P}(x,y,z) = \mathbf{A}u^2 + \mathbf{B}u + \mathbf{C} \tag{6.3}$$

$$\mathbf{S}(x,y,z) = \mathbf{A}u + \mathbf{B} \tag{6.4}$$

This object allows multiple arc types including sections of circles, ellipses and parabolas, however it is somewhat tricky to always keep a constant radius of curvature (if that is what is desired). The plane curve object, as its name implies, is limited to a single 3D plane, but the plane can be in any arbitrary orientation in 3D space. To make construction of a constant radius section easier, a plane circle object was created with the following format:

$$\mathbf{P}(x,y,z) = \mathbf{A}\cos u + \mathbf{B}\cos u + \mathbf{C} \tag{6.5}$$

$$\mathbf{S}(x,y,z) = -\mathbf{A}\sin u + \mathbf{B}\cos u \tag{6.6}$$

where C represents the 3D point at the center of the circle. This equation is for a parameterized full circle. To just get a section of the circle, the u values are scaled. For example, a half-circle would have a u value from 0 to 0.5 internally, but this arc is still represented externally as having values from 0 to 1.

With these simple elements, almost any path can be created. The paths use a limited number of segments to ease the path search space. The paths were either 3 or 5 segment paths with 2 and 4 degrees of freedom, respectively. For a 3 segment path, there are only two degrees of freedom, the start and end radii, because the line that connects the two arcs must be tangent to both. The three segment is created from the two start and end 6D vectors and the values of the start and end radii. This is all the information required to created the 3 segment spline.

The first step is to find the beeline vector from the start point to the end point. Performing two subsequent cross products gets the vector that points along the beeline vector and in the plane normal to the start vector. This vector points to the centerpoint of the first arc. Scaling that vector to the magnitude of the radius and adding it to the start position gets the exact position of the centerpoint of the arc. The process is repeated for the end arc. Two 3D arc segments are formed and the line segment tangent to both arcs is found. This is done with a binary search tree algorithm, shown in Figure 114, that finds the line with the minimum error.

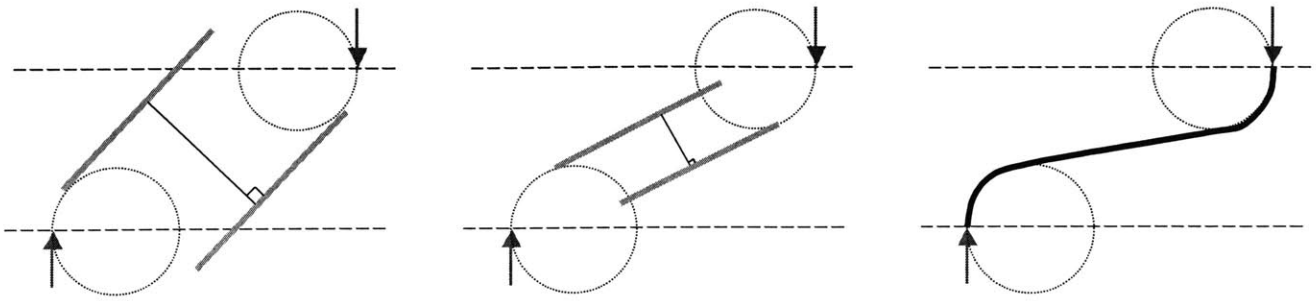

Figure 114 - The binary search algorithm to find the tangent segment

A five segment path has an added two degrees of freedom since the start and end heights can be varied as well.

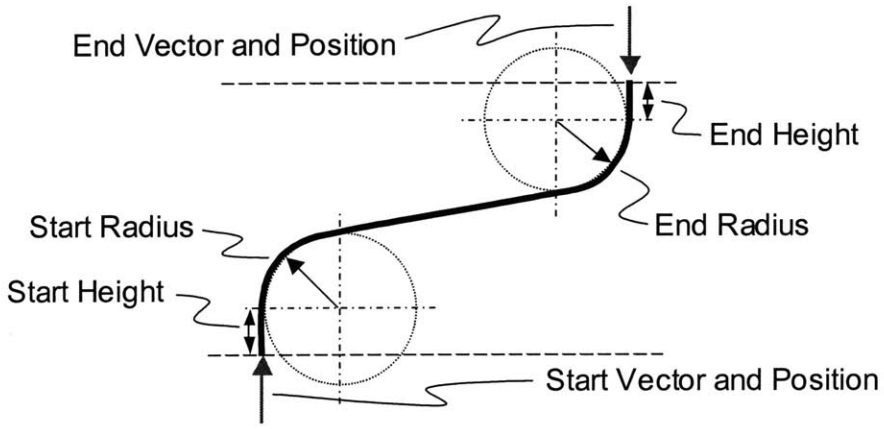

Figure 115 - A five-segment path with four degrees of freedom

An additional degree of freedom can be added to both the 3 and 5 segment paths by allowing a rotation angle.

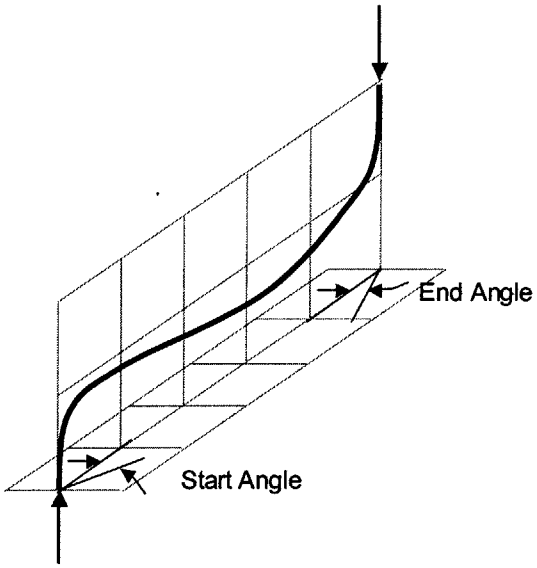

Figure 116 - A 5 segment path with an additional degree of freedom. Start angle equals end angle.

A further degree of freedom can be added to by allowing the start and end angles to vary independently. Both the out-of-plane segments use a space curve. A space curve has the following form:

$$\mathbf{P}(x,y,z) = \mathbf{A}u^3 + \mathrm{B}u^2 + \mathbf{C}u + \mathbf{D} \tag{6.7}$$

$$\mathbf{S}(x,y,z) = \mathbf{A}u^2 + \mathrm{B}u + \mathbf{C} \tag{6.8}$$

6.5.2. Determining curvature

The curvature of a line segment is zero, and the curvature of a plane circle is simply one divided by the radius. The curvature at all points along the line or curve is the same because the radius does not change.

$$\kappa = \left(\frac{1}{R}\right) \tag{6.9}$$

The trick for space curves is to determine what the radius is at any given point. For this we find the 3 orthogonal vectors that form a Frenet frame [25]. They are:

$$\mathbf{T} = \mathbf{P}'(u) \qquad \text{(Tangent vector)} \tag{6.10}$$

$$\mathbf{N} = \frac{\mathbf{P}''(u)}{\left|\mathbf{P}''(u)\right|} \qquad \text{(Principal normal vector)} \tag{6.11}$$

$$\mathbf{B} = \mathbf{v}_1 \times \mathbf{v}_2 \qquad \text{(Binormal vector)} \tag{6.12}$$

Using this framework we can find the curvature at a point using the Frenet-Serret formulas [25]:

$$\mathbf{T}' = \kappa \mathbf{T} \tag{6.13}$$

$$\mathbf{N}' = -\kappa \mathbf{T} + \tau \mathbf{N} \tag{6.14}$$

$$\mathbf{B}' = -\tau \mathbf{B} \tag{6.15}$$

where κ is the curvature and τ is the torsion. The torsion is a measure of the rate of deviation from the osculating plane. The osculating plane is the plane which contains the **T** and **N** vectors. Thus, a curve that stays entirely within a single plane has a torsion of zero.

6.5.3. Segment functions

Each segment object has a number of standard calls that allow all segments to be treated in a similar fashion. The common functions are:

getPoint(u)	returns a 3D point
getSlope(u)	returns a 3D vector
getCurvature(u)	returns a curvature at that point
getLength()	returns length of segment
trim(u_1,u_2)	trims the segment from u_1 to u_2

6.6. Overall program structure

The most basic elements are the 3D point and the 3D vector. From these elements, the path segments were created. Moving up a level of abstraction, paths were created and searched for using the three types of path search algorithms. Finally, the solution searching algorithms utilized the path search algorithms to find global solutions to a problem.

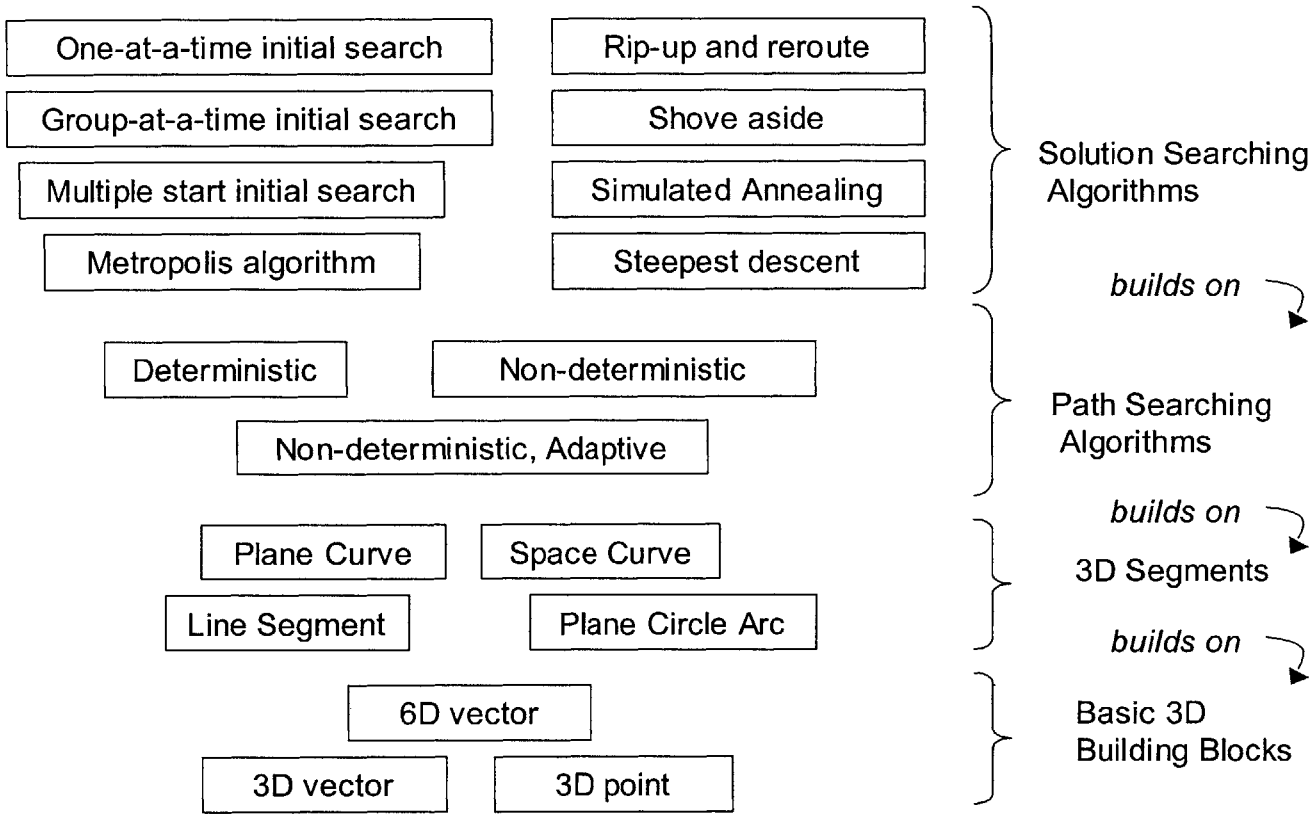

Figure 117 - Outline of the 3D auto-router

6.7. Summary

Multiple algorithms have been created to help find solutions to this NP problem. Most of the algorithms show good success in limited areas, and poor success or very slow performance in others. By using each algorithm at the proper stages in the routing problem, the speed with which a solution is found can be significantly increased. The preprocessor heuristic has been shown to increase the number of good paths found in the initial attempts and the divide and conquer initial search typically yields the best results. Rip up and rerouting is used extensively to get the solution to nearly complete, while the shove aside algorithm is used only to squeeze in the last few paths. The simulated annealing algorithm has been implemented with some success although it is typically very time consuming and in many cases the rip-up and reroute methods find solutions faster than the simulated annealing does. The ability to automatically length match paths allows other pieces of the ATE solution to be less expensive and/or more accurate. A simple check of insertion force is done to verify the force does not exceed some user-defined limit. In the future, more complicated algorithms could check the insertion force at each stage and use the insertion force as part of the energy function and search for paths with minimum insertion force.

The difficulty of routing 3D smooth paths by hand absolutely necessitates the use of a software auto-router. The ability of the program to find fast solutions to simple problems is especially encouraging. This is one of the first programs to try to solve such an intricate routing problem in 3D space and it is hoped that more research in this area will lead to faster and more successful algorithms. Some areas of future work are

discussed in Chapter 8. One area of particular merit is the use of grid computing to implement hundreds or thousands of simultaneous solutions on the search space in a very short period of time.

Chapter 7 – Detail Design & Manufacture

7.1. The Need

The need for a new technology to replace the printed circuit board should be readily apparent. The use of a true coaxial cable allows for higher speeds with lower attenuation, lower crosstalk and the elimination of most discontinuities. No process of build-up by additive manufacturing techniques has been able to successful recreate the performance of semi-rigid coaxial cable and no manufacturing methods for wiring semi-rigid coaxial cable from one surface to another has been publicly disclosed.

7.2. Conceptual Design

The 3DST holds the promise of using semi-rigid coaxial wires for dense point to point wiring. New applications could greatly benefit from the uses of a combination of technologies incorporated by the 3DST tunnels. For example, a single SLA block could combine coaxial cables, fiber optics and cooling channels in a tightly integrated package.

7.2.1. The initial concept

Once the need was established for a better way to get signals to the DUT, the idea of using semi-rigid cables to replace the PCB was clear. The difficulty was there was no way to manufacture such a micro scale cable array of cables. The idea of using SLA with internal tunnels to guide the cables was a unique method to automate the assembly of such an array of cables.

7.2.2. Alternate #1 - Pull cables

One of the first thoughts was that the wires might get stuck on insertion and so if they could be pulled rather than pushed, this problem could be avoided. While this seems attractive at first, the problem occurs with volume manufacturing. A typical block might contain 50 to 250 wires and the time spent inserting the wires will impact the cost of the assembly. The faster wires can be inserted, the cheaper the assembly. The process for installing a wire to be pulled through would first involve pushing a thinner (less stiff) wire down the tunnel. Once this was accomplished, the thin wire would need to be affixed to the coaxial wire. Since density is very important, the method by which the thin wire is affixed to the coaxial wire should not require a greater diameter tunnel than is required for just the coaxial wire. Finally, once securely attached, the wire would be drawn through the tunnel. Once the coaxial cable had been successfully snaked through the tunnel, the first wire would be cut off and the process would be repeated. This process might be acceptable for low volumes or for boards with only a small number of signals. The true power of the 3DST is the ability to route very dense arrays of signals in an arbitrary pattern, but the pulling of wires would jeopardize the density and manufacturability of the assembly.

7.2.3. Alternate #2 - Pre-bend cables

One solution, suggested by many colleagues, was to pre-bend the wires, insert them into plates and then simply fill the gap with an epoxy or other filler material. This would completely avoid the difficulty of inserting wires or creating a stereolithography part, but it also creates a daunting challenge. That is, how can a robot or even a highly

skilled person be expected to route hundreds of overlapping wires to their proper destinations and terminate them to be length matched to within a few thousandths of an inch? For some of the most-demanding ATE applications, this is being done by hand using small wire assemblies that have been carefully length matched and terminated. The cost per line (length matched to another) for just a few inches of cable is roughly fifty dollars. The ability of a human assembler to make dense arrays of cables in a relatively large volume is severely limited by the skill of the assembler and the size of his or her hands (or tools). It is simply not feasible to create thousands of hand wired densely cabled arrays. But could a robot do it? The robot would need to possess a dexterity beyond that of most humans and be able to be programmed for each routing case. The robot would need to determine which wires it would route first so that it did not get too congested and block access to areas that still needed to be filled with more wires. The difficulty designing such a program and creating such a dexterous robot seems infeasible for many years to come.

7.2.4. Alternate #3 - 3D print with multiple materials

As was mentioned in Chapter 2 prior art, people have attempted to create coaxial structures using build-up processes. It would also be reasonable to assume that in the future, additive manufacturing would be able to print multiple materials into the same block. A simple solution which avoids the insertion problem is to print copper shields and cores and Teflon dielectrics directly. There are, unfortunately, a number of issues which were mentioned in Chapter 4. Assuming such a material could be found, the second more daunting problem arises. That is, the surface finish of any small part created by 3D printing is usually pixilated (or in little chunks). While this does not pose much of

an issue for the guiding tunnel, it poses a very big problem when skin effects and impedance control are considered. Surely, as the processes improve, the spot sizes will decrease and thus the geometry can be created to such a fine level that will eliminate this argument, however, unless millions of deposition heads are acting in unison, the build up time to create such a macro scale object with micro-scale features is likely to be so costly as to eliminate this as a possible option for all but the smallest of devices.

7.2.5. Alternate #4 -Multi-wire (5 wire vs. coaxial)

The first concept to achieve a high speed electrical connection that was better than a PCB was to insert 5 wires to form a single 5 wire 50 ohm signal path. In this scenario, the SLA material would be used to guide the single wires (with no dielectric or shield) and the four outer wires would form the ground return. The SLA material would act as the dielectric in this concept. While this has some intriguing possibilities, the SLA material is not an ideal dielectric and the 5 wire structure is not the ideal structure for high speed signals. Finally, the tolerance control on the spacing between the 4 wires and the single wire is not especially good. It is easier for the SLA process, at this time due to the spot size limitations, to create a single 0.040 diameter tunnel than to create five 0.008" diameter tunnels. The major benefit of the 5 wire structure is that it could allow tapering of the coaxial signal on a single line and further, greatly reduce the forces of insertion when compared to coaxial cable. However, the negative electrical effects of the five wire design make the insertion of coaxial wire far better for high speed electrical signals.

Of all these options, inserting coaxial wires in tunnels created by SLA offered the best near term solution. It's major advantage was that the coaxial wire could be

constructed with a well controlled process and then used in the 3DST, rather than relying on the inaccuracies of the additive manufacturing process.

7.3. Embodiment design

With the concept chosen, the details of each manufacturing step needed to be addressed. These steps are detailed in this section.

7.3.1. Use routing software to determine paths to follow

As has been described in Chapter 6, the routing software takes a netlist (a list of the start and end points and vectors for each path) along with details concerning which paths are to be length matched and routes the entire list of paths without intersections. As this is a NP problem, optimum solutions are not guaranteed, but with human intervention and potential changes to the inputs, a near optimum solution can be found for most problems.

7.3.2. Export the data to a CAD package and add any other features

Once the auto-router program has found a successful solution to the problem, the data must be exported to a format that can be given to a stereolithography machine. Because some post-processing may be necessary, it was desired to export the file to a CAD program which could then add other features, such as chamfers, rounded edges, additional holes for screws or any other openings. The process of exporting the parametric splines to SolidWorks was automated using a VBA script. Due to the immense amount of processing required, it typically takes SolidWorks several hours to construct the 3D tunnels in a solid block of material. Luckily, the use of simplified geometry in the 3D router allows for much faster creation and checking for intersections

than a true swept spline. Finally, if mirror or rotational symmetry exists on the part, the swept paths can be patterned using the CAD package features.

Figure 118 - The 512 block shown routed in SolidWorks.
Note the four-fold symmetry allows the 3D router to solve the simpler case of just 128 wires.

7.3.3. Export CAD file to .stl file and send to SLA machine

Once the part has been created in SolidWorks, the built-in preprocessor converts the file into a triangular mesh .stl file. This process (depending on complexity) can take more than 24 hours on the fastest desktop computers today. For reference, most simple parts created for prototyping take less than a minute to convert to a .stl format.

7.3.4. Create SLA block in SLA machine

The next step in the process, is to build the part in a stereolithography machine. For the 512 path block that was created, a 3D Systems Viper was used in its high resolution mode. For the stereolithography machine, the spot size is best focused and smallest directly over the center of the mirror in the center of the build tank. As the beam is scanned across the bath, the angle of the beam makes the spot more elliptical and thus the resolution is reduced somewhat. The high resolution mode places the part in the center of the bath, uses the smallest spot size (0.003") and the smallest step size (0.002"). Because overhangs occur on every tunnel, care must be taken to ensure that overcuring of layers beneath are not accidentally cured.

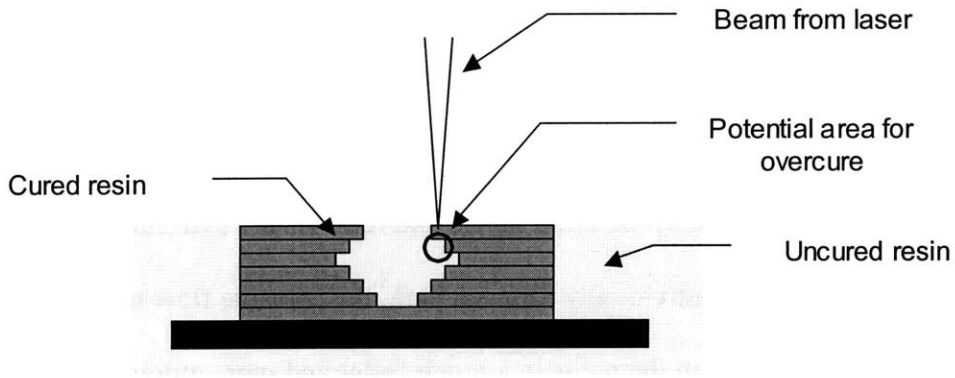

Figure 119 - Possible overcure area when building bridges in the SLA process

Building a bridge over uncured resin is only possible by building a little longer cantilever (from both sides) on each successive build layer. Overcuring occurs because the laser penetrates and cures not only the layer it is currently working on, but some of the laser's power permeates to lower layers. If those layers are uncured they could

partially or completely cure. The software program that interprets the .stl file has some ability to compensate for the overcuring during bridge building, but it typically requires a bit of hand tuning by building a few parts and tweaking the dials of the program to get good results.

7.3.5. Clean and post-cure block

Once the part is finished in the SLA machine, the resin is still not fully cured. Exposure to sun or UV rays will cure the part further and this process is expedited in a post cure oven. However, before the part is placed in the oven, any uncured resin in the SLA tunnels must be extricated or the liquid resin will cure and block the tunnel paths. Compressed air is used to blow out all the resin, and it should be noted that the smaller the tunnel diameter, the greater the surface tension forces and the more difficult it becomes to get the uncured resin out of the tunnels.

7.3.6. Potential finishing steps – abrasive machining

As was mentioned in Chapter 4, a finishing step is sometimes employed to remove the staircase effect of the build layers and remove any extremities in the tunnel. Although this was done individually for each path, the abrasive flow machining could easily be adapted to smooth the paths in a much faster and more automated way.

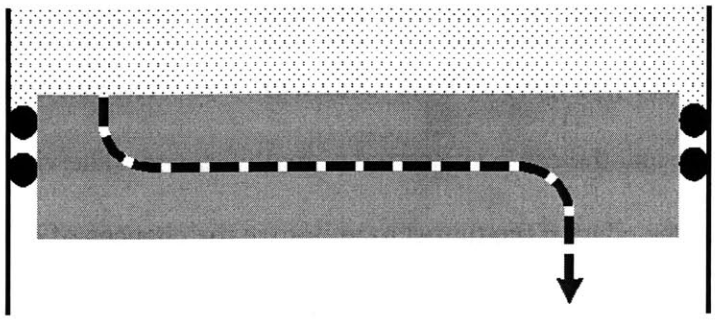

Figure 120 - A schematic view of abrasive flow machining of internal tunnels

The figure above shows a single tunnel with abrasive fluid flowing through it. The ability of this process to process multiple paths in parallel make it particularly attractive. After processing, some type of cleanse operation should be performed to rid the tunnel of any lingering abrasive fluid.

7.3.7. Affix top and bottom plates with epoxy

Once the SLA block has been produced, metal plates are adhesively bonded to the sides that cables exit. The plates have holes for every cable exit with a minimal amount of clearance. The holes in the metal plates can be accurately manufactured with tight positional tolerance and tight control on the diameter by a number of methods. These plates will serve to accurately align the 3DST to the mating components in the ATE system.

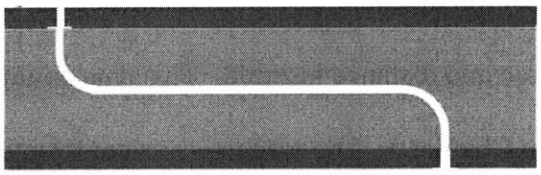

Figure 121 - A schematic of the SLA block with plates affixed to top and bottom

7.3.8. Insert wires

Once the plates have been affixed, the semi-rigid coaxial wires must be inserted. In the early stages this was done by hand using a pin vise. The collet on the pin vise clamps to the cable and the cable is inserted a small distance. The vise must be clamped relatively close to the edge of the tunnel to minimize the chances of buckling as the beam is inserted. This necessitates a repetitive cycle of clamping, pushing, and unclamping.

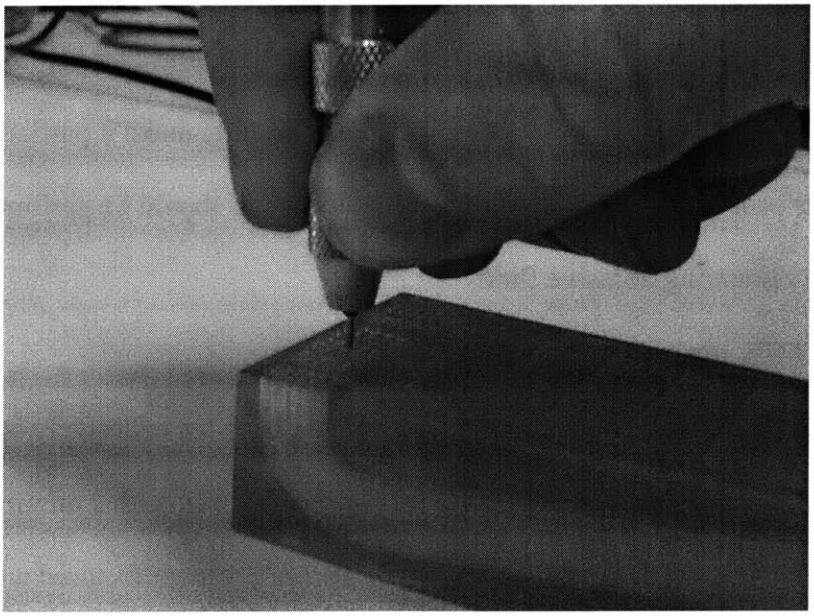

Figure 122 - A picture of a coaxial cable being inserted into a test SLA block

A faster insertion method was sought and a continuous roll drive system was designed. The purpose of the machine was to drive the coaxial cable into the tunnel while measuring the force and distance inserted. This data could then be used to validate the models developed in Chapter 5. The machine was constructed with 3 friction wheels on one side and 3 guidance wheels on the opposite side. The guide wheels are mounted

on springs to apply a large normal force to the cable and the drive wheels to ensure there is enough friction to drive the cable forward through the tunnel.

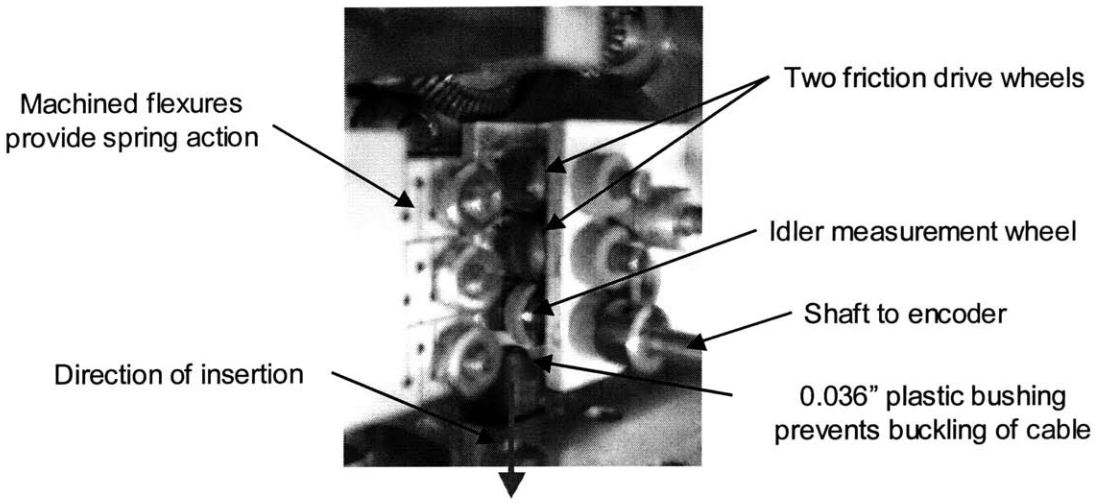

Figure 123 - Close-up of friction roller drive system

7.3.9. Solder wires in place

Once the wires are in place, they can be soldered to the metal plates. This connects all the ground shields together and provides a solid ground plane for interposers to contact. If this is not desired, or some wires need to be isolated, they can simply be affixed with non-conductive epoxy.

7.3.10. Mill surfaces flat

A flat stiff surface is desired for connection to the compliant interposers at either end. To accomplish this, after affixing the wires, both surfaces are milled flat. If very good planarity is desired, a grinding or light finishing of the entire plate can be done.

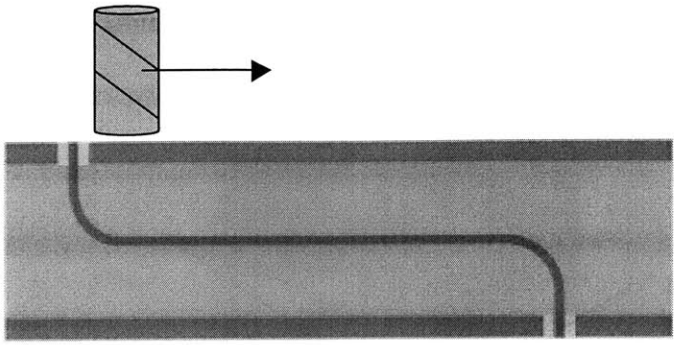

Figure 124 - Milling the cables and plates flat

The solder and milling operations were carried through on a small test block as shown below.

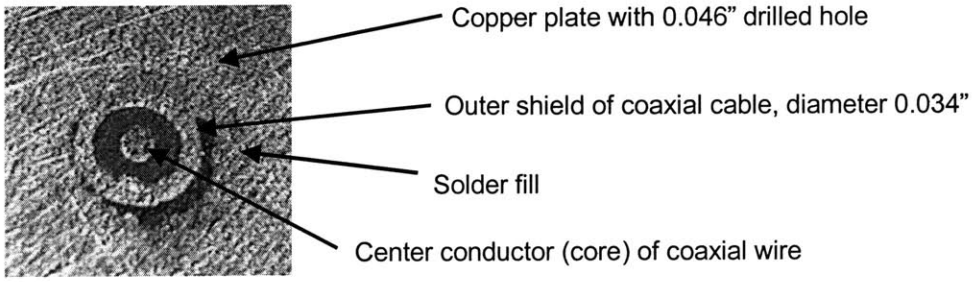

Figure 125 - 0.034" Coaxial wire after insertion in tortous tunnel and mill operation

7.3.11. Nickel and gold plate

On PCBs and other connectors, the surfaces to be contacted are typically plated with gold over nickel. Although this process has not been carried out on a 3D routed test block, machined blocks with semi-rigid cables soldered into them were successfully plated in this way. There was no routing done on these blocks, but the cables were inserted past flush, then soldered and milled flat.

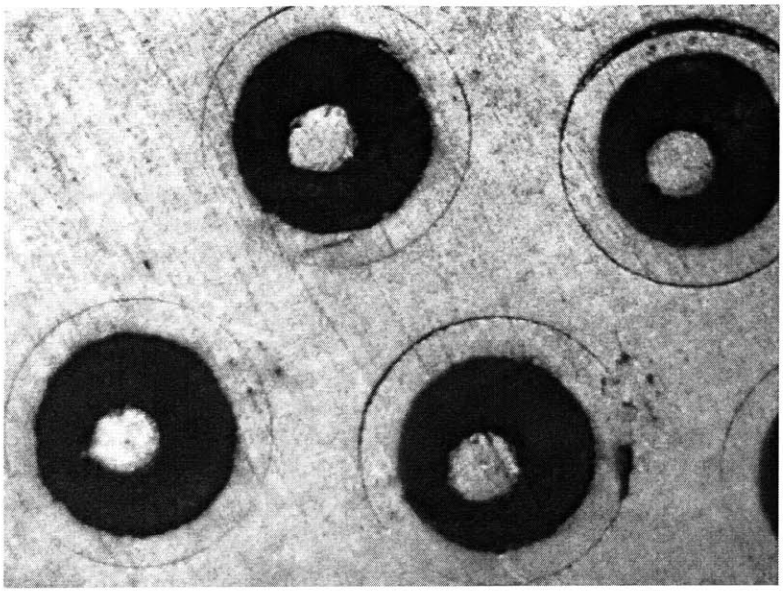

Figure 126 - Semi-rigid coaxial wire milled flat, then plated.

7.4. Prototype Fabrication

Four test blocks have been created to test the validity of the concept, to measure forces of insertion and to test the capabilities of the auto-router. These are shown below.

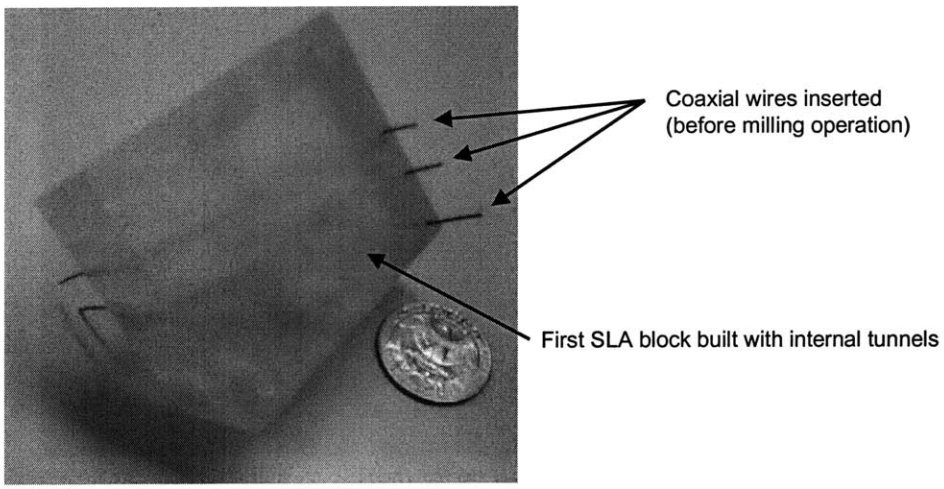

Figure 127 - Picture of SLA test block before machining

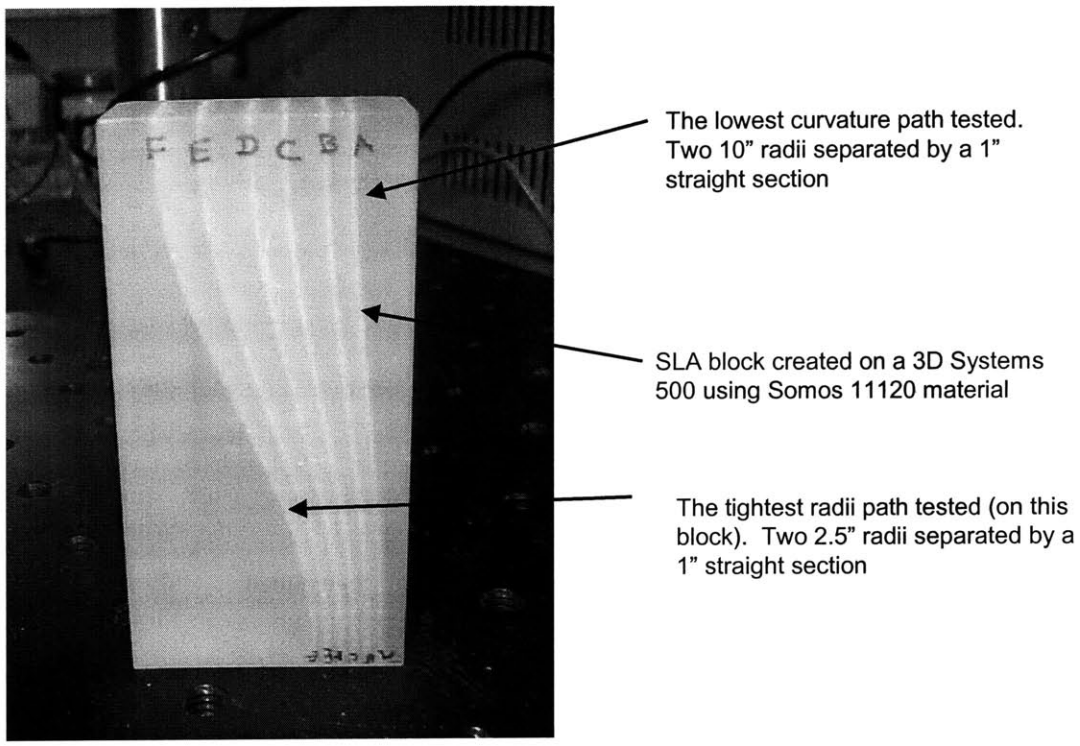

Figure 128 - The large radius test block

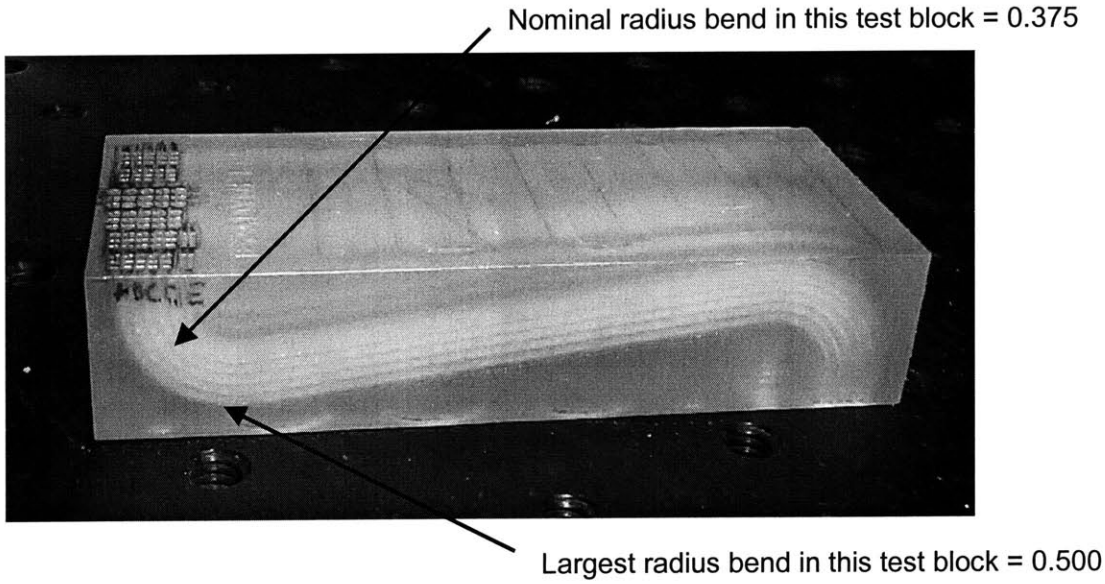

Figure 129 - The small radius test block

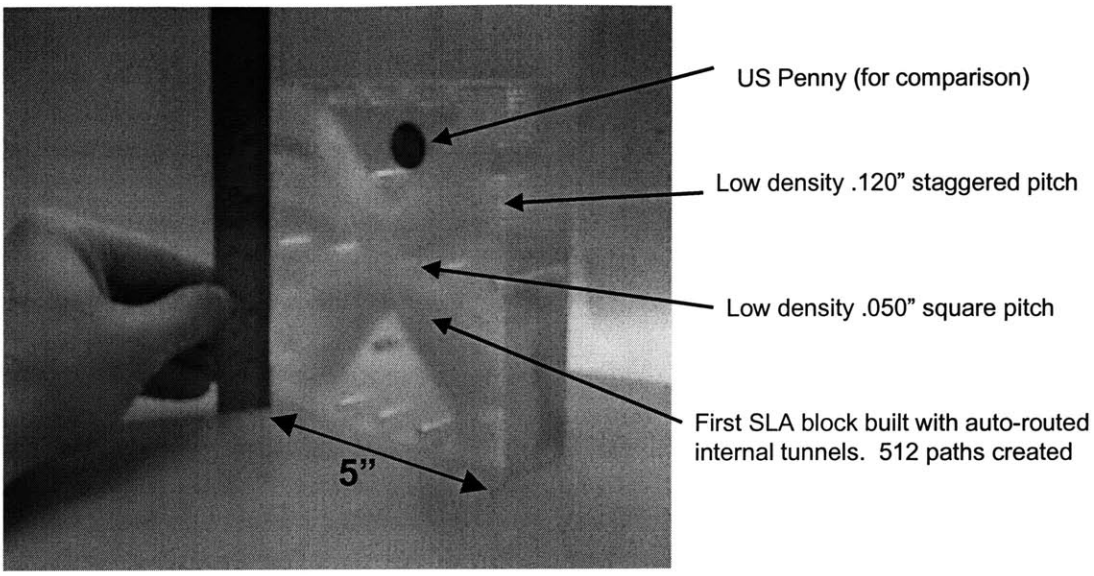

Figure 130 - The 512 auto-routed test block

7.5. Summary

Each development step in the construction of the 3DST has been investigated. The ability to automatically generate 3D non-intersecting, length-matched tunnels in a confined volume has been demonstrated with the auto-router. The ability to insert wires by hand or automatically has also been proven. While there is still significant development required to turn this proof-of-concept work into a well developed manufacturing process, many of the major roadblocks have been cleared.

Chapter 8 – Future Work and Applications

8.1. Future work – Software

8.1.1. Use of grid computing

The 3D router software has been set up to enable grid computing of the problem in many aspects, but it has yet to be implemented. A master computer could receive a problem and send out slightly different instructions to many different computers to route the paths. At some point, the computers would report back to the master computer and the master would potentially take some action. One such action would be to get the few best solutions and have the grid restart the problem with the those solutions. The use of hundreds of computers each working to find solutions will inevitably speed up the search for a near optimum solution. It may also be possible to divide the problem and send pieces of the problem to multiple different computers. The best way to do this would be the use of a well known PCB routing technique called global channel routing.

8.1.2. Global channel routing

Global routing attempts to find multiple paths that travel together and then route larger channels that contain multiple paths. Once the global channels have been successfully routed, each channel that contains a few paths is routed in the volume constrained by the channel. The benefit of this approach is that the global routing problem becomes much more tractable as the number of degrees of freedom has been dramatically reduced. Furthermore, the internal detailed routing of each path in the

channels will typically contain only a few paths and hence the degrees of freedom of the solution space is greatly reduced, which speeds searching. Implementing this algorithm in the case of 3D freeform paths is relatively challenging. Since the density of paths at one end is typically not the same as the other end, the channel will need to taper along its length. Furthermore, once the global channel has been routed, this does not guarantee a solution exists for the detailed routing. An algorithm will likely need to search for a global channel routing, then attempt to create all the detailed routings and if some are not possible, go back and adjust the channel sizes and try again.

8.1.3. Human intervention

Most commercial PCB auto-router programs are considered successful when they route 95% of the available paths. Most auto-routers require some human intervention to route the last few difficult paths or to help direct the algorithms in some way. It is exceedingly difficult for humans to visualize a 3D freeform routing problem on a 2D monitor. A special program that allows a human user to see the intersections or length match issues and interactively drag the spline would be very useful. Additionally, the use of virtual reality or other 3D visualization hardware would assist the human router. Even if the human could not get the path perfect, if the new position of the path was closer to a solution, the simulated annealing algorithm could start from there.

8.1.4. Polynomial time solution

The problem, as stated, is a NP problem and thus the algorithms to solve it are not guaranteed to find a solution, even if it exists. Work has been done in 2D that shows if an initial rough sketch is given, a solution can be proven to exist or not exist and the solution if it exists can be found in polynomial time [42] [44]. This work does not

account for bend radius constraints which will makes it more difficult to prove the existence of a solution. However, application of this work to 3D with bend constraints could lead to a much more efficient solution method. The creation of a rough sketch would need to be done with another computer algorithm, but a more advanced preprocessor should be able to make some good guesses at rough sketches which could then be tested.

Multiple algorithms exist that can be leveraged to solve this problem and it is hoped that as more applications develop, increased research in the area will lead to new algorithms and heuristics for faster and more optimal solutions.

8.2. Future work – Mechanical Modeling

8.2.1. Continuous flow curvature equations

The segmented curvature equations allow quick and easy calculation of the curvature of the beam at each and every segment, however, inaccuracies occur for short segments, and low curvature, large diameter paths. A model which predicts the curvature of the beam in a more contiguous fashion would allow more accurate prediction of the insertion force. This work could leverage previous work done with splines that try to find minimum energy fits between control points. It should be possible to find the proper minimum curvature path of an elastic plastic beam constrained by a tunnel.

8.2.2. More accurate friction measurements

The friction force between the coaxial cable and the SLA material was calculated by a simple pull test on the outside of the test blocks. This test was not inside a tunnel and had low contact pressure (nearly line contact). It was found that the friction coefficient under these conditions was roughly 0.3, but the analytical models matched up

much better to experimental values with a friction coefficient closer to 0.7. Testing to determine the effect of higher contact pressures inside a tunnel may validate the use of the higher friction coefficient. If the friction force cannot be justified, the model may need to include some effects (e.g. surface roughness) that have been neglected to make the model more accurately predict experimental values.

8.2.3. Account for other neglected effects mentioned in Chapter 5

In Chapter 5, many neglected effects were mentioned that could be incorporated into a more sophisticated model. A first order calculation of the compression effects has shown them to be negligible for the paths considered but the shear forces for low curvature paths may be more significant. Other effects, such as gravity, which was not considered, will be a factor for many applications on a larger scale, such as wellbore drilling.

8.2.4. Further mechanical testing

The experimental testing was restricted to coaxial wires of 0.034 diameter and further testing of different size coaxial wires and other simpler structures should be done to further validate the model or find shortfalls. To this end, precisely formed tunnels that do not use the SLA process should be created to eliminate the effects of non-smooth walls. This could be accomplished by bending hollow tubing on a precision fixture.

8.2.5. Non-round wires

The use of non-round wires represents an interesting routing challenge as well as development of modified insertion force models. In particular, routing flat cable in anything other than a plane would try to utilize a twisted path, in which case, the torsion effects of the beam in a tunnel would need to be included in the model.

8.3. Future Applications

8.3.1. Other 3D additive processes

As was mentioned in Chapter 4, the use of SGC would be amenable to larger scale production of parts and the ability to create overhangs, make this a technology to explore. Rapid freeze prototyping, which uses ice as structural material, would also allow the insertion of wires. Once the wires were affixed in the plates, the ice could be melted and replaced with an epoxy. This would likely result in a considerable cost savings.

8.3.2. Other things to insert

While 0.034" coaxial wires have been focused on in this project, other circular and non-circular objects can be inserted into tunnels. Hybrids blocks that contain multiple types of wires could easily be imagined. Heat pipes could be inserted as well as solid conductors. Hollow pipes for transmitting gases or liquids could be used for cooling, transport or to apply pressure. Flat cables and ribbon cables could also be inserted although the SGC process (Chapter 4) would be preferred for creating large bridges required for flat cable. Additionally, fiber optic cable could be installed by driving it in with friction wheels (as described) or by viscous drag of pressurized air flowing around the fiber (as in used in industry). Push-pull mechanical rods, flexible cables and miniature flexible shafts could also be installed. A mechanical "backplane" of cables, shaft couplings and pressurized fluids might be useful in MEMS applications or other complicated mechanical contrivances.

8.3.3. Other applications

Because a number of different "wires" can be installed into a single block, there are a number of applications for this invention. Currently, there is no optical backplane manufacturing technology that is analogous to the PCB industry. This invention could be leveraged to provide a simple, cost-effective method for creating optical backplanes. Next generation PCB motherboards are limited by bus speeds allowed on PCBs. A miniature SLA hypercube, might allow high-speed communications between memory, CPU and other drivers. The ability to combine coaxial cables, power cables, fiber optics and cooling channels on a single block may allow vastly improved computer performance. Fluidic backplanes could also be created and the tube material can be choosen individually for each path. MEMS fluid applications would also benefit from this technology as one of the major difficulties in testing and using MEMS fluid devices is getting the macro-scale connectors to interface to the microchannels. The 3DST could provide a unique tool to do just that. Only a few applications have been described, but the flexibility of this solution allows for a great number of unique applications.

Chapter 9 - Conclusions

9.1. Fundamental Contributions

There are two major academic contributions of this thesis. First, models were developed to describe the insertion force for a beam in a tortuous tunnel (chapter 5). Second, 3D routing algorithms are presented in chapter 6 that build on existing literature from PCB and VLSI routing techniques and global minimization algorithms.

The models developed for insertion force correlate reasonably well to experimental values and were shown to be in good agreement (roughly within 20%) for radius of tunnel to beam diameter ratios of 200:1 to 10:1 (pages 169 to 177). Solutions for perfectly elastic and rigid plastic beams are shown for 3D paths with no clearance. The elastic model uses a very elegant and simple equation ($F_{insert} = EI\kappa^2$) to predict the insertion force. The beauty of the equation is it depends only on the curvature at the tip of the beam as it is inserted along the path. When the curvature is zero, the insertion force is zero; all work done is recovered. This is not the case for the elastic-plastic model that is developed. To properly deal with the intricacies of elastic plastic behavior of curved beams, a numerical solution is needed. However, the simplified elastic plastic model developed in section 5.3.1 gives a good approximation. When friction is included without any clearance between beam and tunnel, infinite insertion forces are predicted. Taking into account the clearance between the wall, the friction forces can be accounted

for without encountering infinite forces as shown in section 5.3.4. The model is used to predict the forces for beam insertion and these predictions are tested against experimental data in section 5.4. The predictions fall short in some areas, and the shortcomings are discussed in detail in section 5.4 and 8.2. One of the most important assumptions made was the beam has constant curvature in a given segment. For insertion problems with little to no clearance, this is a good assumption but as the clearances become large (twice the beam diameter) the predictions fall short. A more complex model of the path shape is needed to accurately model this behavior. The predictions also fall short when used to predict insertion forces for very small curvatures. In this case, the good prediction requires tunnel diameters to be very close to the beam diameter. This discrepancy is exposed in Figure 90 and explained in Figure 91. The use of a more accurate shape description of the beam will improve the predictions of the insertion force for both the low curvature paths and for large clearances.

The 3D auto router has had good success with a number of routing problems. The software used PCB rip-up and reroute and shove aside algorithms leveraged into the 3D domain. The global minimization techniques of multiple start algorithms, simulated annealing and steepest descent were also used with generally good success. For simple problems, with the spacing of start and end points at least double the path diameter and a small number of paths (less than 10), the router will typically find a solution in just a few seconds. For more complicated test cases (page 213), with a denser pitch and more paths, routing may take a few minutes. For the applications with dense pitch and 64 or 128 paths (Figure 111 and Figure 112) the auto-router would find and length match a solution in a matter of a few days. The development of the 3D routing software required

extensive use of 3D geometry, vector algebra and splines. The lowest level code, written in Java, established the basic building blocks of splines, circular arcs, plane curves and space curves. From that geometry, paths made up of multiple segments with tangent continuity were created. Once contiguous paths could be created, path search algorithms were made to find non-intersecting, length-matched paths in a constrained volume. A preprocessor seeded the path searching algorithms to give good initial global search results. Solution searching algorithms built on the path searching methods were shown to have good success for most problems encountered. The field of auto-routing multiple smooth paths in 3D space is almost entirely unexplored. The use of limited DOF splines worked well to limit the search space without sacrificing the necessary freedom to find solutions. When the path searching algorithm is unable to find an appropriate path using a limited DOF path (page 219), the DOF of that path (and others) can be increased until a solution is found. Improvements to the routing algorithm and suggestions for future work are discussed in section 8.1. Other path searching algorithms that are more "intelligent" than the "smart" adaptive search algorithm discussed in section 6.2.3.3 could speed up the search speed and could be a very rich area of research in new algorithms. Very little research has been directed toward 3D smooth path algorithms, likely due to the limited applicability of such an algorithm. It is hoped that this application will spur new research in the relatively unexplored areas of 3D routing.

9.2. Summary

The idea of creating a routing manifold using additive manufacturing is noteworthy. This process has not been disclosed and a patent application has been filed. The use of additive manufacturing (SLA and others) provides a unique way to make a

routing manifold that will improve its capabilities as additive manufacturing capabilities (Chapter 4) mature. Future applications that take advantage of the process are discussed in Section 8.3. It is hoped that many new applications will be found for this unique process.

The process to create a high speed electrical funnel has been investigated in detail and has been shown to be feasible. Two major challenges (the routing and the understanding of the insertion force) has been tackled in this thesis. Each major processing step has been attempted with good success. To bring this solution to medium volume production a few other things must be pursued.

- An automated insertion machine (with a XY stage) to drive coaxial cables into any block. This machine can use the same basic mechanics developed for the experimental test apparatus (shown on page 98).
- More development of the software router. Use of grid computing to speed up solution searching (page 241). Additional development of the software to make it more user-friendly.
- Connector development. As designed, the 3DST requires a small interposer to connect to a printed circuit board for a final connection to the DUT. Many interposers are available that may work, but they have not been tested. Furthermore, it may be possible to forgo the interposer entirely and instead bond a microvia board to the top and bottom sides after the metal plates are applied.

- For high temperature applications, the SLA material chosen may soften and cause issues and thus a new material may be required (possibly one of the high temperature SL materials).

The use of a routing manifold to create a product that is superior to a PCB for high speed signal routing for testing microprocessors and other high speed electronic devices has been disclosed. The use of coaxial wires is superior to PCB trace as was shown in Chapter 3. The ability of the 3DST to improve the process yields is a significant improvement over the PCB it replaces. While this thesis has described a process to create a unique high-speed electrical funnel, the other applications for this technology are immeasurable.

Routing of smooth paths in 3D space is a relatively new field. The use of low DOF path splines made finding solutions relatively straightforward. The use of out-of-plane paths was required for certain solutions (due to crossovers) and adding that degree of freedom to the paths when necessary kept the solution search space from growing unnecessarily large.

The insertion force of the beams into these tunnels was predicted over a relatively wide range of curvatures with generally good accuracy and description of trends as the beam is inserted without resorting to numerical solutions or empirical fits. Better accuracy could certainly be obtained by using one of both of these techniques but that accuracy is not required for this project. The ability to quickly calculate the insertion force at each point along the path is necessary because it is not always obvious where along the path the maximum insertion force occurs. The description of the forces is non-

intuitive at first, but the few relatively simple equations developed help provide a deeper understanding of the insertion forces.

The unique process used to create the 3DST creates a host of unique challenges. The development of a 3D auto-router using simulated annealing and adaptive path searching and a description of the insertion forces of a beam including elastic-plastic forces, clearance between the tunnel walls and friction are the first two challenges that have been tackled. Development of the 3DST to full production will likely bring many new and interesting challenges.

10. References

1. *3D Systems technical literature.* 3D Systems. Valencia, CA. 2002.
2. *A Low Loss Dielectric for High Frequency HDI Substrates and PCBs.* Microwave Journal. pp. 138-146. Dec 2000.
3. *ABAQUS/Standard User's Manual.* Vol 3. Ver 6.2. Hibbitt, Karlsen & Sorensen Inc. pp 23.1.2-1 – 23.3.1-7. 2001.
4. Ahuja, Mehlhorn, Orlin and Trajan. *Faster Algorithms for the Shortest Path Problem.* Technical Report 193, MIT Operations Research Center, 1988.
5. Ashby, M.F. *Materials Selection in Mechanical Design.* Pergammon Press Ltd. Oxford, England. 1992.
6. Baase, Sara. *A Gift of Fire: social, legal and ethical issues in computing.* Prentice-Hall. Inc. Upper Saddle River, NJ. 1997
7. Braun, Douglas, J. Burns, S. Devadas, H. Ma, K. Mayaram, F. Romeo and A. Sangiovanni-Vincentelli. *Chameleon: A New Multi-Layer Channel Router.* IEEE 23rd Design Automation Conference. pp495-502. 1986.
8. Braun, Douglas, J. Burns, F. Romeo, A. Sangiovanni-Vincentelli, K. Mayaram, S. Devadas and H. Ma. *Techniques for Multilayer Channel Routing,* IEEE Transactions on Computer Aided Design. Vol. 7, No 6. June 1988.
9. Brayton, R., G. Hachtel, and A. Sangiovanni-Vincentelli. *A Survey of Optimization Techniques for Integrated Circuit Design,* Proceedings of IEEE, Vol 69, No 10 pp1336-1361, October 1981.
10. Chen, Howard H. *Trigger: A Three-Layer Gridless Channel Router,* Digest of Technical Papers, IEEE International Conference on Computer Aided Design, pp 196-199, November 1986.
11. Cormen, Thomas H., Charles E. Leiserson and Ronald L. Rivest. *Introduction to Algorithms.* McGraw-Hill Book Company, New York, 1990.
12. Crandall, Stephen, Norman Dahl and Thomas Lardner. *An Introduction to the Mechanics of Solids.* 2nd ed. McGraw Hill, Inc. NY, NY. 1978.

13. Dally, Bill. EE482B: *Advanced Computer Organization Interconnection Networks Architecture and Design. Routing* Stanford University. Lecture #6 Notes. April 23, 2001.
14. Dareing, D.W and C.A. Ahlers. *Tubular Bending and Pull-Out Forces in High-Curvature Well Bores*. Journal of Energy Resources Technology, AMSE, pp133-139, Vol 113, June 1991
15. Dees, William and Patrick Karger. *Automated Rip-Up and Reroute Techniques.* Proc. IEEE 19th Design Automation Conference. pp 432-439, 1982.
16. *Dielectric Materials*. www.goreelectronics.com/products/dielectric_materials/Die_Mat.html. 2003.
17. *Differential Geometry of Curves*. mathworld.wolfram.com. 2002.
18. Dijkstra, E.W. *A Note on Two Problems in Connexion with Graphs*. Numerische Mathematik pp 269-271. 1959.
19. Dowling, Norman. *Mechanical Behavior of Materials.* Prentice-Hall. Inc. Upper Saddle River, NJ. 1993
20. Efrat, A., S Kobourov, M. Stepp and C. Wenk. *Growing Fat Graphs.* Proceedings of the Eighteenth Annual Symposium on Computational Geometry. Barcelona, Spain. June 5-7, 2002.
21. Elchalakani, Mohamed, Raphael Grzebieta and Xiao-Ling Zhao. *Plastic Collapse Analysis of Slender Circular Tubes Subjected to Large Deformation Pure Bending*. Advances in Structural Engineering. Vol 5. No 4. 2002.
22. *Embedded Coaxial Wires Speed Printed-Circuit Board.* Electronics. pp. 56-57. Jan 27, 1986.
23. Gonzales, Teofilo F. and Si-Qing Zheng. *Single phase three-layer channel routing algorithms.* Integration. No. 17, pp 141-151. 1994.
24. Goto, S. and Alberto L. Sangiovanni-Vincentelli. *A New Shortest Path Updating Algorithm,* Networks, Vol. 8, No 4, pp 341-372. Winter 1978.
25. Greenberg, Michael. *Advanced Engineering Mathematics*. 2nd. ed. Prentice-Hall, Inc. Upper Saddle River, NJ. 1998.
26. Groover, Mikell. *Fundamentals of Modern Manufacturing*. Prentice-Hall, Inc. Upper Saddle River, NJ. 1996.

27. Hall, Stephen, Garrett Hall and James McCall. *High Speed Digital System Design, A Handbook of Interconnect Theory and Design Practices.* John Wiley & Sons, Inc. NY, NY. 2000.
28. Hama, Toshiyuki and Hiroaki Etoh. *Topological Routing Path Search Algorithm with Incremental Routability Test.* IEEE Transactions on Computer Aided Design of Integrated Circuits and Systems. pp 142-150. Vol. 18, No. 2, Feb 1999.
29. Harper, Charles. *High Performance Printed Circuit Boards.* McGraw-Hill Inc. NY, NY. 2000.
30. Hayes, Brian. *On the Threshold.* American Scientist. pp 12-17. Jan-Feb 2003.
31. Hayt, William. *Engineering Electromagnetics.* 5th ed. McGraw-Hill Co. NY,NY. 1989.
32. Hoschek, Josef and Dieter Lasser. *Fundamentals of Computer Aided Geometric Design.* A.K. Peters Ltd. Wellesley, MA. 1989.
33. *Intel Microprocessor Hall of Fame.* www.intel.com. 2003.
34. Johnson, Howard and Martin Graham. *High-Speed Digital Design: A Handbook of Black Magic.* Prentice-Hall. Inc. Upper Saddle River, NJ. 1993
35. Johnson, Howard and Martin Graham. *High Speed Signal Propagation: Advanced Black Magic.* Prentice-Hall. Inc. Upper Saddle River, NJ. 2003
36. Kalpakjian, Serope and Steven Schmid. *Manufacturing Engineering and Technology.* Fifth Edition. Prentice-Hall. Inc. Upper Saddle River, NJ. 2001
37. Kirkpatrick. S, C Gelatt and M Vecchi. *Optimization by Simulated Annealing.* Science. Vol. 220, No 4598. pp 671-680. May 13, 1983.
38. Kochan, Anna. *Rapid Prototyping Roundup.* Design News. Feb. 16, 1998.
39. Kuru, Ergun, Alexander Martinez, Stefan Miska. *The Buckling Behavior of Pipes and Its Influence on the Axial Force Transfer in Directional Wells.* , Journal of Energy Resources Technology, AMSE, pp129-135, Vol 112, Sept 2000.
40. Lee, C.Y. *An Algorithm for Path Connection and its Applications.* IRE Transactions on Electronic Computers, EC-10(3). pp 346-365, 1961.
41. Leiserson, Charles and Ron Pinter. *Optimal Placement for River Routing.* SIAM Journal of Computing. Vol 12, No. 3, August 1983.

42. Leiserson, Charles and F. Miller Maley. *Algorithms for Routing and Testing Routability of Planar VLSI Layouts.* 17th ACM SIGACT Symposioum on Theory of Computing, Providence, Rhode Island. May 6-8, 1985.
43. Liu, Le-Chin Eugene and Carl Sechen. *Multilayer Chip-Level Global Routing Using an Efficient Graph-Based Steiner Tree Heuristic.* IEEE Transactions on Computer Aided Design of Integrated circuits and Systems. Vol 18, N0 10. Oct. 1999.
44. Maley, F. Miller. *Single Layer Wire Routing.* PhD Thesis MIT. August 1987.
45. McCann, Roger C., P.V.R Suryanarayana. *Horizontal Well Path Planning and Correction Using Optimization Techniques.* Journal of Energy Resources Technology-ASME. pp 187-193. Vol. 123 Sept. 2001
46. Mortenson, M.E. *Mathematics for Computer Graphics Applications.* 2nd ed. Industrial Press, Inc. 1999.
47. Miele A., T. Wang, C. Chao, and J Dabney. *Optimal Control of a Ship for Collision Avoidance Maneuvers.* Journal of Optimization Theory and Applications. Vol 103, No. 3 pp 495-519. December 1999.
48. Miele, A., Huang H.Y. and Hiedeman J.C. *Sequential Gradient Restoration Algorithm for Minimization of Constrained Functions, Ordinary and Conjugate Versions.* Journal of Optim. Theory Applications. pp 213-243 Vol 4. No 4, 1969.
49. Moore, Edward F. *The Shortest Path Through a Maze.* Proceedings of the International Symposium on the Theory of Switching. pp 285-292. Harvard University Press, 1959
50. Moore, Gordon. *Cramming more components onto integrated circuits.* Electronics, vol 38, No 8. April 19, 1965
51. Mosse, CA, Mills, TN, Bell, GD, Swain, CP. *Device for measuring the forces exerted on the shaft of an endoscope during colonoscopy.* Medical and Biological Engineering and Computing. pp 186-190. Vol 36. No 2. Mar 1998.
52. Murphy, Matt. *The Future of Additive Manufacturing.* Time Compression Technologies. Vol. 5 No. 3
53. Myklestad, Nils O. *Statics of Deformable Bodies.* pp316-326. MacMillan Company. New York. 1966

54. Papadimitriou C.H. *An Algorithm for Shortest Path Motion in Three Dimensions.* Information Processing Letters. pp 259-263. Vol 20 1985.
55. Plummer, James, Michael Deal and Peter Griffin. *Silicon VLSI Technology: Fundamentals, Practice and Modeling.* Prentice-Hall. Inc. Upper Saddle River, NJ. 2000.
56. *Processors.* www.harwarecentral.com. June 2001 and December 2002.
57. *Rapid Prototyping.* www.efunda.com. 2003.
58. Rivest, Ronald and Charles Fiduccia. *A "Greedy" Channel Router.* Proc. IEEE 19th Design Automation Conference. pp 418-424, 1982.
59. Salvage, Seward, Aiche Riad and Sedki Riad. *Design and Construction of a Thick Film Shielded Transmission Line.* 1981 IEEE Southeastcon Conference Proceedings. pp 7-11.
60. Sangiovanni-Vincentelli, Alberto and Mauro Santomauro. *Optimal Printed Circuit Board Ordering via Hart-Nilsson-Raphael Algorithm,* International Journal on Circuit Theory and Applications, Vol. 7, No 2, pp 247-256, April 1979.
61. Seibi, A.C. and A.M. Al-Shabibi. *Pipe Bending and Running Forces in Medium to High Curvature Wells Using Finite Element Analysis.* Journal of Energy Resources Technology, AMSE, pp 263-267, Vol 120, Dec 1998
62. Seibi, AC, Gastli, A, Al-Shabibi, A, Abdullah, HA. *Prediction of running forces in high curvature well bores using finite element analysis and artificial neural network.* Petroleum Science and Technology. pp 521-534. Vol 19. 2001
63. *Semi-Rigid Micro-Coax.* www.microcoax.com/semirigid/semirigid_MIL17.html. 2002.
64. Shin, Hyunchui and Alberto Sangiovanni-Vincentelli. *Mighty: A 'Rip-Up and Reroute' Detailed Router.* Proc. IEEE ICCAD Santa Clara CA. Nov.1986
65. Shigley, J. and C. Mischke. *Mechanical Engineering Design.* 5th ed. NY, NY. McGraw-Hill, Inc. 1989.
66. Singh, Gurkirpal, Fred Hadaegh. *Autonomous Path-Planning for Formation Flying Applications.* NASA Tech Brief, Vol 26, No.3. March 2002.
67. *Suhner RF Connector Guide.* Huber+Suhner AG. Switzerland, 1996.

68. Swengel, Robert C. Timothy Lemke and Fredrick Villard. *A Coaxial Interconnection System for High Speed Digital Processors.* IEEE Transactions on Parts, Hybrids and Packaging Vol. PHP. 10, No. 3. September 1974. pp181-187

69. Szczerba, Robert J., Danny Z. Chen and John J Uhran Jr. *Planning Shortest Paths among 2D and 3D Weighted Regions Using Framed Subspaces.* International Journal of Robotics Research. Vol. 17 No 5. pp 531-546. May 1998

70. Szykman, S. and J. Cagan. *Synthesis of Optimal Nonorthogonal Routes.* Journal of Mechanical Design, ASME. Vol. 118, pp 419-424, Sept. 1996.

71. Tan , X.C. and B. Forsman. *Buckling of Slender String in Cylindrical Tube Under Axial Load: Experiments and Theoretical Analysis*, Experimental Mechanics. pp55-60, March 1995

72. *The Abacus: Introduction.* www.ee.ryerson.ca:8080/~elf/abacus/intro.html. 2003.

73. *The Leary Tetrahedron: A New Approach to Global Optimization.* NPACI & DSC Online. Vol. 3, Issue 19. www.npaci.edu/online/v3.19/leary.html September 15, 1999.

74. Timoshenko S. *Theory of Elastic Stability.* McGraw-Hill Book Company. New York, 1936.

75. Ulaby, Fawwaz. *Fundamentals of Applied Electromagnetics.* Prentice-Hall, Inc. Upper Saddle River, NJ. 1997.

76. Umakanta Choudhury and Alberto L. Sangiovanni-Vincentelli. *Constraint Based Channel Routing for Analog and Mixed Analog/Digital Circuits.* , IEEE Transactions on Computer Aided Design of Integrated Circuits and Systems. pp. 497-510, April 1993.

77. Vaillette, D.P. and G.G. Adams, *An Elastic Beam Contained in a Frictionless Channel.* ASME Journal of Applied Mechanics, Vol. 50, No. 3, 1983, pp. 693-694.

78. Veen, Frederick. *Teradyne: The First Forty Years.* Teradyne, Inc. 2001.

79. Wadell, Brian. *Transmission Line Design Handbook.* Artech House, Norwood MA. 1991

80. Wehrmeyer, JA, Barthel, JA, Roth, JP, Saifuddin, T. *Colonoscope flexural rigidity measurement.* Medical and Biological Engineering and Computing. pp 475-479 Vol 36. No 4. Jul 1998.
81. Wu, J. and H.C. Juvkam-Wold. *The Effect of Well bore Curvature on Tubular Lockup*, Journal of Energy Resources Technology, AMSE, pp214-218, Vol 117, Sept 1995
82. Xiong, J.G. *Algorithms for Global Routing,* Proc. of 23rd Design Automation Conference. pp 824-830, July 1986
83. Xiong, J.G. *Gridless Maze Router: DBM (Diffraction Boundary Method,* Digest of Technical Papers, IEEE International Conference on Computer Aided Design, pp 192-195, November 1986.
84. Xiong, Xiao-Ming. *A New Algorithm for Topological Routing and Via Minimization,* Digest of Technical Papers, IEEE International Conference on Computer Aided Design, pp 410-413, November 1988.
85. Young, Warren. *Roark's Formulas for Stress and Strain.* 6th ed. McGraw Hill, Inc. NY, NY. 1989.

11. Appendix

The elastic-plastic bending moment for a solid circular beam

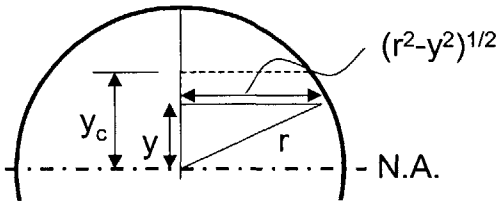

Figure 131 - An elastic beam cross-section under pure bending

$$M = \int EI / R$$

$$M = 4E / R \iint y^2 dA$$

$$M = 4E / R \iint y^2 dw dh$$

$$M = 4E / R \int_0^{y_c} y^2 \left(r^2 - y^2\right)^{1/2} dy$$

INTEGRATE

$$M = 4E / R \left[-\frac{1}{4} y \left(r^2 - y^2\right)^{3/2} + \frac{1}{8} r^2 y \left(r^2 - y^2\right)^{1/2} + \frac{1}{8} r^4 \tan^{-1} \left(\frac{y}{\left(r^2 - y^2\right)^{1/2}} \right) \right]_0^r$$

$$M = 4E / R \left(\frac{1}{8} r^4 (\pi / 2) \right)$$

$$M = \pi E r^4 / 4R$$

The elastic bending moment for a partial circular beam (from 0 to y_c)

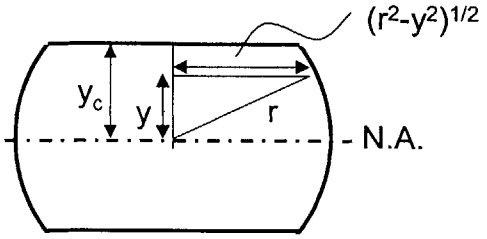

Figure 132 - The elastic part of a beam under pure bending

$$M = \int EI / R$$

$$M = 4E / R \iint y^2 dA$$

$$M = 4E / R \iint y^2 dwdh$$

$$M = 4E / R \int_0^{y_c} y^2 \left(r^2 - y^2\right)^{1/2} dy$$

INTEGRATE

$$M = 4E / R \left[-\frac{1}{4} y \left(r^2 - y^2\right)^{3/2} + \frac{1}{8} r^2 y \left(r^2 - y^2\right)^{1/2} + \frac{1}{8} r^4 \tan^{-1} \left(\frac{y}{\left(r^2 - y^2\right)^{1/2}} \right) \right]_0^{y_c}$$

Let $X = \left(r^2 - y_c^2\right)^{1/2}$

$$M = 4E / R \left[-\frac{1}{4} y_c X^3 + \frac{1}{8} r^2 y_c X + \frac{1}{8} r^4 \tan^{-1} \left(\frac{y_c}{X} \right) \right]$$

The plastic bending moment for a partial circular beam (from to y_c to r)

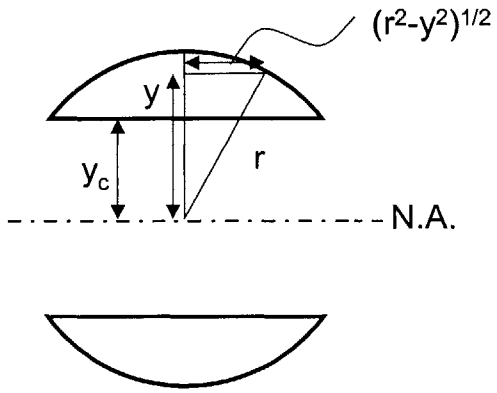

Figure 133 - The plastic part of a beam under pure bending

$$M = 4\sigma_y \iint y dA$$

$$M = 4\sigma_y \iint y dw dh$$

$$M = 4\sigma_y \int_{y_c}^{r} y\left(r^2 - y^2\right)^{1/2} dy$$

INTEGRATE

$$M = 4\sigma_y \left(\frac{1}{3}\left(r^2 - y_c^2\right)^{3/2} \right)$$

Let $X = \left(r^2 - y_c^2\right)^{1/2}$

$$M = \frac{4\sigma_y}{3} X^3$$

Determination of d_c – when a straight beam hits the curved wall

R_o = Outer radius of tunnel
R_i = Inner radius of tunnel
R = Center radius of tunnel
d_{beam} = Diameter of beam
d_{tunnel} = Diameter of tunnel

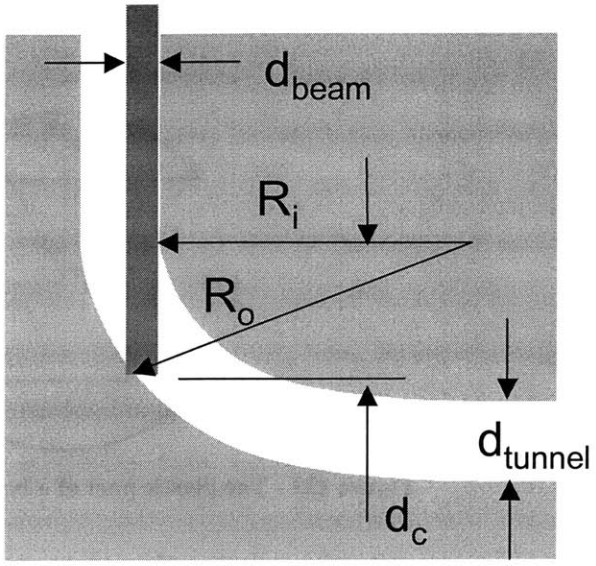

Figure 134 - A straight beam inserted into a curved segment at first contact with the wall

$$d_c^2 + \left(R_i + d_{beam}\right)^2 = R_o^2$$

$$R_i = R - \tfrac{1}{2} d_{tunnel}$$

$$R_o = R + \tfrac{1}{2} d_{tunnel}$$

COMBINE

$$d_c^2 + \left(R - d_{tunnel}/2 + d_{beam}\right)^2 = \left(R + d_{tunnel}/2\right)^2$$

$$d_c = \sqrt{2Rd_{tunnel} - 2Rd_{beam} + d_{tunnel}d_{beam} - d_{beam}^2}$$

Determine the curvature of an elastic beam in a tunnel with clearance

R_o = Outer radius of tunnel
R_i = Inner radius of tunnel
r_o = Outer radius of beam
d = Diameter of beam
c = Clearance in tunnel
θ_3 = Insertion Angle
x = distance from centerpoint of tunnel radius to centerpoint of beam radius

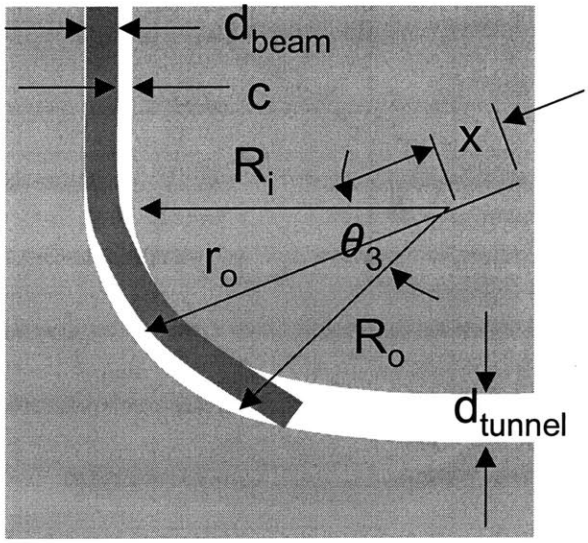

Figure 135 - A straight beam taking the minimum curvature when inserted into a curved segment

$$x = d + R_i - r_o$$

$$d + c + R_i = R_o$$

$$r_o^2 = R_o^2 + x^2 - 2R_o x\cos(\theta_3/2) \quad \text{Law of cosines}$$

COMBINE

$$r_o^2 = R_o^2 + d^2 + 2dR_i - 2dr_o + R_i^2 - 2R_i r_o + r_o^2 - 2R_o(d + c + R_i)\cos(\theta/2)$$

$$r_o = \frac{R_o^2 + d^2 + 2dR_i + R_i^2 - 2R_o(d + R_i)\cos(\theta_3/2)}{2(d + R_i - R_o\cos(\theta_3/2))}$$

Determine the curvature of an initially curved beam in a straight segment

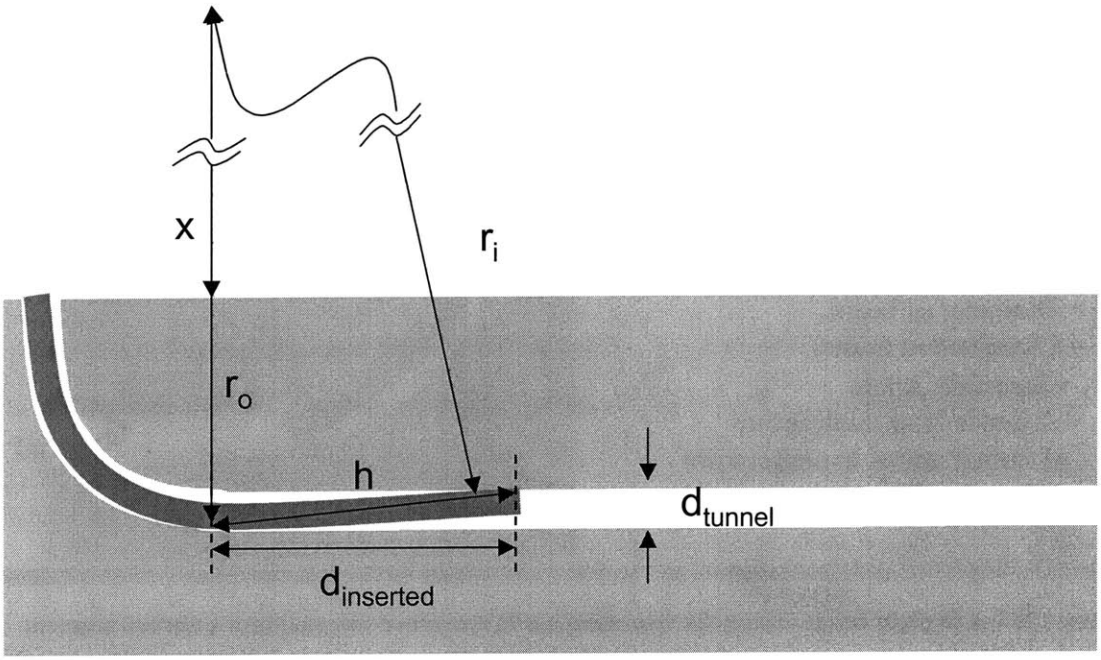

Figure 136 - An initially curved beam inserted into a straight segment

h = Distance from start point to tip of beam
$d_{inserted}$ = Linear distance inserted along tunnel
r_o = Outer radius of beam
d_{beam} = Diameter of Beam

$$h^2 = d_{inserted}^2 + d_{tunnel}^2$$

$$x = r_o - d_{tunnel}$$

$$x^2 + d_{inserted}^2 = r_i^2$$

$$r_i = r_o - d_{beam}$$

COMBINE

$$\left(r_o - d_{tunnel}\right)^2 + \left(d_{inserted}\right)^2 - \left(r_o - d_{beam}\right)^2 = 0$$

$$2r_o\left(d_{beam} - d_{tunnel}\right) + d_{tunnel}^2 + d_{inserted}^2 - d_{beam}^2 = 0$$

$$r_o = \frac{d_{beam}^2 - d_{tunnel}^2 - d_{inserted}^2}{2\left(d_{beam} - d_{tunnel}\right)}$$

Determine the curvature of an initially curved beam into lower curved segment

R_o = Outer radius of tunnel
R_i = Inner radius of tunnel
r_o = Outer radius of beam
r_i = Inner radius of beam
d = Diameter of beam
θ_3 = Insertion Angle
x = distance from centerpoint of beam radius to inner edge of tunnel wall
y = distance from inside edge of tunnel at start of segment to tip of beam

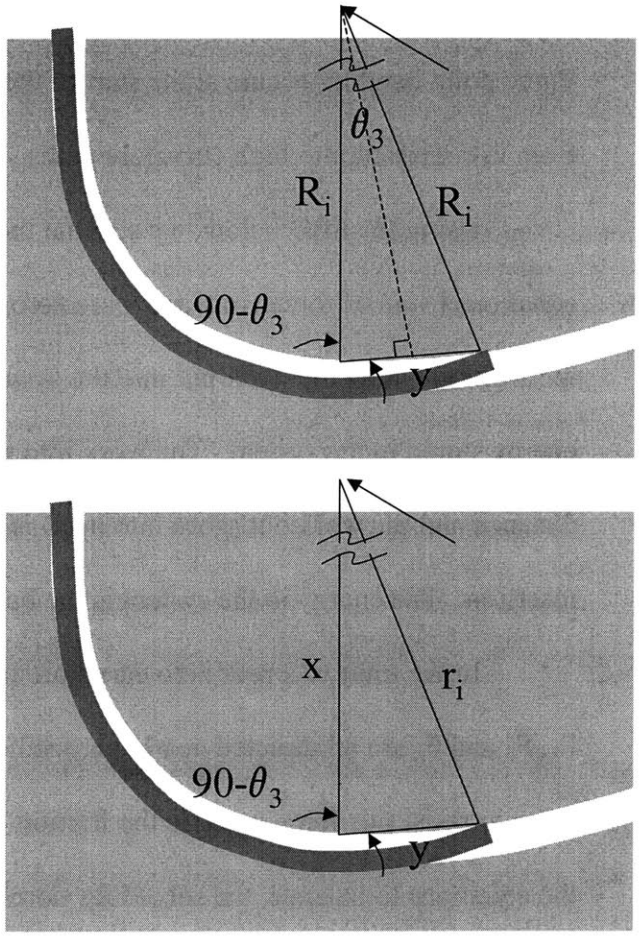

Figure 137 - An initially curved beam inserted into a segment of lesser curvature

$$x = r_o - d_{tunnel}$$

$$y = 2R_i \sin(\theta_3/2)$$

$$x^2 + y^2 - 2xy\cos(90 - \theta_3/2) = r_i^2 \qquad \text{Law of cosines}$$

COMBINE

$$(r_o - d_{tunnel})^2 + y^2 - 2(r_o - d_{tunnel})y^2\cos(90 - \theta_3/2) = (r_o - d_{beam})^2$$

EXPAND and SET $\cos(90 - \theta_3/2) = \sin(\theta_3/2)$

$$r_o^2 - 2d_{tunnel}r_o + d_{tunnel}^2 + y^2 - 2r_o y\sin(\theta_3/2) + 2d_{tunnel}y\sin(\theta_3/2) = r_o^2 - 2d_{beam}r_o + d_{beam}^2$$

$$r_o = \frac{d_{beam}^2 - d_{tunnel}^2 - y^2 - 2yd_{tunnel}\sin(\theta_3/2)}{2(d_{beam} - d_{tunnel} - y\sin(\theta_3/2))}$$

Three point bending model

Three point bending occurs at the start of the first curved segment and at the transition from low curvature to high curvature paths.

Using the FBD below, we see that there are 4 unknown forces and just 3 equations (Sum of forces in x and y are zero, sum of the moments is zero.) Fortunately, we also know that the work put into the system equals the work out of the system plus the energy stored in the system. The work into the system is the force of insertion times the distance and the work out (goes into heat) is generated from the friction force that resists insertion. The energy in the system is the bending strain energy in the beam.

In the limit of a near zero curvature (the radius is very large), the normal forces F_1, F_2 and F_3 are all directed nearly perpendicular to the insertion force. Thus, the only thing to resist this force must be the friction force generated by the normal forces. For all the equations to balance, the solved for normal forces must be high enough to create enough friction force to resist F_{insert}. This would imply that as the coefficient of friction decreased, the normal forces have to increase to balance the forces along the direction of the beam. Of course this is not the case, the normal forces depend on the moment required to bend the beam.

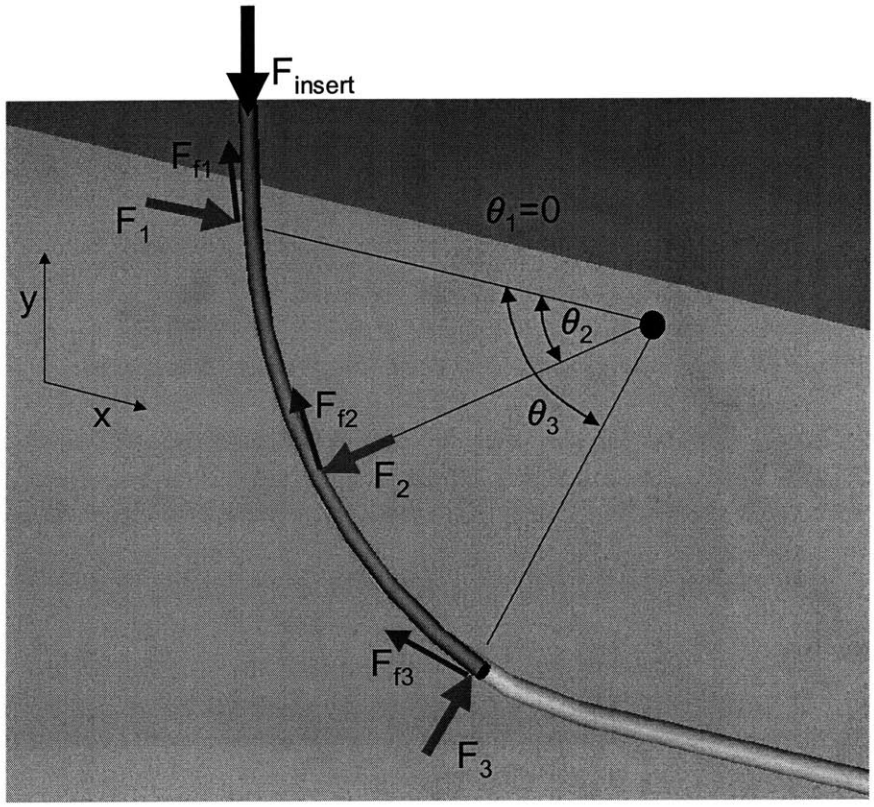

Figure 138 - FBD of three point bending model

$$\sum F_x = 0$$

$$F_1\cos\theta_1 - F_2\cos\theta_2 + F_3\cos\theta_3 - \mu F_1\sin\theta_1 - \mu F_2\sin\theta_2 - \mu F_3\sin\theta_3 = 0$$

$$F_1\left(\cos\theta_1 - \mu\sin\theta_1\right) - F_2\left(\cos\theta_2 + \mu\sin\theta_2\right) + F_3\left(\cos\theta_3 - \mu\sin\theta_3\right) = 0$$

$$\sum F_y = 0$$

$$F_1\sin\theta_1 - F_2\sin\theta_2 + F_3\sin\theta_3 + \mu F_1\cos\theta_1 + \mu F_2\cos\theta_2 + \mu F_3\cos\theta_3 - F_{insert} = 0$$

$$F_1\left(\sin\theta_1 + \mu\cos\theta_1\right) - F_2\left(\sin\theta_2 - \mu\cos\theta_2\right) + F_3\left(\sin\theta_3 + \mu\cos\theta_3\right) - F_{insert} = 0$$

$$\sum M_{@point1} = 0$$

$$F_{insert}\left(d_{beam}/2\right) + \left(F_2\cos\alpha_2 - \mu F_2\sin\alpha_2\right)\ell_2 - \left(F_3\cos\alpha_3 - \mu F_3\sin\alpha_3\right)\ell_3 = 0$$

$$F_{insert}\left(d_{beam}/2\right) + F_2\ell_2\left(\cos\alpha_2 - \mu\sin\alpha_2\right) - F_3\ell_3\left(\cos\alpha_3 - \mu\sin\alpha_3\right) = 0$$

$$\Delta W_{in} = \Delta U_{beam} + \Delta W_{out}$$

$$F_{insert}\Delta x = F_{insert(w/o\ friction)}\Delta x + \mu\left(F_1 + F_2 + F_3\right)\Delta x$$

$$F_{insert} = F_{insert(w/o\ friction)} + \mu\left(F_1 + F_2 + F_3\right)$$

This gives four equations and four unknowns.

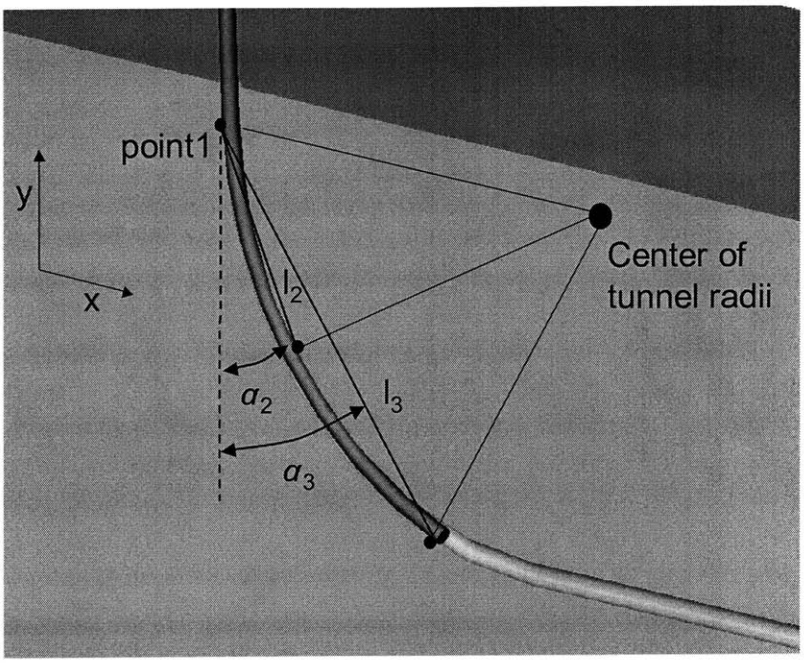

Figure 139 - The 3 point bending model with the variables used for summation of the moments

The insertion force has been solved for, however the equations predict exceedingly high forces (one to two orders of magnitude higher than experimental values). As was stated above, the fourth energy balance equation when used in low curvature tunnels predicts the normal forces must increase dramatically for lower friction coefficients and a different fourth equation should likely be used. This is left for future work.